

**Imaging the uptake, distribution and  
metabolism of agrochemicals  
using MALDI mass spectrometry imaging**

**DISSERTATION**

Submitted for the degree of doctor of natural sciences  
(Dr. rer. nat.)

Submitted to the  
Department of Chemistry and Chemical Biology  
TU Dortmund

by  
**Michael Kubicki**  
from Recklinghausen



This work was done from May 2016 till July 2019 under the guidance and supervision of Priv.-Doz. Dr. Souvik Kusari, at the Institute of Environmental Research (INFU), Department of Chemistry and Chemical Biology, Chair of Environmental Chemistry and Analytical Chemistry, TU Dortmund, Germany.

1. Referee: Priv.-Doz. Dr. Souvik Kusari

2. Referee: Prof. Dr. Daniel Rauh

*„Von M für M“*

Parts of this work have already been published or are planned for publication:

### **Publication**

Kubicki, M., Giannakopoulos, G., Lamshöft, M., Dittgen, J. Spatially resolved investigation of herbicide - safener interaction in maize (*Zea mays* L.) by MALDI-imaging mass spectrometry in *J Agric Food Chem*, 2022, Under Review.

### **Poster**

Kubicki, M., Lamshöft, M., Spiteller, M. Imaging the uptake, distribution and metabolism of agrochemicals using MALDI-imaging mass spectrometry. Thermo Scientific User Treffen, Monheim, July 2017.

Kubicki, M., Lamprecht, S., Doughty, K., Lamshöft, M., Spiteller, M. Spatially resolved investigation of a systemic plant protection product in grape vine (*Vitis vinifera*) by MALDI-imaging mass spectrometry. 11· Tag der Chemie, Dortmund, February 2018.

Kubicki, M., Lamshöft, M., Spiteller, M. Imaging the distribution of agrochemicals in plant by MALDI-MSI. Innovation Day, Monheim, August 2018.



## **Acknowledgment**

First, I would like to express my special thanks to Priv.-Doz. Dr. Souvik Kusari, Head of Chemical Microbiology at the Institute for Environmental Research of the Faculty of Chemistry and Chemical Biology of the University of Dortmund, not only for taking over the supervision, but also for the unswerving scientific exchange, the supervision of all research approaches and support, especially for any topics in the field of microbiology.

I would like to thank Prof. Dr. Daniel Rauh from the Department of Medical Chemistry and Chemical Biology of the Faculty of Chemistry and Chemical Biology of the University of Dortmund for his willingness to take over the co-department.

I would like to thank Prof. Dr. Dr. h.c. Michael Spiteller for the opportunity to do this work in his research group. The outstanding technical equipment at the Institute for Environmental Research of the Faculty of Chemistry and Chemical Biology of the University of Dortmund made the thesis in this framework possible. It gave me a very interesting insight into the special field of mass spectrometry.

Further thanks are due to Bayer AG Division Crop Science in Monheim for the cooperation and partly financial support of this work. My special thanks go to Dr. Marc Lamshöft for his intensive support and constant suggestions during all parts of the work. I would also like to thank all Metabolism & Kinetics group employees for the pleasant working atmosphere in Monheim. Finally, I would like to thank Dr. Birgit Neumann, Dr. Andreas Stork, DI Andreas Lagojda and the whole structure elucidation team for the possibility to run mass spectrometry measurements and Thomas Jantzen and his team for radiochemical analysis.

I would like to thank all employees and students at the Institute for Environmental Research for the lovely working atmosphere in Dortmund, especially Philipp Püttmann, Andreas Hermann, Carina Seitz, Lars Janniak, Reyhaneh Armin and Gabriele Hardes. I would like to thank Dr. Sebastian Zühlke for his support during the whole time. I would like to thank my group colleagues, Dr. Selahaddin Sezgin and Dr. Dennis Eckelmann, for the nice atmosphere in the daily lab work as well as for the wiliness to help by any questions or problems.

Finally, I would especially like to thank my wife Jennifer, my parents, and my family for their endless support in every situation in my life. Without them, this work would not have been possible.





## Table of content

<b>Abstract</b> .....	1
<b>Zusammenfassung</b> .....	3
<b>1 Introduction</b> .....	5
<b>1.1. Plant protection products</b> .....	5
<b>1.1.1. Fungicides</b> .....	6
<b>1.1.2. Herbicides</b> .....	11
<b>1.1.3. Insecticides</b> .....	12
<b>1.2. Pesticide Analysis</b> .....	14
<b>1.3. Mass Spectrometry Imaging of plant tissues</b> .....	17
<b>1.4. Matrix-assisted laser desorption/ionization mass spectrometry</b> .....	19
<b>1.5. Sample preparation for MALDI mass spectrometry imaging of plant tissues</b> .	22
<b>2 Aims and objectives</b> .....	25
<b>3. Material and methods</b> .....	27
<b>3.1. Instruments</b> .....	27
<b>3.2. Software</b> .....	28
<b>3.3. Chemicals</b> .....	29
<b>3.3.1. Isotope labeled chemicals</b> .....	29
<b>3.3.2. Reference and standard chemicals</b> .....	30
<b>3.4. HPLC solvents</b> .....	31
<b>3.5. MALDI matrices</b> .....	31
<b>3.6. Plants</b> .....	31
<b>3.6.1. Nutrient solution</b> .....	31
<b>3.6.2. Cultivation</b> .....	32
<b>3.6.3. Hydroponic test system</b> .....	32
<b>3.6.4. Single droplet application</b> .....	32
<b>3.6.5. Greenhouse conditions</b> .....	33
<b>3.6.6. Vegetation hall</b> .....	33
<b>3.7. HPLC measurements</b> .....	33
<b>3.8. Radioactivity measurements</b> .....	35
<b>3.9. Sample preparation MALDI mass spectrometry imaging</b> .....	35
<b>3.10. Histochemical staining of plant issues</b> .....	36
<b>3.11. MALDI Mass Spectrometry Imaging</b> .....	37
<b>4. Results and Discussion</b> .....	39
<b>4.1. Phytotoxicity of isotianil and its metabolite DCIT-acid</b> .....	39

4.1.1. Optimization of detection of isotianil and DCIT-acid with MALDI MS .....	39
4.1.2. Spatial distribution of isotianil and DCIT-acid in hydroponic grown wheat..	41
4.1.3. Uptake of isotianil and DCIT-acid in hydroponic grown tomato.....	43
4.1.4. Uptake and surface adsorption of isotianil on tomato leaves after droplet application.....	48
4.1.5. Uptake and surface adsorption of Isotianil on banana leaves after droplet application.....	49
4.1.6. Uptake and surface adsorption of DCIT-acid on banana leaves after droplet application.....	59
4.2. Phytotoxicity of Fluopyram and its metabolite PCA in grape vine .....	67
4.2.1. Root uptake and translocation of PCA in hydroponic grown grape vine.....	67
4.2.2. Uptake and quantification of fluopyram in grape vine after foliar application .....	71
4.2.3. Spatial distribution of fluopyram after spray application in grape vine .....	75
4.3. Distribution of tebuconazole and BCS-CX51842 after seed treatment .....	83
4.3.1. Distribution of tebuconazole in wheat ( <i>Triticum aestivum</i> 'Triso') after seed treatment.....	83
4.3.2. Distribution of BCS-CX51842 in wheat ( <i>Triticum aestivum</i> 'Orcas') and soybean ( <i>Glycine max.</i> ) after seed treatment .....	86
4.4. Interactions and localization of the safener cyprosulfamide with the herbicide thien carbazone-methyl .....	91
4.4.1. Distribution of thien carbazone-methyl and cyprosulfamide in maize ( <i>Zea mays</i> ) after application on different leaves .....	92
4.4.2. Spatially resolved investigation of herbicide - safener interaction in maize ( <i>Zea mays</i> L.) .....	94
4.5. Systemicity of ethiprole and distribution in reproductive tissues .....	101
4.5.1. Systemicity of ethiprole and distribution in reproductive tissues.....	101
4.6. Uptake and surface adsorption of propineb on adaxial leaf surface.....	105
4.6.1. Uptake and surface adsorption of propineb on tomato leaves after droplet application.....	105
4.6.2. Uptake and surface adsorption of propineb on tomato leaves in real field samples .....	113
6 References .....	117
Appendix.....	129
Abbreviations .....	129
Supplementary Figures.....	133
Supplementary Tables .....	143
Mass Spectra .....	154
List of figures.....	161

<b>List of tables</b> .....	171
-----------------------------	-----



## Abstract

Agrochemicals such as fungicides, herbicides, or insecticides are widely used worldwide to control weeds, pests, and diseases to reduce the loss in crop production and increase yield and quality of crop products. Successful control and safe usage of these types of compounds depend on the compound reaching the target site within the crop plant. Therefore, monitoring agrochemical distribution within plant tissues delivers significant insights into agrochemicals adsorption, distribution, metabolism, and elimination (ADME). In the present dissertation, matrix-assisted laser desorption/ionization mass spectrometry imaging (MALDI MSI) has been used to examine the uptake and distribution of a range of agrochemicals into a various number of crop plants and to complement their results with conventional methods such as autoradiography, liquid scintillation, and HPLC-MS.

The uptake and movement of the fungicide isotianil and its metabolite DCIT-acid was investigated after micro droplet application on adaxial leaf surfaces of tomato (*Solanum lycopersicum*) and banana (*Musa*) leaves. In contrast, the uptake via the roots was studied using a hydroponic system to visualize the systemic movement in tomato (*Solanum lycopersicum*) and wheat (*Triticum*) plants. The results showed that the uptake of isotianil via the roots led to a systemic distribution in the plant by detecting it mainly in the vascular bundles (xylem and phloem), whereas isotianil was not taken up via the leaf. Imaging experiments of the leaf surface and transversal cross-sections revealed that the parent compound stuck on the leaf surface and was not taken up into the leaf via the plant cuticle, resulting in a depot effect of the compound on the leaf, while the metabolite DCIT-acid showed rapid uptake and movement within the plant. In addition, DCIT-acid could be detected in tissues of tomato flowers and fruits after uptake by roots in a hydroponic test system, highlighting the systemic properties of the metabolite.

To investigate the uptake, distribution, metabolic behavior, and the nature of the residue of the fungicide fluopyram, MALDI MSI was combined with LC-HRMS measurements. Fluopyram was shown to be transported mainly through the phloem (transportation tissue of food and nutrients) and stored in the stem during the late stages (engustment, leaf fall, and winter dormancy) of the annual growth cycle in grapevine (*Vitis vinifera*). In addition, transport via the phloem into newly growing plant parts was also detected during the early phases (bud break and flowering). In contrast, the metabolite fluopyram-pyridyl-carboxylic acid (PCA) showed acropetal and basipetal translocation suggesting both xylem and phloem mobility after root uptake in grapevine (*Vitis vinifera*) in a hydroponic test system.

To compare the plant uptake of a new developing candidate fungicide with the well-known fungicide tebuconazole, several MALDI MSI experiments were done to track and compare the uptake, movement, and metabolism of both fungicides after seed treatment. Tebuconazole is known to be rapidly taken up into the vegetative part of plants and translocated mainly acropetally, which was shown by MSI in different plant organs after seed treatment in wheat (*Triticum aestivum*) and soybean (*Glycine max*). The results showed the metabolic activity of the grain during germination, which is a crucial stage of plant development and the systemic distribution of both fungicides in parallel. The rapid and systemic uptake was underlined by detecting phase-I metabolites in different parts of the leaves.

Investigations of the interaction of the safener cyprosulfamide with the herbicide thien carbazon-methyl showed that cyprosulfamide enhanced the phytotoxic effect of the herbicide in maize (*Zea mays*). Comparison of different treatments (co-application on the same leaf and separate application on different leaves) also showed that cyprosulfamide induces the metabolism of the herbicide mainly in tissues where it is directly present, rather than via systemic signaling.

Furthermore, the systematicity of the insecticide ethiprole was demonstrated after single spray application in soybean flowers (*Glycine max.*). Ethiprole and three phase-I metabolites could be found within different flower tissues and in parts of the stem, facilitating the consideration of bee-relevant matrices.

MSI studies of the uptake and surface adsorption of the fungicide propineb on the adaxial leaf surface of tomato (*Solanum lycopersicum*) showed that the active ingredient completely covered the treated leaves and sticks on the leaf surface. Labeling studies with stable isotope-labeled propineb-DIDT showed that the hydrolysis metabolite Propineb-DIDT was already present in the application solution at the beginning of the experiment. The established measurement protocol was finally used to study actual field samples and showed that the fungicide was almost wholly degraded on the leaf surface after 28 days under natural weather conditions such as wind and rain, while the metabolites were detected with increased signal intensity.

MALDI MSI has a great potential for applications to studies involving the distribution of agrochemicals in plants and the environment. Spatial information about the uptake and systemicity of agrochemicals within a crop plant is a significant element of the successful use of such products in agriculture. Nevertheless, technological developments to increase the sensitivity are still needed for further integration of MSI to detect agrochemicals in plants.

## Zusammenfassung

Chemische Pflanzenschutzmittel werden weltweit zur Bekämpfung von Unkräutern, Schädlingen und Krankheiten eingesetzt, um Ernteverluste zu vermeiden, den Ertrag sowie die Qualität der pflanzlichen Produkte zu erhöhen. Die erfolgreiche Kontrolle und sichere Anwendung dieser vielfältigen chemischen Verbindungen hängen davon ab, ob die Verbindung nach der Anwendung den Zielort innerhalb der Nutzpflanze erreicht. Daher liefern Studien zur Verteilung von Pflanzenschutzmitteln wichtige Erkenntnisse über deren Adsorption, Verteilung, Metabolismus und Elimination (ADME). In der vorliegenden Arbeit wurde die matrixunterstützte Laser Desorption/Ionisation Massenspektrometrie (MALDI MSI) eingesetzt, um die Aufnahme und Verteilung von ausgewählten Pflanzenschutzmitteln in verschiedenen Kulturpflanzen zu untersuchen und deren Ergebnisse mit klassischen Methoden wie Autoradiographie, Flüssigszintillation und HPLC-MS zu ergänzen und vergleichen.

Die Aufnahme und Verteilung des Fungizids Isotianil und seines Metaboliten DCIT-acid wurde zum einen nach Tröpfchenapplikation auf Blattoberflächen von Tomaten- und Bananenblättern untersucht, während die Aufnahme über die Wurzeln mit Hilfe eines hydroponischen Testansatzes untersucht wurde, um die systemische Aufnahme in Tomaten- und Weizenpflanzen sichtbar zu machen. Die Ergebnisse zeigten, dass die Aufnahme von Isotianil über die Wurzeln zu einer systemischen Verteilung innerhalb der Pflanze führt, indem es hauptsächlich in den beiden Leitgeweben (Xylem und Phloem) detektiert wurde, während Isotianil nicht über das Blatt aufgenommen wird. MALDI MSI Messungen der Blattoberfläche und Querschnitte zeigten, dass das Fungizid auf der Blattoberfläche haftet und nicht über die Cuticula von der Pflanze aufgenommen wird. Dies führt zu einem Depoteffekt der Verbindung auf dem Blatt, während der Metabolit DCIT-acid eine schnelle Aufnahme und Verteilung innerhalb der Pflanze zeigte.

Um die Aufnahme und die Art der Rückstände des Fungizids Fluopyram zu untersuchen, wurde MALDI MSI mit LC-MS-Messungen kombiniert. Es zeigte sich, dass Fluopyram in der Weinrebe während der späten Vegetationsphasen (Austrieb, Blattfall im Spätherbst und winterlichen Ruhephase) hauptsächlich über das Phloem (Leitgewebe zum Transport von Zuckern und Aminosäuren) transportiert und im Stamm gespeichert wird. Darüber hinaus wurde der Transport über das Phloem in neu wachsende Pflanzenteile auch während der frühen Phasen (Austrieb und Blüte) nachgewiesen. Weiter zeigte der Metabolit Fluopyram-Pyridylcarbonsäure eine akropetale und basipetale Translokation, was auf eine Xylem- und Phloemmobilität nach der Wurzel Aufnahme in Weinreben in einem hydroponischen Testsystem schließen lässt.

Um die Aufnahme eines in der Entwicklung befindliches Fungizid mit dem bekannten Fungizid Tebuconazol zu vergleichen, wurden MALDI MSI Experimente durchgeführt, um die Aufnahme beider Fungizide nach Saatgutbehandlung zu vergleichen. Es ist bekannt, dass Tebuconazol schnell im vegetativen Teil der Pflanze aufgenommen und hauptsächlich akropetal verlagert wird. Dies wurde mittels MSI in verschiedenen Pflanzenorganen nach der Saatgutbehandlung von Weizen und Sojabohnen visualisiert. Die Ergebnisse zeigten die Stoffwechselaktivität des Saatkorns während der Keimung und die schnelle und systemische Aufnahme durch den Nachweis von Phase-I-Metaboliten, wie Hydroxy-Tebuconazol, in verschiedenen Teilen der Blätter.

Untersuchungen der Wechselwirkung des Safeners Cyprosulfamid mit dem Herbizid Thiencarbazon-methyl zeigten, dass Cyprosulfamid die phytotoxische Wirkung des Herbizids in Mais verstärkt. Der Vergleich der gemeinsamen Anwendung auf demselben Blatt und getrennte Anwendung auf verschiedenen Blättern zeigte zudem, dass Cyprosulfamid den Metabolismus des Herbizids wahrscheinlich nur beeinflusst, wenn beide im gleichen Gewebe präsent sind, und eher nicht über systemische Signalübertragung.

Weiter wurde die systemische Aufnahme des Insektizids Ethiprol nach einmaliger Sprühanwendung in Blüten von Sojabohnen nachgewiesen. Ethiprol und drei Phase-I-Metaboliten konnten in verschiedenen Blütengeweben und in Teilen des Stängels gefunden werden, was die toxikologische Betrachtung bienenrelevanter Matrices verbessern kann.

MALDI MSI Messungen zur Aufnahme und Adsorption des Fungizids Propineb auf der adaxialen Blattoberfläche von Tomate zeigten, dass der Wirkstoff die behandelten Blätter vollständig bedeckt und auf der Blattoberfläche haften bleibt. Markierungsstudien mit stabil isotopenmarkiertem Propineb-DIDT zeigten, dass der Hydrolysemetabolit bereits zu Beginn des Versuchs in der Applikationslösung vorhanden war. Untersuchungen realer Feldproben zeigten, dass der Wirkstoff unter natürlichen Witterungsbedingungen wie Wind und Regen nach 28 Tagen auf der Blattoberfläche fast vollständig abgebaut ist.

MALDI MSI bietet ein großes Anwendungspotential für Studien zur Verteilung von Pflanzenschutzmitteln in Nutzpflanzen und der Umwelt und kann wichtige Informationen für die Risikobewertung und sichere Anwendung von chemischen Pflanzenschutzmitteln liefern. Nichtsdestotrotz sind weitere technologische Entwicklungen zur Verbesserung der Empfindlichkeit bei der Detektion dieser Substanzen notwendig.



## 1 Introduction

### 1.1. Plant protection products

Plant protection methods are widely used in agriculture to control weeds, pests, and diseases to reduce the loss in crop production and increase yield and quality of crop products. Since arable farmland is limited worldwide, plant protection plays a significant role in securing the provision of food and feed (Godfray *et al.*, 2010, Loso *et al.*, 2017). Various techniques have been used for over 4500 years to preserve the yield and quality. The use of Sulphur compounds by the Sumerians to control the attack of insects and mites on their food sources leading to significant loss of yield is documented back to 2500 BC (Achilladelis *et al.*, 1987). Nowadays, plant protection is based on mechanical, physical, biological, and chemical methods (Krieger, 2010, Gerwick and Sparks, 2014, Jeschke *et al.*, 2019). Mechanical plant protection uses physical instruments such as fences, barriers, electronic wires, or changes in conditions like temperature to control pests. Gardeners can perform even the use of hands to remove harmful insects. Nevertheless, this can be very cheap and simple, but it is ineffective and not suitable when the size of the farmland increase. Physical plant protection includes warm water treatment, soil sterilization, or physical barriers like a fence sunk. Biological control relies on predation, parasitism, and herbivory of potential natural antagonists, which are used to control pests such as insects, mites, and weeds (Gross *et al.*, 2014, Lorsbach *et al.*, 2019). These natural enemies can be introduced into the environmental system (classical), by a large population for quick pest control (inductive), or measures are taken to maintain natural enemies through regular reestablishment (inoculative). Although biological plant protection continues to grow, chemical plant protection is still by far the largest area of plant protection (Jeschke, 2016, Jeanmart *et al.*, 2016). The active ingredients used in chemical crop protection are characterized by high variability of structural properties and mode of action (Zhang *et al.*, 2018). Apart from a few inorganic representatives such as copper and sulfur compounds of the first and second generation of active ingredients, they are synthetically produced organic compounds (Umetsu and Shirai, 2020). There are over 800 registered pesticides worldwide, and new agrochemicals are introduced to the market continuously. The compounds belong to more than 100 chemical classes, whereas benzoylureas, carbamates, organophosphorus, pyrethroids, sulfonylureas, and triazine are the most important ones (Alder *et al.*, 2006, Krieger, 2010, MacBean, 2012, Jeschke *et al.*, 2016). Based on their site of action against the target organism, pesticides can be classified as fungicides (against fungal diseases), insecticides (against insects), and herbicides (against plants).

### 1.1.1. Fungicides

Figure 1 and table 1 shows important representatives of fungicidal active ingredients and their classification according to the Fungicide Resistance Action Committee (FRAC) based on their chemical structures and mode of actions (Herman and Stenzel, 2019).

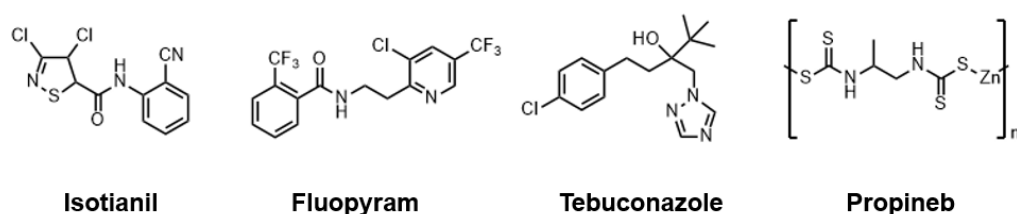


**Figure 1.** Chemical structures of selected fungicides.

**Table 1.** Mode of actions and FRAC code of selected fungicides (Hermann and Stenzel, 2019).

Fungicide	Mode of action	Chemical group	FRAC Code
Isotianil	Salicylic acid pathway	Thiadiazole- carboxamide	P3
Fluopyram	Inhibition of succinate-dehydrogenase (SDH)	Pyridinyl-ethyl- benzamides	C2
Tebuconazole	Inhibition of sterol biosynthesis	Triazoles	G1
Propineb	Multi-site contact activity	Dithiocarbamates and relatives	M03

Isotianil (3,4-dichloro-2'-cyano-1,2-thiazole-5-carboxanilide) is a thiadiazole carboxamide fungicide and belongs to the group of plant activator compounds, which induce the host plant defense (FRAC code P3) (Maienfisch and Edmunds, 2017). Other fungicides within this group are for example probenazole or tiadinil (Hermann and Stenzel, 2019). This type of plant protection product merely initiates plants defense systems by providing signals via the signal transduction pathway mediated by the phytohormone salicylic acid and do not target pathogens directly. Neither the active ingredient nor the metabolites have direct antifungal or antibacterial activity *in vitro* or in *planta* (Toquin *et al.*, 2011, Du *et al.*, 2013). This impact on different stages of the salicylic pathway similarly to local pathogens attacking the plant leads to a systemic acquired resistance (SAR). This resistance typically activates pathogenesis-related genes, via a pathway of positive regulators (mainly NPR1) and transcription factors (TGA and WRKY). Additionally, plants are set into a primed state of enhanced defense, which

gives them the capacity to react to subsequent pathogen infections, herbivores, or abiotic stresses (Conrath *et al.*, 2015). Nevertheless, this artificial defense induction can sometimes reduce the plants fitness because the plant activator compounds or their metabolites are insufficiently tolerated by the crop plant (Gozzo and Faoro, 2013). Isotianil is used against rice blast, which is caused by the ascomycete fungus *Magnaporthe grisea* and can be found in over 85 countries across the world and is the most important disease concerning the rice crop (Ogawa *et al.*, 2011). In contrast to other plant activator fungicides like probenazole, isotianil shows a systemic effect and activity over a more extended period. The metabolism of isotianil in rice includes the cleavage of the amid linkage leading to DCIT-acid and the corresponding anthranilonitrile (Figure 2). DCIT-acid is further metabolized by sequential dechlorination to 1,2-thiazole-5-carboxylic acid. Hydrolysis studies of isotianil followed the same degradation pathways via cleavage of the amid linkage at pH 7 with half-lives of 60.8 – 71.4 days (Ogawa *et al.*, 2011).

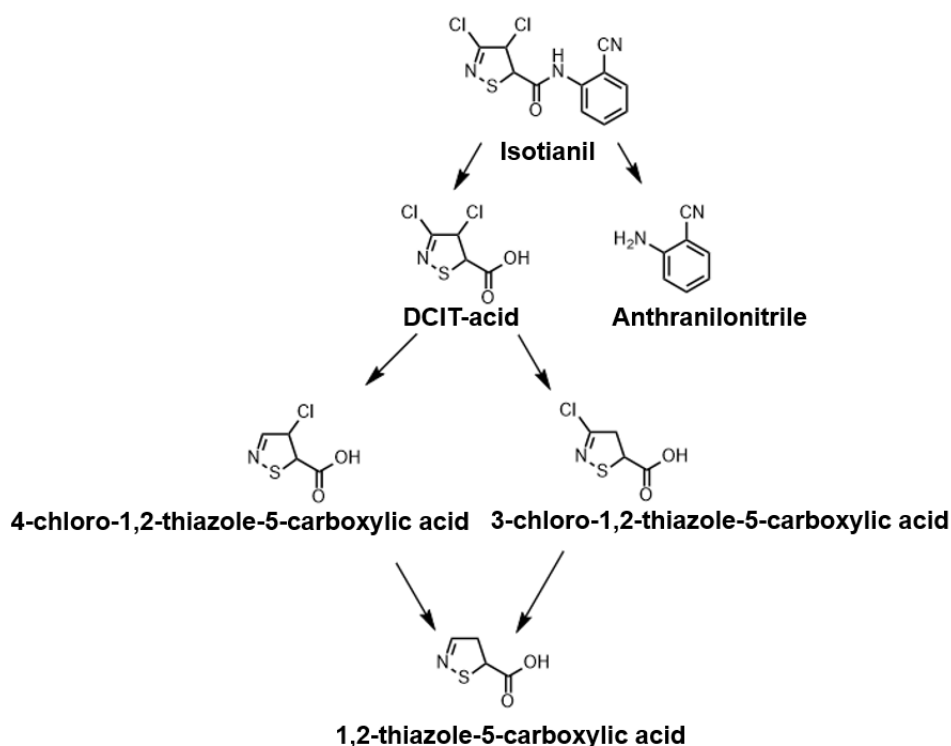


**Figure 2.** Major metabolic pathway of isotianil in rice (Ogawa *et al.*, 2011).

Fluopyram (N-{2-[3-chloro-5-(trifluoromethyl)-2-pyridyl]ethyl}- $\alpha, \alpha, \alpha$ -trifluoro-o-toluamide) is a broad-spectrum fungicide belonging to the subgroup of pyridinyl ethylbenzamides, a chemical group within the class of succinate dehydrogenase inhibitors (SDHIs, (FRAC code 7). The

action mode consists of inhibiting the complex II in the mitochondrial respiratory chain, also known as succinate:quinone oxidoreductase (SQR) or succinate dehydrogenase (SDH). SDH can be found in bacteria and mitochondria of eukaryotic cells and is of central importance for energy metabolism, while it is involved in both the citric acid cycle and the electron transport chain. The inhibition leads to a block of the cell energy cycle. Fluopyram is biologically active against all stages of fungal growth, from spore germination to spore production, and its activity spectrum includes several pathogens belonging to Ascomycetes and Deuteromycetes, such as *Botrytis* spp., *Sclerotinia* spp. or *Monilinia* spp. (Veloukas and Karaoglanidis, 2012). The metabolism of fluopyram in plants include a hydroxylation at C-7 or C8, followed by cleavage of the amid bond and further glycosylation (Robatscher *et al.*, 2019, Vargas-Pérez *et al.*, 2020).

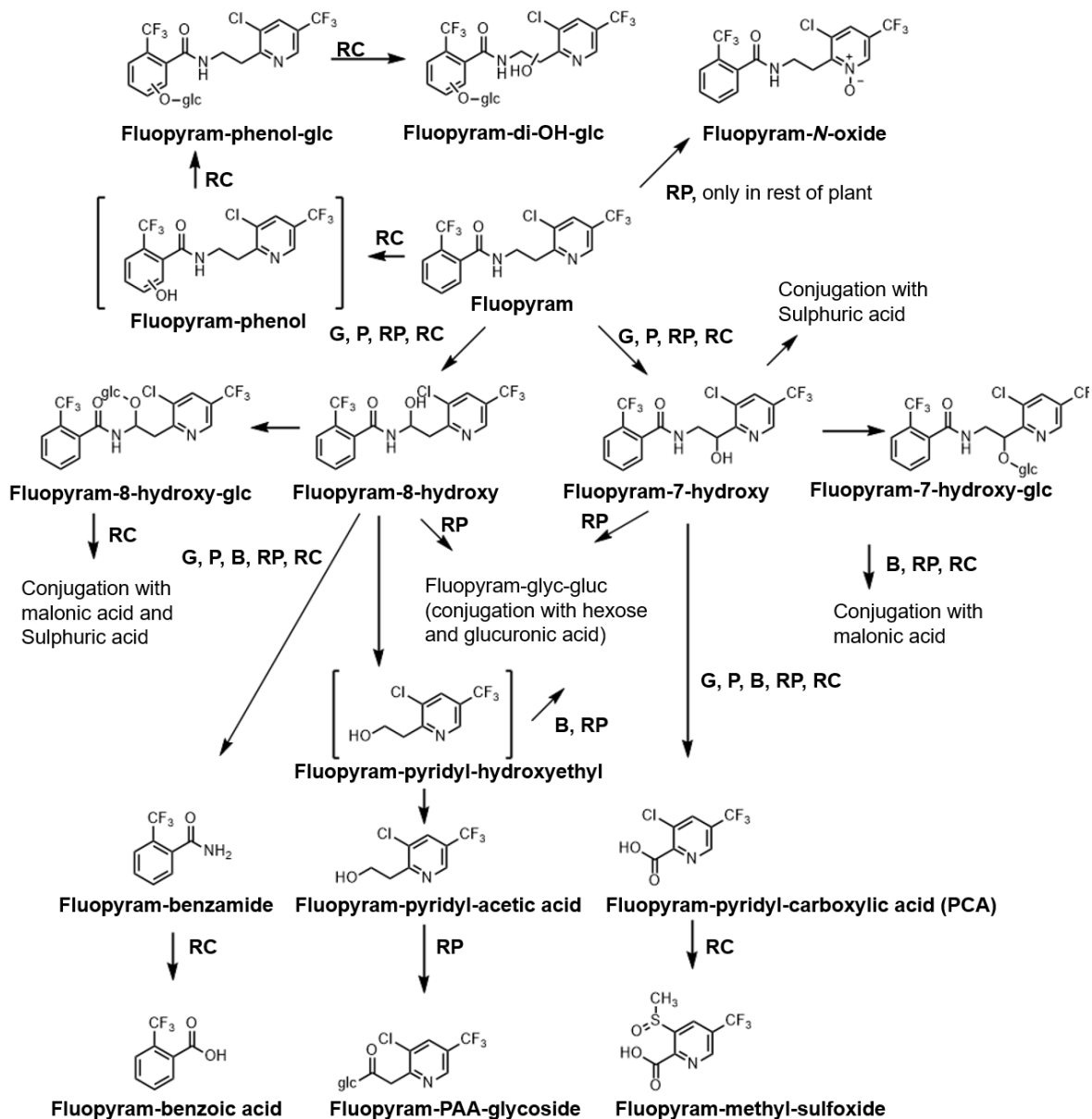


**Figure 3.** Proposed metabolic pathway of fluopyram in several crop plants. Metabolites in brackets are postulated intermediates. G = grapes, P = potatoes, B = beans, RP = red pepper RC = rotational crops (Vargas-Pérez *et al.*, 2020).

Tebuconazole, [(RS)-1-p-chlorophenyl]-4,4-dimethyl-3-(1H-1,2,4-triazol-1-ylmethyl)pentan-3-ol] (Fig. 1), is a broad-spectrum triazole fungicide used to control many plant diseases by inhibiting the biosynthesis of ergosterol to prevent fungal mycelium development (Burden *et al.*, 1989). Particularly, it displays an outstanding curative and protective efficacy to control numerous pathogens in various cereals, fruits, and vegetable crops. It is used against *Alternaria brassicae*, *Puccinia asparagi*, powdery mildew (*Erysiphe graminis*) by inhibiting the biosynthesis of ergosterol. The sterol is essential of plasma membrane of most pathogens of

*Ascomycota* and *Basidiomycota* and cannot be found in plants or animals. As a sterol biosynthesis inhibitor fungicide (SBI fungicide), tebuconazole inhibits the enzyme C14 demethylase within the ergosterol synthesis via lanosterol. Tebuconazole is rapidly absorbed into the vegetative part of the plants and translocated principally acropetally. The plant metabolism of tebuconazole includes hydroxylation at the aromatic ring or isopropyl group, followed by cleavage of the aliphatic chain leading to 1,2,4-Triazole and several carboxylated triazole derivatives and 4-chlorobenzoic acid (Jeschke *et al.*, 2019).

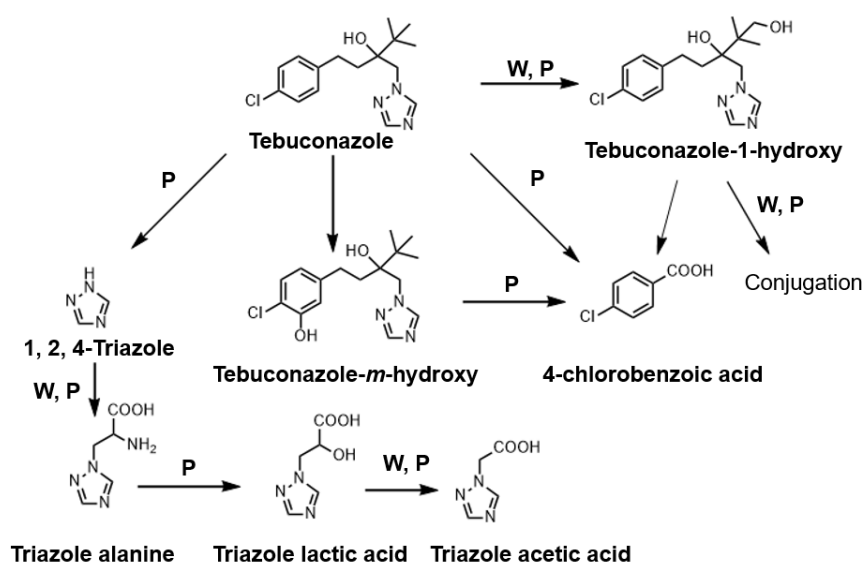


**Figure 4.** Proposed metabolic pathway of tebuconazole in selected crop plants. P = peanut, W = wheat (Jeschke *et al.*, 2019).

Propineb (Polymeric zinc 1,2-propylenebis (dithiocarbamate)) is a bisdithiocarbamate fungicide and belongs to plant protection products with multi-site activity (FRAC code M03). It is non-phytotoxic and provides complete coverage of treated leaves with good sticking property so that it is not easily washed off by rains, deepening on its low water solubility (< 0.01 g/L) and low logP<sub>OW</sub> (-0.26). It is widely used against blight disease of potato (*Solanum tuberosum*), tomato (*Solanum lycopersicum*) and onion (*Allium cepa*) as well as for protective control of apple scab (*Venturia inaequalis*), apple leaf spot, downy mildew in grapes (*Vitis vinifera*), tobacco (*Nicotiana*), onion (*Allium cepa*) and vegetables. Therefore, it is applied as water-dispersible granules (WG) or wettable powder (WP) formulation mainly sprayed (Gullino *et al.*, 2010, Thind and Hollomon, 2018).

### 1.1.2. Herbicides

Herbicides are used to inhibit the growth of unwanted plants, while they can control specific weed species by leaving the desired crop unharmed (selective) or control a broad range of weeds (non-selective). Representatives of active ingredients and their classification according to the Herbicide Resistance Action Committee (HRAC) based on their chemical structures and mode of actions are shown in figure 5 and table2.

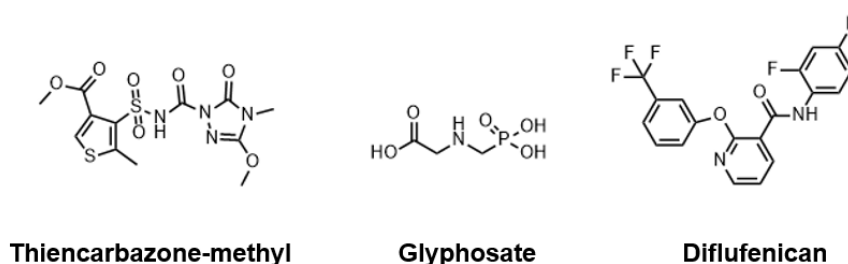


**Figure 5.** Chemical structures of selected herbicides.

**Table 2.** Mode of actions and HRAC code of selected herbicides (Befa *et al.*, 2019).

Herbicide	Mode of action	Chemical group	HRAC Code
Thien carbazone-methyl	Inhibition of acetolactate synthase (ALS)	Triazolinones	B
Glyphosate	Inhibition of enolpyruvylshikimate phosphate synthase	Glycine	G
Diflufenican	Inhibition of phytoene desaturase (PDS)	Pyridine	F1

Thien carbazone-methyl (Methyl 4-[(3-methoxy-4-methyl-5-oxo-1,2,4-triazole-1-carbonyl)sulfamoyl]-5-methylthiophene-3-carboxylate) is an herbicide in the sulfonyl-amino-carbonyl-triazolinone (SACT) chemical class, which are inhibitors of the ALS-enzyme (HRAC code B). In commercial herbicide products TCM is always combined with safener technology like the safener cyprosulfamide (N-[4-(cyclopropylcarbonyl) phenylsulfonyl]-o-anisamide) and with other herbicidal active ingredients like isoxaflutole, foramsulfuron or iodosulfuron (Giannakopoulos *et al.*, 2020). Safener reliably protects the crop plants from damage after soil application and after foliar application of the herbicide through induction of enhanced herbicide metabolism via gene activation. When applied alone, safeners generally have minor visible effects on crop or weed species. Because of that, the herbicidal activity maintained in the

presence of the safener (Giannakopoulos *et al.*, 2020). Safeners are a chemically diverse group of agrochemicals, which despite being in commercial use for 50 years, their mode of action remains to be determined (Riechers *et al.*, 2010). These compounds act as enablers of herbicide selectivity by selectively enhancing herbicide metabolism in monocot crops through the upregulation of xenobiotic detoxification enzymes (Davies *et al.*, 1999, Riechers *et al.*, 2010, Kraehmer *et al.*, 2014).

One of the most important and widely used, non-selective broad-spectrum herbicides is glyphosate, a glycine derivative. It disrupts the shikimic acid pathway through inhibition of the chloroplast enzyme 5-enolpyruvylshikimate-3-phosphate synthase (EPSPS) and the resulting deficiency EPSPS production leads to a reduction in aromatic amino acids such as tyrosine, phenylalanine, and tryptophan which are vital for protein synthesis and plant growth (Benbrook, 2016, Green, 2018). The introduction of glyphosate-tolerant crops by genetic engineering in crops like cotton, soybeans, and canola had a significant impact on weed control in plant protection (Shaner, 2000) and glyphosate can be used as a selective herbicide. Phytoene desaturase (PDS) is an essential plant carotenoid biosynthetic enzyme and a prominent target of certain inhibitors, such as diflufenican belonging to the chemical class of pyridines. Carotenoids are participants of the photosynthetic reaction centers and play a vital role in protecting of the chloroplasts against photo-oxidative damage (Haynes and Kirkwood, 1992). Blocking the formation of the pigment biosynthesis of carotenoid lead to the destruction of plant pigments, and such agrochemicals are also classified as “bleaching herbicides”.

### **1.1.3. Insecticides**

The third type of agrochemicals are insecticides. Next to natural insecticides like nicotine, rotenone, or pyrethrum, synthetic insecticides improve efficacy, high selectivity, minimal acute and long-term toxicity (Jeschke *et al.*, 2019). Representatives of active ingredients and their classification according to the Insecticide Resistance Action Committee (IRAC) based on their chemical structures and mode of actions are shown in figure 6 and table 3. These compounds can be classified into two major groups: systemic insecticides have residual or long-term activity and contact insecticides have no residual activity (Sparks, 2013, Swale, 2019, Sparks *et al.*, 2019).



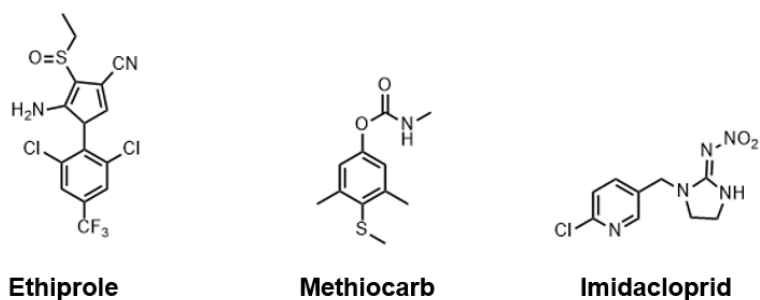


**Figure 6.** Chemical structures of selected insecticides.

**Table 3.** Mode of actions and IRAC code of selected insecticides (Nauen *et al.*, 2019).

Insecticide	Mode of action	Chemical group	IRAC Code
Ethiprole	GABA-gated chloride channel blocker	Phenylpyrazole	2B
Methiocarb	Inhibition of acetylcholinesterase (AChE)	Carbamates	1B
Imidacloprid	Inhibition of nicotinic acetylcholine receptor ( <i>n</i> AChR) competitive modulators	Neonicotinoids	4A

The systemic and phenylpyrazole insecticide ethiprole blocks the gamma-aminobutyric acid (GABA) receptor present in invertebrates such as insects but not in mammals (Lamberth, 2007). It is effective against a wide range of insects such as aphids, grasshoppers, hoppers, leaf miners, leaf beetles, stink bugs, termites, thrips, and weevils. Primary metabolic pathways of ethiprole in plants proceeded via oxidation to yield sulfone and sulfonate metabolites, while dichlorination of one chlorine atom on the phenyl ring to yield ethiprole monodechloro. Oxidation of carbonitrile result in the formation of ethiprole carboxamide (Figure 7).

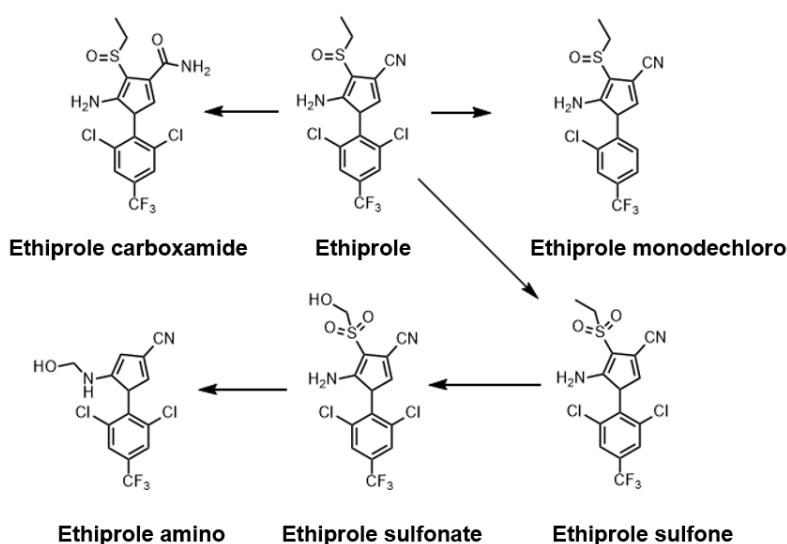


**Figure 7.** Proposed metabolic pathway of ethiprole in plants (Lamberth *et al.*, 2007).

The non-systemic carbamate insecticide methiocarb acts as an acetylcholinesterase (AChE) inhibitor. AChE is essential for life and its inhibition is lethal (Simon-Delso *et al.*, 2015). The most widely used class of insecticides worldwide belongs to the chemical class of neonicotinoids (Taillebois *et al.*, 2018) targeting the nicotinic acetylcholine receptor (*nAChR*). The receptor is needed to mediate fast excitatory synaptic transmission in the insect central nervous system. One representative neonicotinoid is imidacloprid, which is effective by contact or ingestion against chewing insects including termites, soil insects, and fleas (Mullins, 1993).

## 1.2. Pesticide Analysis

While the use of pesticides like herbicides, fungicides and insecticides in agriculture positively affects plant health, growth, and yield, the impact on ecosystems is manifold and can be harmful. The successful control of pesticides is dependent on the compound reaching the target site within the plant, fungi, or insect (Buchholz and Trapp, 2016). Therefore, information about the uptake and translocation of agrochemicals is important in developing new active ingredients. The uptake of pesticides in crop protection includes three major ways while they can be applied via spraying on leaf surfaces resulting in foliar adsorption, uptake via the roots after soil application or seed treatment followed by subsequent translocation into the main plant transportation tissues (xylem and phloem) (Briggs *et al.*, 1982, Baker *et al.*, 1992, Kirkwood, 1999, Forster and Kimberly, 2015). For this reason, analytical techniques to assess the uptake, translocation, and metabolism in the early stages of development are required. Conventional and established analytical methods for determining uptake and translocation include

autoradiography, liquid scintillation and chromatographic techniques coupled to mass spectrometry (Klittich *et al.*, 2008). Autoradiography is used to visualize the adsorption and translocation of a pesticide following both uptake via the roots within the water uptake and adsorption via the leaves following foliar application. It provides a very sensitive method and quantifiable results. A major limitation of these experiments and techniques is that they are limited to isotope labeled test items. These radioactive beta-emitters, such as  $^3\text{H}$  or  $^{14}\text{C}$  are used to visualize the radioactivity distribution at relatively low resolution ( $> 200 \mu\text{m}$ ) in large samples, such as the entire plant (Kaneal *et al.*, 1995, Nollet and Rathore, 2009, Liu *et al.*, 2014). In addition, despite the method's many benefits, one further intrinsic limitation of autoradiography is the inability to distinguish the parent compound distribution from potential metabolite distribution up to the invisibility of possible metabolites, which loses the radiolabel in their structure. Furthermore, the synthesis of (radio)labeled compounds is expensive, and many safety issues for handling radiolabeled material are required. Therefore, data from autoradiography are often combined with qualitative and quantitative data from tissue extracts. Gas chromatography coupled to mass spectrometry (GC-MS) and high-performance liquid chromatography coupled to mass spectrometry (HPLC-MS) allows the identification and quantification of the pesticide and its metabolites with high specificity and high sensitivity (Frenich *et al.*, 2005, Alder *et al.*, 2006). One of the biggest challenges in pesticide analysis of plant tissues is the very low concentration (typically ppb) of the target analyte in complex biological matrices. To increase the specificity and sensitivity by detecting pesticide residues by GC- or LC-MS, the sample preparation needs to be optimized to extract the analyte quantitatively and separate interferences from the biological matrix as far as possible. This can be done either by solid-phase extraction (SPE) or solvent extraction (SE), whereas this can be done by solid-liquid extraction (SLE) or liquid-liquid extraction (LLE) (Lehotay, 1997, Richter *et al.*, 1996, Kadam *et al.*, 2013). Pesticide analysis usually uses solvent extraction, which can be added by solid-phase extraction. To optimize and minimize time and costs, the QuEChERS protocol was developed and combines the high selectivity of solid-phase extraction with the simple handling of solid extraction. QuEChERS allows multi-residue analysis up to 600 pesticides residues of various chemicals classes within a high polarity range ( $\text{LogP}_{\text{ow}} -1.5 - 7$ ; polar – nonpolar) from several biological matrices (Alder *et al.*, 2006, Anastassiades *et al.*, 2007). For the quantification and qualification, the sample extracts are nowadays standardly measured by GC- or LCMS. Liquid chromatography is performed using suitable eluents to ensure both chromatographic separation and ionization in mass spectrometric detection. The choice of an analytical HPLC column consists of the solid adsorbent material, column length and particle size. The relationship between the linear velocity of the mobile phase and the height of the theoretical separation soils is described by the Van Deemter equation. The separation efficiency increases when the particle size decreases. Thus, shorter columns with

smaller particle size can be used, while the number of theoretical separation plates does not decrease, since sufficient particles are available for adsorption of the analyte. In addition, separation efficiency is not affected with increasing flow rates or linear velocities, as smaller particles are used, and lower resistance is produced at the same flow rate. Reverse phase (RP) chromatography and C<sub>8</sub>, C<sub>18</sub>- and phenyl phase HPLC columns are typically used for pesticide residue analysis (Hogendoorn and Zoonen, 2000, Alder *et al.*, 2006). Highly hydrophilic, ionic, and polar pesticide or their metabolites can be also analyzed using hydrophilic interaction liquid chromatography (HILIC) columns (Tölgyes *et al.*, 2010, Yoshioka *et al.*, 2011).

The main method of ionization in the analysis of pesticides residues by LC-MS/MS is based on electrospray ionization (ESI). Atmospheric pressure chemical ionization (APCI) or photo-ionization (PPI) can be further used for more polar pesticides (Silva *et al.*, 2019). While ESI is a soft ionization technique, the quasi-molecular ions ( $[M+H]^+$  in positive ion mode,  $[M-H]^-$  in negative ion mode) are predominant in the mass spectra. Further adducts ions such as  $[M+Na]^+$ ,  $[M+K]^+$ ,  $[M+NH_4]^+$  or  $[M-HCOO]^-$  can be also detected in ESI spectra. Furthermore, dimer formation ( $[2M+H]^+$  or  $[2M+Na]^+$ ) can also occur at high concentrations, while multiple charged ions ( $[M+nH]^{n+}$  or  $[M+nNa]^{n+}$ ) are possible at higher molecular weights of the analytes (Kruve *et al.*, 2013, De O. Silva *et al.*, 2019). In contrast to that, the standard ionization technique for GC-MS analysis is electron impact ionization (EI) with electrons of 70 eV kinetic energy. EI allows the ionization of organic compounds with a comparable efficiency, but they are usually heavily fragmented during the ionization process due to the high energy. While the resulting fragmentation ion pattern represents a specific fingerprint of the target analyte, the molecular mass peak is almost never detected in the mass spectra, because the molecule is too fragile (Agüera *et al.*, 2002). Beside the target analyte's ionization, the second important basic parameter for pesticide analysis using mass spectrometry is the mass analyzer. Due to the low concentration of pesticides in complex biological matrices, the mass analyzer needs to allow analysis with a high mass accuracy and high resolving power. Therefore, Tandem MS techniques, MS/MS and MS<sup>n</sup> are predominant in the analysis of agrochemicals (Alder *et al.*, 2006, Anastassiades *et al.*, 2007). Regarding the detection techniques, several mass analyzers are currently available to analyze pesticides. Quadrupole mass analyzers (Q-MS) and triple quadrupole mass analyzers (QqQ-MS) are used based for their prize and easy use. While the sensitivity in the full-scan mode of Q-MS is very low ( $10^2$ - $10^3$ ), selected ion monitoring (SIM) and selected reaction monitoring (SRM) with QqQ-MS allows the analysis and quantification of pesticides in complex matrices with high sensitivity and selectivity. The SIM mode is used to quantify the parent compound or metabolites, when authentic standards are available and is the most sensitive mode for quantitative measurements, while the SRM mode can be used for targeted quantitative analysis. SRM is further used for structure

elucidation providing MS/MS fragmentation data. Time-of-flight (ToF) mass spectrometer determines the  $m/z$  ratio of the generated ions by measuring characteristic times that take the movement of different  $m/z$  ions from the entrance point of the analyzer, where they have been accelerated by an electric field, to hit the detector. It delivers good mass accuracy ( $> 5$  ppm) at a high resolving power ( $10^3$ - $10^4$ ) and rapid mass scanning in a theoretically unlimited scan range (Gentili *et al.*, 2008, Radjenovic *et al.*, 2009, Perez *et al.*, 2009). Ion storage-based mass spectrometers include ion trap (IT-MS), Fourier transform ion cyclotron resonance (FT-ICR-MS) and orbitrap mass spectrometers. FT-ICR and orbitrap mass analyzers trap ions in a cyclotron or orbitrap motion inside a cell, either with a magnetic or electric field. The cyclotron or orbitrap frequency of the ions leads to the  $m/z$  values after Fourier transformation analysis. The resolving power of such instruments with  $10^5$  FWHM is much higher than of time-of-flight or quadrupole instruments. Next to the very high-resolving power, FT-ICR and orbitrap mass spectrometer provide excellent mass accuracy (1 – 5 ppm), a high dynamic range and high sensitivity. Additionally, orbitrap mass analyzers are usually interfaced to a linear ion trap or a quadrupole mass filter in hybrid configurations allowing MS/MS and  $MS^n$  analysis (Radjenovic *et al.*, 2009, Perez *et al.*, 2009).

### 1.3. Mass Spectrometry Imaging of plant tissues

Mass spectrometry imaging (MSI) is a rapidly developing method to measure the spatial distribution of target compounds in plant tissues *in-situ* (Mullen *et al.*, 2005, Peukert *et al.*, 2012, Nimesh *et al.*, 2013). In contrast to mass spectrometry coupled to liquid or gas chromatography, where the spatial information is limited to the size of the tissue sample being extracted, MSI allows the combination of spatial information and molecular information for a wide range on compounds within a single MSI measurement. As well as for the analysis of pesticides using GC- or LC-MS, the ability to form ions affect both the sensitivity and selectivity in a mass spectrometry imaging experiment (Lee *et al.*, 2012; Li *et al.*, 2016; Ding *et al.*, 2016; Qin *et al.*, 2018). Many ionization methods have been applied to MSI, although matrix-assisted laser desorption ionization (MALDI) is the most common ionization method used for mass spectrometry imaging in plant science (Peukert *et al.*, 2012). Other important spatially resolvable ionization methods are desorption electrospray ionization (DESI) (Gerbig *et al.*, 2015), secondary ion mass spectrometry (SIMS) (Benninghoven, 1994), laser ablation electrospray ionization (LA-ESI) and laser ablation inductively coupled plasma (LA-ICP) (Table 4.) (Nemes *et al.*, 2008, Boughton *et al.*, 2016).

**Table 4.** Overview of ionization methods for mass spectrometry imaging (Benninghoven, 1994, Nemes *et al.*, 2008, Gerbig *et al.*, 2015, Boughton *et al.*, 2016).

Method	Ionization source	Spatial resolution	Favorable compounds
MALDI	Matrix, UV or IR Laser	UV < 10 $\mu\text{m}$ IR 100 – 200 $\mu\text{m}$	Metabolites, lipids, proteins, fatty acids, carbohydrates
DESI	ESI stream	50 - 200 $\mu\text{m}$	Lipids, peptides, small metabolites
SIMS	Primary ion beam	< 10 $\mu\text{m}$	Elements, lipids, fatty acids
LA-ESI	IR Laser coupled to ESI source	300 – 500 $\mu\text{m}$	Metabolites, peptides, proteins, carbohydrates
LA-ICP	Laser beam	> 10 $\mu\text{m}$	Elements

In DESI-MSI experiments, charged droplets are directed to the sample surface via a spray capillary and the ESI stream impacts the surface extraction and ionization of the target analyte. Due to the size of the droplets of the ESI stream, DESI or nanoDESI allows lateral resolutions of 50-200  $\mu\text{m}$  respectively 20  $\mu\text{m}$ . Due to the fact that no intensive sample preparation nor high-vacuum conditions for the ionization process are required, DESI allows direct spatial analysis of plant surfaces. The distribution of the insecticides imidacloprid and methiocarb on the leave surface and in cross-sections of stem and leaf were investigated using DESI-MSI with a spatial resolution of 50-100  $\mu\text{m}$  (Gerbig *et al.* 2015). Another essential and matrix-free ionization method used for MSI is SIMS. Secondary ion mass spectrometry was introduced during the 1960`s for imaging of inorganic elements like  $\text{Mg}^+$ ,  $\text{Al}^+$  and  $\text{Si}^+$  by Castaing and Slodzian (Liebl, 1980). A beam of high-energy (15-25 keV) primary ions are supplied by an ion gun and sputters atoms off a conductive surface. A wide range of ion sources such as ions of noble gases ( $^{40}\text{Ar}^+$ ,  $\text{Xe}^+$ ), oxygen ( $^{16}\text{O}^-$ ,  $^{16}\text{O}_2^+$ ,  $^{16}\text{O}_2^-$ ) or ionized molecules ( $\text{SF}_5^+$ ) can be used in SIMS experiments. The beam dimension of the primary ion gun allows high spatial resolution of < 10  $\mu\text{m}$  and 3D depth profiling to a depth of 1-2 nm, but high vacuum is required during the imaging experiment to prevent secondary ion collision with background gases. Therefore, the target analyte needs to be vacuum-stable and the high-energy of the laser beam leads to significant fragmentation of the target analytes during the ionization process, especially in biological molecules with high molecular weights (Benninghoven, 1996). Unique fragment ions for individual target analytes, created from complex biological matrices such as plant tissues, SIMS in plant science is limited to detecting small molecules such as elements, lipids of fatty acids. Ambient ionization techniques are based on laser ablation, including electrospray ionization (LA-ESI) and laser ablation inductively coupled plasma (LA-ICP). These techniques combine laser ablation on the sample surface from a mid-infrared laser with a secondary

electrospray ionization process. The laser ablation creates a plume of predominantly neutral particles and molecules, and the collision with charged droplets from the electrospray ionization finally generates multiply charged target ions (Boughton *et al.*, 2016, Buchberger *et al.*, 2018). Lateral imaging (lateral resolution 300 -500  $\mu\text{m}$ ) and depth profiling (30 – 40  $\mu\text{m}$ ) of chimeric *Aphelandra squarrosa* leaf tissue was performed to identify the metabolites characteristic for the green and yellow sectors of variegation. LA-ICP can perform ultra-highly sensitive chemical analysis of elements on complex surfaces down to ppb-level without any sample preparation, but only elemental and isotopic analyses of plant tissues are possible (Nemes *et al.*, 2008).

Beside the target analyte's ionization, the second crucial basic parameter for MSI experiments is the mass analyzer itself. Due to the low concentration of the agrochemicals in the environment, the mass analyzer needs to allow analysis with a high mass accuracy and high resolving power in complex biological matrices (Table 5).

**Table 5.** Overview of mass spectrometers used for mass spectrometry imaging (Boughton *et al.*, 2016, Buchberger *et al.*, 2018).

Mass spectrometer	Mass accuracy	Mass resolution	Mass range	Speed [Hz]
QIT	Low 50-100 ppm	Low $10^3$ - $10^4$	Up to $2 \times 10^4$	1-30
Q, QqQ	Low 100 ppm	Low $10^2$ - $10^3$	$4 \times 10^3$	1-20
ToF, qToF	Good 5-50 ppm	High $10^3$ - $10^4$	Up to $10^5$	$10^1$ - $10^4$
FT-ICR	Excellent 1-5 ppm	Very high $10^5$ - $10^6$	$> 10^4$	0.001-10
Orbitrap	Excellent 2-5 ppm	Very high $1.5 \times 10^5$	$6 \times 10^3$	1-4

#### 1.4. Matrix-assisted laser desorption/ionization mass spectrometry

Matrix-assisted laser desorption/ionization mass spectrometry imaging (MALDI MSI) allows direct, *in-situ* and label-free measurements of target analytes (e.g., pesticides and their metabolites) in several plant tissues (Boughton *et al.*, 2016). MALDI is, besides ESI, a soft ionization technique that enables detection of mainly singly charged molecular ions. Desorption and ionization of the relatively harsh laser ablation energy relies a secondary

matrix, which absorbs the laser beam energy and protects the target molecules from disruptive energy during the desorption and ionization process. Both processes are usually described separately when considering the physical processes during desorption and ionization. Since the processes are at least partially parallel, they are difficult to distinguish from a mechanical point of view. First, using MALDI matrix substances leads to a mixture of matrix and analyte in the sample. A co-crystallization of analytes and matrix molecules occurs, whereby the analyte molecules are spatially separated due to their statistical distribution. The energy in the form of photons of the laser light is preferentially absorbed by the matrix molecules and by electron transfer within the crystal the desorption of both analyte and matrix molecules occurs. The majority of MALDI experiments were done using ultraviolet (UV) laser with an emission wavelength ( $\lambda$ ) of either 337 nm or 355 nm. 337 nm is characteristic for a nitrogen laser and 355 nm is typically emitted by a neodymium-doped yttrium aluminum garnet (Nd:YAG) laser (Kompauer *et al.*, 2017). While nitrogen lasers have a shorter lifetime than Nd:YAG laser and the photon energy is lower at higher wavelengths, new generations of MALDI ion sources are using mainly Nd:YAG laser (Soltwisch *et al.*, 2014). In addition to solid-state laser with a wavelength at 355nm some MALDI experiments are performed using IR laser, which are quite useful by allowing the use of ice as the MALDI matrix (Pirkl *et al.*, 2012). The highly pulsed lasers (2 - 10 ns for UV-MALDI) lead to the formation of a desorption plume above the irradiated surface (typically 100  $\mu\text{m}$ ), which increases in volume within the time. The MALDI plume consists of a dense gas of matrix molecules, aggregations, analyte molecules and other charged and uncharged particles. Since MALDI is a soft ionization method, it mainly leads to the formation of single charged ions such as quasi-molecular ions ( $[\text{M}+\text{H}]^+$  or  $[\text{M}-\text{H}]^-$ ) or adduct ions ( $[\text{M}+\text{Na}]^+$ ,  $[\text{M}+\text{K}]^+$ ,  $[\text{M}+\text{NH}_4]^+$ ). Two different models exist for the ionization of the analyte. According to Ehring *et al.* 1992, the older pooling model assumes that neutral charged analyte molecules are present in the matrix co-crystal. Ionization of the analyte molecules occurs by photoionization of matrix molecules during laser bombardment followed by energy transfer in the MALDI plume (Ehring *et al.*, 1992). Primary ionization occurs after the adsorption of the laser pulse and leads to a multitude of excited matrix molecules. The matrix molecules each absorb the energy of one photon and by exciton transition (hopping) between matrix molecules energy is transferred. One excited matrix molecule goes into the double high energy state and the other into its lower energy state. Thus, the energy difference between the photon energy ( $E_{h\nu} = 3.7 \text{ eV}$ ) and the ionization energy of a matrix molecule ( $E_{\text{ion}} \approx 8 \text{ eV}$ ) can be linked. Secondary ionization describes the charge transfer between excited matrix molecules and the analyte molecules. The transfer occurs in the MALDI plume or by collisions of the desorbed analyte molecules with charged matrix ions in the gas phase. The Lucky Survivor model according to Karras *et al.* has an additional idea of the ionization process (Karras *et al.*, 2000, Nimesh *et al.*, 2013). Analyte molecules, as well as matrix molecules, are partly already



protonated or deprotonated in the sample and retain their charge during crystallization. The laser pulse leads to the desorption of large matrix/analyte clusters into the gas phase, where they disintegrate into single ions by collisions within the MALDI plume.

The correct choice of the matrix compound is a major challenge in MALDI experiments. No MALDI matrix can be used for all analytical questions and analytes. There are a wide range and number of matrices that are either in common use or have been recently reported in the literature and there are basically three classes of matrices available: organic matrices, liquid crystalline matrices, and inorganic matrices (Leopold *et al.*, 2018). Classical organic matrices are  $\alpha$ -cyano-4-hydroxycinnamic acid (HCCA) and 2,5-dihydroxybenzoic acid (DHB), which are typically used in positive ion mode. 2-mercaptobenzothiazole (MBT) or maleic anhydride proton sponge (MAPS) are suitable for measurements in negative ion mode. While classical organic matrixes are the most common ones, liquid crystalline matrices such as 3-Nitrobenzyl alcohol (3-NBA) are getting more focus, because of their particular soft ionization (Jackson *et al.*, 2004). Inorganic matrices such as graphite provide only a weak background, but only a few studies are available (Chen *et al.*, 2010, Friesen *et al.*, 2015, Zhou *et al.*, 2017).

To find a helpful matrix for the target analyte is usually a “trial and error” process. The target analyte needs to be ionized by the matrix and should result in an excellent signal-to-noise (S/N) ratio, highly resolved mass spectra, low or less fragmentation of the analyte and a low matrix background to avoid interferences between the matrix and target analyte. To fulfill these requirements, functional MALDI matrixes must have different properties. The matrix must have strong adsorption at the emission wavelength of the laser. All commonly used matrices (Figure 8) contain an aromatic ring system with delocalized  $\pi$  electrons, while the ionization efficiency increases with an increasing adsorption coefficient. The second structural element is a carboxylic acid or thiol functional group to ensure the solubility of the matrix in polar solvents and the protonation or deprotonation of the analyte (Boughton *et al.*, 2016, Leopold *et al.*, 2018).

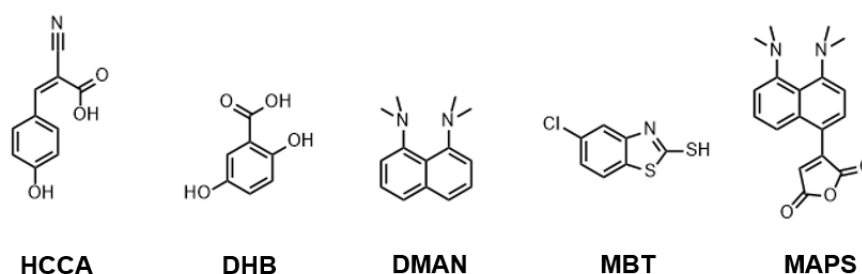


**Figure 8.** Chemical structure of commonly used MALDI matrices.  $\alpha$ -Cyano-4-hydroxycinnamic acid (HCCA), 2,5-Dihydroxybenzoic acid (DHB), 1,8-bis(dimethyl-amino)naphthalene (DMAN), 2-Mercaptobenzothiazole (MBT), 4-maleicanhydridopron sponge (MAPS) (Boughton *et al.*, 2016).

The crystallization between the matrix and the analyte leads to co-crystals which need to be as homogeneous as possible. Within the co-crystallization, the matrix should isolate the target analyte ions and prevent the generation of analyte clusters (e.g., dimer formation) during the ionization in the MALDI plume. Such clusters lead to a more complex spectra and decreases the sensitivity of the detection of the target analyte (Horneffer *et al.*, 1999, Szájli *et al.*, 2008, O'Rourke *et al.*, 2018, Leopold *et al.*, 2018). To facilitate the matrix selectivity, many approaches either by using additives to matrix preparations or by mixtures of matrix compounds (e.g., super DHB) can be done (Billeci and Stults, 1993, Rosinke *et al.*, 1995, Laugesen and Roepstorff, 2003).

### **1.5. Sample preparation for MALDI mass spectrometry imaging of plant tissues**

Sample handling is a crucial step in MSI experiments and needs to ensure the original spatial distribution of the target analyte within the plant tissue (Bhandari *et al.*, 2015, Dong *et al.*, 2016). Plant tissues have a higher water content and plant cells are generally larger compared to mammalian tissues (20-100  $\mu\text{m}$ ; mammalian tissues 10-50  $\mu\text{m}$ ). Therefore, sample preparation methods for plant tissues poses a bigger challenge during cryosectioning, because there are more fragile upon freezing and it is more difficult to get thin and intact histological slices from water-rich plant samples. Cryosectioning is the most commonly used method to prepare histological slices from plant tissues with a thickness between 10-40  $\mu\text{m}$ , typically used in MSI measurements. While plant cells also have rigid cell walls and large intercellular spaces, embedding materials are often used to maintain the tissue morphology and ensure precise sample sectioning, which is necessary for MALDI MSI experiments (Bjarnholt *et al.*, 2014). Nevertheless, many of commonly used embedding media such as optimum cutting compound (OCT) or paraffin wax are incompatible for MSI, because of strong interferences in the mass spectra, especially in the range of small molecules ( $< 500 m/z$ ). MSI-compatible embedding media are carboxymethyl cellulose (CMC), gelatin, paraplast embedding medium, ice or even combination of those (Dong *et al.*, 2016). After the plant tissue of interest is embedded in the media, the whole sample is snap frozen at various low temperature conditions. This can be done inside a deep freezer, powdered dry ice, liquid nitrogen or liquid nitrogen-chilled isopentane. Rapid freezing using liquid nitrogen can make plant tissues brittle and form ice crystals inside the tissue, and therefore plunging in liquid nitrogen is not optimal for plant tissues. Dried tissues such as wood with dense and relatively hard structures like plant stem can be also sectioned at room temperature (Boughton *et al.*, 2016). Section thickness is an essential parameter because it directly influences the signal intensity of the ion signal in the MSI measurement. While a tissue section between 5 and 20  $\mu\text{m}$  is recommended for MALDI

MSI analysis in mammalian tissues, samples of plant tissues are thicker within a range of 20-50  $\mu\text{m}$  (Sugiura *et al.*, 2006, Peukert *et al.*, 2012).



## 2 Aims and objectives

In this thesis, the technique of MALDI MSI has been used to investigate the uptake and distribution of a range of agrochemicals into several crop plants. Mass spectrometry imaging allows the combination of spatial information and molecular information for a wide range of compounds and microscopic histological information within the same measurement. Therefore, sophisticated sample preparation and measurement protocols were developed to enable a sensitive detection of the compounds. To compare mass spectrometry imaging with conventional methods for determining the uptake and movement of agrochemicals like autoradiography, liquid scintillation and chromatographic techniques coupled to mass spectrometry such as GC-MS and HPLC-MS, different use cases were studied.

- Phytotoxicity of the fungicide isotianil and its metabolite DCIT-acid. The uptake, movement, and metabolism of isotianil and its metabolite DCIT-acid should be investigated using different imaging techniques like autoradiography and mainly MALDI mass spectrometry imaging to track the target analytes after different applications on selected crop plants. The improved retention and coverage of the target compounds should be examined after micro droplet application on adaxial leaf surfaces of tomato (*Solanum lycopersicum*) and banana (*Musa*) leaves. At the same time, the uptake via the roots should be studied using a hydroponic system to visualize the systemic movement in tomato (*Solanum lycopersicum*) and wheat (*Triticum*) plants.
- Phytotoxicity of the fungicide fluopyram and its metabolite PCA in grape vine. Root uptake and translocation of radiolabeled PCA should be studied in hydroponic grown grapevine (*Vitis vinifera*), while the metabolic behavior and the nature of the residue during the winter period of fluopyram after foliar application should be investigated by tacking samples at different stages of the annual growth cycle.
- Distribution of the fungicide tebuconazole and a development candidate fungicide after seed treatment. The comparison of the classic fungicide tebuconazole, which is known to be rapidly absorbed into the vegetative part of plants and translocated principally acropetally with a development fungicide should be examined after seed treatment in wheat (*Triticum aestivum*) and soybean (*Glycine max.*). MALDI MSI should be used to get a closer look into the germination process of the seeds and to track the target analytes in the early stages of developing plants.

- Interaction and localization of the safener cyprosulfamide with the herbicide thien carbazon-methyl. The visualizing how the safener affects herbicide metabolism should be performed by applying the target compounds in the same or in different tissues of maize (*Zea mays*) as a representative monocotyledon plant.
- Systemicity of the insecticide ethiprole and distribution in reproductive tissues. The nature of residue in bee-relevant matrices of soybean (*Glycine max*) should be investigated after a single pre-flowering spray of radiolabeled ethiprole. MALDI-imaging experiments of flowers should be performed directly in flower tissues (banner, wing) and in transversal cross-sections of whole flowers (pedicel, stamen, pistil).
- Uptake and surface adsorption of the fungicide propineb on adaxial leaf surfaces. In this study, MALDI MSI should be used to investigate the degradation and metabolism of propineb on tomato leaves (*Solanum lycopersicum*). The combination of MALDI MSI with stable isotope labeled propineb-DIDT should be used to investigate the residues on the leaf surfaces *in-situ* with limited sample preparation to avoid degradation due to the sample preparation itself. Finally, the established sample preparation protocol should be used for the fast and direct analysis of real field samples to examine the behavior of propineb under naturally weather conditions (e.g., wind, rain).

### 3. Material and methods

#### 3.1. Instruments

- HPLC-system Agilent 1200 series consist of: autosampler (G1367B HiP-ALS), pump (G1312B Binary pump SL), column oven (G1316B TCC SL), PDA (G1315C DAD SL) and degasser (G1379B) from Agilent Technologies (Waldbronn, Germany).
- HPLC-system Agilent 1290 Infinity series consist of: autosampler (H4226A HiP-ALS), pump (G4220A Binary pump SL), column oven (G1316C TCC SL), PDA (G4212A DAD SL) from Agilent Technologies (Waldbronn, Germany).
- HPLC-system UltiMate 3000 consist of: pump, flow manager, PDA detector and autosampler from Dionex Softron GmbH (Germering, Germany).
- HPLC-system Agilent 1200 series consist of: autosampler (G1367B HiP-ALS), pump (G1312B Binary pump SL), column oven (G1316B TCC SL), PDA (G1315C DAD SL), degasser (G1379B) from Agilent Technologies (Waldbronn, Germany) coupled to a radiodetector Ramona 2000 (Raytest, Straubenhardt, Germany).
- Mass spectrometer: LTQ-Orbitrap from Thermo Fisher Scientific (Waltham, USA).
- Mass spectrometer: LTQ-Orbitrap XL from Thermo Fisher Scientific (Waltham, USA).
- Mass spectrometer: Orbitrap Fusion from Thermo Fisher Scientific (San Jose, USA).
- AP-SMALDI10 Q Exactive: MALDI ion source AP-SMALDI10 (TransMIT GmbH, Giessen, Germany) coupled to a high-resolution mass spectrometer Q Exactive (Thermo Scientific GmbH, Bremen, Germany).
- AP-SMALDI5AF Q Exactive: MALDI ion source AP-SMALDI5AF (TransMIT GmbH, Giessen, Germany) coupled to a high-resolution mass spectrometer Q Exactive (Thermo Scientific GmbH, Bremen, Germany).
- AP-SMALDI5AF Q Exactive HF-X: MALDI ion source AP-SMALDI5AF (TransMIT GmbH, Giessen, Germany) coupled to a high-resolution mass spectrometer Q Exactive HF (Thermo Scientific GmbH, Bremen, Germany).
- SMALDI Prep spray device (TransMIT GmbH, Giessen, Germany).
- Cryostat Microm HM550 (Thermo Scientific GmbH, Bremen, Germany).
- Cryostat CryoStar NX70 (Thermo Scientific GmbH, Bremen, Germany).
- Optical microscope S8AP0 with an EC3 digital camera (Leica Mikrosysteme GmbH, Wetzlar, Germany).
- Digital microscope VHX-5000 (Keyence Deutschland GmbH, Neu-Isenburg, Germany).

- Digital microscope VHX-6000 (Keyence Deutschland GmbH, Neu-Isenburg, Germany).
- Liquid Scintillation Counter (LSC): LS 6500 (Beckmann Coulter GmbH, Brea, USA).
- Liquid Scintillation Counter Tri-Carb 2910 TR (Perkin Elmer Life Science, Waltham, USA).
- Oxidizer 501 (Zinsser Analytic GmbH, Frankfurt am Main, Germany).
- Oxidizer 501 with robot control (Zinsser Analytic GmbH, Frankfurt am Main, Germany).
- BAS-2000 Phosphorimager (Fuji Photo Film Co. Ltd., Tokyo, Japan).
- Plant growth chamber Percival (CLF PlantClimatics GmbH, Wertingen, Germany).
- Lyophiliser Vaco5 (Zirbus technology GmbH, Bad Grund, Germany).
- Centrifuge Allegra 21R (Beckmann Coulter GmbH, Brea, USA).
- Centrifuge Avanti J-25 (Beckmann Coulter GmbH, Brea, USA).

### **3.2. Software**

- Control of LC-HRMS measurements: Software XCalibur, version 2.0.7, service pack 1.0 (Thermo Fisher Scientific, Waltham, USA).
- Data evaluation of LC-HRMS measurements: Software XCalibur, version 2.2, service pack 1.48 (Thermo Fisher Scientific, Waltham, USA).
- Control and Tuning of Q-Exactive coupled to AP-SMALDI10 ion source: Software Thermo Q-Exactive Tune Software, version 2.3 (Thermo Scientific GmbH, Bremen Germany).
- Control and Tuning of Q-Exactive coupled to AP-SMALDI5AF ion source: Software Thermo Q-Exactive Tune Software, version 2.3 (Thermo Scientific GmbH, Bremen Germany).
- Control and Tuning of Q-Exactive HF-X coupled to AP-SMALDI5AF ion source: Software Thermo Q-Exactive Tune Software, version 2.9 (Thermo Scientific GmbH, Bremen Germany).
- Control of SMALDI Prep Spray device: Matrix Sprayer Control, version 1.9.2890 (TransMIT GmbH, Giessen, Germany).
- Data evaluation of MALDI MSI measurements: Software Mirion, version 3.2.64.10, (TransMIT GmbH, Giessen, Germany).
- Data evaluation of MALDI MSI measurements: Software ImageQuest, version 1.1, (Thermo Scientific GmbH, Bremen, Germany).
- Data evaluation of MALDI MSI measurements: Software MSIReader, version 0.09, (Robichaud *et al.*, 2013).



- Data evaluation of LC-RD measurements: Software Gina Star, version 5.6.11.5056 (Raytest GmbH, Straubenhardt, Germany).

### 3.3. Chemicals

- Ammonium chloride, CAS 12125-02-9 (Merck KGaA, Darmstadt, Germany).
- Astra blue Solution, CAS 82864-57-1 (Waldeck GmbH & Co. KG, Münster, Germany).
- Bromomaleic anhydride, CAS 5926-51-2 (Sigma-Aldrich, Steinheim, Germany).
- Carboxymethylcellulose sodium salt, CAS 9004-32-4 (Sigma-Aldrich, Steinheim, Germany).
- Chloroform p.a., CAS 67-66-3 (AppliChem GmbH, Darmstadt, Germany).
- Dichloromethane, CAS 75-09-2 (AppliChem GmbH, Darmstadt, Germany).
- Disodium dihydrogen ethylenediaminetetraacetic acid, CAS 6381-92-6 (Sigma-Aldrich, Steinheim, Germany).
- Ethanol, CAS 64-17-5 (VWR International GmbH, Darmstadt, Germany).
- Gelatin, CAS 9000-70-8 (Merck KGaA, Darmstadt, Germany).
- Gram's safranin solution, CAS 477-73-6 (Sigma-Aldrich, Steinheim, Germany).
- Hoagland's No. 2 Basalt Salt Mixture (Sigma-Aldrich, Steinheim, Germany).
- Hydrochloric acid, conc., CAS 7647-01-0 (AppliChem GmbH, Darmstadt, Germany).
- Magnesium sulfate, CAS 7487-88-9 (Merck KGaA, Darmstadt, Germany).
- MALDI Calibration Kit MSCAL4 (Merck KGaA, Darmstadt, Germany).
- MES buffer; CAS 145224-94-8 (Sigma-Aldrich, Steinheim, Germany).
- Methanol, techn. Faculty-owned purification, CAS 67-56-1 (VWR International GmbH, Darmstadt, Germany).
- OCD-Compound Embedding medium (Leica Biosystems Inc., Richmond, USA).
- Paraplast Plus®, CAS 125387-89-5 (McCormick Scientific, St. Louis, USA).
- Phloroglucinol, CAS 6099-90-7 (Sigma-Aldrich, Steinheim, Germany).
- Quicksafe A (Zinsser Analytic GmbH, Frankfurt am Main, Germany).
- Safranin O, CAS 477-73-6 (Thermo Fisher Scientific, Waltham, USA).
- Sodium chloride, CAS 7647-14-5 (Merck KGaA, Darmstadt, Germany).
- Sodium hydroxide, CAS 1310-73-2 (Merck KGaA, Darmstadt, Germany).
- Trifluoroacetic acid, CAS 76-05-1 (Sigma-Aldrich, Steinheim, Germany)

#### 3.3.1. Isotope labeled chemicals

- [<sup>13</sup>C<sub>3</sub>, <sup>15</sup>N]Propineb-PTU, chemical purity >99%, isotope enrichment 99.2% (Bayer AG, Wuppertal, Germany).
- [isothiazole-3-<sup>14</sup>C, carboxylic acid-<sup>14</sup>C]DCIT-acid, chemical purity >98%, radiochemical purity 97.2% (Bayer AG, Wuppertal, Germany).

- [isothiazole-3-<sup>14</sup>C, carboxamide-<sup>14</sup>C]Isotianil, chemical purity >99%, radiochemical purity >99% (Bayer AG, Wuppertal, Germany).
- [phenyl-UL-<sup>14</sup>C]Isotianil, chemical purity >99%, radiochemical purity >99% (Bayer AG, Wuppertal, Germany).
- [phenyl-UL-<sup>14</sup>C]Tebuconazole, chemical purity >98%, radiochemical purity >98% (Bayer AG, Wuppertal, Germany).
- [triazole-UL-<sup>14</sup>C]Tebuconazole, chemical purity >99%, radiochemical purity >99% (Bayer AG, Wuppertal, Germany).
- [2,6-<sup>13</sup>C<sub>2</sub>, carboxylic acid-<sup>13</sup>C]PCA, chemical purity >98%, isotope enrichment 98.4% (Bayer AG, Wuppertal, Germany).
- [pyridyl-2,6-<sup>14</sup>C, carboxylic acid-<sup>13</sup>C]PCA, chemical purity >99%, radiochemical purity >99% (Bayer AG, Wuppertal, Germany).
- [phenyl-UL-<sup>14</sup>C]Ethiprole, chemical purity >99%, radiochemical purity >99% (Bayer AG, Wuppertal, Germany).

### 3.1.2. Reference and standard chemicals

- Cyprosulfamid, PESTANAL® analytical standard, CAS 221667-31-8 (Sigma-Aldrich, Steinheim, Germany).
- 3,4-Dichloroisothiazole-5-carboxylic acid (DCIT-acid), CAS 18480-53-0 (Bayer AG, Wuppertal, Germany).
- Fluopyram, CAS 658066-35-4 (Bayer AG, Wuppertal, Germany).
- Isotianil, CAS 224049-04-1 (Bayer AG, Wuppertal, Germany).
- Isotianil, PESTANAL® analytical standard, CAS 224049-04-1 (Sigma-Aldrich, Steinheim, Germany).
- Propineb, PESTANAL® analytical standard, CAS 12071-83-9 (Sigma-Aldrich, Steinheim, Germany).
- Propineb, CAS 12071-83-9 (Bayer AG, Frankfurt, Germany).
- Propineb-DIDT, chemical purity 97.8% (Bayer AG, Frankfurt, Germany).
- Propineb-PU, chemical purity 97.2%, CAS 6531-31-3 (Bayer AG, Frankfurt, Germany).
- Propineb-PTU, chemical purity 99.7%, CAS 2122-19-2] (Bayer AG, Frankfurt, Germany).
- Thiencarbazon-methyl, PESTANAL® analytical standard, CAS 317815-83-1 (Sigma-Aldrich, Steinheim, Germany).

### 3.4. HPLC solvents

- Methanol, Ultra Gradient HPLC-grade (J.T. Baker, Deventer, Netherlands).
- Acetonitrile, Ultra Gradient HPLC-grade (J.T. Baker, Deventer, Netherlands).
- Dist. water.
- Formic acid, 98% (Sigma-Aldrich, Steinheim, Germany).

### 3.5. MALDI matrices

- 2,5-Dihydroxybenzoic acid (DHB), CAS 490-79-9 (Alfa Aesar, Heysham, UK), 30 mg/mL in acetone:water (+0.2% TFA) 1:1 v/v).
- $\alpha$ -Cyano-4-hydroxycinnamic acid (HCCA), CAS 28166-41-8 (Sigma-Aldrich, Steinheim, Germany), 7 mg/mL in acetone:water (+0.2% TFA) 1:1 v/v).
- $\alpha$ -Cyano-4-hydroxycinnamic acid (HCCA), CAS 28166-41-8 (Sigma-Aldrich, Steinheim, Germany), 7 mg/mL in acetonitrile:water (+0.2% TFA) 1:1 v/v).
- 2-Mercaptobenzothiazole (MBT), CAS 149-30-4 (Alfa Aesar, Heysham, UK), 5 mg/mL in acetone:water 8:1 v/v).
- 1,8-bis(dimethyl-amino)naphthalene (Proton-sponge®, DMAN), CAS 20734-58-1 (Sigma-Aldrich, Steinheim, Germany), 50 mg/mL in toluene.
- 4-maleicanhydridoproton sponge (MAPS) 10 mg/mL in toluene.  
Synthesis of 4-maleicanhydridoproton sponge (Tyler *et al.*, 2010):  
1,8-Bis(dimethylamino)naphthalene (500 mg, 0.23 mmol) in 5 mL of THF was added to bromomaleic anhydride (200 mg, 0.11 mmol) in 3 mL of THF with stirring. The mixture immediately turned deep red upon mixing and was stirred for 30 min. The solvent was removed under reduced pressure, and the residue was redissolved in 25 mL of THF and filtered to remove PSHBr. The solvent was removed under reduced pressure, yielding a purple hygroscopic solid (323 mg, 92%).
- Isovanillin (ISO), CAS 621-59-0 (Sigma-Aldrich, Steinheim, Germany), 10 mg/mL in acetonitrile:water (+0.2% TFA) 7:3 v/v).
- Universal matrix (7 mg/mL HCCA + 30 mg/mL DHB in acetonitrile:acetone:water (+0.2% TFA) 1:1:2 v/v/v).
- Universal matrix (20 mg/mL HCCA + 20 mg/mL DHB in acetonitrile:acetone:water (+0.2% TFA) 1:1:2 v/v/v).

### 3.6. Plants

#### 3.6.1. Nutrient solution

All plants were either watered with a nutrient solution (Hoagland No. 2 basal salt mixture containing 2-(*N*-morpholino)-ethanesulfonic acid (MES) buffer, pH 5.5). For 1-liter nutrient

solution, 0.8 g Hoagland's No. 2 basal salt mixture, 2.06 g MES buffer and 0.75 ml of 1.5% Ferric EDTA (ethylenediaminetetraacetic acid) solution were solved in an appropriate amount of demineralized water. The pH was adjusted to 5.5 using potassium hydroxide (KOH) and finally the nutrient solution was filled up to 1 L with demineralized water.

### **3.6.2. Cultivation**

Plants were pre-grown either in a plant growth chamber Percival (CLF PlantClimatics GmbH, Wertingen, Germany) or in a greenhouse under controlled conditions. For plant uptake studies using a hydroponic system, plants were pre-grown in perlite until a specific development stage (e.g., BBCH 12, two-leaf stage) and transferred to the hydroponic system afterwards. Furthermore, foliar, drench or droplet-application plants were pre-grown in selected soil (e.g., "Monheim3") until a specific development stage. All plants were watered daily with the nutrient solution.

### **3.6.3. Hydroponic test system**

Plants for plant uptake studies in the hydroponic test system were taken out if the perlite at a specific growth stage (e.g., BBCH11-12, one- or two-leaf stage). For the transfer into the hydroponic system, the perlite was removed from the root system by washing with an untreated nutrient solution designated for the hydroponic test. One single plant was placed into a brown glass vessel (e.g.,  $V = 250 \text{ mL}$ ) filled with nutrient solution. This volume ensures that the root system is fully submerged. An appropriate stream of air aerated each flask. Plants were acclimatized to the new growth conditions for 4-10 days. Each bottle was closed with polyurethane (PU) foam plugs and to establish aerobic conditions throughout the study, each flask was aerated using ventilation. After the acclimatization, the plants were selected based on health, size and morphology and transferred in the hydroponic test system thereafter.

### **3.6.4. Single droplet application**

Using an Eppendorf pipette, pesticides were applied onto the adaxial surface of intact leaves of selected crop plants. A specific volume (e.g.,  $0.4 \mu\text{L}$ ) were deposited as single droplets.



**Figure 9.** Single droplet application of 3.0  $\mu\text{L}$  propineb-solution on the adaxial leaf surface of tomato (*Solanum lycopersicum*).

### 3.6.5. Greenhouse conditions

Experiments in the greenhouse of the test facility were performed under controlled growth conditions (e.g., a light:dark cycle of 16 hrs:8 hrs, a temperature range of day/night of approx. 22/16 °C, and a relative humidity approx. 50-85%).

### 3.6.6. Vegetation hall

Experiments in a vegetation hall were done under natural sunlight and temperature.

### 3.7. HPLC measurements

The heated electro-spray ionization MS spectra (H-ESI) or atmospheric-pressure chemical ionization MS spectra (APCI) were obtained with a LTQ-Orbitrap, LTQ-Orbitrap XL, or Orbitrap Fusion Tribrid mass spectrometer (all Thermo Fisher Scientific, Waltham, USA). The LTQ-Orbitrap mass spectrometer was operating at a mass resolution of 60,000 @  $m/z$  200 in positive and negative ion mode in a mass range of  $m/z$  100-1000. The ionization with the heated electrospray ionization interface was done with a spray voltage of 5 kV, capillary voltage and tube lens voltage was set to 20 and 100 V, respectively. The ion source was set to 250 °C vaporizer temperature and the ion transfer capillary to 200 °C. The gas flows in the ion source unit were set as follows: sheath gas 50 arb. u., auxiliary gas 8 arb. u. and sweep gas 0 arb. The chromatographic conditions for the MS experiments are given below.

**Table 6.** Chromatographic Parameters LTQ-Orbitrap.

HPLC Instrument and Setup	Solvents	Linear gradient
MS Instrument: LTQ-Orbitrap (Orbitrap, FT-MS)		
HPLC: Agilent 1200 Column: Luna® C18, 3 µm 50 x 3 mm (Phenomenex, Torrance, USA) Flow: 0.3 mL/min	A: 0.1% formid acid in water B: 0.1% formid acid in acetonitrile	0-0.5 min 5% B at 10 min 95% B at 13 min 95% B

The LTQ-Orbitrap XL mass spectrometer was operating at a mass resolution of 100,000 @  $m/z$  200 in positive and negative ion mode in a mass range of  $m/z$  100-1000. The ionization with the heated electrospray ionization interface was done with a spray voltage of 5 kV, capillary voltage, and tube lens voltage was set to 20 and 100 V, respectively. The ion source was set to 250 °C vaporizer temperature and the ion transfer capillary to 200 °C. The gas flows in the ion source unit were set as follows: sheath gas 50 arb. u., auxiliary gas 8 arb. u. and sweep gas 0 arb. The chromatographic conditions for the MS experiments are given below.

**Table 7.** Chromatographic Parameters LTQ-Orbitrap XL.

HPLC Instrument and Setup	Solvents	Linear gradient
MS Instrument: LTQ-Orbitrap XL (Orbitrap, FT-MS)		
HPLC: Agilent 1200 Column: Luna® C18, 3 µm 50 x 3 mm (Phenomenex, Torrance, USA) Flow: 0.3 mL/min	A: 0.1% formid acid in water B: 0.1% formid acid in acetonitrile	0-0.5 min 5% B at 10 min 95% B at 13 min 95% B

The Orbitrap Fusion Tribid mass spectrometer was operating at a mass resolution of 500,000 @  $m/z$  200 in positive and negative ion mode in a mass range of  $m/z$  75-1100. The ionization with the heated electrospray ionization interface was done with a spray voltage of 3.5 - 5 kV, capillary voltage and tube lens voltage was set to 20 and 100 V, respectively. The ion source was set to 100 °C vaporizer temperature and the ion transfer capillary to 350 °C. The gas flows in the ion source unit were set as follows: sheath gas 50 arb. u., auxiliary gas 10 arb. u. and sweep gas 0 arb. The chromatographic conditions for the MS experiments are given below.

**Table 8.** Chromatographic Parameters Fusion.

HPLC Instrument and Setup	Solvents	Linear gradient
MS Instrument: Tribid Fusion (Orbitrap, FT-MS)		
HPLC: Agilent 1290 Column: Nucleodur C18 Gravity, 1.8 $\mu$ m 150 x 2 mm (Macherey- Nagel, Düren, Germany) Flow: 0.3 mL/min	A: 0.1% formid acid in water B: 0.1% formid acid in acetonitrile	0-0.5 min 5% B at 10 min 95% B at 13 min 95% B

### 3.8. Radioactivity measurements

The radioactivity measurements in liquid samples were carried out by liquid scintillation counting (LSC). For this purpose, the entire volume of the sample was determined, and aliquot samples (100  $\mu$ L; 3 replicates) were subjected to LSC using either a Tri-Carb 2910 TR scintillation counter (Perkin Elmer Life Science, Waltham, USA) or a LS 6500 scintillation counter (Beckmann Coulter GmbH, Brea, USA). The counting times of the samples were generally between a few seconds and 10 minutes, depending on the amount of radioactivity present in the sample. Quench correction procedures were used to deduce spectral quench parameters.

Solid samples were weighted and combusted in an oxygen atmosphere using an oxidizer 501 (Zinsser Analytic GmbH, Frankfurt am Main, Germany) and the released  $^{14}\text{CO}_2$  was trapped in a scintillation cocktail and the radioactivity was finally determined by LSC.

Autoradiography of selected plant tissues was performed using phosphor screens BAS III (20x25 cm; Fuji Photo Film Co. Ltd., Tokyo, Japan) and developed with a Phosphorimager (Fuji Photo Film Co. Ltd., Tokyo, Japan). Therefore, dried plant material was placed on the phosphor screens in film cassettes BAS 2040 (Fuji Photo Film Co. Ltd., Tokyo, Japan) and development times between 4 and 16 hours were performed depending on the amount of radioactivity present in the plant tissues.

### 3.9. Sample preparation MALDI mass spectrometry imaging

Plant tissues (e.g., roots, seeds, stem, fruit, leaf) for cryosectioning were either embedded in gelatin (2 - 10% in water) or carboxymethylcellulose sodium salt (4 - 6% in water) and frozen at  $-20\text{ }^\circ\text{C}$  for at least 12 hours. Samples were equilibrated in the cryostat Microm HM550 (Thermo Scientific GmbH, Bremen, Germany) for approximately 30 min at the optimal cutting

temperature for each tissue ( $-25 - -15$  °C). Histological slices ( $15 - 35$   $\mu\text{m}$ ) of each tissue were mounted either on microscope slides ( $18 \times 18 \times 1$  mm, Paul Marienfeld GmbH & Co. KG, Lauda-Königshofen, Germany) directly or using thin double-sided adhesive tape (3M, Saint Paul, USA). The samples were dried in a desiccator at room temperature for a minimum of 30 min before matrix deposition. MALDI matrices were sprayed on the sample using a SMALDI Prep spray device (TransMIT GmbH, Giessen, Germany) and matrix flow rate ( $16-22$   $\mu\text{L min}^{-1}$ ), nitrogen flow rate ( $3 - 3.5$   $\mu\text{L min}^{-1}$ ), sample platform revolution speed ( $120 - 300$  rpm) and spray intervals ( $N = 1 - 4$ ), optimized for each matrix and tissue. Before and after matrix deposition, the sample surfaces were checked with an optical microscope S8 APO (Leica Mikrosysteme GmbH, Wetzlar, Germany), a VHX-5000 or VHX-6000 digital microscope (both Keyence Deutschland GmbH, Neu-Isenburg, Germany). The matrix-coated target was stored in a vacuum desiccator at room temperature in the dark until analysis. Plant tissues (e.g., seed, leaf) for direct surface mass spectrometry imaging experiments were dried at room temperature for a minimum of 30 min and placed on thin double-sided adhesive tape (3M, Saint Paul, USA) to a glass slide (Superfrost® Plus,  $20 \times 70$  mm, Fisher Scientific GmbH, Schwerte, Germany). MALDI matrix were sprayed on the sample using the same SMALDI Prep spray device in the area spraying mode with a matrix flow rate ( $14-20$   $\mu\text{L min}^{-1}$ ), nitrogen flow rate ( $5$   $\mu\text{L min}^{-1}$ ), application speed ( $2$   $\text{mm s}^{-1}$ ), and spray intervals (Raster,  $N = 1-2$ ), optimized for each matrix and tissue.

### **3.10. Histochemical staining of plant issues**

#### **Phloroglucinol stain of Lignin**

Lignin in plant cell walls was stained using phloroglucinol ( $30$  mg/mL in ethanol:HCL  $1:1$  v/v). The samples were prepared in 70% ethanol for 5 min, stained with phloroglucinol solution for 5 min and washed in two changes of 70% ethanol, each for 2 min.

#### **Safranin stain of wood cell walls**

Safranin Astra blue staining was performed to distinguish between lignified (xylem) and non-lignified (phloem) tissues. The samples were prepared in 50% ethanol for 5 min, stained with 1% safranin O in ethanol for 5 min, followed by 1% astrablue in ethanol for 10 min. The samples were washed in two changes of 70% ethanol, each for 2 min followed by two changes of water for 2 min.



### 3.11. MALDI Mass Spectrometry Imaging

MALDI MSI experiments were performed either at a high-resolution atmospheric-pressure MALDI ion source AP-SMALDI10 (TransMIT GmbH, Germany) coupled to a high-resolution mass spectrometer Q Exactive (Thermo Scientific GmbH, Bremen, Germany). The AP-SMALDI10 ion source was working with a nitrogen laser MNL 100 (LTB Lasertechnik Berlin GmbH, Berlin, Germany) at a wavelength of 337.1 nm, operating at a pulse frequency of 60 Hz. Automatic gain control (AGC) was disabled during all measurements, and the injection time (IT) was either fixed at 300 or 500 ms (microscans = 1). Full scan measurements in positive and negative ion mode were recorded at a mass resolution of 140,000 @  $m/z$  200 with selected mass ranges between  $m/z$  100 - 2000. For each target analyte, spray voltage was optimized in a range between 3 – 4. kV and S-Lens level was set to 35 – 80. Further MSI experiments were done using a high-resolution atmospheric-pressure MALDI ion source AP-SMALDI5AF (TransMIT GmbH, Germany), coupled to a high-resolution mass spectrometer Q Exactive (Thermo Scientific GmbH, Bremen, Germany) or to a high-resolution mass spectrometer Q Exactive HF-X (Thermo Scientific GmbH, Bremen, Germany). Desorption and ionization of analytes were initiated by a short-pulsed diode-pumped solid-state laser Flare NX 343 (Coherent, Santa Clara, USA) with a wavelength of 343 nm, operating at a repetition rate of 100 Hz. MSI measurements were measured with a high resolution in mass (Q Exactive: 140,000 @  $m/z$  200; Q Exactive HF-X: 240,000 @  $m/z$  200). For each target analyte spray voltage was optimized in a range of 3 – 4.3 kV and S-Lens level was set to 35 – 80 (Q Exactive), while Funnel RF level was set to 35 - 90 (Q Exactive HF-X). Automatic gain control (AGC) was disabled during all measurements and the injection time was either fixed at 500 ms (microscans = 1). Calibration of the mass spectrometer were performed weekly using the MALDI Calibration Kit MSCAL4 (Merck KGaA, Darmstadt, Germany) or with DHB matrix cluster ions ( $[2M+H-2H_2O]^+$ ,  $m/z$  273.03937;  $[2M+Na-2H_2O]^+$ ,  $m/z$  295.02131;  $[3M+Na-3H_2O]^+$ ,  $m/z$  431.03736;  $[4M+Na-3H_2O]^+$ ,  $m/z$  585.06397;  $[6M+NH_4-5H_2O]^+$ ,  $m/z$  852.14066;  $[7M+NH_4-6H_2O]^+$ ,  $m/z$  988.15671) using the customize calibration mode. Internal mass calibration was used by utilizing MALDI matrix cluster ions for lock mass (e.g. HCCA,  $[M+K]^+$ ,  $m/z$  228.00575; DHB,  $[2M+H-2H_2O]^+$ ,  $m/z$  273.03937; MBT,  $[M-H]^-$ ,  $m/z$  165.97906). Lateral scan resolution was adjusted for each sample individually in the range between 5 and 70  $\mu$ m. Scan mode was fixed to 2D pixel-to-pixel for the AP\_SMALDI10 ion source, while the AP-SMALDI5AF ion source ran in 2D pixel-to-pixel, 3D pixel-to-pixel, 2D-Full Pixel, and 3D Full-Pixel, depending on each sample type. Ion image generation was done with a bin width of  $\pm$  2 ppm for positive ion mode and  $\pm$  5 ppm for negative ion mode. The signal intensities were made visible using a color-coding system ranging from low intensity (blue) to high intensity

(red) using the software package ImageQuest (v. 1.1.0; Thermo Fisher Scientific, Germany) and the software Mirion (v. 3.2.64.10; TransMIT GmbH, Giessen, Germany).

## 4. Results and Discussion

### 4.1. Phytotoxicity of isotianil and its metabolite DCIT-acid

Successful control of plant protection products depends on how agrochemicals reaching specific target sites within the targeted organism. In this work, the uptake, translocation, and metabolism of isotianil and its metabolite DCIT-acid was investigated using different imaging techniques like autoradiography and mainly MALDI mass spectrometry imaging to track the target analytes after different types of applications on selected crop plants. The improved retention and coverage of the target compounds were either investigated after micro droplet application on adaxial leaf surfaces of tomato (*Solanum lycopersicum*) and banana (*Musa*) leaves, while the uptake via the roots was studied using a hydroponic system to visualize the systemic movement in tomato (*Solanum lycopersicum*) and wheat (*Triticum*) plants.

#### 4.1.1. Optimization of detection of isotianil and DCIT-acid with MALDI MS

In a MALDI mass spectrometry experiment, the used MALDI matrix fulfills several tasks, while the most important ones are the homogenous co-crystallization with the target analyte, its desorption and finally ionization (Karas *et al.*, 1987, Leopold *et al.*, 20018). While the desorption and ionization process are still not fully understood, the search for a useful matrix for sensitive detection of the target analyte is an empirical process and is done mainly based on “trial and error” (Glückmann *et al.*, 2001, Shroff *et al.*, 2009). Physicochemical properties like vacuum stability, polarity, and the maximum adsorption at the laser wavelength can be used to select a suitable MALDI matrix. However, screening of several matrices still needs to be done for each target analyte individually to ensure high sensitivity. Classic matrices used for UV-laser based MALDI mass spectrometry imaging are  $\alpha$ -cyano-4-hydroxycinnamic acid (HCCA) and 2,5-dihydroxybenzoic acid (DHB), which are suitable for the detection of a range of analytes from various chemical classes, such as small molecules like amino acids, lipids, polysaccharides or macromolecules like proteins and peptides (Krause *et al.*, 1996). In addition to these, several other MALDI matrices were also selected for matrix screening using the dried-droplet method in this work. *N,N,N',N'*-tetramethyl-1,8-naphthalenediamine (DMAN), 9-aminoacridine (9-AA), 2-mercaptobenzothiazole (MBT), 4-maleicanhydridoproton sponge (MAPS), Isovanillin (ISO) and a mixture of DHB and HCCA (1;1 v:v, Universal-matrix) were tested either in negative and positive ion mode. Therefore, a reference standard of isotianil and DCIT-acid (500  $\mu\text{g/mL}$ ) was mixed with the MALDI matrix (1:1, v/v) and 0.5  $\mu\text{L}$  of each solution were spotted on a stainless steel MALDI target plate. The sample was dried in a desiccator at room temperature for approx. 30 min and the MALDI MS measurements were

done afterward. 20 single full scan mass spectra with a mass range of  $m/z$  100-1000 and a mass resolution of 140.000 (@  $m/z$  200) were recorded for each spot ( $n = 3$  per target analyte) and the spatial resolution was set to 30  $\mu\text{m}$ . The average signal intensities of all 20 single spectra were calculated and normalized to a matrix cluster ion (e.g., HCCA,  $[\text{M}+\text{H}]^+$ ,  $m/z$  190.04987,  $[\text{M}-\text{H}]^-$ ,  $m/z$  188.03532) using the software Mirion (Table 9)

**Table 9.** MALDI matrix selection based on the signal intensity for isotianil and DCIT-acid using the dried-droplet method.

Matrix	Isotianil		DCIT-acid	
	pos ion mode	neg ion mode	pos ion mode	neg ion mode
DHB	2.4E3	n.d.	n.d.	n.d.
HCCA	1.3E4	n.d.	n.d.	n.d.
DMAN	n.d.	n.d.	n.d.	1.3E3
9-AA	n.d.	n.d.	n.d.	2.9E2
MBT	n.d.	n.d.	n.d.	4.1E2
MAPS	n.d.	n.d.	n.d.	2.3E3
ISO	n.d.	n.d.	n.d.	1.0E3
Universal	7.3E3	n.d.	n.d.	n.d.

n.d. not detected, mass deviation  $\pm 2$  ppm in positive ion mode and  $\pm 5$  ppm in negative ion mode,  $n$  (Spots) = 3

The screening of suitable MALDI matrices for the detection of isotianil and DCIT-acid showed highest signal intensities for isotianil in positive ion mode detected as the quasi-molecular ion ( $[\text{M}+\text{H}]^+$ ;  $m/z$  297.9603) using HCCA as the matrix, while DCIT-acid was only detected in negative ion mode as the quasi-molecular ion ( $[\text{M}-\text{H}]^-$ ;  $m/z$  195.9032). The potassium and sodium adduct ions of isotianil ( $[\text{M}+\text{Na}]^+$ ;  $m/z$  335.9162,  $[\text{M}+\text{K}]^+$ ;  $m/z$  335.9162) were detected in parallel, but the signal intensities were far lower compared to the quasi-molecular ion. It shows that the used MALDI MS instrument was less sensitive for the detection of DCIT-acid and a parallel detection of both target analytes within the same MALDI mass spectrometry experiment was not possible with the selected MALDI matrixes in this work.

Experiments to determine the sensitivity of the detection of both analytes were done using the dried-droplet method and various analyte solutions with different concentrations (0.1, 0.5, 1, 5, 10, 50 and 100  $\mu\text{g ml}^{-1}$ ). Optical calculation of the droplet area after evaporation of the solvent was done with a digital microscope to determine the concentration/area ( $\mu\text{g/mm}^2$ ) leading to an estimated limit of detection/ $\text{mm}^2$  (LOD/ $\text{mm}^2$ ) of 80  $\text{pg/mm}^2$  for isotianil and 400  $\text{pg/mm}^2$  for DCIT-acid. These values need to be interpreted as estimated ones, because the droplet

deposition was done manually, which leads to different sizes of dried droplets on the MALDI sample plate and furthermore, the measurement was not performed on biological negative control tissues.

#### 4.1.2. Spatial distribution of isotianil and DCIT-acid in hydroponic grown wheat

Isotianil was applied in a rate of 100 µg/L and 200 µg/L to the root system of hydroponic grown wheat plants (*Triticum*) at the two-leaf stage (BBCH 12) and its uptake and translocation were followed using MALDI mass spectrometry imaging. The concentrations in the hydroponic test system represents the pore water situation, when a plant is surrounded by a solution of an agrochemical. After the uptake via the roots, an agrochemical can follow the apoplastic pathway via the cell walls, the symplastic pathway via the plasmodesma or transcellular pathway from vacuole to vacuole (Lamshöft *et al.*, 2018.). Due to its physiochemical properties (solubility in water 0.5 mg/L, LogP<sub>ow</sub> 2.96), only low amounts of isotianil could be detected inside the shoots after 10 days. The parent compound was found to be distributed in transversal cross-sections of young seminal roots in the zone of maturation, where the water uptake takes places in plants (Figure 10). Transverse sections of roots in the root hair zone reveal an epidermis in which some cells have become long unicellular root hairs and cortex of parenchymatous cells. The endodermis surrounds an inner cylinder of tissue (stele), where alternate bands of xylem and phloem are arranged around a central metaxylem vessel. The detection of the monoisotopic masses of the quasi-molecular ion ( $[M+H]^+$ ,  $m/z$  297.9603) and the potassium adduct ion of isotianil ( $[M+K]^+$ ,  $m/z$  335.9162) in positive ion mode with consist ion images, thereby confirming the accurate detection of the target compound. Even the fact that this mass region of the spectra produced intense background ion signals (especially using HCCA as MALDI matrix in positive ion mode), the presence of chlorine in the chemical structure of isotianil (and DCIT-acid) provided a unique isotopic pattern in the spectra. While the quasi-molecular ion was mainly distributed in the cortex, the potassium adduct ion showed the highest signal intensities in the vascular bundles, including xylem and phloem. This pattern of accumulation on the one hand in the cortex and on the other hand, in the vascular bundle system might lends evidence of the ongoing uptake of isotianil during the water consumption of the plant. The formation of specific adduct ions ( $[M+K]^+$ ,  $[M+Na]^+$ ) might originate from the intrinsic inorganic salt content in different plant tissues. Potassium is the predominant mineral of plant cells in the shoots and is most important for cell growth and metabolism. Plant roots absorb potassium ions by the roots and transport them afterward in the xylem (water transport tissue) via the acropetal transpiration stream to the shoots. There, in source tissues where enough chemical energy (ATP) is available, potassium ions are loaded into the phloem

(photosynthate tissue) and then transported with the phloem stream to other parts of the plants, resulting in transport back to the roots (Karley and White, 2009). Endogenous plant metabolites like amino acids or carbohydrates were detected in parallel by MALDI MSI and asparagine showed a wide distribution in the cortex and in the vascular bundle. Free asparagine is predominant in all plant tissues and plays a central role in nitrogen storage. It accumulates to high concentrations during several plant development processes such as seed germination or during plant growth in the early stages of young plants. Amino acids are present in both xylem and phloem and can be withdrawn from the vascular system by cells that depend on an external supply, such as apices, newly developing tissues, and reproductive organs.

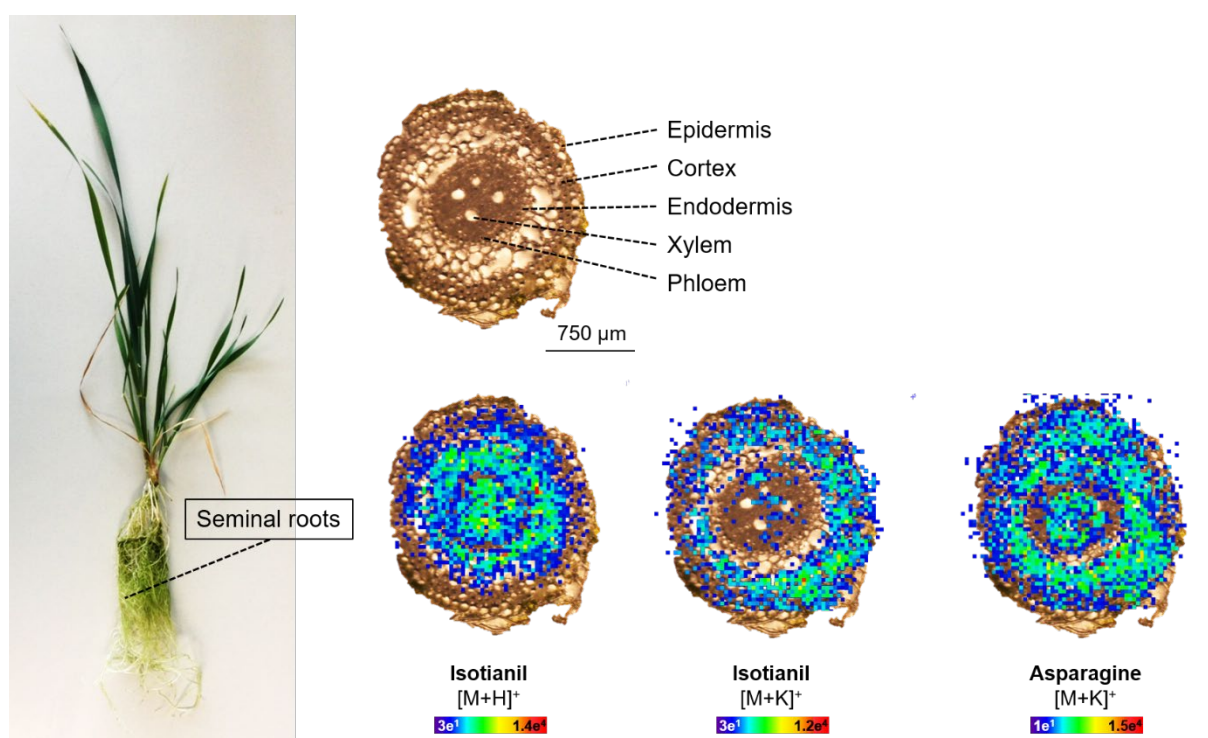


**Figure 10** MALDI-imaging-HRMS of isotianil in hydroponic grown wheat (*Triticum*) roots 10 days after treatment with isotianil (200 µg/L, spatial resolution: 30 µm, scan area: 2370x1710 µm). Localization of Isotianil ( $[M+H]^+$ ;  $m/z$  297.9603,  $[M+K]^+$ ;  $m/z$  335.9162) and primary plant metabolite asparagine ( $[M+K]^+$ ;  $m/z$  171.0167).

MALDI Imaging experiments of DCIT-acid-treated (100 µg/L) wheat plants showed the presence of the target analyte in different parts of the root system after 10 days of uptake (Figure 11). DCIT-acid was detected as the quasi-molecular ion ( $[M-H]^-$ ;  $m/z$  195.9032) in negative ion mode, while it could not be detected either in the positive ion mode. DCIT-acid could be visualized in the zone of lateral seminal roots of the total root system with a higher abundance in the vascular bundles, including xylem and phloem. These type of roots are of

greatest importance during seedlings early growth before higher internodes begin to establish. In the radicle and seminal roots, DCIT-acid was also detected as the quasi-molecular ion in negative ion mode, mainly in the vascular bundle system.

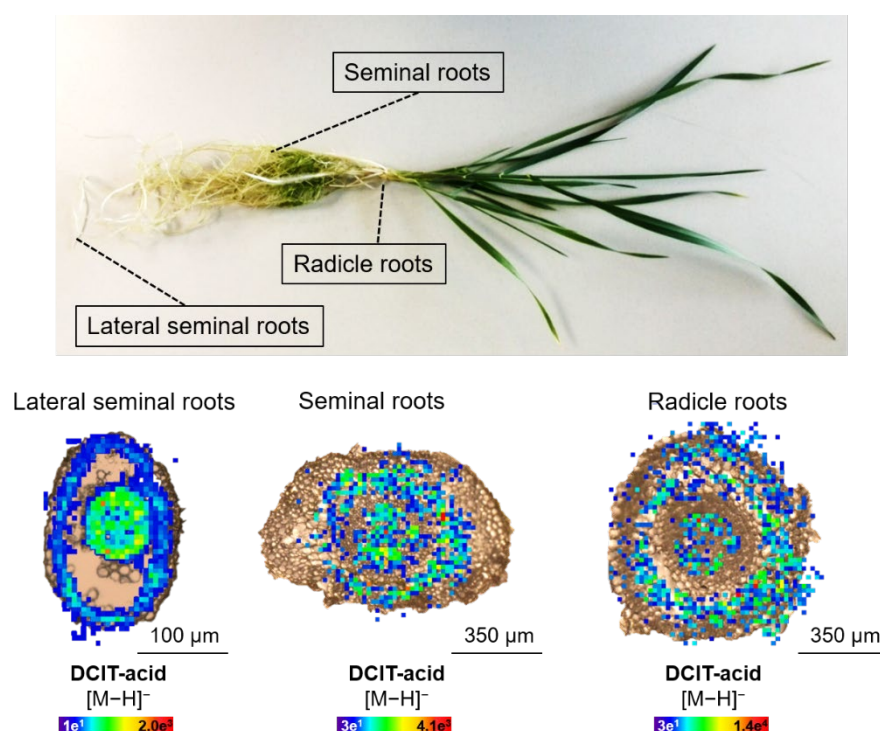


**Figure 11.** MALDI-imaging-HRMS of DCIT-acid in hydroponic grown wheat (*Triticum*) roots 10 days after treatment with DCIT-acid (100 µg/L, spatial resolution: 25 µm). Localization of DCIT-acid ([M-H]<sup>-</sup>; *m/z* 195.9032).

#### 4.1.3. Uptake of isotianil and DCIT-acid in hydroponic grown tomato

The uptake and translocation of <sup>14</sup>C-labeled isotianil (200 µg/L, [isothiazole-3-<sup>14</sup>C, carboxamide-<sup>14</sup>C]) and <sup>14</sup>C-labeled DCIT-acid (250 µg/l, [isothiazole-3-<sup>14</sup>C, carboxylic acid-<sup>14</sup>C]) in tomato plants (*Solanum lycopersicum*) were studied, using the previous hydroponic system. The plants were grown till the flower development stage (BBCH 69-72). All plants showed normal and healthy plant growth like the untreated control plant (Table 10). The values for isotianil are 30% higher compared to DCIT-acid and no direct influence on the plant growth could be observed, because all plants reached nearly the same phenological development stage (BBCH ≈ 71, flowers open and first fruit cluster). Furthermore, no phytotoxic symptoms were discovered, and all treated plants developed flowers nearly 25 days after application and appear as dichotomously branched cyme. The flowers were partly hand pollinated by shaking

them gently to support the pollination because of the missing wind or honeybees in the greenhouse.

**Table 10.** Uptake results of isotianil and DCIT-acid in hydroponic grown tomato.

	DCIT-acid		Isotianil		Control
	0.2 ppm <sup>a</sup>	0.25 ppm <sup>a</sup>	0.2 ppm	0.25 ppm	-
Water uptake [%]	66.8 ± 2.9	60.0 ± 1.3	73.7	64.4	67.4
Biomassfactor	19.9 ± 0.3	20.7 ± 4.6	33.5	36.0	25.4
Plant weight [g]	145 ± 3.2	141 ± 5.7	154	130	142
PUF	0.88 ± 0.21			- <sup>a</sup>	-
Flower	+	+	+	+	+
Fruit	+	+	+	+	+

n = 3. <sup>a</sup> not calculated. + developed.

**Table 11.** Distribution of [<sup>14</sup>C]-DCIT-acid in tomato plants.

Part	Biomass [g]	DCIT-acid relative to concentration in whole plant [%]	DCIT-acid [ng/mg <sub>FW</sub> ]
Root	34	3.8	0.5
Stem	45	11.1	0.7
Leaf	57	77.5	3.8
Flower/fruit	6	7.6	21.5

n = 1.

Analyses employing LC-HRMS of the different plant parts (root, stem, leaf, and flowers) showed a high accumulation of DCIT-acid in new grown areas of the tomato plants (treated with 25 within a good acropetally translocation to shoots and leaves (excellent xylem mobility). The highest residues are found in the leaves (78%) meanwhile, the highest concentration per biomass was found in the flowers (21.5 ng/mg FW), cause of the high differences in their biomasses. It underlines the high mobility of DCIT-acid within the water uptake in the hydroponic test system which is also confirmed by the calculated plant uptake factor (PUF) of  $0.88 \pm 0.21$ , depending on its physicochemical properties, mainly high-water solubility (5.0 g/L) and an octanol/water-partition coefficient ( $\log P_{ow}$  2.15). PUF describes the change in concentration in soil solution due to water and compound uptake via the plant roots (Figure 12, Lamshöft *et al.*, 2018):



$$PUF = \frac{\ln\left(\frac{m_{End}}{m_{Start}}\right)}{\ln\left(\frac{V_{End}}{V_{Start}}\right)}$$

$m_{Start}$  : mass of compound in solution at the start of the experiment

$m_{End}$  : mass of compound in solution at the end of the experiment

$V_{Start}$  : volume of nutrient solution at the start of the experiment

$V_{End}$  : volume of nutrient solution at the end of the experiment

**Figure 12.** Calculation of the plant uptake factor (Lamshöft *et al.*, 2018).

HPLC-ESI-HRMS analyses of the different plant tissues treated with isotianil validates only the presence of the parent compound in the leaves at very low concentration (< 15 ng/ g FW). The metabolites DCIT-acid and anthranilonitrile were not detected in isotianil treated plants. Either there is an extensively degradation/metabolism during water uptake after 34 days or the uptake of isotianil in the hydroponic test system takes place only in small amounts depending on its low water solubility (0.5 mg/L). However, the focus was to investigate the translocation and phytotoxicity of DCIT-acid in the reproductive organs. Therefore, autoradiography followed by combustion for LSC measurements of flower tissues of radiolabeled DCIT-acid treated plants were performed to determine the distribution of [<sup>14</sup>C] DCIT-acid in the different flower tissues as shown in table 12 and figure 13.

**Table 12.** Distribution of [<sup>14</sup>C] DCIT-acid in tomato flower after root uptake of DCIT-acid (250 µg/L) for 34 days.

Part	$m_{FW}$ [mg]	dpm	dpm/mg <sub>FW</sub>	$m_{abs.}$ [ng]	$m/m_{FW}$ [ng/mg]
Peduncle (1)	5.1	863	169	4.0	0.8
Sepal (2)	15.1	70955	4699	332	22.0
Petals (3)	17.7	15269	863	71.5	4.0
Pistil (4)	17.6	50607	2875	237	13.5
Stamen (5)	3.8	4263	1122	20.0	5.3
Sum	59.3	141956	9728	665	45.5

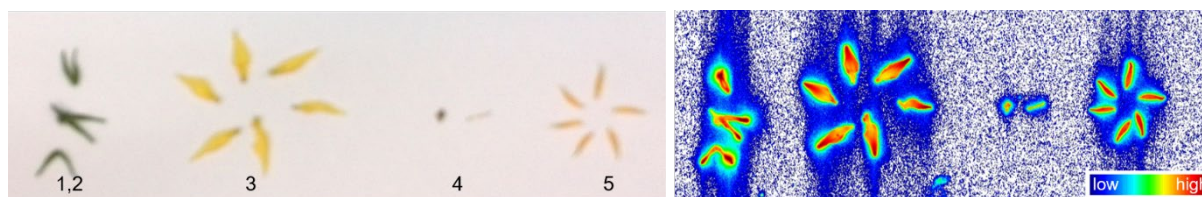


**Figure 13.** Translocation of [ $^{14}\text{C}$ ] DCIT-acid in tomato flower. Highest radioactivity is in red.

Residues of [ $^{14}\text{C}$ ] DCIT-acid were found in all four main parts of the flower. The highest residue was detected in the sepal, which protect the flowers before opening. Tomato flowers reproduce sexually and both female and male organs are located within the same flower. The female genetic information is located in the ovule, which is part of the pistil (4), meanwhile the male genetic information is located in the pollen, which is part of the stamen (5). The residue levels of DCIT-acid in both sexual organs are relatively high (13.5 respectively 5.3 ng/mg FW). During the fruit development, the petals, stamen, and stigma dry up and fall off.

The ionization of DCIT-acid using classic MALDI matrixes like HCCA, DHB or MBT was very problematic. DCIT-acid was only detected in low signal intensities in negative ion mode using MBT. Therefore, additional matrices were tested and optimized for MALDI mass spectrometry imaging measurements. A classic matrix used in MALDI mass spectrometry analysis of small molecules in negative ion mode is 1,8-bis(dimethylamino)naphthalene (DMAN), which belongs to a class of compounds called proton sponges (Shroff *et al.* 2009, Weißflog *et al.* 2016). These highly alkaline bases can deprotonate (acidic) analytes in solution, depending on their high thermodynamic basicity. Even though DMAN showed better signal/noise ratios for the detection of DCIT-acid followed by an accurate high limit of detection, while testing with the dried-droplet method, DMAN was not suitable in MALDI imaging experiments. Matrix application of DMAN done with automatic droplet deposition using the SMALDI Prep spray device leads to inhomogeneous sample surfaces after matrix crystallization, which are not suitable for MALDI imaging measurements with a high lateral resolution ( $< 50 \mu\text{m}$ ). Giampà *et al.* published 2016 maleic anhydride proton sponge (MAPS) as a novel MALDI matrix for the detection of small molecules in negative ion mode. This study demonstrated the potential of MAPS by detecting chloride, lactate and 2-hydroxyglutarate in human diffuse glioma tissue with a spatial resolution of  $70 \mu\text{m}$  in negative ion mode. Unfortunately, MAPS was not suitable for MALDI imaging experiments in a range of high spatial resolution ( $10\text{-}35 \mu\text{m}$ ), because spraying with an automatic spray device like the SMALDI Prep spray device in this work, is performed with thin capillaries ( $\varnothing 150 \mu\text{m}$ ) and the MALDI matrix solution of MAPS in toluene leads to extensive wear of capillaries.

Additional MALDI matrices were tested and optimized for MSI analysis to avoid higher signal intensities in addition to better signal/noise ratios followed by the lower limit of detection especially for low-molecular-weight acids like DCIT-acid in negative mode. Isovanillin was one of the new tested MALDI matrices and showed higher signal intensities for DCIT-acid in negative ion mode. However, Isovanillin is a commonly used matrix for detecting organic molecules via MALDI-MS, it is not used for MALDI-imaging so far. Therefore, extensive optimization was performed to lead homogenous crystal structure during spray application with the SMALDI Prep spray device.

Using MALDI mass spectrometry imaging DCIT-acid could be visualized in a transversal tissue section of a tomato fruit (Figure 14). The metabolite is mainly localized in the seeds in relative high signal intensities. Furthermore, it also shows a wide distribution in the mesocarp and placenta. It underlines the high mobility of DCIT-acid in the whole tomato plants during water consumption. To get first hints about the concentration of DCIT-acids in the MALDI-samples serial cut slices were collected and combusted in an oxygen atmosphere (efficiency  $\geq 85\%$ ) using an Oxidizer followed by quantification of the combustion product  $^{14}\text{CO}_2$  with a liquid scintillation counter. This experimental setup led to a calculated value of approx.  $0.12 \text{ ng/mm}^2$  DCIT-acid in the whole tomato fruits. Furthermore, combustion of different numbers of histological slices ( $N= 1, 2, 3, 5, 10$  and  $20$ ) indicated a relatively homogenous distribution of radiolabeled DCIT-acid in the tomato, because the detected radioactivity showed equal average values for all LSC samples.

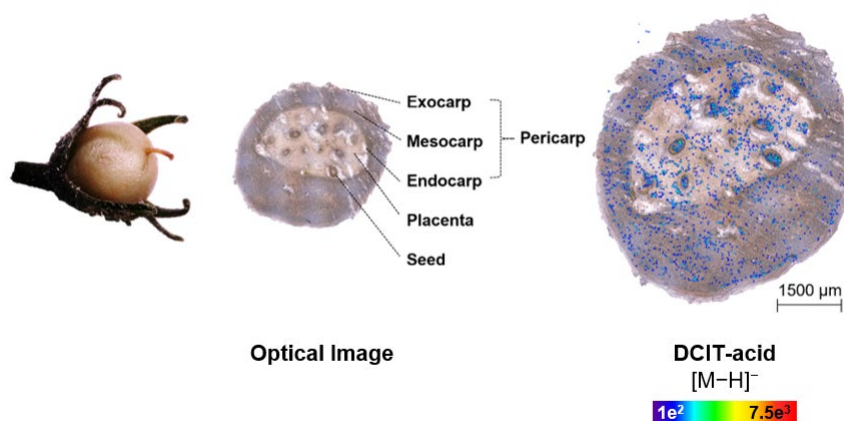


**Figure 14.** Spatial distribution of DCIT-acid ( $[\text{M}-\text{H}]^-$ ;  $m/z$  195.9032) in tomato fruit of hydroponic grown tomato incubated with 0.2 ppm DCIT-acid after 34 days (spatial resolution:  $25 \mu\text{m}$ , scan area:  $6766 \times 6766 \mu\text{m}$ ).

#### 4.1.4. Uptake and surface adsorption of isotianil on tomato leaves after droplet application

Studies about the uptake and translocation of isotianil via the roots in a hydroponic system already showed, that the parent compound is taken up only in small amounts and can be detected only in low concentrations in the shoots. In the following experiment the uptake and translocation via the leaves after microdroplet droplet application was investigated to get information about the possibility of isotianil to translocate via the cuticle. Therefore,  $^{14}\text{C}$ -labeled isotianil was applied as a SC200 formulation (250 ppm a.i.) on the adaxial site of tomato leaves (*Solanum lycopersicum*). The hydrophobic cuticle, composed of cutin and waxes, is critically important in limiting water loss via evaporation of the plant. Adsorption and uptake of plant protection products by leaves is depending on physiological and biological processes, while the adsorption can be improved by increasing the duration of sprays on the leaf surface (Xu *et al.*, 2010, Xu *et al.*, 2011). Autoradiography and MALDI MSI was further used to obtain information about the behavior of the applied droplets on the leaf surface. The formation of droplet deposition and retention is influenced by the tomato leaf cuticle, which consist of plates and protuberances of wax imbedded in various layer of cutin, a mixture of polymers of dicarboxylic hydrocarboxylic esters.

2 Days after treatment with  $^{14}\text{C}$  labeled isotianil, the area of droplet deposition is clearly visible on the phosphor image with autoradiography (Figure 15). The distribution of the radioactivity shows, on the one hand, the dried droplets with highest signals intensities and on the other hand (systemic) distributed radioactivity in areas of the leaf veins (e.g. midrip, lateral vein and sublateral vein) and less intensities in the stem. MALDI MSI measurement of the adaxial leaf surface confirms the homogenous distribution of isotianil in the area of the droplet placement. In contrast to the autoradiography no isotianil was observed in tissues of the leaf veins. While the metabolite anthranilonitrile was detected with a similar distribution in parallel, the signal in the leaf veins in the phosphorimage might originate from DCIT-acid, which contains the radiolabel in its chemical structure.

The plant hormone indole-3-acetic acid (IAA) was detected in parallel and showed a wide distribution all over the leaf with a slight enrichment in the lateral veins. It is the most common natural plant hormone of the auxin class and is necessary for the development of plant organs and coordination of growth.

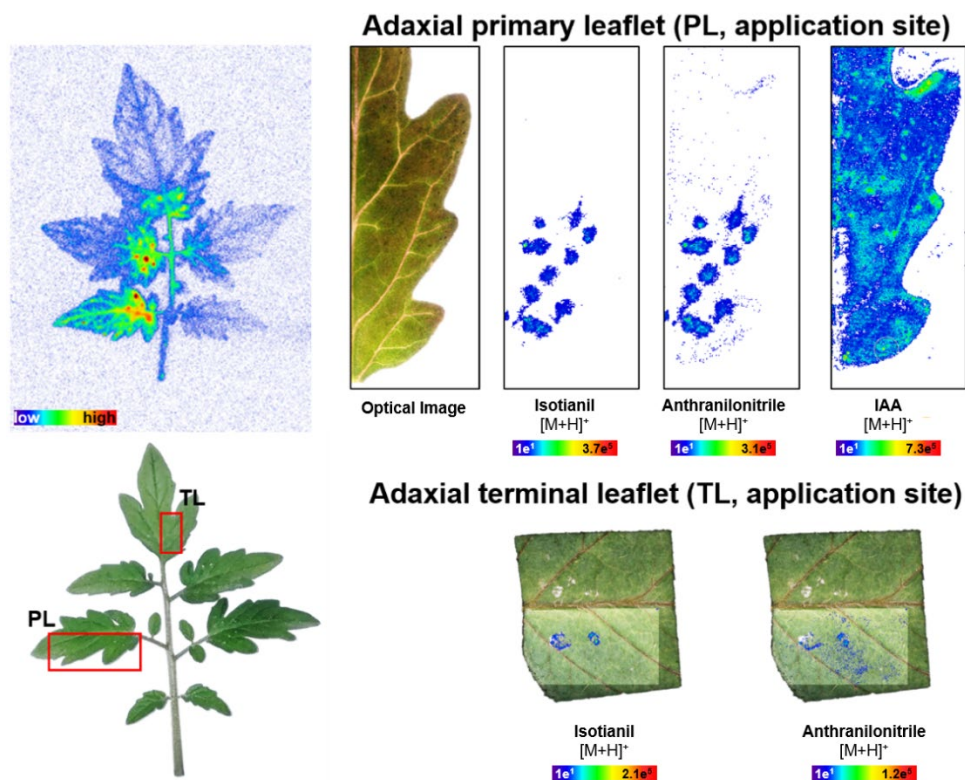


**Figure 15.** Autoradiography and MALDI-imaging-HRMS of tomato leaf 2 days after treatment with Isotianil (spatial resolution: 75  $\mu\text{m}$ , scan area: 156x395  $\mu\text{m}$ ). Translocation of [isothiazole-3-<sup>14</sup>C, carboxamide-<sup>14</sup>C]-Isotianil. Localization of Isotianil ([M+H]<sup>+</sup>;  $m/z$  297.9603), anthranilonitrile ([M+H]<sup>+</sup>;  $m/z$  119.0603) and plant hormone Indole-3-acetic acid ([M+H]<sup>+</sup>;  $m/z$  176.07061).

#### 4.1.5. Uptake and surface adsorption of Isotianil on banana leaves after droplet application

In the following experiment the uptake, translocation, and metabolism of <sup>14</sup>C-labeled isotianil after micro droplet application on the adaxial surface of banana leaves (*Musa*) was investigated using MALDI mass spectrometry imaging in area of interest and autoradiography of whole leaves. Banana leaves are difficult to wet because of their waxy surface. In general, banana leaf anatomy consisted of an adaxial epidermis, hypodermis, palisade layer, spongy layer, bundle sheath cell, and an abaxial epidermis (Harijati *et al.*, 2013). The epidermis is a thin cuticular membrane that encloses leaves functions to protect leaves from most environmental hazards. The protection also includes the impact of insect pests, pathogens, dust, and the excessive evaporation of water from the leaf surface. For these leaves, successful application of any plant protection product is difficult because of rebounding droplets that might scatter or roll the leaves after contact with the leaf surface (Xu *et al.*, 2010). Because of that water containing foliar application solutions of pesticides must then first penetrate waxes on the leaf

surface and then into the leaf tissue through cell walls and stomata. Adjuvants alter spray formulations and support the process of deposition, retention and spread of spray droplets on the leaf surface and the followed penetration into the plant via the leaves. Therefore, isotianil was applied via micro droplet application as a suspension concentrate (SC200) formulation (200 ppm a.i.).

Leaves for autoradiography were excised immediately after the experiment, placed in 100 mL solution of acetonitrile:water (4:1, v/v) shaken for 30 s, dried and the phosphor images developed. Samples for MALDI imaging were directly analyzed without surface washing at a spatial resolution of 25  $\mu\text{m}$ . Furthermore, the measurements of the leaf surface were performed in three following measurements of the same area to obtain more information about the penetration depth of the target compound without additional MALDI matrix applications between the measurements. Isotianil was found to have a homogenous coverage throughout the leaf surface, still cover most of the area of the droplet placement 3 days after application (Figure 16, Figure 19), in the 60% RH and 100% RH samples. Plants grown under 100% RH showed slightly homogeneous spreading over the entire droplet application area during the whole experiment, but the target compound is still more pronounced in the area of droplet placement. Isotianil is hardly soluble in water and spread over the area of the droplet placement area and does not diffuse to the center of the water droplets during the drying process. The second and third measurement of the same area showed similar signal intensities for the protonated signal ( $[\text{M}+\text{H}]^+$ ,  $m/z$  297.9603) and the potassium adduct ion ( $[\text{M}+\text{K}]^+$ ,  $m/z$  335.9162). The transfer from the surface to the interior of the leaf depends on the penetration properties of the cuticle, which covers all aerial portions of the plants and any chemical compound entering the aerial portions of the plant must pass through the cuticle. Isotianil was not taken up and the penetration via the cuticle of the adaxial epidermis could not be observed or was still ongoing ( $< \text{LOD}$ ). Additional autoradiography indicates the accumulation of [isothiazole-3- $^{14}\text{C}$ , carboxamide- $^{14}\text{C}$ ] Isotianil in the area of the applied droplets and the single droplets are still visible. DCIT-acid was not detected in Isotianil treated plants, while the metabolite anthranilonitrile could be observed in similar spatial distribution and signal intensities are comparable to the parent compound. The major metabolic pathway of isotianil includes the cleavage of the amide linkage to produce the corresponding carboxylic acid and aniline. DCIT-acid seems readily taken up and translocated via the transportation stream, indicating the systemic properties of the metabolite after droplet application. Furthermore, the endogenous plant metabolites salicylic acid and salicylic acid 2-O- $\beta$ -D-glucoside were detected in parallel using MALDI mass spectrometry imaging. Salicylic acid as a phenolic phytohormone can be found in plants with different roles in plant growth and development and induce pathogenesis-related proteins in the resistance to pathogens (Lee *et al.* 1995). Isotianil as an inducing host plant defense activator fungicide providing signals which directly interacts

with the signal transduction pathway of salicylic acid. In *Arabidopsis*, the basal level of cellular SA is kept at ~15  $\mu\text{M}$ , while during defense responses; it reaches ~200  $\mu\text{M}$  by quick biosynthesis via the isochorismate pathway. Both endogenous metabolites could be detected in leaf tissues where isotianil was applied. However, an effect of the fungicide on the biosynthesis of salicylic acid in leaf tissues could not be observed with MALDI MSI, because the differences in the concentration levels of the plant hormone might be too low for visualizing the effect using this imaging technique and more biological replicates are needed for statistical analysis.

Similar spatial distributions of Isotianil and anthranilonitrile in the MALDI-images were found on the banana leaves 7 and 14 days after application, while the phosphor imaging autoradiographs show a slight enrichment of radioactivity in the distal parts of the leaves. Due to the [isothiazole-3- $^{14}\text{C}$ , carboxamide- $^{14}\text{C}$ ]-label of Isotianil, it is not possible to distinguish between Isotianil and DCIT-acid in the autoradiographs. Additional LSC measurements of surface wash solutions (30s, acetonitrile:water, 4:1, v/v) underline, that approximately 80% of the applied activity was still on the leaf surface.

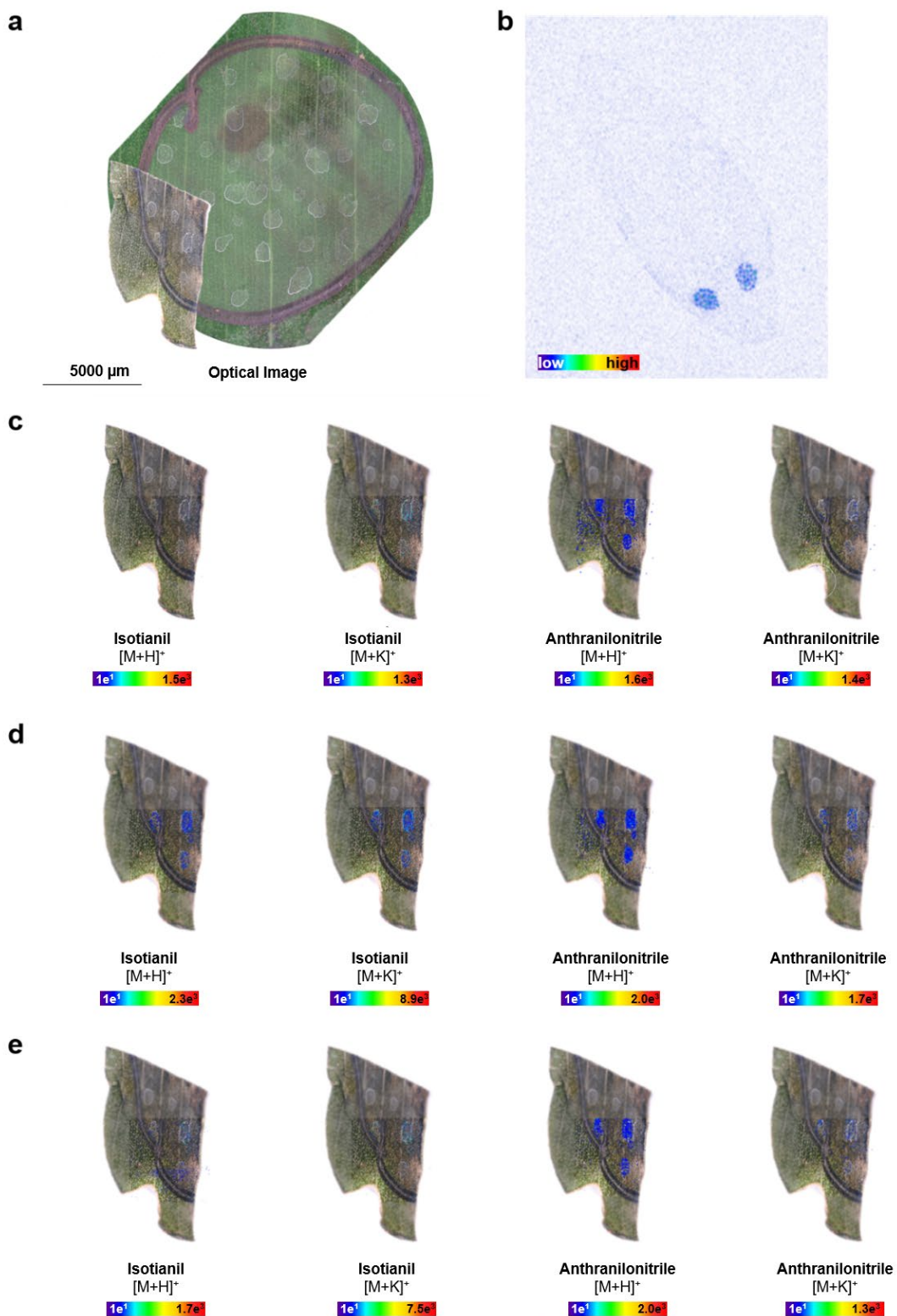


**Figure 16.** Autoradiography and MALDI-imaging-HRMS of banana leaf 3 days after treatment (60% RH) with Isotianil (spatial resolution: 25  $\mu\text{m}$ , scan area: 5500x5500  $\mu\text{m}$ ). **a:** Optical image of droplet application area. **b:** Translocation of [isothiazole-3- $^{14}\text{C}$ , carboxamide- $^{14}\text{C}$ ]-Isotianil by autoradiography. **c-e:** Localization of Isotianil ( $[\text{M}+\text{H}]^+$ ;  $m/z$  297.9603,  $[\text{M}+\text{K}]^+$ ;  $m/z$  335.9162) and anthranilonitrile ( $[\text{M}+\text{H}]^+$ ;  $m/z$  119.0603,  $[\text{M}+\text{K}]^+$ ;  $m/z$  157.0163).



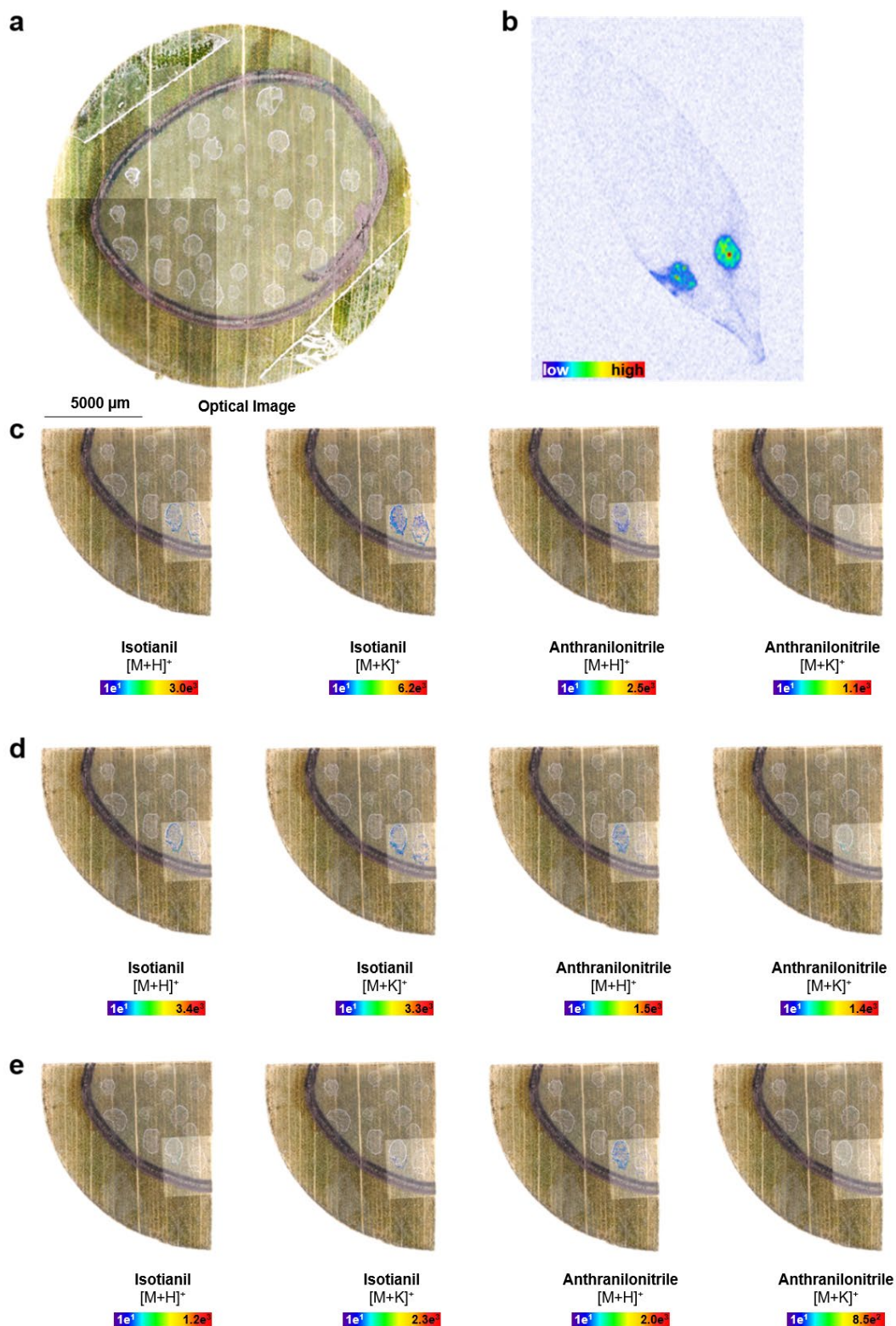


**Figure 17.** Autoradiography and MALDI-imaging-HRMS of banana leaf 7 days after treatment (60% RH) with Isotianil (spatial resolution: 25  $\mu\text{m}$ , scan area: 5500x5500  $\mu\text{m}$ ). **a:** Optical image of droplet application area. **b:** Translocation of [isothiazole-3- $^{14}\text{C}$ , carboxamide- $^{14}\text{C}$ ]-Isotianil by autoradiography. **c-e:** Localization of Isotianil ( $[\text{M}+\text{H}]^+$ ;  $m/z$  297.9603,  $[\text{M}+\text{K}]^+$ ;  $m/z$  335.9162) and anthranilonitrile ( $[\text{M}+\text{H}]^+$ ;  $m/z$  119.0603,  $[\text{M}+\text{K}]^+$ ;  $m/z$  157.0163).

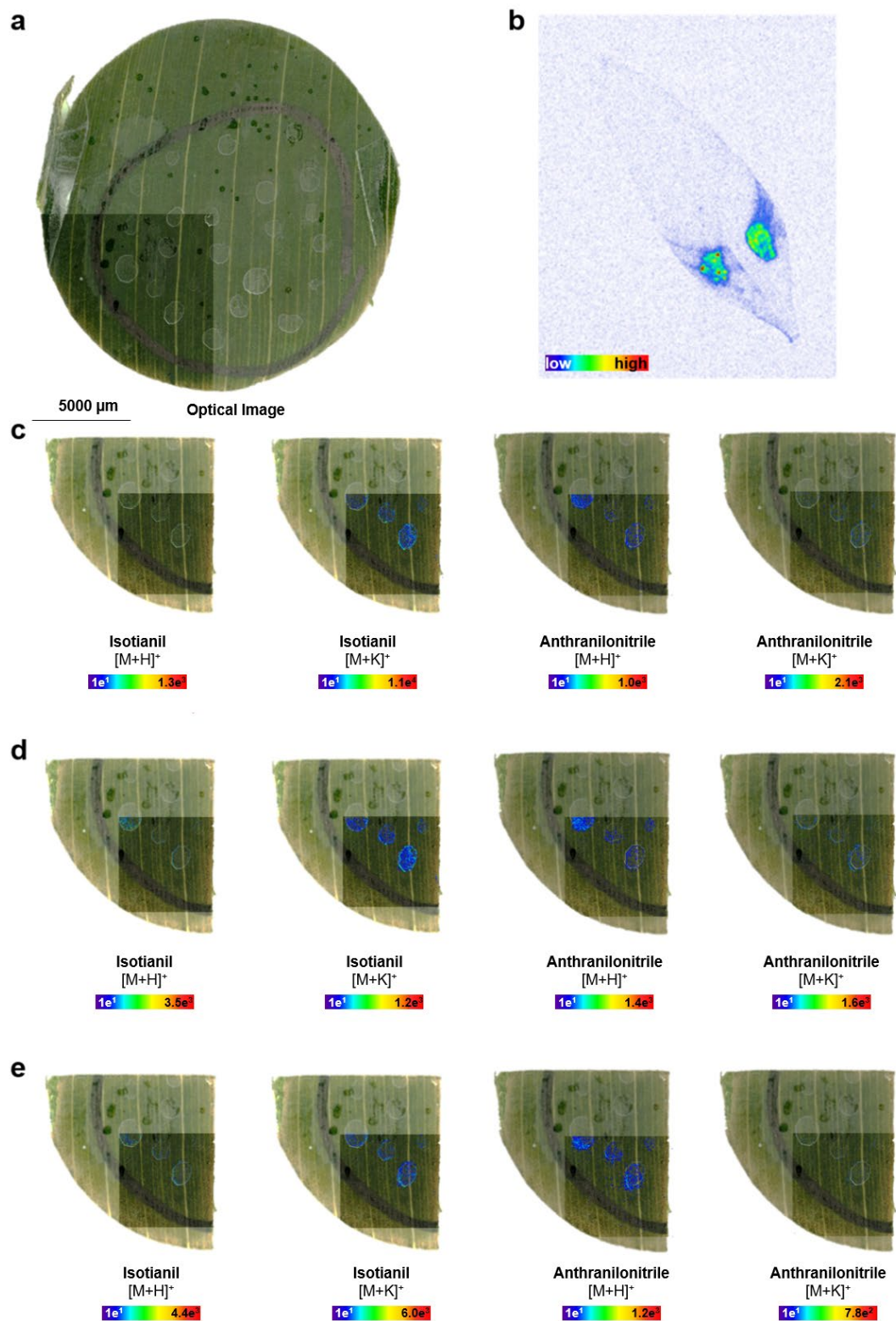


**Figure 18.** Autoradiography and MALDI-imaging-HRMS of banana leaf 14 days after treatment (60% RH) with Isotianil (spatial resolution: 25  $\mu\text{m}$ , scan area: 5500x5500  $\mu\text{m}$ ). **a:** Optical image of droplet application area. **b:** Translocation of [isothiazole-3- $^{14}\text{C}$ , carboxamide- $^{14}\text{C}$ ]-Isotianil by autoradiography. **c-e:** Localization of Isotianil ( $[\text{M}+\text{H}]^+$ ;  $m/z$  297.9603,  $[\text{M}+\text{K}]^+$ ;  $m/z$  335.9162) and anthranilonitrile ( $[\text{M}+\text{H}]^+$ ;  $m/z$  119.0603,  $[\text{M}+\text{K}]^+$ ;  $m/z$  157.0163).

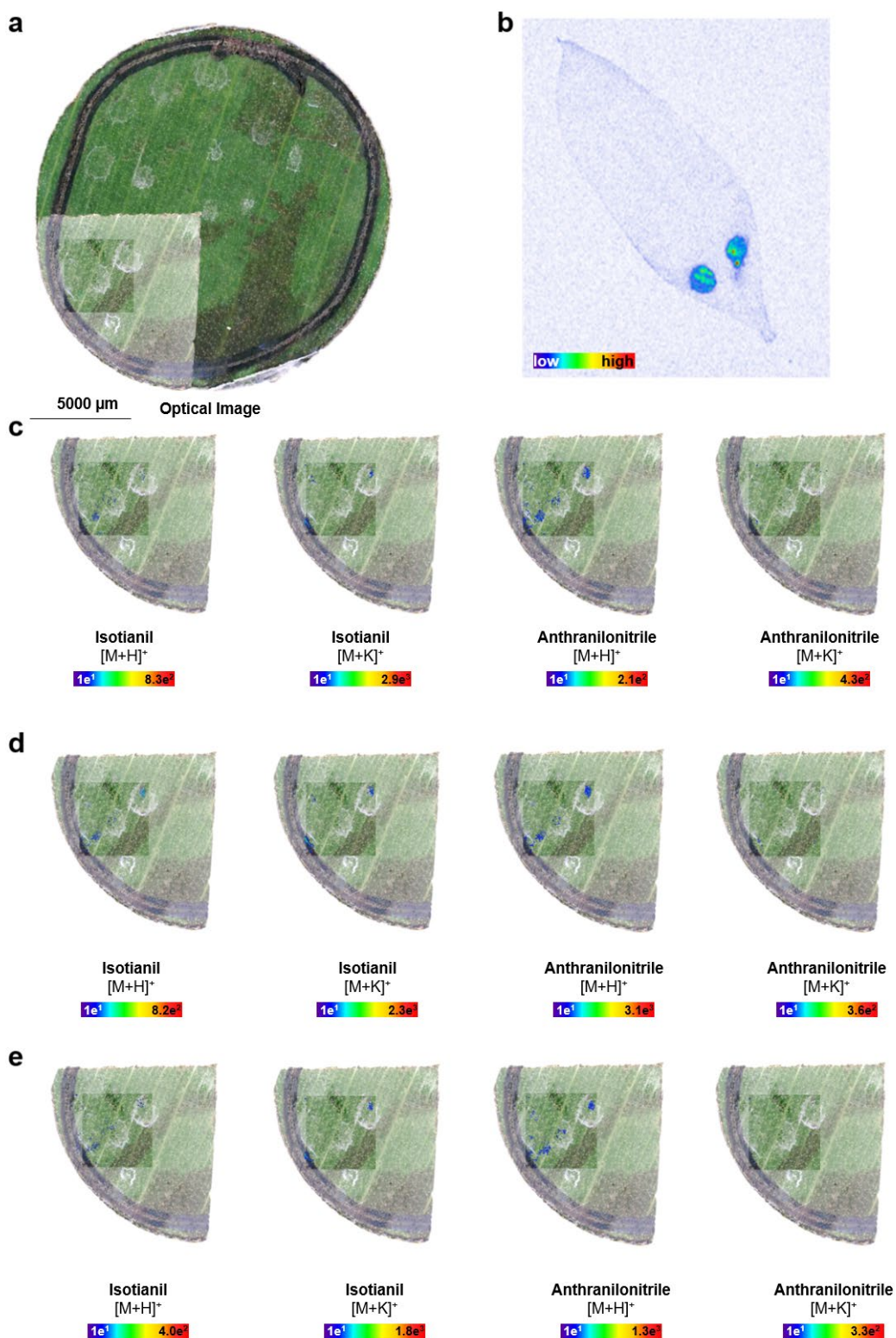


**Figure 19.** Autoradiography and MALDI-imaging-HRMS of banana leaf 3 days after treatment (100% RH) with Isotianil (spatial resolution: 25 µm, scan area: 5500x5500 µm). **a:** Optical image of droplet application area. **b:** Translocation of [isothiazole-3-<sup>14</sup>C, carboxamide-<sup>14</sup>C]-Isotianil by autoradiography. **c-e:** Localization of Isotianil ([M+H]<sup>+</sup>;  $m/z$  297.9603, [M+K]<sup>+</sup>;  $m/z$  335.9162) and anthranilonitrile ([M+H]<sup>+</sup>;  $m/z$  119.0603, [M+K]<sup>+</sup>;  $m/z$  157.0163).

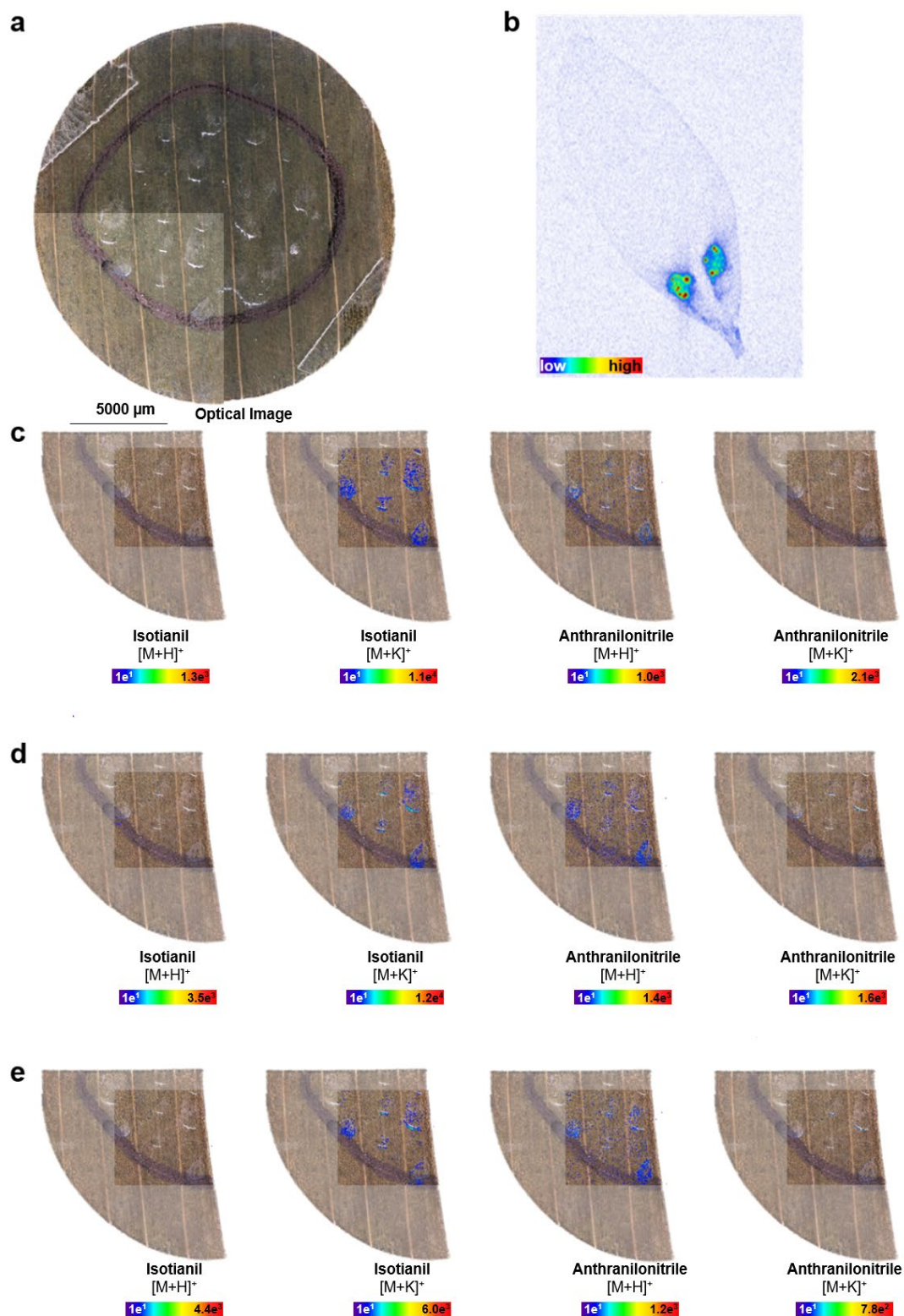


**Figure 20.** Autoradiography and MALDI-imaging-HRMS of banana leaf 7 days after treatment (100% RH) with Isotianil (spatial resolution: 25  $\mu\text{m}$ , scan area: 5500x5500  $\mu\text{m}$ ). **a:** Optical image of droplet application area. **b:** Translocation of [isothiazole-3-<sup>14</sup>C, carboxamide-<sup>14</sup>C]-Isotianil by autoradiography. **c-e:** Localization of Isotianil ([M+H]<sup>+</sup>;  $m/z$  297.9603, [M+K]<sup>+</sup>;  $m/z$  335.9162) and anthranilonitrile ([M+H]<sup>+</sup>;  $m/z$  119.0603, [M+K]<sup>+</sup>;  $m/z$  157.0163).

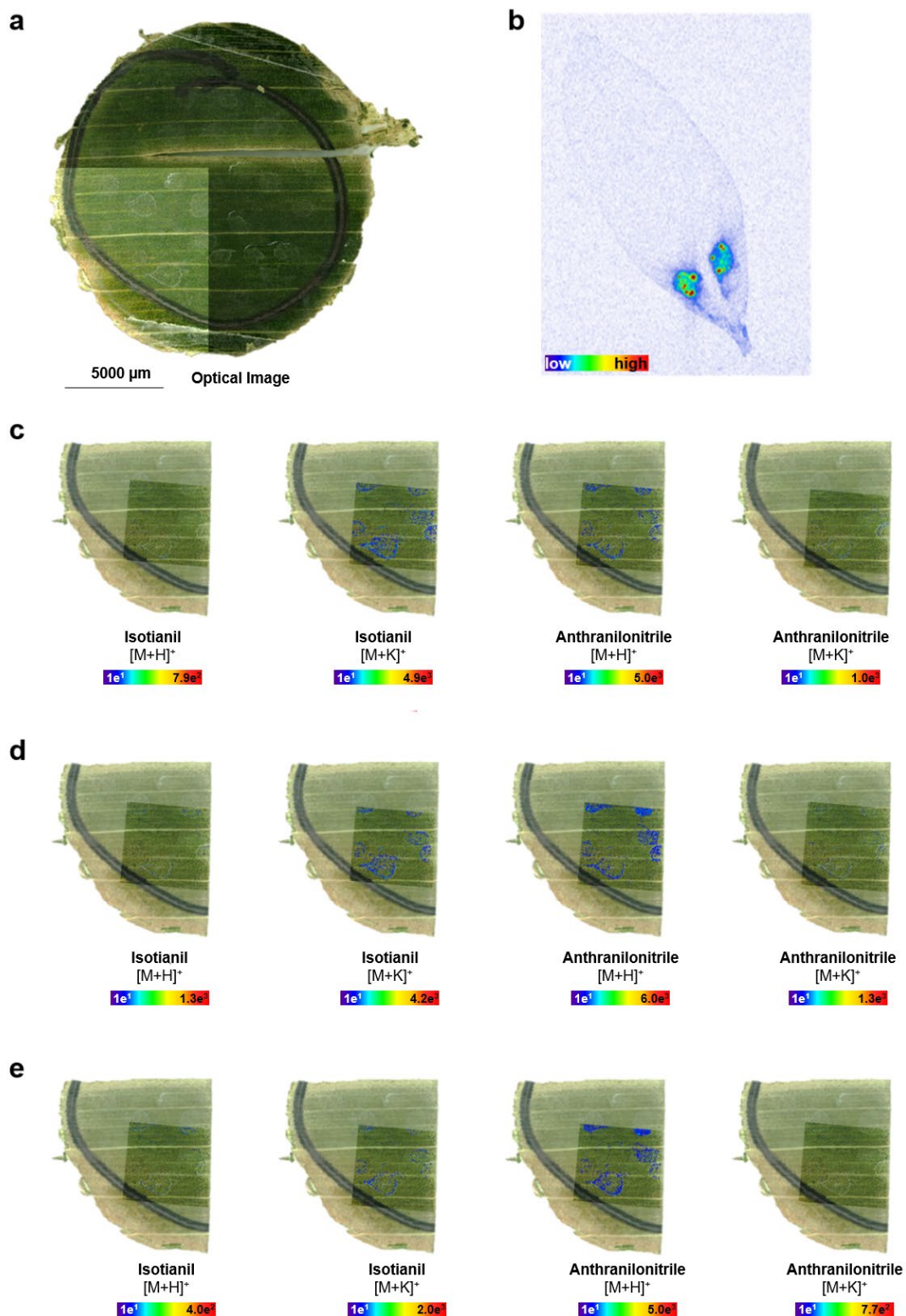


**Figure 21.** Autoradiography and MALDI-imaging-HRMS of banana leaf 14 days after treatment (100% RH) with Isotianil (spatial resolution: 25 µm, scan area: 5500x5500 µm). **a:** Optical image of droplet application area. **b:** Translocation of [isothiazole-3-<sup>14</sup>C, carboxamide-<sup>14</sup>C]-Isotianil by autoradiography.

**c-e:** Localization of Isotianil ( $[M+H]^+$ ;  $m/z$  297.9603,  $[M+K]^+$ ;  $m/z$  335.9162) and anthranilonitrile ( $[M+H]^+$ ;  $m/z$  119.0603,  $[M+K]^+$ ;  $m/z$  157.0163).

Supplementary MALDI-imaging experiments of cross-sections of the banana leaf confirmed, that isotianil does not penetrate via the cuticle of the adaxial epidermis. The leaf has a thickness of approximately 250  $\mu\text{m}$  and the samples were analyzed with a spatial resolution of 20  $\mu\text{m}$ , to enable the optimal visualization of details. The microscopic image of the leaf obtained after cryosectioning and the MALDI-imaging HRMS images of the leaf cross-sections can be seen in figure 22. Important structures of the leaf, like the cuticle, epidermis, and the vascular transport system (xylem and phloem), are indicated. Isotianil was detected as the protonated molecule ion in the highest intensities. The sodium and potassium adduct ions were observed, but the intensities were low compared to the signal intensities of the quasi-molecular ion. 3 days after application Isotianil was strongly enriched in the droplet application area outside the leaf (Figure 22 (b)). The adaxial epidermis of *musa acuminata* leaves consist of simple and small sized cells with convex outer cells. Even 7 days after application Isotianil was still only detectable on top of the leaf surface leaf without penetration via the adaxial epidermis. DCIT-acid was not observed in cross sections inside the droplet area. Because of its high mobility, the intensities during the imaging experiments were probably below the detection limit (caused by pre-set pixel size of 20  $\mu\text{m}$ , which is necessary to visualize the leaf's morphological detail).

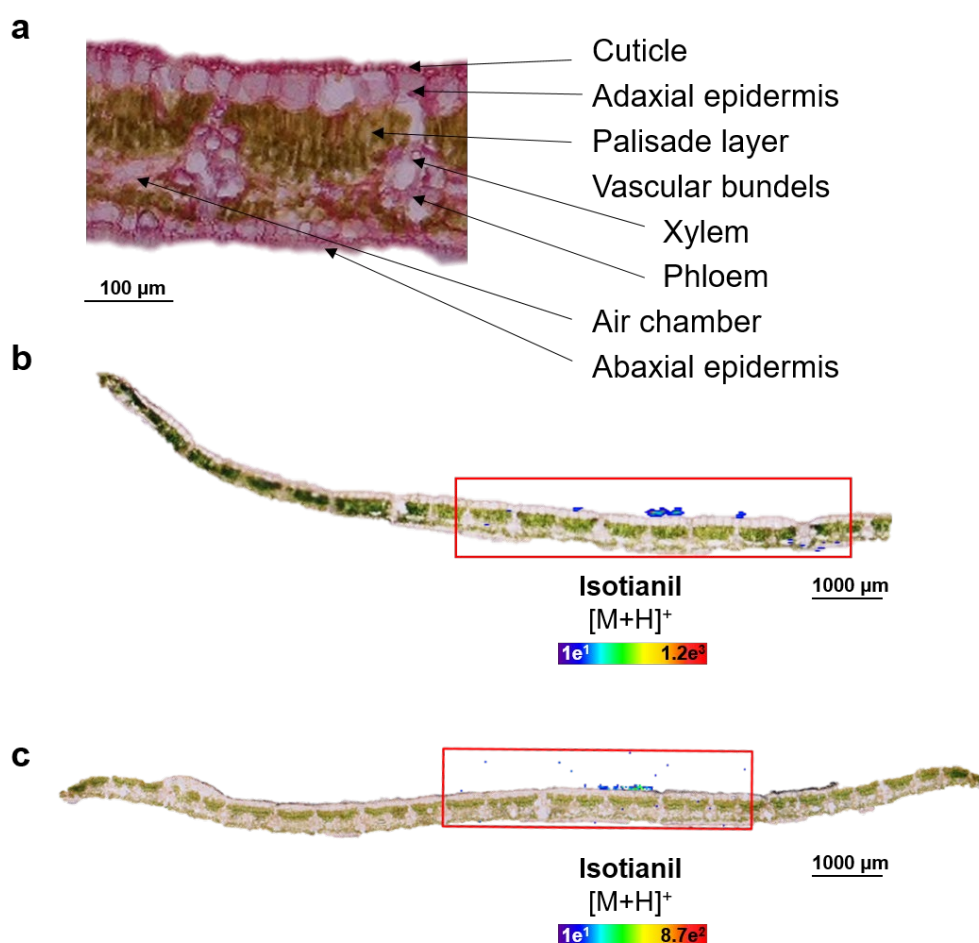


**Figure 22.** MALDI-imaging-HRMS throughout the leaf section of banana leaf (spatial resolution: 20  $\mu\text{m}$ , scan area: 5500x5500  $\mu\text{m}$ ); the red frame indicates the scanned area of the imaging experiment. **a:** Safranin-stained cross section. **b:** Localization of Isotianil ( $[\text{M}+\text{H}]^+$ ;  $m/z$  297.9603) 3 days after treatment (60% RH). **c:** Localization of Isotianil ( $[\text{M}+\text{H}]^+$ ;  $m/z$  297.9603) 7 days after treatment (60% RH).

#### 4.1.6. Uptake and surface adsorption of DCIT-acid on banana leaves after droplet application

The distribution of DCIT-acid after single droplet application showed significant differences during MALDI-imaging HRMS analyses compared to isotianil. DCIT-acid was applied via micro droplet application as a SC200 formulation (200 ppm a.i.). DCIT-acid was only detected in low signal intensities as the deprotonated molecular ion in negative ion mode. The distribution 3 days after application shows homogenous distribution in the droplet deposition area (Figure 23). At the later sampling points, the respective images indicate that most of the target compound was taken up and only low residues can be detected outside the adaxial leaf surface. The phosphor imaging autoradiographs reveal the accumulation of [isothiazole-3- $^{14}\text{C}$ ,

carboxylic acid-<sup>14</sup>C]-DCIT-acid in the leaf's distal parts, suggesting apoplastic transport via the vascular bundles in the leaf after uptake through the cuticle of the adaxial epidermis. LSC measurements of surface wash solutions underline that most of DCIT-acid was taken up, while less than 20% of the applied activity was found on the leaf surface. MALDI MSI measurements of cross-sections of DCIT-acid treated banana leaves were not successful for all timepoints and even 3 days after application no DCIT-acid could be detected in measurements with a spatial resolution of 20 μm. While the surface's autoradiography and mass spectrometry imaging measurements showed a high uptake of radioactivity leading to an accumulation at the leaf edges, the signal intensities in the cross-sections might be below the detection limit (< LOD). Also, possible degradation products of DCIT-acid such as 3-chloro-1,2-thiazole-5-carboxylic acid, 4-chloro-1,2-thiazole-5-carboxylic acid and 1,2-thiazole-5-carboxylic acid were not detected with MALDI MSI, while these metabolites are indistinguishable to the applied radiolabeled DCIT-acid in the phosphor image, because all of them still contain the radiolabel in their chemical structure.



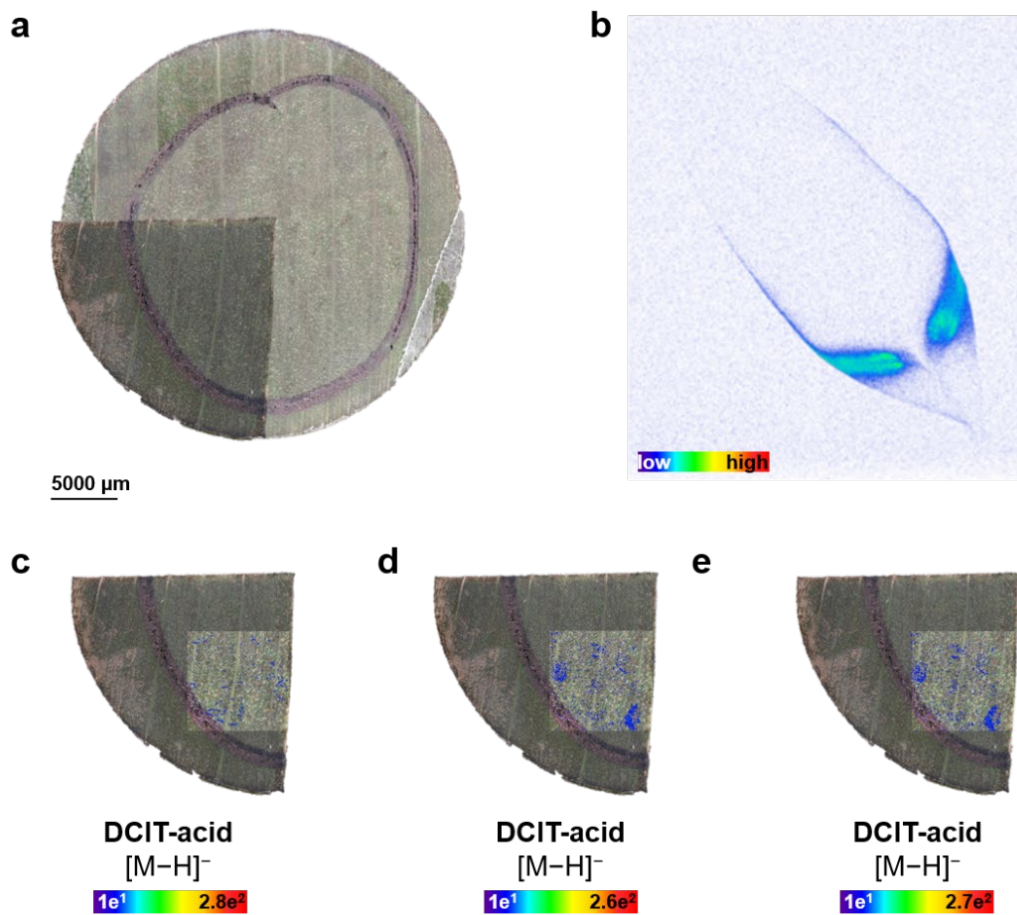


**Figure 23.** Autoradiography and MALDI-imaging-HRMS of banana leaf 3 days after treatment (60% RH) with DCIT-acid (spatial resolution: 25 μm, scan area: 5500x5500 μm). **a:** Optical image of droplet application area. **b:** Translocation of [isothiazole-3-<sup>14</sup>C, carboxylic acid-<sup>14</sup>C]-3,4- dichloro-1,2-thiazole-5-carboxylic acid. **c-e:** Localization of DCIT-acid ([M-H]<sup>-</sup>; *m/z* 195.9032).

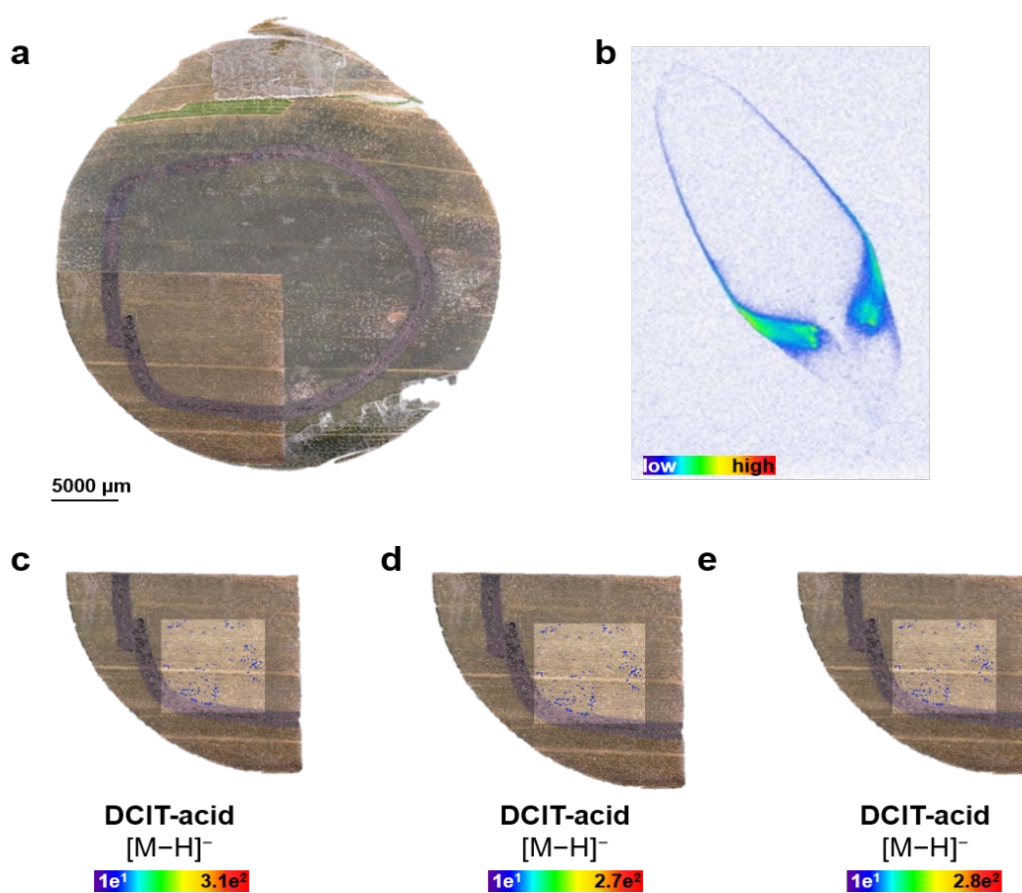


**Figure 24.** Autoradiography and MALDI-imaging-HRMS of banana leaf 7 days after treatment (60% RH) with DCIT-acid (spatial resolution: 25 μm, scan area: 5500x5500 μm). **a:** Optical image of droplet application area. **b:** Translocation of [isothiazole-3-<sup>14</sup>C, carboxylic acid-<sup>14</sup>C]-3,4-dichloro-1,2-thiazole-5-carboxylic acid. **c-e:** Localization of DCIT-acid ([M-H]<sup>-</sup>; *m/z* 195.9032).

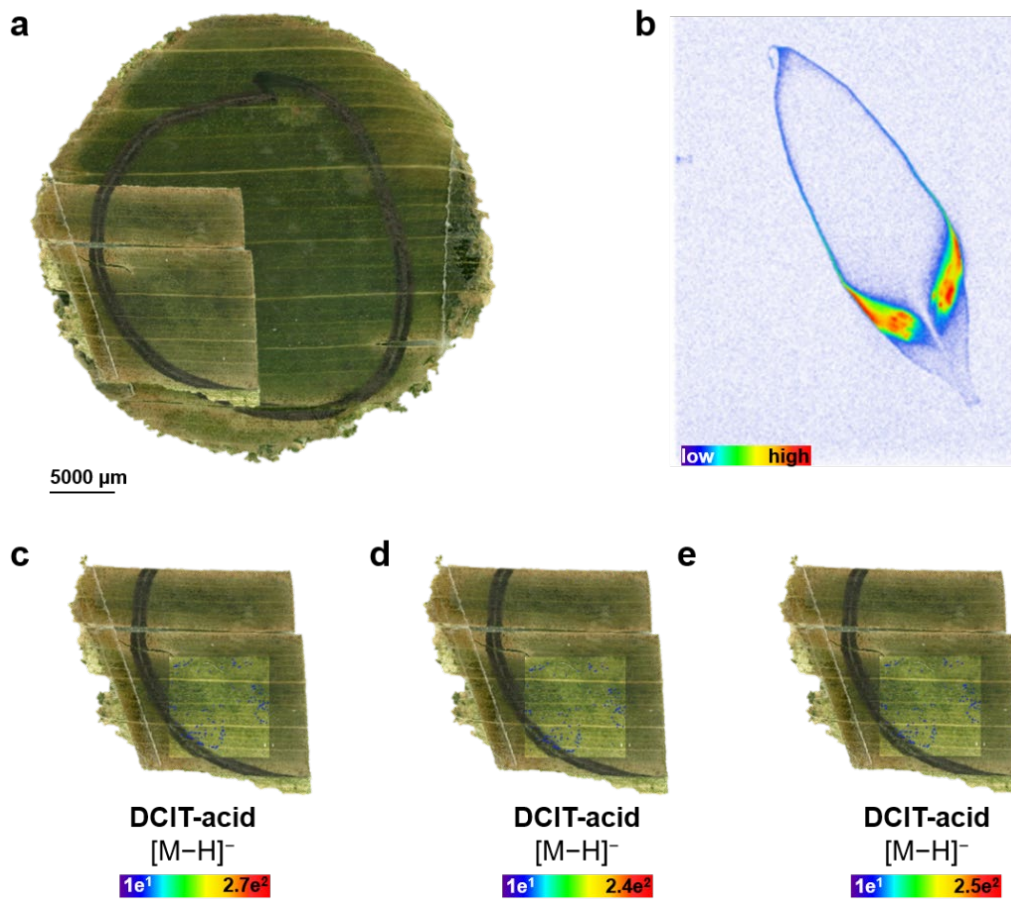


**Figure 25.** Autoradiography and MALDI-imaging-HRMS of banana leaf 14 days after treatment (60% RH) with DCIT-acid (spatial resolution: 25  $\mu\text{m}$ , scan area: 5500x5500  $\mu\text{m}$ ). **a:** Optical image of droplet application area. **b:** Translocation of [isothiazole-3- $^{14}\text{C}$ , carboxylic acid- $^{14}\text{C}$ ]-3,4-dichloro-1,2-thiazole-5-carboxylic acid. **c-e:** Localization of DCIT-acid ( $[\text{M}-\text{H}]^-$ ;  $m/z$  195.9032).

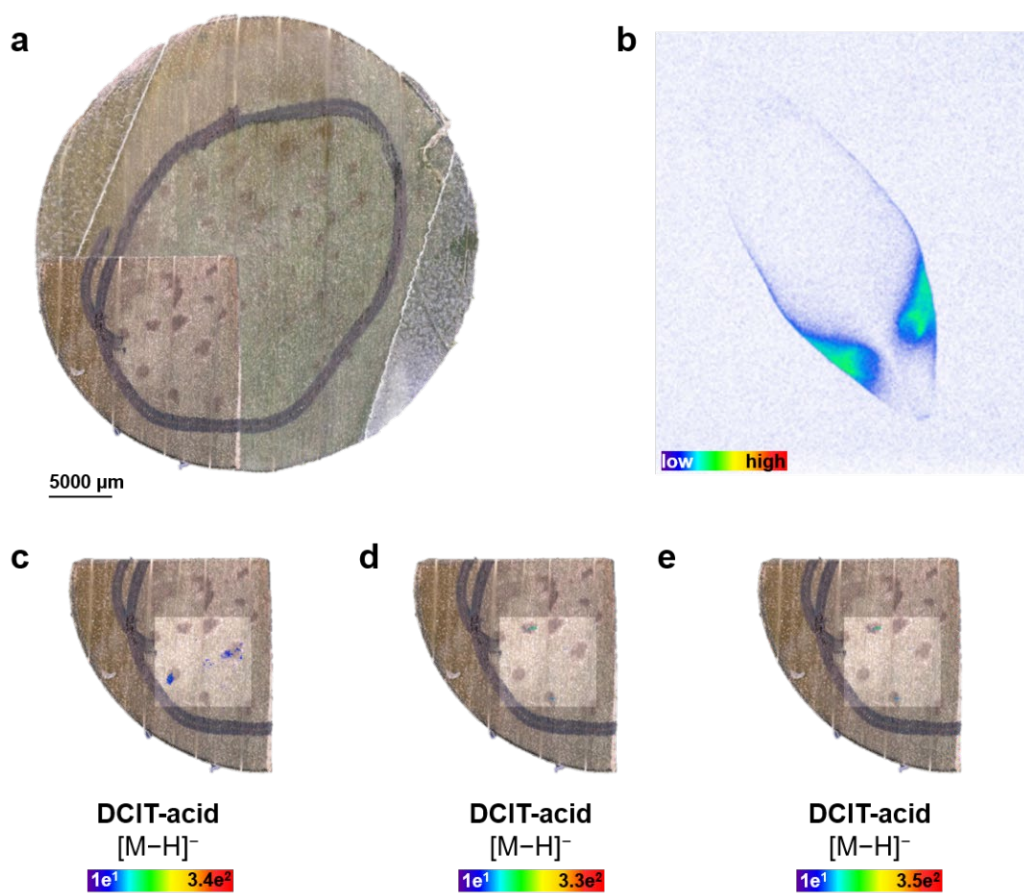


**Figure 26.** Autoradiography and MALDI-imaging-HRMS of banana leaf 3 days after treatment (100% RH) with DCIT-acid (spatial resolution: 25 μm, scan area: 5500x5500 μm). **a:** Optical image of droplet application area. **b:** Translocation of [isothiazole-3-<sup>14</sup>C, carboxylic acid-<sup>14</sup>C]-3,4-dichloro-1,2-thiazole-5-carboxylic acid. **c-e:** Localization of DCIT-acid ([M-H]<sup>-</sup>; *m/z* 195.9032).

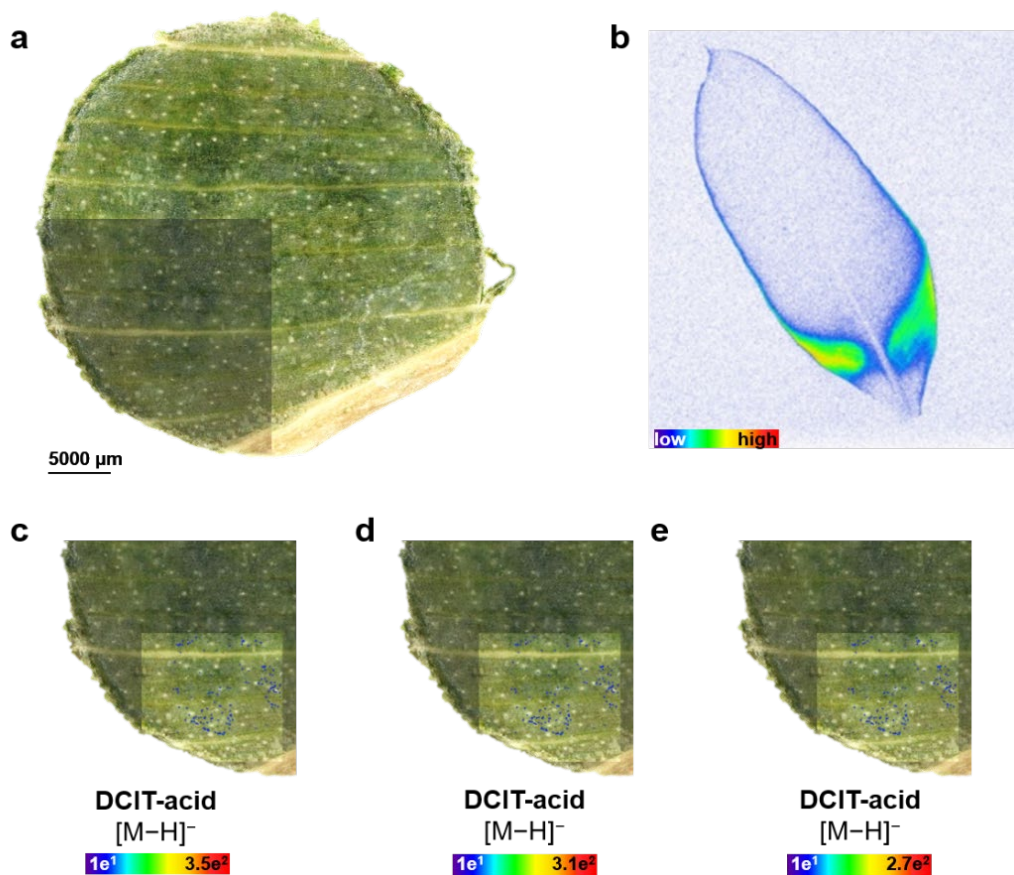


**Figure 27.** Autoradiography and MALDI-imaging-HRMS of banana leaf 7 days after treatment (100% RH) with DCIT-acid (spatial resolution: 25  $\mu\text{m}$ , scan area: 5500x5500  $\mu\text{m}$ ). **a:** Optical image of droplet application area. **b:** Translocation of [isothiazole-3- $^{14}\text{C}$ , carboxylic acid- $^{14}\text{C}$ ]-3,4- dichloro-1,2-thiazole-5-carboxylic acid. **c-e:** Localization of DCIT-acid ( $[\text{M}-\text{H}]^-$ ;  $m/z$  195.9032).

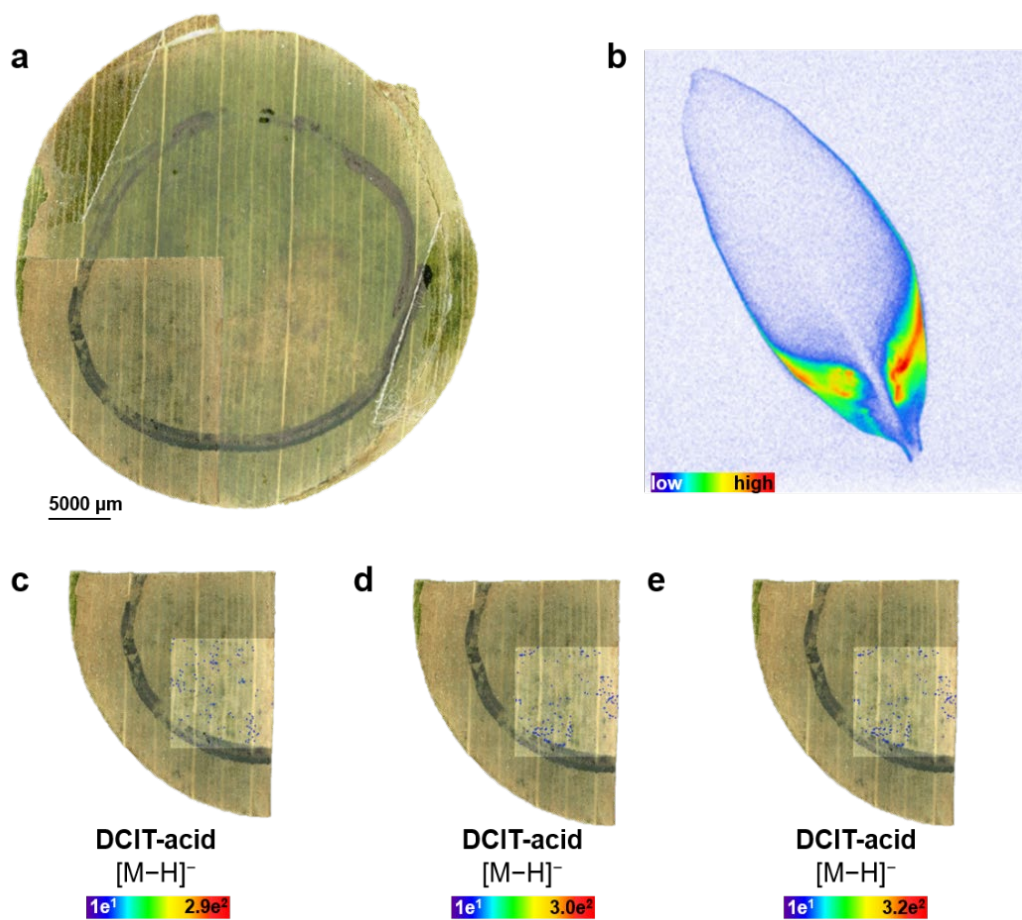


**Figure 28.** Autoradiography and MALDI-imaging-HRMS of banana leaf 14 days after treatment (100% RH) with DCIT-acid (spatial resolution: 25  $\mu\text{m}$ , scan area: 5500x5500  $\mu\text{m}$ ). **a:** Optical image of droplet application area. **b:** Translocation of [isothiazole-3- $^{14}\text{C}$ , carboxylic acid- $^{14}\text{C}$ ]-3,4-dichloro-1,2-thiazole-5-carboxylic acid. **c-e:** Localization of DCIT-acid ( $[\text{M}-\text{H}]^-$ ;  $m/z$  195.9032).

## **4.2. Phytotoxicity of Fluopyram and its metabolite PCA in grape vine**

Fluopyram penetrates continuously after foliar application into the plant and is acropetally redistributed, resulting in effective protection of untreated plant parts and new growth (Vargas-Pérez *et al.*, 2020). In 2015 grapevine growth disorders were observed in several countries of the world causing in significant loss of harvest. These unprecedented herbicide-like damage might originate from the metabolite 3-Chloro-5-trifluoromethylpyridine-2-carboxylic acid (PCA) (Robatscher *et al.*, 2019). To study the uptake, transport, and metabolism of the fungicide fluopyram and the metabolite PCA into grapes, <sup>14</sup>C-labeled PCA was investigated using the imaging techniques autoradiography and MALDI mass spectrometry imaging after root uptake of hydroponic grown grape vine (*Vitis vinifera*). In an additional study, fluopyram was applied as the commercially available suspension concentrate formulation Luna® Privilege (500 g/L a.i.) after foliar application in grapevine and imaging analysis was performed at different distinct development stages during the whole growing season.

### **4.2.1. Root uptake and translocation of PCA in hydroponic grown grape vine**

The uptake and translocation of <sup>14</sup>C-labeled PCA (100 µg/L, [pyridyl-2,6-<sup>14</sup>C, carboxylic acid-<sup>13</sup>C]) in grape vine (*Vitis vinifera*) were studied, using the previous hydroponic system. Depending on the plant growth in the hydroponic test system, the pH value of the nutrient solution increased from 6.5 at the beginning to 7.2 at day 10. Furthermore, the oxygen level decreased from above 101% to 65%. The water consumption increases with the plant growth and 4 days after application (4DAA) 19% and after 10 days (10DAA) after application 54% of the water is taken up (Table 14). All plants (n = 8) showed a normal and healthy plant growth in order to the untreated control plants. After 4 days, the biomass is elevated with factor 1.2 and with factor 1.9 after 10 days and is in the same range as the control plants. At this point, we can say that PCA with concentration of 100 µg/L in the test solution has no direct influence on plant growth or water consumption and on top of that, no growth distortion like jellyfish symptom or irregular growth of the leaf was visible.

**Table 13.** Uptake of  $^{14}\text{C}$ -PCA in hydroponic grown grapevine.

	4 Days after application	10 Days after application
Water uptake [%] <sup>a</sup>	18.6 ± 2.7	53.5 ± 7.0
Biomassfactor <sup>a</sup>	1.2 ± 0.2	1.9 ± 0.1
Translocation roots [%] <sup>b</sup>	11	19
Translocation shoots [%] <sup>b</sup>	89	81
Radioactive recovery [%] <sup>b</sup>	98	95

<sup>a</sup> Total of 8 plants per time point.

<sup>b</sup> Combustion aliquots of 1 plant per time point.

The phosphor images of PCA in hydroponic grown grape vine (*Vitis vinifera*) showed basipetal translocation of  $^{14}\text{C}$ -PCA suggesting xylem mobility of the analyte. The  $^{14}\text{C}$  material is translocated in the whole root system and more radiolabeled material was shown to translocate into shoots after 4 and 10 days after application. The basipetal xylem movement towards the leaf tips of new grown leaves underline PCA's fast uptake and movement of PCA within grape vine plants (Figure 29).

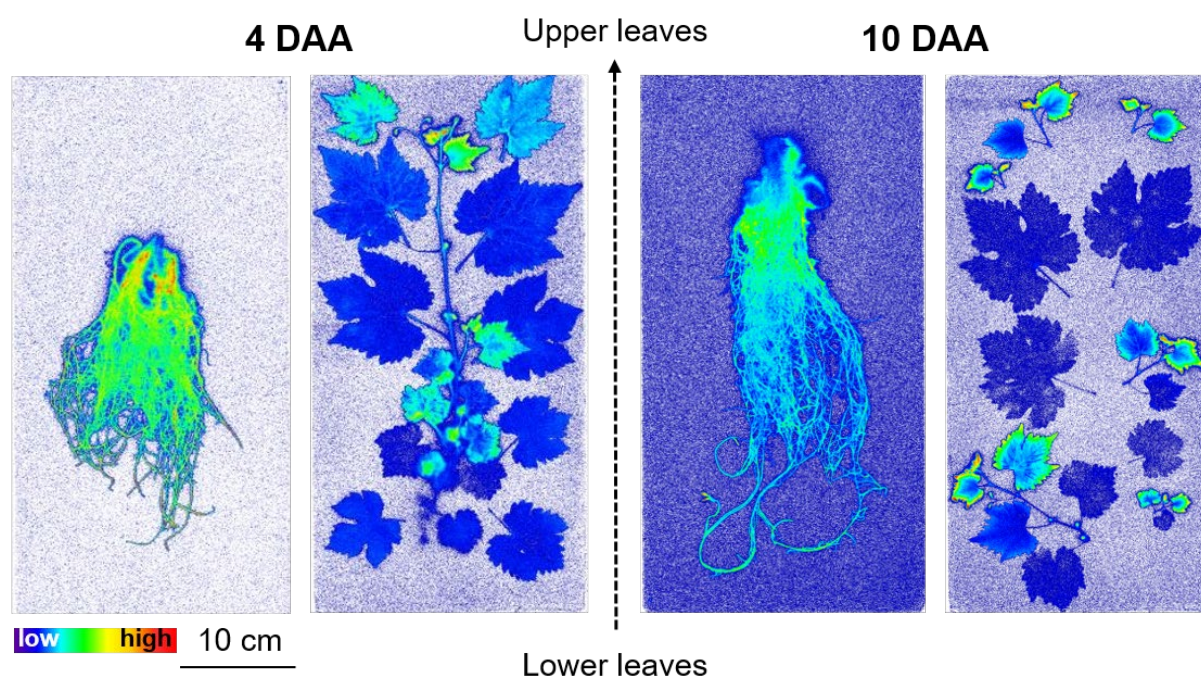


**Figure 29.** Distribution of [pyridyl-2,6- $^{14}\text{C}$ , carboxylic acid- $^{13}\text{C}$ ]PCA in root system and leaf system of grape vine plants after 4 and 10 days of root uptake.



At all-time points after application of PCA to plant roots, more radiolabeled material was shown to translocate into shoots of grapes.

The following experiment was done to quantify the minimum PCA concentration in the plant, which lead to growth distortion in the leaves (Figure 30). The concentrations of the test solution in the evaluated hydroponic test system were set to 250 µg/L, 500 µg/l, 1000 µg/L, 2000 µg/L, and 5000 µg/L, respectively. 7 days after application first symptoms were visible for plants with the highest concentration (5000 µg/l). Only on 1-4 leaves at the apical meristem at the shoot tip irregular growth of the leaves were visible. After 10 days first symptoms were also visible for plants at a concentration of 2000 µg/L. 18 days after application plants of all concentration down to 250 µg/L showed growth distortion. At day 20 most of the water in the test solution (volume 1 L) was taken up and the experiment was completed (Table 15).

**Table 14.** Uptake of PCA in hydroponic grown grape vine (*Vitis vinifera*).

	10 Days after application				
Concentration in the test solution [µg/L]	250	500	1000	2000	5000
Water uptake [%]	22.6	12.3	21.1	13.3	20.0
Biomassfactor	1.9	1.6	1.9	2.1	2.2
	18 Days after application				
Water uptake [%]	31.5 ± 2.5	41.9 ± 1.9	35.6 ± 5.6	31.5 ± 3.8	33.4 ± 2.5
Biomassfactor	3.4 ± 0.2	3.3 ± 0.6	2.8 ± 0.0	2.9 ± 0.3	3.6 ± 0.2
	20 Days after application				
Water uptake [%]	85.4	86.0	85.3	73.2	74.4
Biomassfactor	3.5	2.9	2.9	3.0	3.2

<sup>a</sup> n = 1, <sup>b</sup> n= 2

The systemic concentration of PCA in hydroponic grown grape vine which led to growth distortion like jelly fish symptom or irregular growth was determined by quantification pf PCA, done by LC-ESI-HRMS/MS using [2,6-<sup>13</sup>C, <sup>15</sup>N; carboxylic acid-<sup>13</sup>C]pyridyl carboxylic acid as an internal standard. The samples were measured in selected reaction monitoring (SRM) scanning mode in positive mode. The results are shown in table 16.

After 10 days first symptoms were visible for plants with the highest concentrations (2.0, 5.0 ppm). Nearly 15 wt% of the whole leaf system showed PCA symptoms for both concentrations and 38.46 µg/g FW was found in leaves treated with 5.0 ppm PCA. The concentration

increases not significant at the second harvest, indeed nearly 27 wt% of the whole leaf system showed distortions. At the end of experiment (20 days after application) it was interesting, that the concentration in the damaged leaves decreased (24.20  $\mu\text{g/g}$  FW at 5.0 ppm), but it can be explained by the fact, that in the end the old leaves showed also symptoms, which are much higher in their biomass (Figure 30). At the end, nearly 37 wt% (5.0 ppm) of the leaf system showed PCA symptoms and 2 wt% for plants treated with 0.25 ppm. The systemic concentration of PCA needs to be relatively high ( $\geq 1.90$   $\mu\text{g/g}$  FW) to generate the PCA symptoms, but with the shown enrichment in the new grown leaves within the time it is difficult to say, when the concentration is reached.

**Table 15.** Quantification of PCA in grape vine (*Vitis vinifera*).

Concentration [ $\mu\text{g/L}$ ]	10 DAA		18 DAA		20 DAA	
	No symptoms	Growth distortion	No symptoms	Growth distortion	No symptoms	Growth distortion
0.25	< LOD	- <sup>a</sup>	< LOD	- <sup>a</sup>	< LOD	1.90
0.50	< LOD	- <sup>a</sup>	< LOD	1.89	< LOD	2.08
1.00	< LOD	- <sup>a</sup>	< LOD	7.83	< LOD	4.58
2.00	< LOD	19.5	0.91	28.1	0.68	6.30
5.00	0.84	38.4	4.46	39.8	7.90	24.20

<sup>a</sup> No symptom at timepoint. Unit ppm. LOD = 0.05 ppm

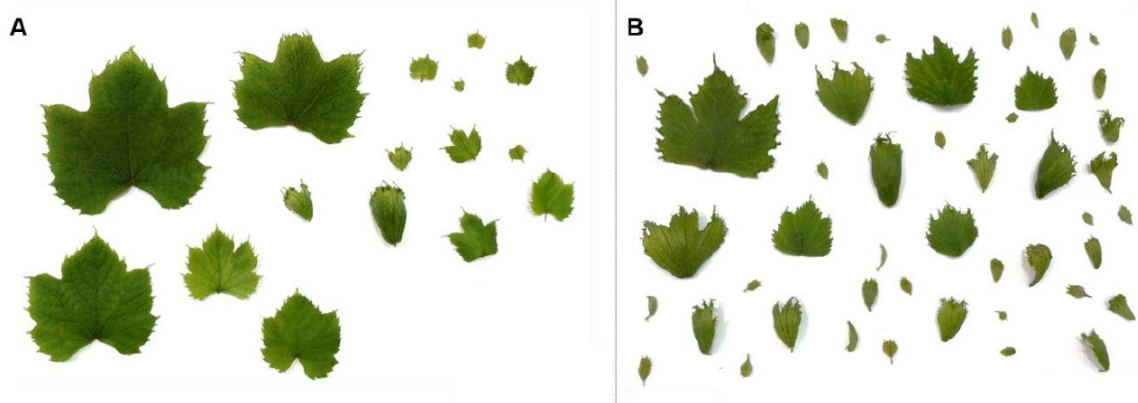


**Figure 30.** Total of damaged leaves 20 days after treatment with PCA. A: 500  $\mu\text{g/L}$ . B: 5000  $\mu\text{g/L}$ .

#### 4.2.2. Uptake and quantification of fluopyram in grape vine after foliar application

To investigate the metabolic behavior and the nature of residue during the winter period of grape vine (*Vitis vinifera*), plants were treated with fluopyram as the commercially available suspension concentrate formulation Luna® Privilege (500 g/L fluopyram) with a spray lance (750 g a.i./ha) at the end of wood maturation (BBCH91) and samples were collected at 7 representative growth stages (50% leaves fallen (BBCH95), end of leaf fall (BBCH97), budswell (BBCH02), 3<sup>rd</sup> leaves unfolded (BBCH 13), fruits begin to swell (BBCH 71), berries pea-size (BBCH76), and berries harvest ripe (BBCH 84)) (Figure 31). Furthermore, the application was either done by adding Basfoliar active, a liquid mineral fertilizer with trace elements and bio-stimulator, which lead to strengthening of plant tissues.

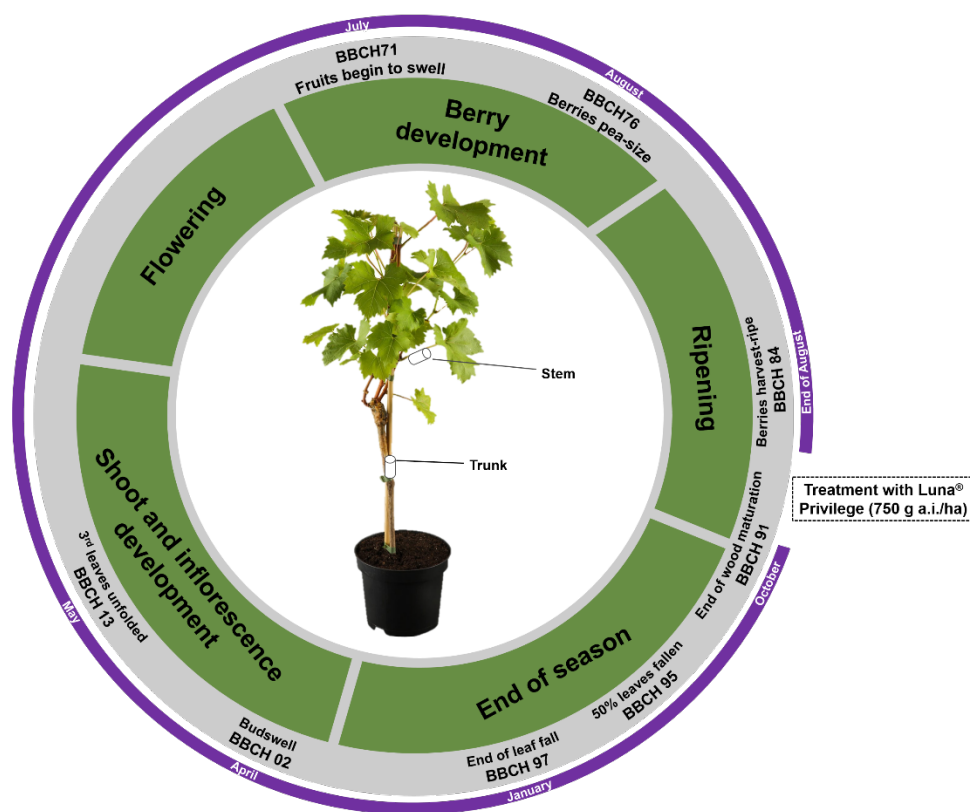


**Figure 31.** Investigated growth stages of grape vine (*Vitis vinifera*) treated with fluopyram.

Before extraction, the plants were separated into different parts (root, trunk, stem, petiole and leaves) as representative parts for uptake, transport and storage. The trunk was further separated into outer bark, cork cambium and vascular bundles including phloem, xylem and pith. Additionally, the soil around the root system has been collected by shaking the root system gently and the dropped leaves were collected from the soil surface and analyzed

individually. The surface of attached leaves from the grapevine plants at the beginning of the experiment (BBCH97, end of leaf fall) was washed, while newly grown leaves from sampling points t5-t8 were extracted without surface washing. Stable isotope-labeled PCA ([2,6-<sup>13</sup>C, <sup>15</sup>N; carboxylic acid-<sup>13</sup>C]) was used as an internal standard for the quantification of fluopyram/PCA and the samples were measured with LC-ESI-HRMS/MS in positive ion mode using an LTQ Orbitrap mass spectrometer.

During the experiment, all plants showed healthy growth and nonvisible PCA caused symptoms like the Jellyfish syndrome were observed. fluopyram was found at high rates on the leaf surface and in the cork of the stock, resulting from direct spray contact and wash-off at the beginning of the winter dormancy period, especially at the first three sampling points (BBCH91, end of wood maturation; BBCH95, 50% leaves fallen; BBCH97, end of leaf fall). (Table 17).

**Table 16.** Fluopyram residues [mg/kg] in selected tissues of grape vine (*Vitis vinifera*) after foliar application (750 g a.i./ha) during the whole winter period.

	Foliar application of fluopyram 750 g a.i./ha + Basfoliar active							
	Days after application							
	1	44	95	164	199	259	291	308
Soil	< LOD	0.002	0.250	0.239	0.188	0.207	0.191	0.207
Root	< LOD	0.001	0.014	0.059	0.073	0.070	0.074	0.061
Cork	0.138	0.022	0.325	0.059	0.244	0.309	0.403	0.408
Bark	0.007	< LOD	0.278	0.198	0.231	0.199	0.155	0.166
Vascular bundle	< LOD	0.015	0.074	0.100	0.156	0.110	0.123	0.135
Stem	0.002	0.028	0.454	0.046	0.020	0.051	0.061	0.075
Petiole	0.005	0.149	- <sup>a</sup>	- <sup>a</sup>	0.181	0.154	0.154	0.142
Leaf	1.150	0.368	- <sup>a</sup>	- <sup>a</sup>	0.003	0.140	0.120	0.122
Leaf (Abcission)	0.011	0.079	- <sup>a</sup>	- <sup>a</sup>	- <sup>b</sup>	- <sup>b</sup>	- <sup>b</sup>	- <sup>b</sup>

	Foliar application of fluopyram 750 g a.i./ha							
	Days after application							
	1	44	95	164	199	259	291	308
Soil	< LOD	0.002	0.305	0.255	0.116	0.174	0.200	0.201
Root	< LOD	0.001	0.041	0.018	0.082	0.070	0.085	0.074
Cork	0.100	0.018	0.325	0.527	0.054	0.323	0.384	0.401
Bark	< LOD	< LOD	0.232	0.160	0.133	0.200	0.188	0.143
Vascular bundle	< LOD	0.013	0.049	0.124	0.133	0.136	0.151	0.168
Stem	0.002	0.015	0.261	0.082	0.001	0.073	0.060	0.050
Petiole	0.004	0.064	- <sup>a</sup>	- <sup>a</sup>	0.153	0.199	0.114	0.134
Leaf	1.079	0.214	- <sup>a</sup>	- <sup>a</sup>	0.007	0.123	0.110	0.134
Leaf (Abcission)	0.009	0.060	- <sup>a</sup>	- <sup>a</sup>	- <sup>b</sup>	- <sup>b</sup>	- <sup>b</sup>	- <sup>b</sup>

<LOD Below limit of detection. LOD = 0.05 ppm.

<sup>a</sup> No leaves and petioles depending on the principal growth stage.

<sup>b</sup> No leaves on ground depending on the principal growth stage.

Furthermore, the concentration of fluopyram decreases from upper to lower part of the plants and the concentration in the trunk increases with the time after application and fluopyram might be stored in this part of the vine plant until the xylem sap sprout to the growing parts in spring. With the bud swelling (BBCH02) the concentration of fluopyram increases in the plant's upper parts (stem, petiole, leaves) and the fluopyram residues in the following sampling points were in a similar range. In the vascular tissues of the trunk, the level of fluopyram increases at the beginning of the winter dormancy period and was nearly constant for the sampling points t4-t8 with a range of 100 – 170 ng/g. It underlines the systemic properties of fluopyram, and it might be transported within the xylem water or within the nutrient-rich phloem sap to the new growing areas of the plants. This fact also confirms this, that fluopyram was found in concentration between 120 – 140 ng/g in the new grown leaves of the latest sampling points (BBCH71, fruits begin to swell; BBCH76, berries pea-size; BBCH84, berries harvest ripe). The soil's residues in the soil increase with the first two sampling points and show nearly similar concentrations in the following samples. These residues on the soil are mainly from wash off via rain after the spray application. On top of that no PCA or 2-(trifluoromethyl)-benzamide (BZM) was detected in the different plant tissues. Even the hydroxylation of the parent compound to 7-OH and 8-OH metabolites, which lead to PCA after cleavage of the amid bond of the activated parent, was not found. Residue distribution of fluopyram and significant metabolites in grape following foliar treatments with radio-labelled fluopyram in previous studies at BCS showed, that the parent was the main residue with values > 97% and less than 1% PCA and BZM. Because of that, the concentration of the metabolites might be lower than the detection limit, depending on the number and the size of the plants.

#### 4.2.3. Spatial distribution of fluopyram after spray application in grape vine

As described above, extraction and HPLC-HRMS analyses confirmed the presence of fluopyram in the different plant tissues, MALDI-HR-MSI was done to gain further insights into the transportation of fluopyram after foliar application with Luna® Privilege (500 g/L fluopyram) and a concentration of 750 g a.i./ha. Therefore, transversal cross-sections of the stem and trunk were analyzed at the three main stages (end of season BBCH 95; shoot and inflorescence development BBCH 13; ripening BBCH 84) (Figure 31). The parent is mainly localized in the primary phloem at the trunk and stem in high intensities at all sampling points (Figure 32-37). Several secondary plant metabolites such as amino acids and carbohydrates were detected in parallel by MALDI-MSI. Glutamine is one of the primary amino acids in nitrogen assimilation and from the leaves, excess amino acids can be exported via the phloem. Amino acids are present in both xylem and phloem and can be withdrawn from the vascular system by cells that depend on an external supply, such as apices, newly developing tissues, and reproductive organs. In most plants, the spectra of amino acids found in the phloem and xylem appear to be similar, the major components being amides such as glutamine and asparagine, and acidic amino acids such as glutamate and aspartate. Photosynthates, such as sucrose, raffinose and stachyose, are produced and transported from the formation site in the mesophyll cells of photosynthesizing leaves. They are translocated mainly through the phloem to other plant parts for, e.g., storage and as structural components. All selected secondary plant metabolites show similar distribution to fluopyram and are mainly located in the phloem. Thus, the plants take up fluopyram and it is stored within the carbohydrate storage during the winter dormancy period. All secondary plant metabolites showed highest signal intensities for the potassium adduct, similar to fluopyram. Signal intensities are decreased during the winter period, due to low activity of the grape vine. During the leaf decoloration the photosynthesis stopped, and the synthesis of these carbohydrates is down regulated. Within the bud break in spring the developing leaves starts the photosynthesis again. The concentration of the carbohydrates increases, and they are transported mainly via the phloem from the new leaves to all other growing parts.

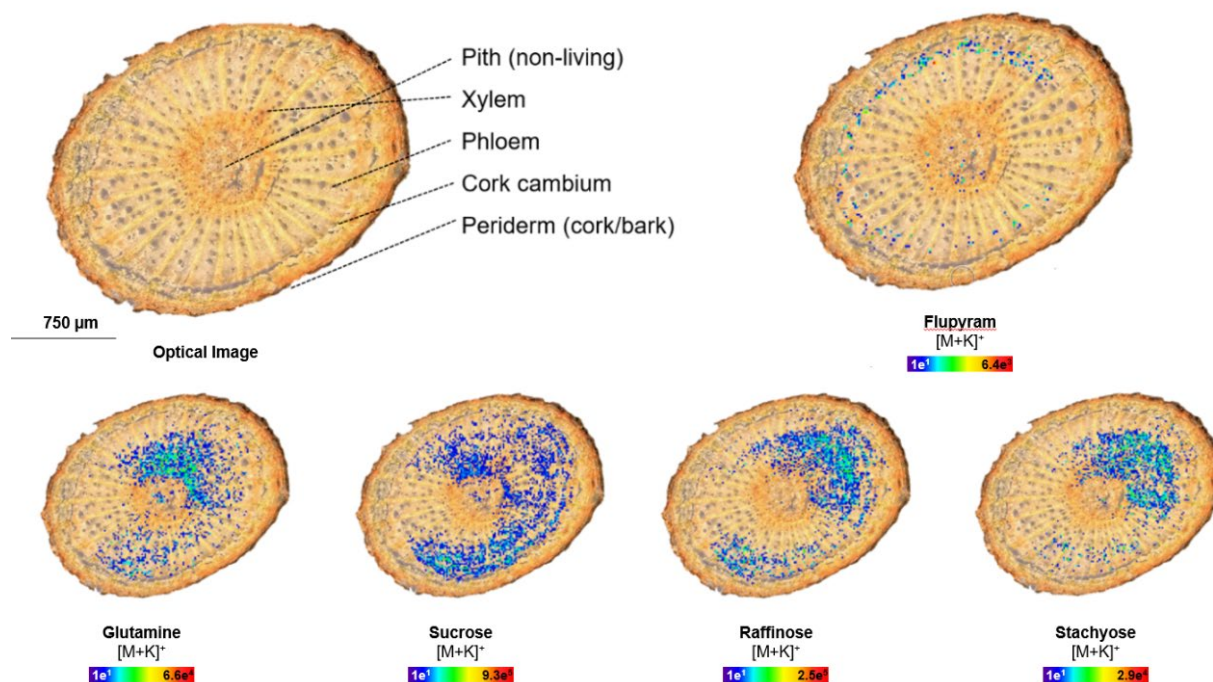


**Figure 32.** MALDI-imaging-HRMS of grape vine (*Sauvignon blanc*) stem cross sections at BBCH95, 50% leaves fallen (spatial resolution: 25 μm, scan area: 3300x3300 μm). Localization of fluopyram ( $[M+K]^+$ ;  $m/z$  435.0096). Localization of primary plant metabolites: Glutamine ( $[M+K]^+$ ;  $m/z$  185.0323), Sucrose ( $[M+K]^+$ ;  $m/z$  381.0794), Raffinose ( $[M+K]^+$ ;  $m/z$  543.1322), Stachyose ( $[M+K]^+$ ;  $m/z$  705.1850).



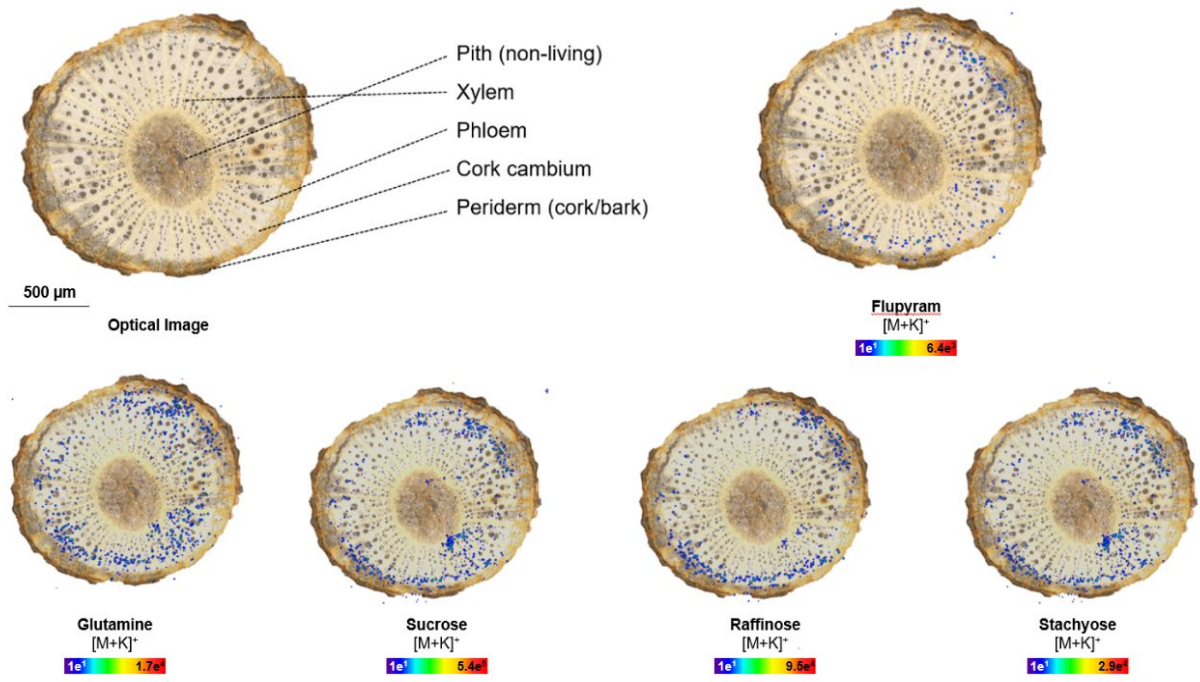


**Figure 33.** MALDI-imaging-HRMS of different grape vine (*Sauvignon blanc*) stem cross sections at BBCH97, end of leaf fall (spatial resolution: 25 μm, scan area: 2800x2800 μm). Localization of fluopyram ([M+K]<sup>+</sup>; *m/z* 435.0096). Localization of primary plant metabolites: Glutamine ([M+K]<sup>+</sup>; *m/z* 185.0323), Sucrose ([M+K]<sup>+</sup>; *m/z* 381.0794), Raffinose ([M+K]<sup>+</sup>; *m/z* 543.1322), Stachyose ([M+K]<sup>+</sup>; *m/z* 705.1850).

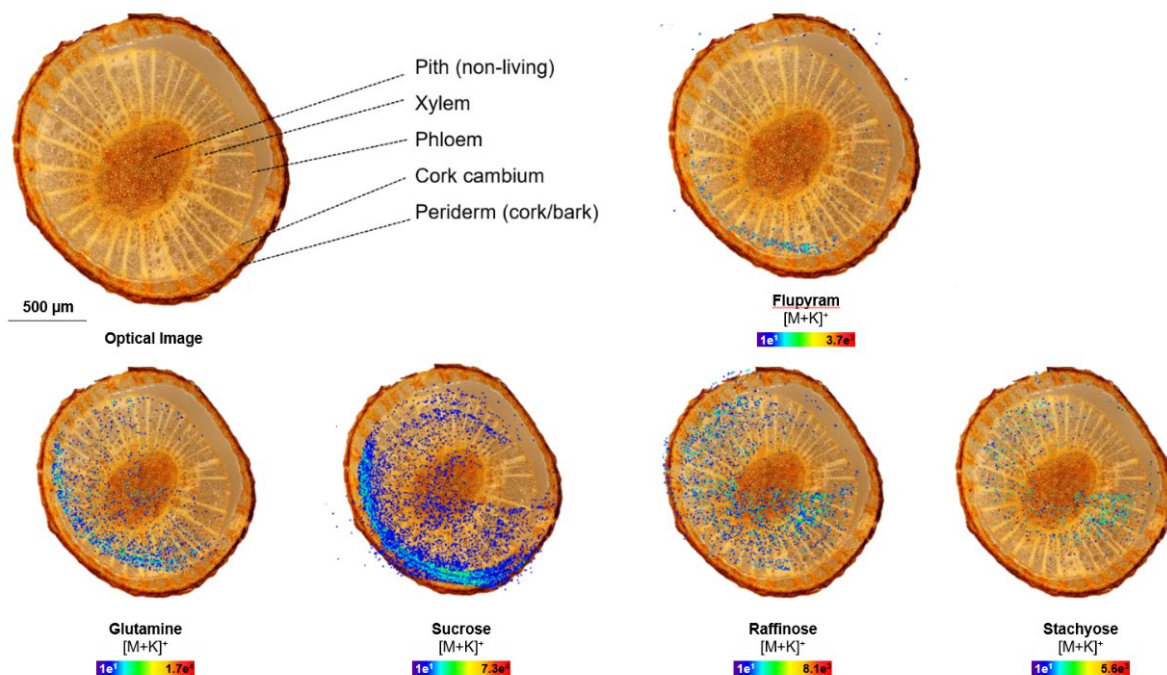


**Figure 34.** MALDI-imaging-HRMS of different grape vine (*Sauvignon blanc*) stem cross sections at BBCH13, 3<sup>rd</sup> leaves unfolded (spatial resolution: 25 μm, scan area: 3000x3000 μm). Localization of fluopyram ([M+K]<sup>+</sup>;  $m/z$  435.0096). Localization of primary plant metabolites: Glutamine ([M+K]<sup>+</sup>;  $m/z$  185.0323), Sucrose ([M+K]<sup>+</sup>;  $m/z$  381.0794), Raffinose ([M+K]<sup>+</sup>;  $m/z$  543.1322), Stachyose ([M+K]<sup>+</sup>;  $m/z$  705.1850).

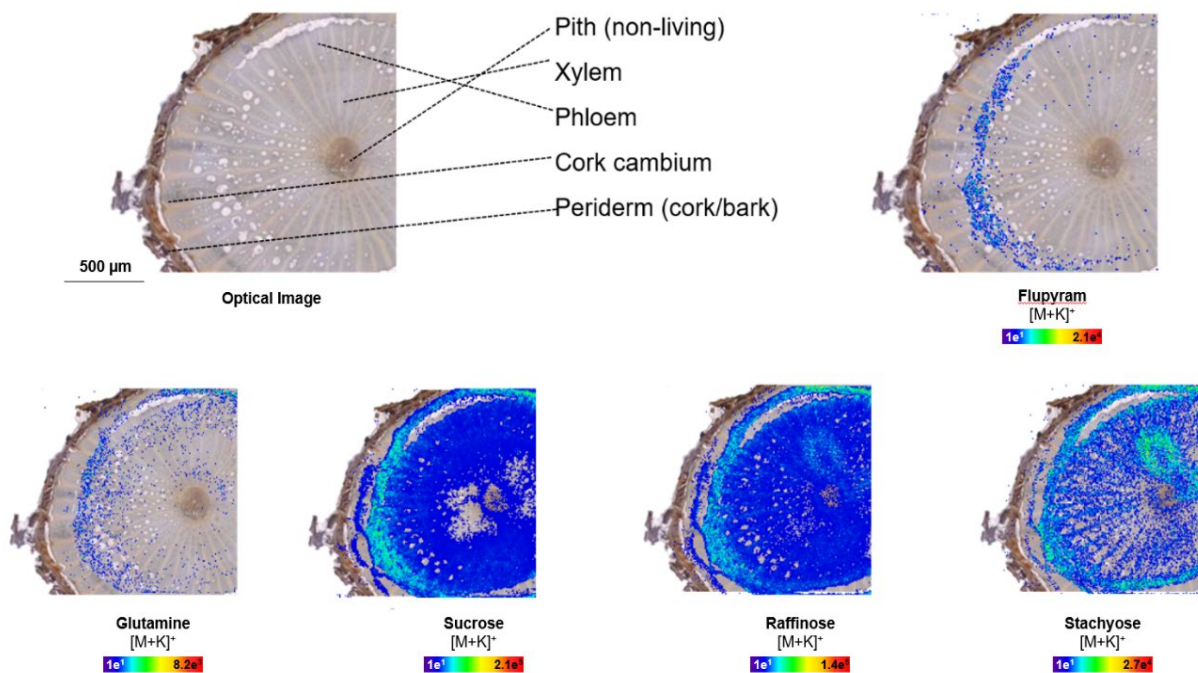


**Figure 35.** MALDI-imaging-HRMS of different grape vine (*Sauvignon blanc*) trunk cross sections at BBCH13, 3<sup>rd</sup> leaves unfolded (spatial resolution: 25 μm, scan area: 2000x2000μm). Localization of fluopyram ([M+K]<sup>+</sup>;  $m/z$  435.0096). Localization of primary plant metabolites: Glutamine ([M+K]<sup>+</sup>;  $m/z$  185.0323), Sucrose ([M+K]<sup>+</sup>;  $m/z$  381.0794), Raffinose ([M+K]<sup>+</sup>;  $m/z$  543.1322), Stachyose ([M+K]<sup>+</sup>;  $m/z$  705.1850).

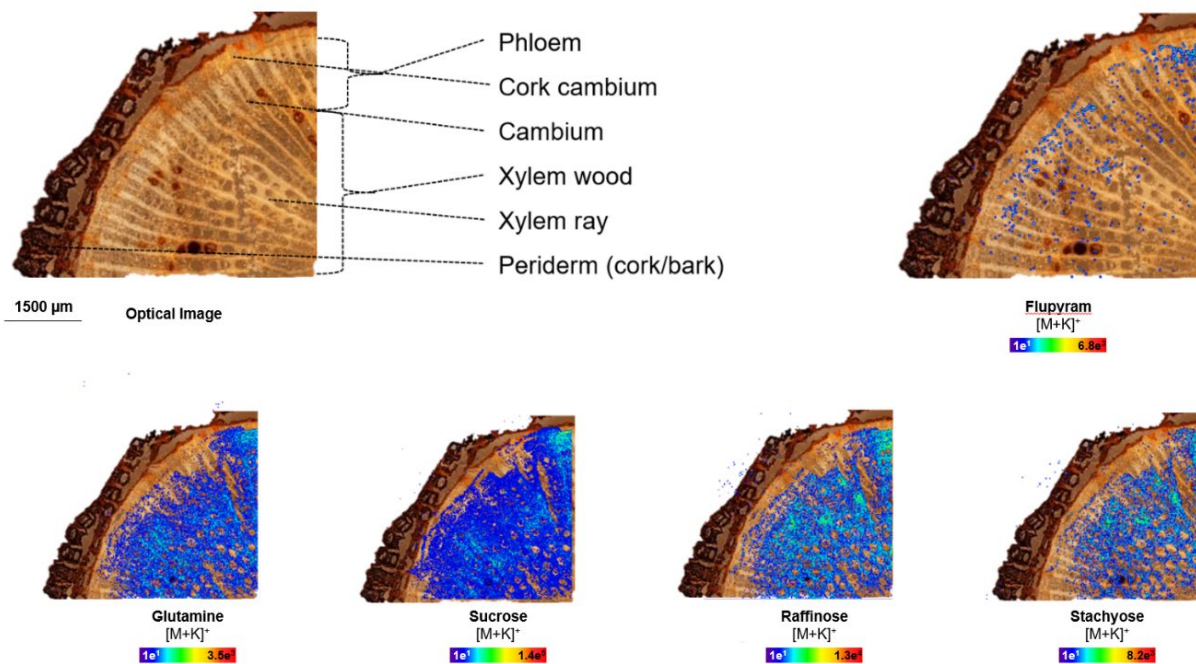


**Figure 36.** MALDI-imaging-HRMS of different grape vine (*Sauvignon blanc*) stem trunk cross sections at BBCH76, berries pea-size (spatial resolution: 25  $\mu\text{m}$ , scan area: 4500x4000 $\mu\text{m}$ ). Localization of flupyram ( $[\text{M}+\text{K}]^+$ ;  $m/z$  435.0096). Localization of primary plant metabolites: Glutamine ( $[\text{M}+\text{K}]^+$ ;  $m/z$  185.0323), Sucrose ( $[\text{M}+\text{K}]^+$ ;  $m/z$  381.0794), Raffinose ( $[\text{M}+\text{K}]^+$ ;  $m/z$  543.1322), Stachyose ( $[\text{M}+\text{K}]^+$ ;  $m/z$  705.1850).

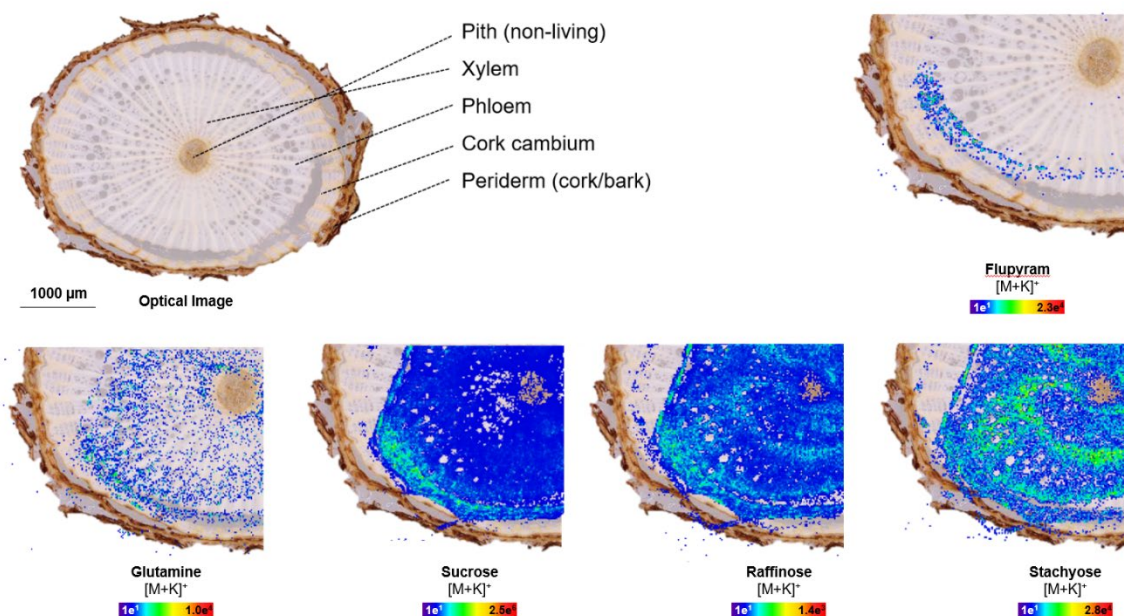


**Figure 37.** MALDI-imaging-HRMS of different grape vine (*Sauvignon blanc*) stem cross sections at BBCH76, berries pea-size (spatial resolution: 25 μm, scan area: 4000x4000μm). Localization of fluopyram ([M+K]<sup>+</sup>; *m/z* 435.0096). Localization of primary plant metabolites: Glutamine ([M+K]<sup>+</sup>; *m/z* 185.0323), Sucrose ([M+K]<sup>+</sup>; *m/z* 381.0794), Raffinose ([M+K]<sup>+</sup>; *m/z* 543.1322), Stachyose ([M+K]<sup>+</sup>; *m/z* 705.1850).

PCA was not detected in any plant tissue analyzed by MALDI-MSI, assumed to be below the detection limit, similar to the results from the residue analysis done by LC-MS.



### **4.3. Distribution of tebuconazole and BCS-CX51842 after seed treatment**

While pesticides can be applied during the growth of the crop by foliar or drench application, they can be added to the seed prior to planting as well. Applying the agrochemical directly to the seed can be substantially more efficient and effective than broadcast crop protection methods (Jeschke *et al.*, 2019).

#### **4.3.1. Distribution of tebuconazole in wheat (*Triticum aestivum* 'Triso') after seed treatment**

MALDI mass spectrometry imaging was performed to study tebuconazole's uptake, movement, and metabolism after seed treatment of wheat seed (*Triticum aestivum* 'Triso') during the germination process and early growth of the plants. A wheat grain has a 5-10 mm length and a weight of 30-50 mg. The grain has a single cotyledon (Monocotyledon) and can be divided into three main parts. The wheat bran is the outer layer and protects the main part of the kernel. Endosperm is the main part of the seed and consists of starchy endosperm and endosperm cell (protein, carbohydrates, iron, and the major B-vitamins). The wheat germ is located at the one end of the seed and is responsible for germination when planted. Tebuconazole could not be visualized in transverse cross-sections of non-germinated wheat seed after seed treatment with ArenaC<sup>®</sup> (1 g/dt tebuconazole), because it might be below detection limit. However, the seed coating colorant Pigment Red 112, which is part of the formulation in ArenaC<sup>®</sup> to identify treated seeds, showed a homogenous distribution all over the surface of the wheat bran (Figure 38). Furthermore, endogenous plant metabolites like amino acids and polysaccharides, which are predominant in plant tissues of wheat seeds, could be visualized in parts of the endosperm and inside the wheat bran in parallel. The seed exhibited typical development stages with the softening of the endosperm after moistening and the growth of the embryo shoot and its roots during the germination process. The seed was placed in standard HPLC brown-glass vials, stored at 4 °C in the dark and just the tip at the radicle site of the grain was attached to water to guarantee germination and to avoid washing of tebuconazole of the surface of the grain. Target compounds were profiled by MALDI MSI in longitudinal and transversal orientations in the seeds at different time points during germination. Polysaccharides with two or three hexose units (Fructose and Sucrose) were detected parallel as sodium and potassium ion adducts in positive ion mode. While sodium and potassium adduct ions are co-localized in the central endosperm at early germination, they were detected near the aleurone layer at later germination time points. The merge of both adducts underlined their complimentary localizations. 48 h after germination tebuconazole was detected on the outer part of the wheat bran and in the radicle, which burst of the embryo during the germination process. The nutrients glutamine, fructose and sucrose are highly

concentrated in the same tissues of the radicle and this pattern of accumulation underlined the ongoing plant growth during the germination process.

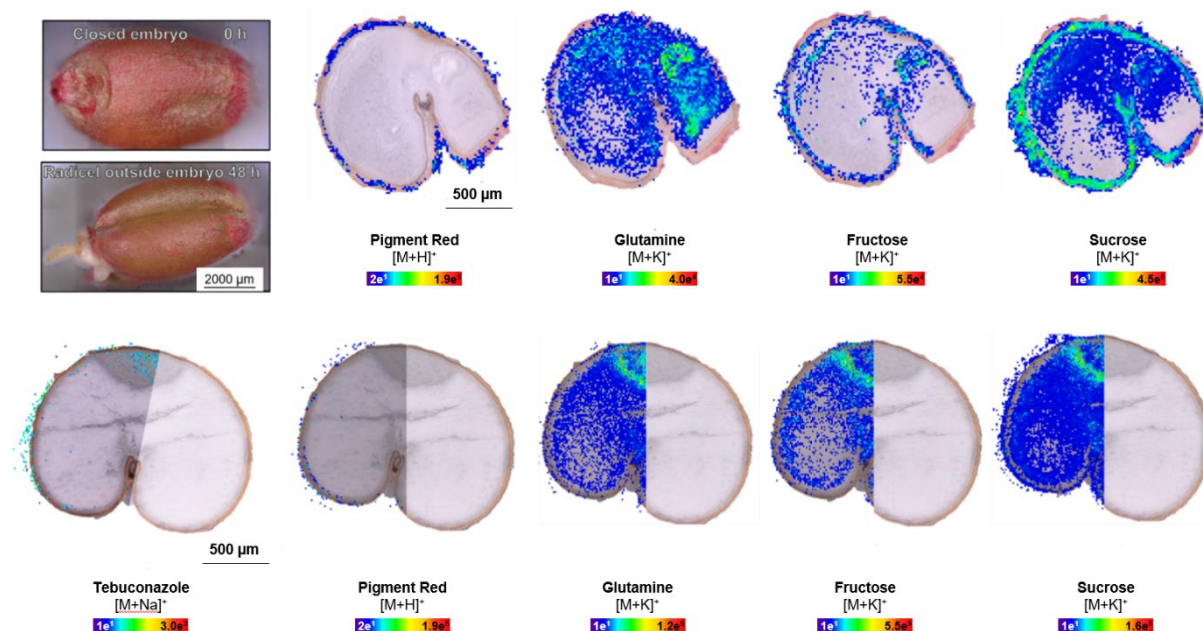


**Figure 38.** MALDI-imaging-HRMS of non-germinated (upper part) and 48 h germinated wheat (lower part) (*Triticum aestivum* 'Triso') seeds after seed-treatment with tebuconazole. Localization of tebuconazole ( $[M+Na]^+$ ;  $m/z$  330.1344), seed coating colorants (Pigment Red 112  $[M+H]^+$ ;  $m/z$  484.0381) and selected endogenous plant metabolites (Glutamine  $[M+K]^+$   $m/z$  185.0323; Fructose  $[M+K]^+$   $m/z$  219.0266; Sucrose  $[M+Na]^+$   $m/z$  365.1054).

14 Days after application tebuconazole was found to be distributed in transversal cross sections of seminal roots and in parts near the root tip in the zone of maturation, where the water uptake actually takes place in plants. Tebuconazole is localized mainly in the vascular bundles of the roots with an increased accumulation towards the xylem (Figure 39). Investigations of different parts of the shoots (first and second leaf) using MALDI MSI showed a homogenous distribution all over the leaves with highest signal intensities in the blade tips. Tebuconazole is taken up quickly, highly mobile throughout the plant and metabolic transformation was already ongoing in the whole shoot system, showing the systemic properties of the fungicide. Tebuconazole could be visualized by detecting the potassium adduct and sodium adduct ion ( $[M+Na]^+$ ;  $m/z$  330.1344;  $[M+K]^+$ ;  $m/z$  346.1083), while the sodium adduct ion was predominant during all measurements of the roots and the potassium adduct ion in shoot tissues. The first step of the metabolism of tebuconazole in plants is hydroxylation to hydroxy-tebuconazole, and it was also detected with the highest signal



intensities as the potassium adduct ion ( $[M+K]^+$ ;  $m/z$  362.1032). The formation of specific adducts might originate from the intrinsic inorganic salt content in different plant tissues. Potassium is the predominant mineral of plant cells in the shoots and is most important for cell growth and metabolism. The presence of chloride in the chemical structure of tebuconazole provides a unique isotopic pattern in the mass spectra and thus, confirms the identity of the target compounds.

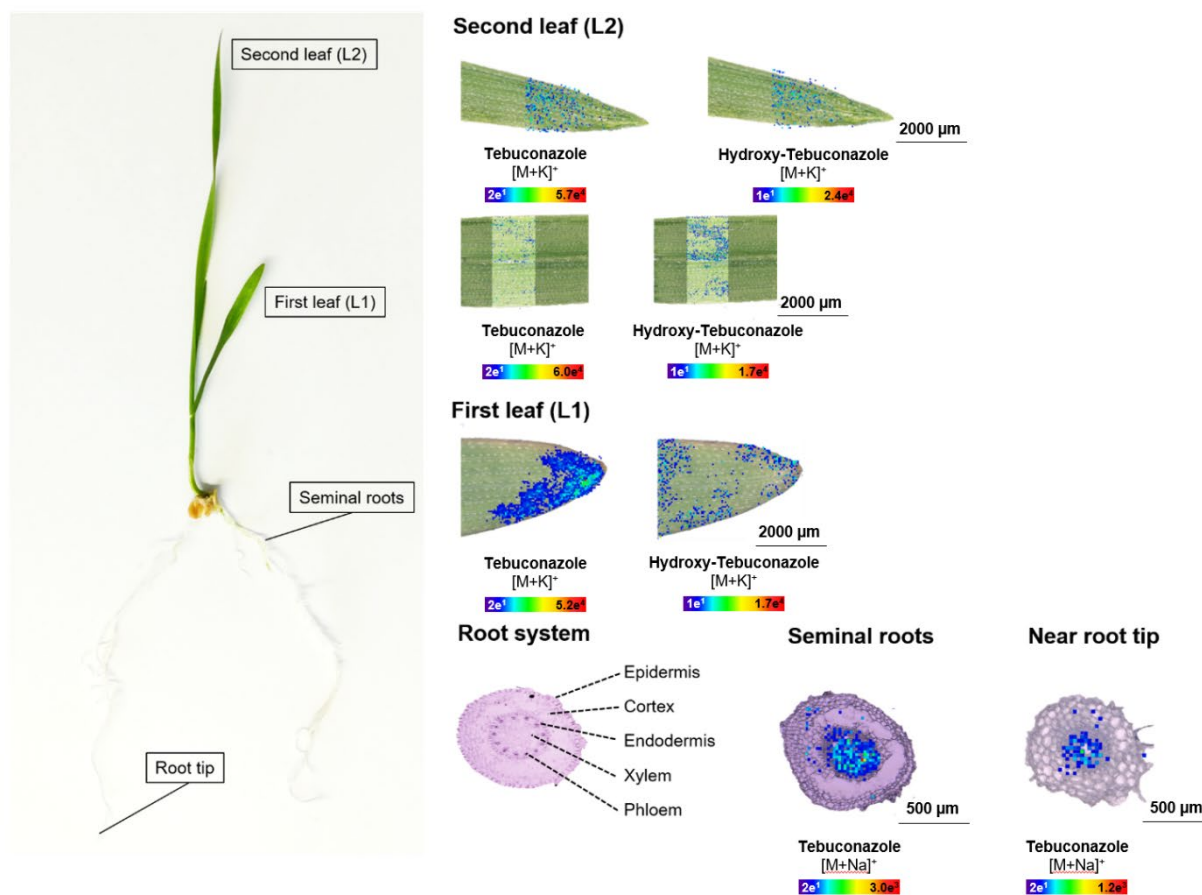


**Figure 39.** MALDI-imaging-HRMS of tebuconazole in wheat (*Triticum aestivum* 'Triso') after seed treatment with ArenaC® (1 g/dt) at the two-leaf stage after 14 days. Localization of tebuconazole ( $[M+Na]^+$ ;  $m/z$  330.1344,  $[M+K]^+$ ;  $m/z$  346.1083) and hydroxy-tebuconazole ( $[M+K]^+$ ;  $m/z$  362.1032).

At the three-leaf stage (24 days after application, Figure 40), tebuconazole was again distributed throughout the plant with a slightly higher accumulation in growing parts (blade tips). The Phase-I- metabolites hydroxy-tebuconazole and *p*-Chlorobenzoic acid showed similar distribution and emphasized the ongoing metabolism. Tebuconazole continues to be taken up and can be found in the higher parts of the plant due to its systemic properties.

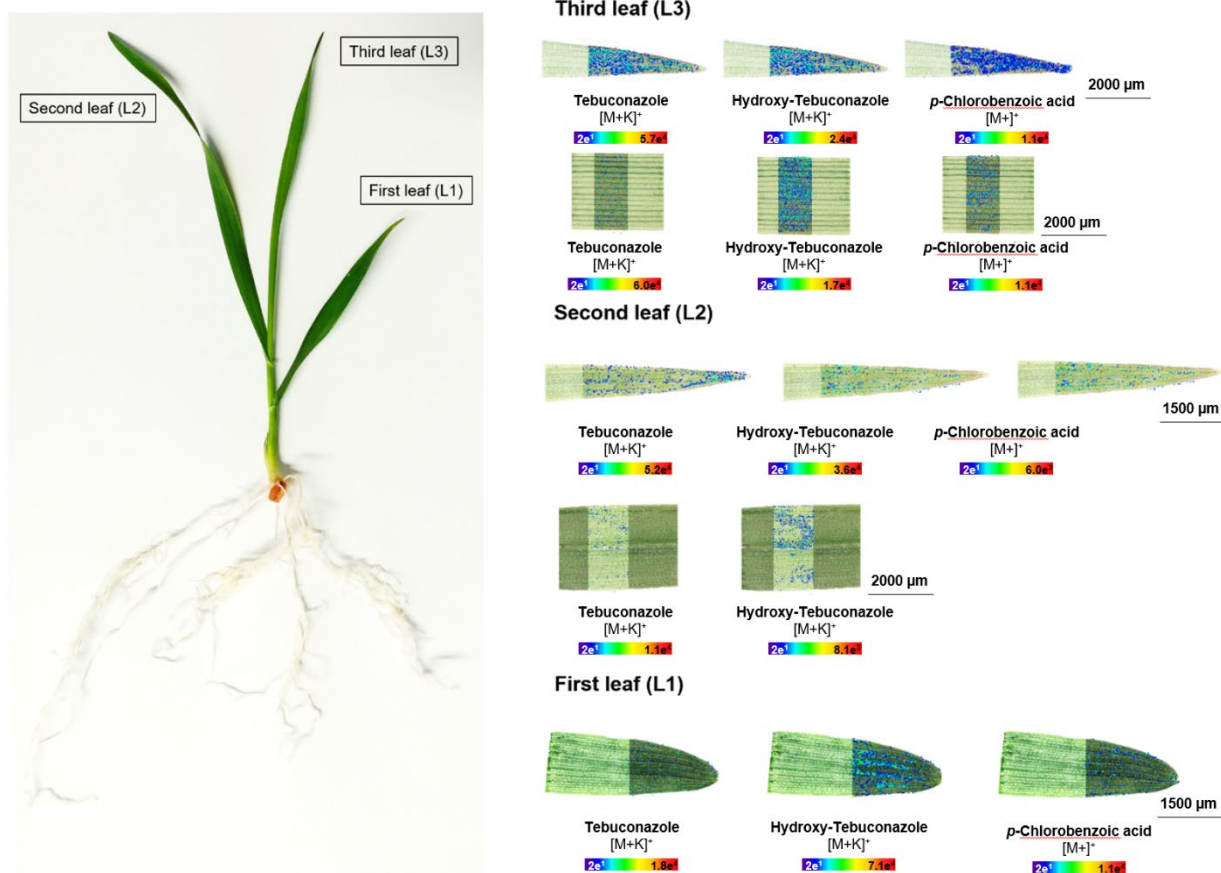


**Figure 40.** MALDI-imaging-HRMS of tebuconazole in wheat (*Triticum aestivum* 'Triso') at the three-leaf stage after 24 days after seed treatment with ArenaC® (1 g/dt). Localization of tebuconazole ([M+K]<sup>+</sup>; *m/z* 346.1083), hydroxy-tebuconazole ([M+K]<sup>+</sup>; *m/z* 362.1032) and *p*-Chlorobenzoic acid ([M+Na]<sup>+</sup>; *m/z* 178.9870).

#### 4.3.2. Distribution of BCS-CX51842 in wheat (*Triticum aestivum* 'Orcas') and soybean (*Glycine max.*) after seed treatment

The fungicide BCS-CX51842 was applied to wheat and soybean grains by dropping 10 μL of a stock-solution of BCS-CX51842 (0.5 mg/mL for wheat and 2.5 mg/mL for soybean) in acetone to ensure homogeneous coating and rapid evaporation at room temperature on the grain surface.

Imaging the surface of wheat grains exhibited the homogenous distribution of the parent compound after seed treatment (Figure 41). Longitudinal cross-sections of the non-germinated seed also showed a homogenous distribution of BCS-CX51842 on the outer layer of the seed

surface. Additionally, endogenous plant metabolites like glutamine were detected in the embryo with localization in the embryo center close to the scutellum in elongated shoots.

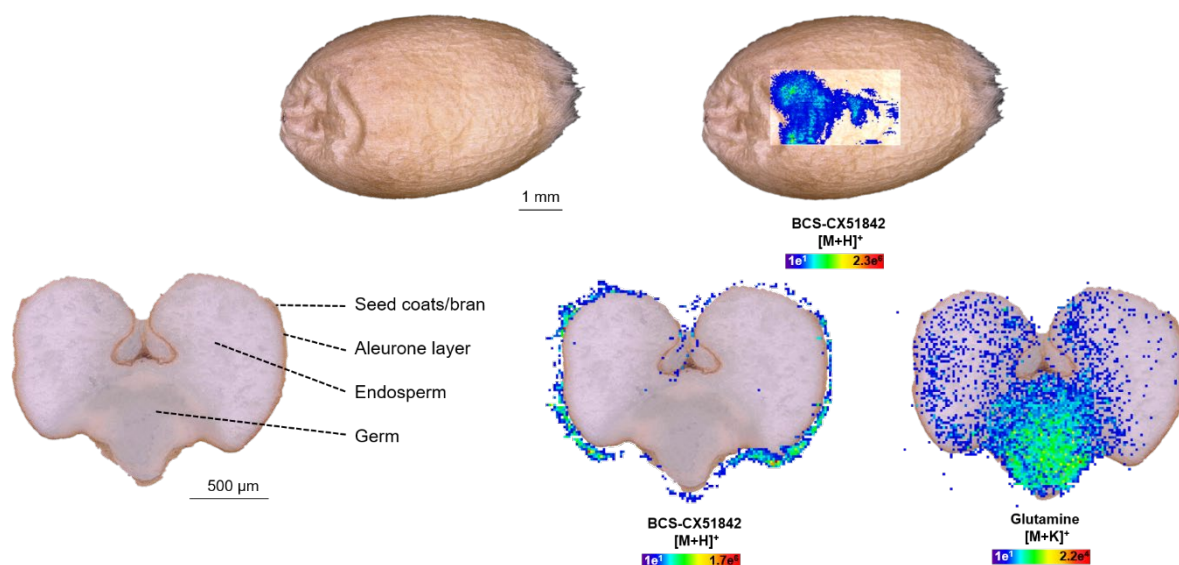


**Figure 41.** MALDI-imaging-HRMS of non-germinated wheat (*Triticum aestivum* 'Orcas') seeds after seed-treatment with BCS-CX51842 (10 g/dt). Localization of BCS-CX51842 ( $[M+H]^+$ ;  $m/z$  342.1413) and selected endogenous plant metabolite (Glutamine  $[M+K]^+$ ;  $m/z$  185.0323).

14 Days after application at the two-leaf stage, BCS-CX51842 showed a homogenous distribution over the entire leaf tissues but is still more pronounced at the leaf tips (Figure 42, 36). The uptake and transport into roots and shoots were ongoing since there were still high amounts of parent compound detectable in the roots. It is mainly localized in the vascular bundles and especially in the xylem, which is the main acropetally transport tissue for water and nutrients from the root to the upper part of the plant. Hydroxy-BCS-CX51842 was detected in parallel within the same tissues as the parent compound.

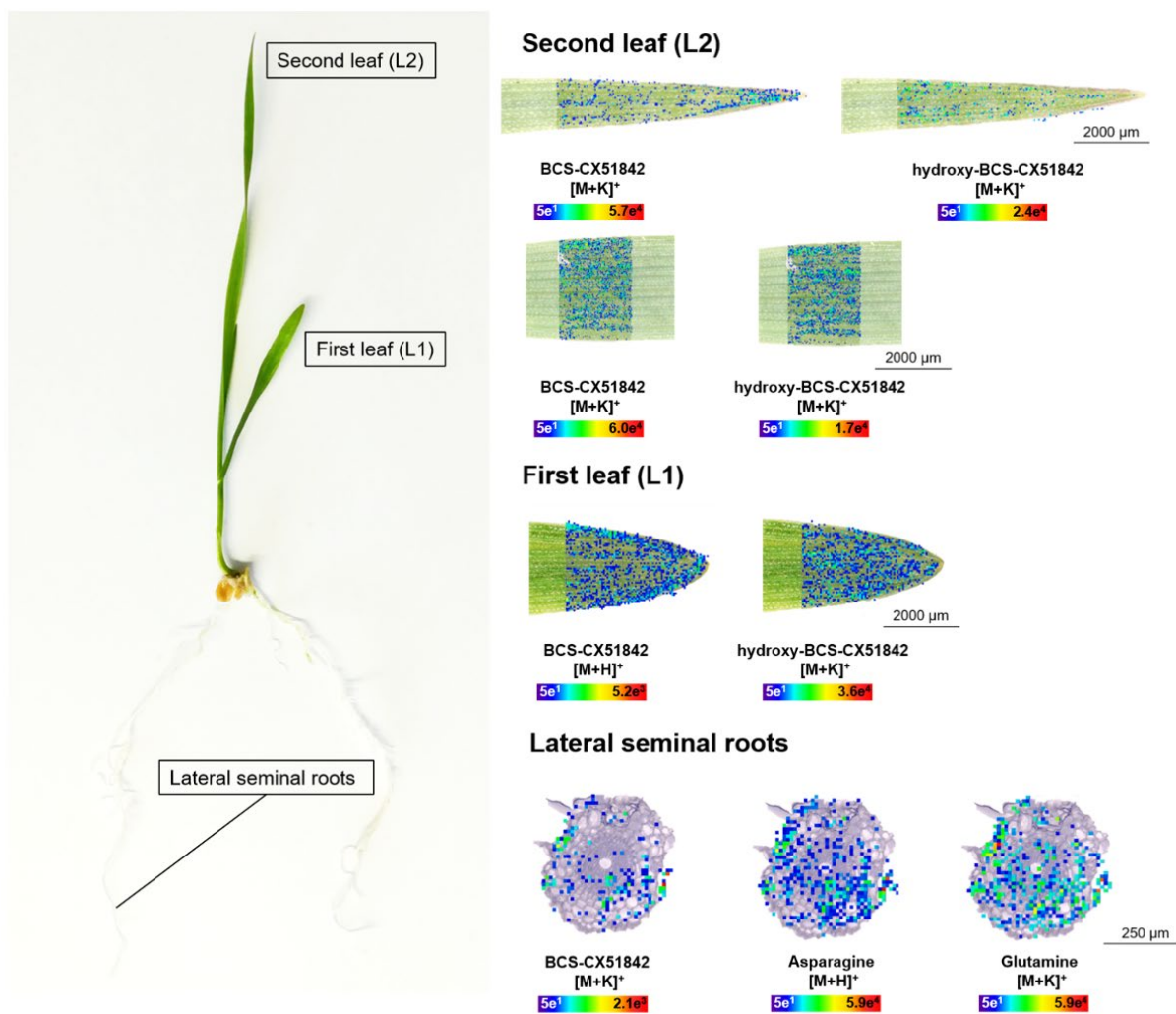


**Figure 42.** MALDI-imaging-HRMS of tebuconazole in wheat (*Triticum aestivum* 'Orcas') at the two-leaf stage after 14 days after seed treatment with BCS-CX-51842 (10 g/dt). Localization of BCS-CX51842 ([M+H]<sup>+</sup>;  $m/z$  342.1413; [M+K]<sup>+</sup>,  $m/z$  380.0971), hydroxy-BCS-CX51842 ([M+K]<sup>+</sup>;  $m/z$  396.0920) and selected endogenous plant metabolites (Glutamine [M+K]<sup>+</sup>;  $m/z$  185.0323; Asparagine [M+H]<sup>+</sup>;  $m/z$  133.0608).

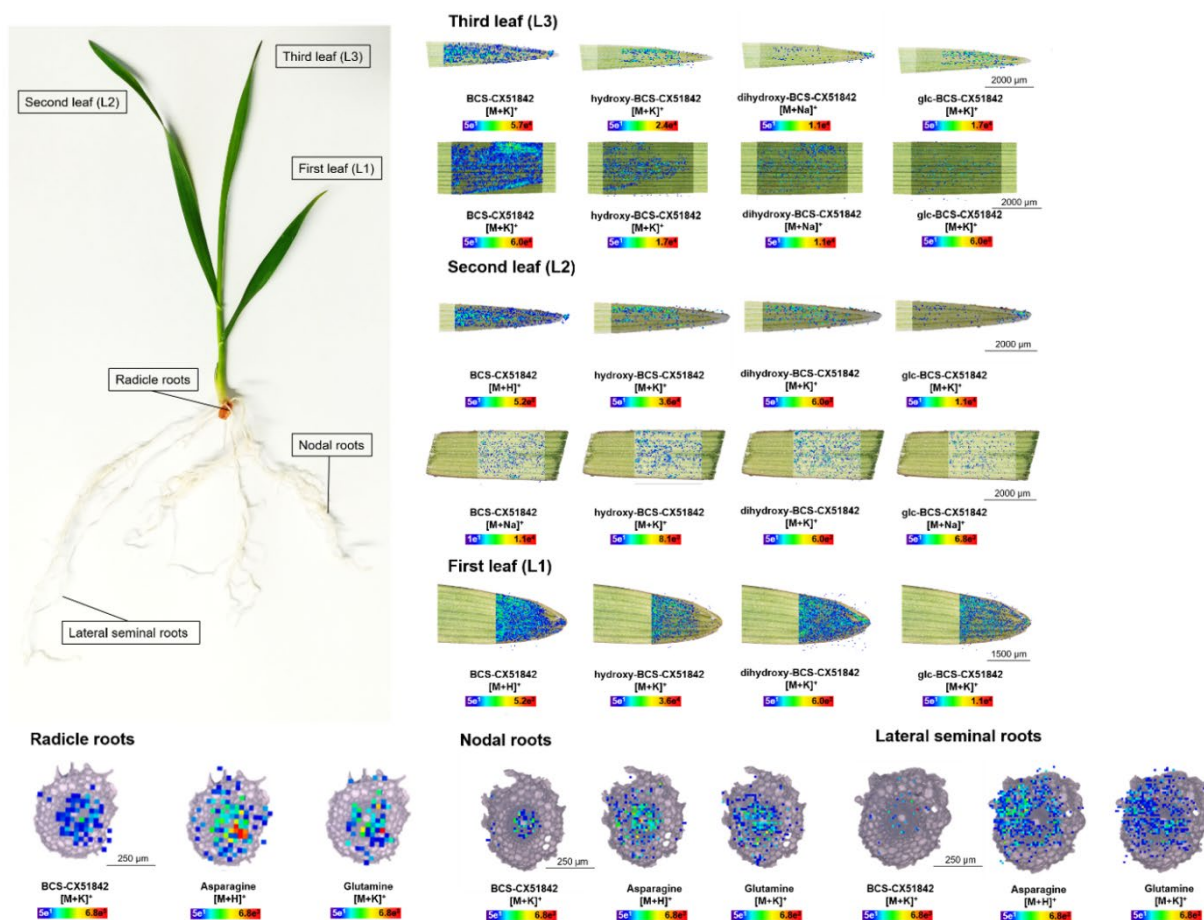


**Figure 43.** MALDI-imaging-HRMS of tebuconazole in wheat (*Triticum aestivum* 'Orcas') at the three-leaf stage after 24 days after seed treatment with BCS-CX-51842 (10 g/dt). Localization of BCS-CX51842 ( $[M+H]^+$ ;  $m/z$  342.1413,  $[M+K]^+$ ;  $m/z$  380.0971;  $[M+Na]^+$ ;  $m/z$  364.1232), hydroxy-BCS-CX51842 ( $[M+K]^+$ ;  $m/z$  396.0920), dihydroxy-BCS-CX51842 ( $[M+K]^+$ ;  $m/z$  412.0870,  $[M+Na]^+$ ;  $m/z$  396.1130), glc-BCS-CX51842 ( $[M+K]^+$ ;  $m/z$  542.1500,  $[M+Na]^+$ ;  $m/z$  364.526.1760) and selected endogenous plant metabolites Asparagine ( $[M+H]^+$ ;  $m/z$  133.0608), Glutamine ( $[M+K]^+$ ;  $m/z$  185.0323).

MALDI-imaging of BCS-CX51842 in dicotyledonous like soybean showed similarities to the imaging experiments in monocotyledons like wheat. The new seed treatment candidate is taken up rapidly through the roots and high amounts were detected as the potassium adduct ion mainly localized in the vascular bundles and especially in the xylem. In the hypocotyl and upper stem below the first trifoliate leaves, BCS-CX51842 was also detected in the secondary xylem. The primary amino acid in soybean, asparagine was detected in parallel in both tissues showing a similar distribution, which confirmed the uptake process of the applied parent compound. The metabolite hydroxy-BCS-CX51842 was first detected in cross-section of the hypocotyl and showed similar distribution in the upper stem, while it is pronounced in the parent containing tissues. We also investigated the cotyledons, which supply the nutrient needs of the seedling for approx. 10 days after germination but could not detect BCS-CX51842 or

metabolites (< LOD) after 26 days. In the first trifoliolate leaves, BCS-CX51842 and dihydroxy-BCS-CX51842 was visualized using MALDI-MSI. Both compounds were detected at the leaf blades and near the midrib above the petiole.

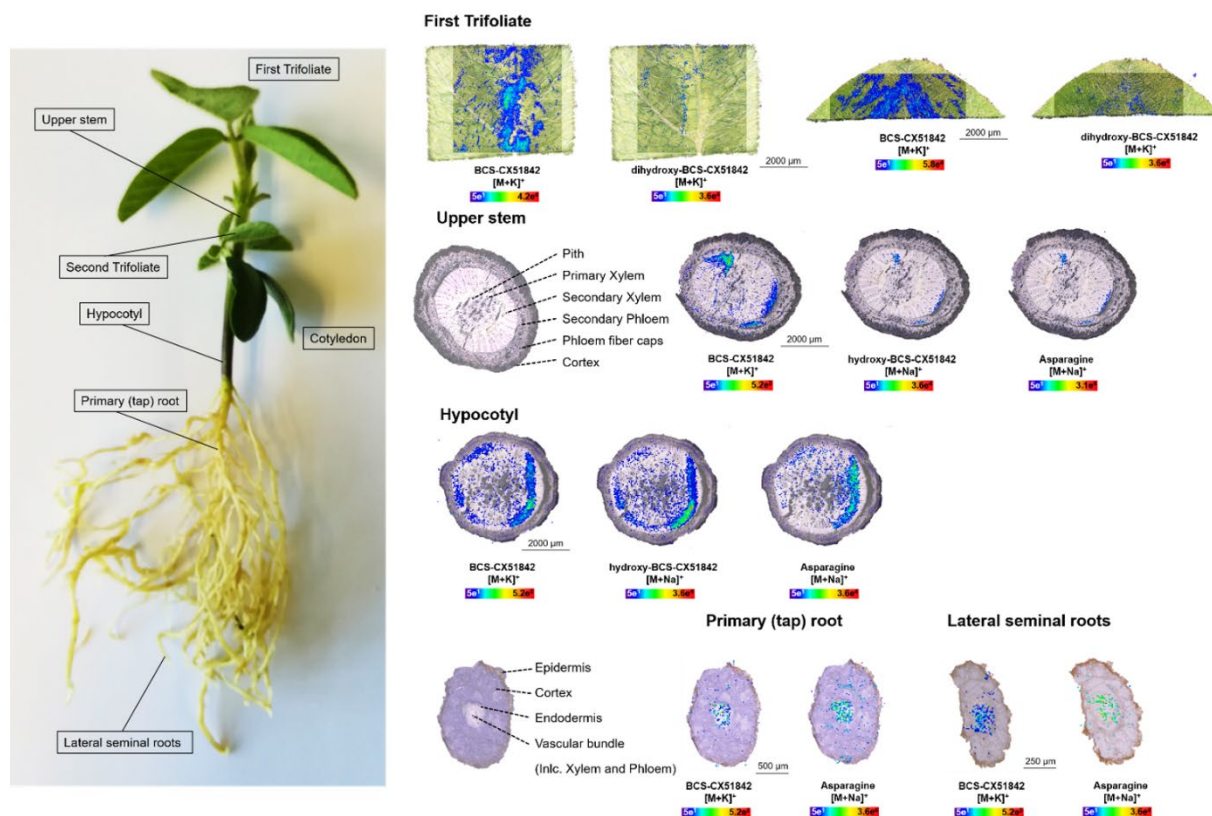


**Figure 44.** MALDI-imaging-HRMS of BCS-CX51842 in soybean (*Glycine max.*) at the two trifoliolate leaf stage after 26 days after application after seed treatment (10 g/dt). Localization of BCS-CX51842 ( $[M+K]^+$ ,  $m/z$  380.0971), Hydroxy-BCS-CX51842 ( $[M+Na]^+$ ;  $m/z$  380.1181), dihydroxy-BCS-CX51842 ( $[M+K]^+$ ;  $m/z$  412.0870) and selected endogenous plant metabolite (Asparagine ( $[M+Na]^+$ ;  $m/z$  155.0427)).

#### **4.4. Interactions and localization of the safener cyprosulfamide with the herbicide thien carbazone-methyl**

This study was initiated to understand if uptake, translocation, or metabolism of the safener cyprosulfamide (CSA) influence the efficacy of the herbicide thien carbazone-methyl (TCM) in maize (*Zea mays*). CSA's protective action is concrete in maize due to specific recognition of the safener resulting in enhanced TCM metabolism. CSA metabolism was also correlating with its activity, but its early metabolites were found to be inactive safeners. MALDI mass spectrometry imaging was used to visualize how CSA affects TCM metabolism when applied in the same or in different tissues. Key information to be determined was uptake and translocation from single and co-application using either standard solutions (1000 ppm) with or without adjuvants. MALDI MSI was used to investigate the uptake and translocation of both herbicide and safener after micro droplet application (10  $\mu$ L in total) on leaves of maize to get information if the safening effect correlates with enhanced herbicide metabolism. Studies about the safener herbicide interactions showed that the parent compounds are responsible for the safener effect and the metabolites did not directly influence the plants. The co-application of either TCM and CSA on the same leaf and the application of both on different leaves were used, to compare if the parent compounds need to be present in the same tissue of the plant to enhance the metabolism and safener effect. Therefore, the safener cyprosulfamide was applied on the first leaf of maize (BBCH code 11-12), while the herbicide thien carbazone-methyl was applied on the second leaf of the same plant. Samples were taken 3, 6, 18, 24 h and then daily up to 7 days. In another experiment the herbicide and safener were applied on the same leaf (first leaf) as a mixture (1000 ppm a.i.). While the biosynthesis of the branched chain amino acid valine is directly inhibited by TCM as the herbicide inhibit the ALS enzyme, MALDI MSI was used to investigate the distribution of the amino acids in different tissues in parallel. The inhibition of the ALS enzyme includes branched-chain amino acids, whose biosynthesis is directly inhibited by TCM as it inhibits the ALS enzyme (Ren *et al.*, 2000) or signaling molecules such as SA or ABA, which have been linked to safener action (Brazier-Hicks *et al.*, 2019, Behringer *et al.*, 2011, Dashevskaya *et al.*, 2013).

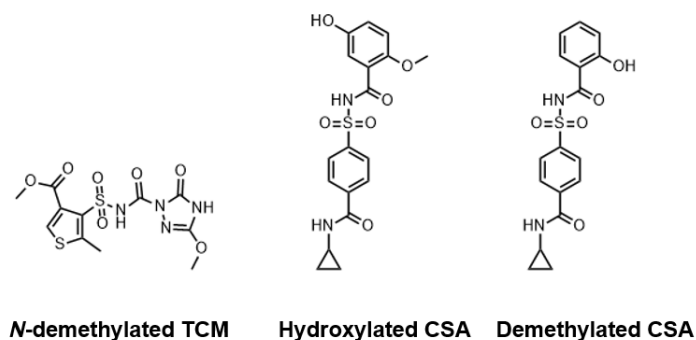


**Figure 45.** Chemical structures of thiencarbazono-methyl and cyprosulfamide metabolites detected by MALDI MSI in maize leaves.

#### 4.4.1. Distribution of thiencarbazono-methyl and cyprosulfamide in maize (*Zea mays*) after application on different leaves

Leaf surface analysis of maize (*Zea mays*) leaves after treatment with the herbicide thiencarbazono-methyl and the safener cyprosulfamide after application on different leaves were performed using MALDI mass spectrometry imaging. TCM and CSA were applied by microdroplet application on the upper part of the first and second leaf using a pipette, respectively. Approximately 20 droplets (single droplet = 0.5  $\mu$ L) on each plant over a leaf surface of about 4 cm<sup>2</sup> were applied, corresponding to an application rate of approx. 50 g/ha at 300 L/ha. The sample preparation and matrix application were done using the pneumatic sprayer leading to a relative wet deposition of the MALDI matrix  $\alpha$ -cyano-4-hydroxycinnamic acid. We reasoned that the matrix condensed on the surface and penetrated the leaf tissues. Thus, not only analytes from the leaf surface would be ionized.

The parent compounds thiencarbazono-methyl and cyprosulfamide were both detected 24 hours after application in the area of the droplet deposition (Figure 46). The used WP formulation leads to run-off of the applied droplets and the herbicide and safener could be measured as the quasi-molecular ion ( $[M+H]^+$ ) on the leaves, where they were applied. The on-tissue calibration spots (1=10, 2=100 and 3=1000 ppm) on the leaf surface showed strong signal intensities. The metabolite demethyl-CSA showed even strong signals after 24 hours, with ongoing transport inside the tissue, while the metabolites *N*-Demethylated-TCM and Hydroxy-CSA were detected in low signal intensities inside the droplet placement area.



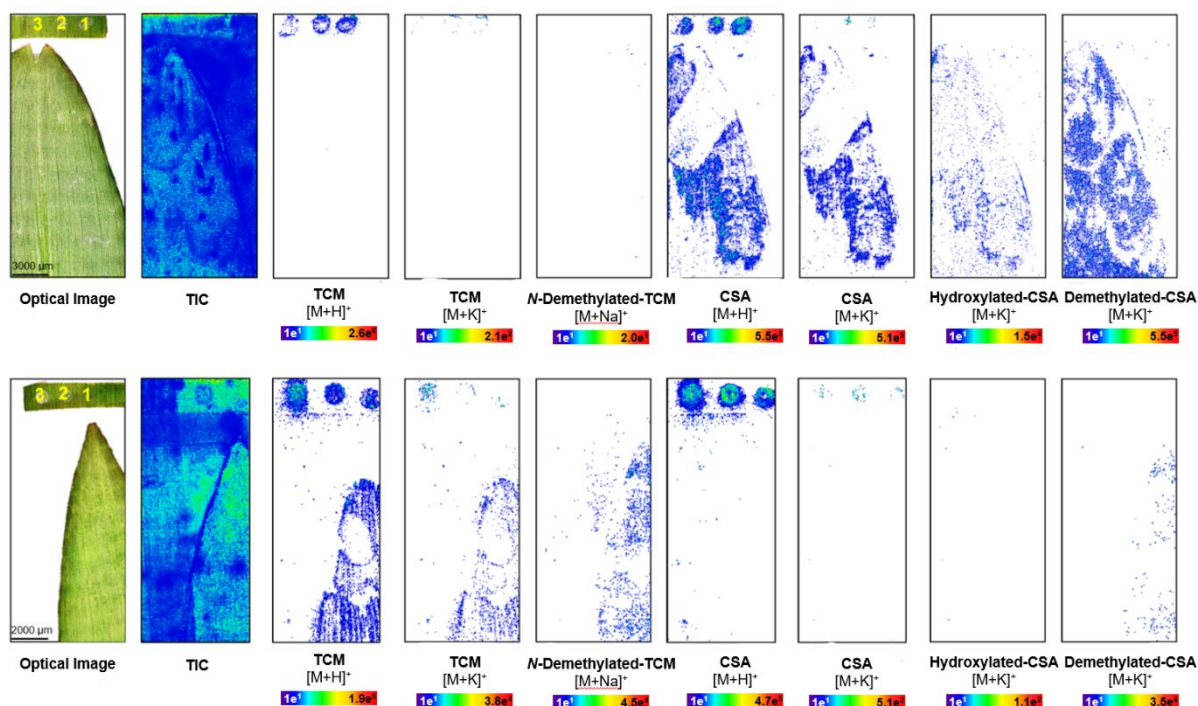


**Figure 46.** MALDI-imaging-HRMS of maize leaves 24 hours after micro droplet application of cyprosulfamide and thiencazabone-methyl on different leaves (spatial resolution: 50  $\mu\text{m}$ , scan area: 9300x21250  $\mu\text{m}$ ; 6250x15350). Localization of thiencazabone-methyl ( $[\text{M}+\text{H}]^+$ ;  $m/z$  391.0377,  $[\text{M}+\text{K}]^+$ ;  $m/z$  428.9936), *N*-Demethylated-TCM ( $[\text{M}+\text{Na}]^+$ ;  $m/z$  399.0040), cyprosulfamide ( $[\text{M}+\text{H}]^+$ ;  $m/z$  375.1009,  $[\text{M}+\text{K}]^+$ ;  $m/z$  413.0568), Hydroxylated-CSA ( $[\text{M}+\text{K}]^+$ ;  $m/z$  429.0517) and Demethylated-CSA ( $[\text{M}+\text{K}]^+$ ;  $m/z$  399.0412).

4 Days after application CSA and TCM was still detected on the first and on the second leaf respectively (Figure 47). The metabolite Demethylated-CSA was again detected with high signal intensities and a wide distribution as the potassium adduct ion ( $[\text{M}+\text{K}]^+$ ) on the first leaf, while it was also detected in the second leaf, underlining the ongoing transport in the plant. While CSA was not detected in the second leaf, the mobile form of the safener inside the plant after the application seems to be the metabolite Demethylated-CSA. Furthermore, *N*-Demethylated-TCM was detected as the potassium adduct ion ( $[\text{M}+\text{Na}]^+$ ) with a wide and homogenous distribution all over the second leaf, representing the ongoing metabolism of the herbicide. Like Demethylated-CSA, *N*-Demethylated-TCM was also detected in the other leaf, but with less signal intensities.

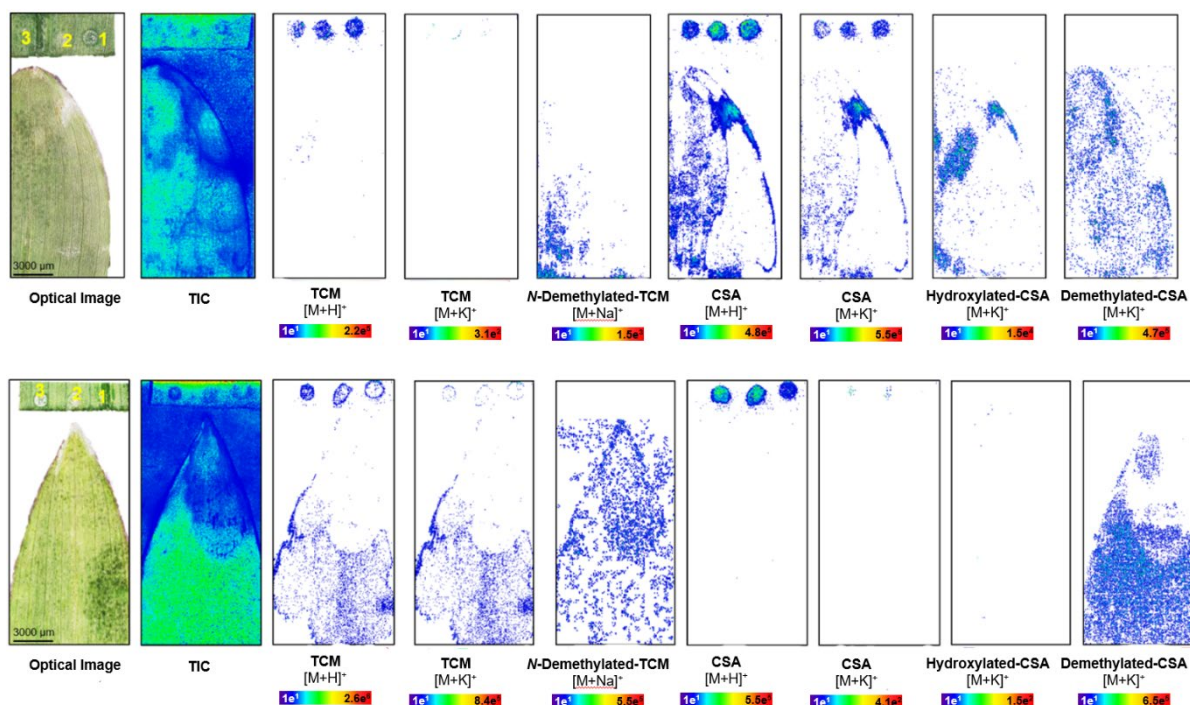


**Figure 47.** MALDI-imaging-HRMS of maize leaves 4 days after micro droplet application of cyprosulfamide and thien carbazone-methyl on different leaves (spatial resolution: 50  $\mu\text{m}$ , scan area: 9300x21250  $\mu\text{m}$ ; 6250x15350). Localization of thien carbazone-methyl ( $[\text{M}+\text{H}]^+$ ;  $m/z$  391.0377,  $[\text{M}+\text{K}]^+$ ;  $m/z$  428.9936), *N*-Demethylated-TCM ( $[\text{M}+\text{Na}]^+$ ;  $m/z$  399.0040), cyprosulfamide ( $[\text{M}+\text{H}]^+$ ;  $m/z$  375.1009,  $[\text{M}+\text{K}]^+$ ;  $m/z$  413.0568), Hydroxylated-CSA ( $[\text{M}+\text{K}]^+$ ;  $m/z$  429.0517) and Demethylated-CSA ( $[\text{M}+\text{K}]^+$ ;  $m/z$  399.0412).

By using MALDI Imaging, in the following study, the interaction of TCM and CSA were investigated in more detail, by visualizing how CSA affects TCM metabolism when applied in the same or in different tissues at different time points.

#### 4.4.2. Spatially resolved investigation of herbicide - safener interaction in maize (*Zea mays L.*)

The fate of CSA and TCM in maize was monitored by assessing its uptake, distribution and metabolism *in situ* using MALDI mass spectrometry imaging. The experiments were carried out on the adaxial surface of intact leaves of maize and the target search was performed using three different application approaches using individual maize seedlings. The first set of plants was treated with CSA and TCM where both the safener and the herbicide were applied on the upper part of the first leaf by microdroplet application. The compounds were applied on different leaves with TCM on the first leaf and CSA on the second leaf in the second set. As a

control treatment, the third set of maize plants was treated with TCM only, which was applied on the first leaf. The effect of CSA on TCM metabolism was investigated at different timepoints (3 hours, 24 hours, 4 days, and 7 days after application). Studies about TCM metabolism in wheat and maize showed that *N*-demethylation is the dominant route in both crops (Giannakopoulos *et al.*, 2020). Thus *N*-demethylated TCM was used as a marker for (enhanced) metabolism in the MALDI MSI experiments. Imaging experiments were carried out without any further treatment except the MALDI matrix application, thereby ensuring authentic pesticide distribution and allowing for fast and accurate analysis. TCM belongs to the herbicide class of ALS inhibitors, which inhibit the enzyme acetolactate synthase (ALS). The protein catalyzes the first step in the biosynthesis pathway of the branched-chain amino acids (valine, leucine and isoleucine) (Garcia *et al.*, 2017). Valine was chosen for visualization in parallel, as leucine and isoleucine are generally indistinguishable by mass spectrometry due to their identical molecular masses.

No major differences in herbicide metabolism were detected by MALDI MSI between the different applications of CSA and TCM after 3 hours. The distribution of TCM following co-application of CSA and control without safener showed, that the herbicide distribution was similar across the entire application area. However, no substantial metabolism was observed, with only small traces of *N*-demethylated TCM being detected after 3 hours (Figure 48).

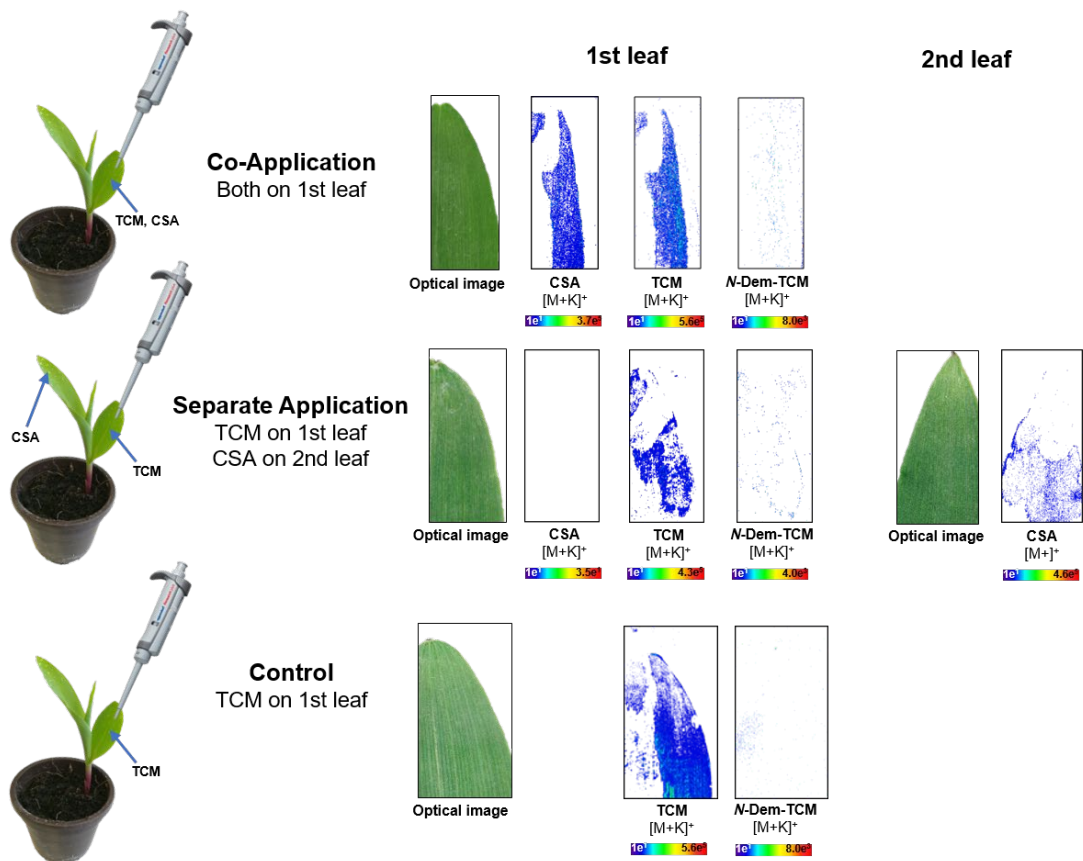


**Figure 48.** MALDI mass spectrometry imaging of maize leaves 3 hours after micro droplet application of cyprosulfamide and thien carbazole-methyl (spatial resolution: 50  $\mu\text{m}$ ). Localization of thien carbazole-methyl ([M+K]<sup>+</sup>;  $m/z$  428.9936), *N*-Demethylated TCM ([M+K]<sup>+</sup>;  $m/z$  414.9780), cyprosulfamide ([M+K]<sup>+</sup>;  $m/z$  413.05680) and valine ([M+K]<sup>+</sup>;  $m/z$  156.04214) on adaxial leaf surface.

Direct MALDI MSI analyses of the leaves after 24 hours showed distinct differences in TCM metabolite appearance. While *N*-Demethylated TCM was detected neither in the control without safener nor in the set with CSA on the 2nd leaf, the co-application on the same leaf resulted in significant appearance of *N*-demethylated TCM (Figure 49). These findings suggest that CSA induces enhanced herbicide metabolism only in tissues where it is directly present, rather than via systemic signaling. All target analytes were detected in highest signal intensities mainly as the potassium adduct ion, while the quasi-molecular ion and sodium adduct ion were detected in parallel, but with less signal intensities. These might originate from the intrinsic nutrient content (nitrogen, phosphor and potassium) in maize leaves, while potassium is the predominant mineral of plant cells in the shoots and is most important for cell growth and metabolism (Karlen *et al.*, 1988, Hanway, 1962).

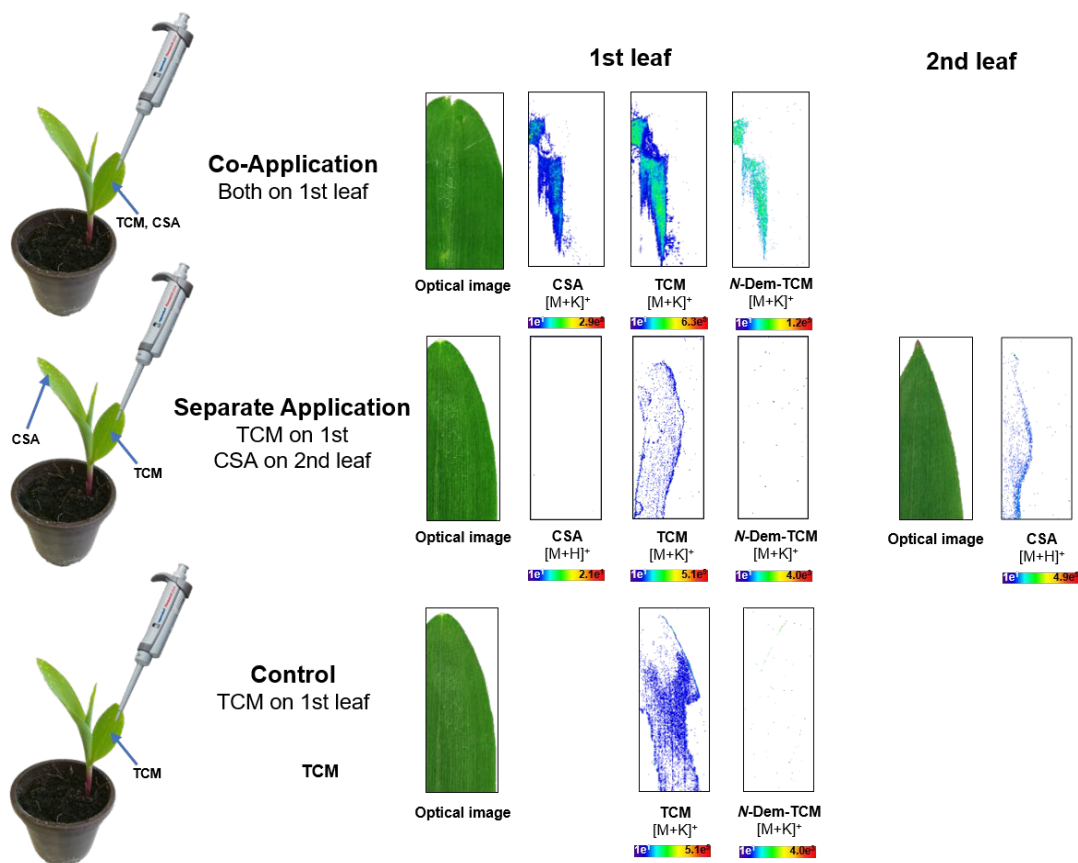


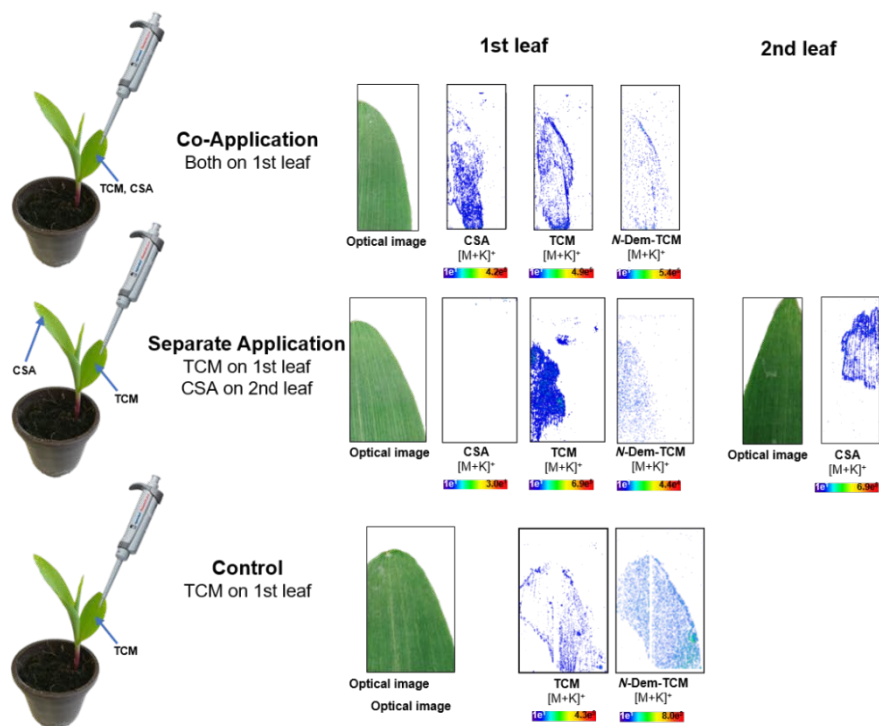
**Figure 49.** MALDI mass spectrometry imaging of maize leaves 24hours after micro droplet application of cyprosulfamide and thien carbazole-methyl (spatial resolution: 50  $\mu\text{m}$ ). Localization of thien carbazole-methyl ([M+K]<sup>+</sup>;  $m/z$  428.99355), *N*-Demethylated TCM ([M+K]<sup>+</sup>;  $m/z$  414.9780), cyprosulfamide ([M+K]<sup>+</sup>;  $m/z$  413.05680) and valine ([M+K]<sup>+</sup>;  $m/z$  156.04214) on adaxial leaf surface.

The spatial distribution and selectivity of CSA after 24 hours suggested that the protection against herbicide injury in maize by TCM is a rapid process. 4 days and 7 days, after application *N*-Demethylated TCM was found in similar distribution either in the co-application or in the control samples without CSA. The ion images seen in the MALDI scans support the hypothesis of a rapid interaction between CSA and TCM since the *N*-demethylation of TCM showed similar results at later timepoints (Figure 50).

Finally, the visualization of valine distribution was less informative than expected, as similar levels and uniform distributions were observed in most samples across all timepoints (Figure 51). The aim was to observe whether safener induced enhancement of TCM metabolism correlated with higher signal intensity of valine, as it should theoretically reverse the inhibitory action of the herbicide on branched chain amino acid biosynthesis. However, this could not be clearly observed. It should be noted that the amount of TCM applied on the maize seedlings

was not sufficient to induce herbicide injury during the trial, suggesting that higher rates of TCM are required to inhibit the biosynthesis of valine effectively. Furthermore, the difference in the concentration levels of the amino acid is might be too low for visualizing the effect using mass spectrometry imaging. The association between branched-chain amino acid depletion and herbicide-induced growth inhibition has been well-documented in the literature (Anderson & Kenneth, 1985, Rost & Reynolds, 1985) and there is a growing number of studies suggesting that MALDI MSI is a suitable technique for visualizing amino acids (Berisha *et al.*, 2014, Korte *et al.*, 2015). However, the study indicated that further optimization may be needed to account for complexities such as differences between developmental stages and the anatomy of a C4 plant such as maize.

4 d



7 d

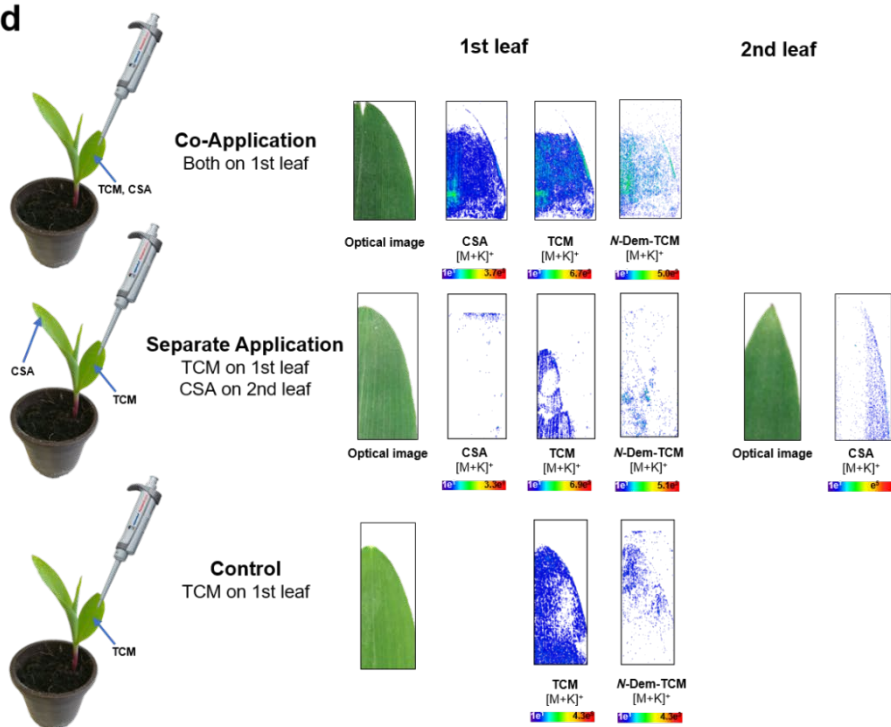


**Figure 50.** MALDI mass spectrometry imaging of maize leaves 4 days and 7 days after micro droplet application of cyprosulfamide and thien carbazole-methyl (spatial resolution: 50  $\mu\text{m}$ ). Localization of thien carbazole-methyl ([M+K]<sup>+</sup>;  $m/z$  428.99355), N-Demethylated TCM ([M+K]<sup>+</sup>;  $m/z$  414.9780), cyprosulfamide ([M+K]<sup>+</sup>;  $m/z$  413.05680) and valine ([M+K]<sup>+</sup>;  $m/z$  156.04214) on adaxial leaf surface.

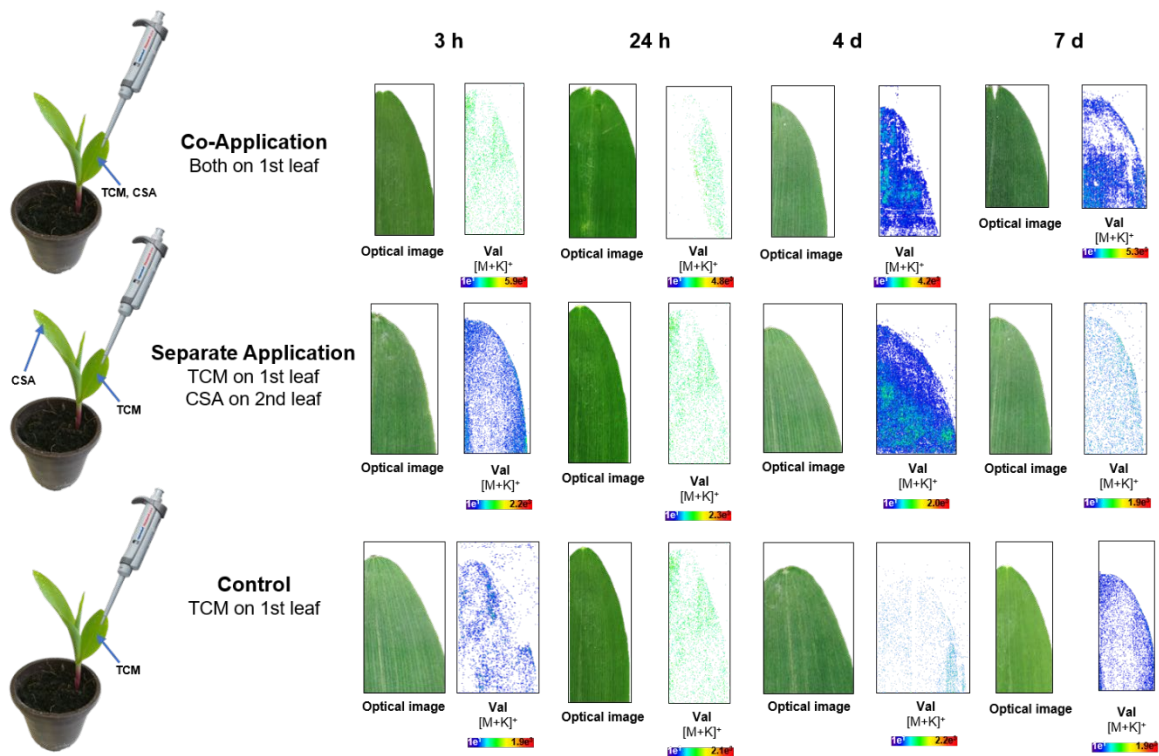


**Figure 51.** MALDI mass spectrometry imaging of maize leaves 24 after micro droplet application of cyprosulphamide and thien carbazole-methyl (spatial resolution: 50  $\mu\text{m}$ ). Localization of valine ( $[M+K]^+$ ;  $m/z$  156.04214) on adaxial leaf surface.



#### **4.5. Systemicity of ethiprole and distribution in reproductive tissues**

The nature of the residues of the insecticide ethiprole in bee-relevant matrices of soybean (*Glycine max*) was investigated after single pre-flowering spray. Ethiprole is a non-systemic and broad-spectrum phenyl-pyrazole insecticide effective against a wide range of insects (plant hoppers, thrips, aphids, weevils, flies, and maggots). The mode of action is different from many other insecticides, including pyrethroids, organophosphates or carbamates and there is a small potential for cross-resistance (Lamberth, 2007). MALDI-imaging experiments of bee relevant matrixes (flowers) were performed directly on flower tissues (banner, wing) and in transversal cross-sections of whole flowers (pedicel, stamen, pistil).

##### **4.5.1. Systemicity of ethiprole and distribution in reproductive tissues**

Many studies have explored the potential mechanisms of the specific toxicity of insecticides to honeybees, but the spatial distribution of these agrochemicals in honeybees through direct contact or oral contact is still poorly understood (Lamberth, 2007). Therefore, insights into the spatiotemporal distribution of pesticides within bee-relevant matrices such as flowers are key to deciphering the mechanisms behind their specific toxicity. The soybean flower is a typical papilionaceous flower having a corolla composed of a standard, two wings, and two keel petals, typical of a legume. The corolla has five petals, a sizeable posterior banner petal, two lateral wing petals and two anterior keel petals. The translocation of ethiprole into bee-relevant matrices was studied after single pre-flowering spray approx. 14 days before flowering. [phenyl-UL-<sup>14</sup>C]Ethiprole was applied as a suspension concentrate (SC200) formulation (200 ppm a.i.) diluted in water at application rates of approx. 250 g a.i./ha. Samples were collected at the principal growth stage of full flowering (at least 50% flowers open). Within MALDI-MSI measurements ethiprole and three Phase-I metabolites (Figure 52) could be visualized in different plant tissues of soybean flowers and upper parts of the main stem *in-situ*. Application of pesticides during flowering of crops can result in exposure of pollinating insects such as honeybees (*Apis*), bumble bees (*Bombus*) and wild bees (*Apoidea*).

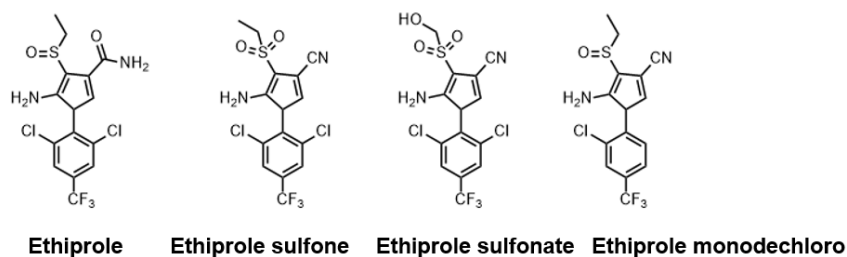


**Figure 52.** Chemical structures of ethiprole and its metabolites detected by MALDI MSI in soybean flowers.

Direct imaging measurements of soybean flowers showed mainly a homogenous distribution of ethiprole in the area of the banner petal and in the carpel including stigma, style, and ovary. Furthermore, the metabolite ethiprole sulfonate was detected in the same tissues in the area of the banner petal. Ethiprole was detected as the sodium adduct ion ( $[M+Na]^+$ ;  $m/z$  418.9718) in all plant tissues, originating from the intrinsic sodium and potassium content in reproductive plant tissues. This is because nectar is predominantly a sugar solution and contains a complex array of chemicals in addition to sugars: amino acids, lipids, proteins, organic acids, vitamins, and inorganic minerals.

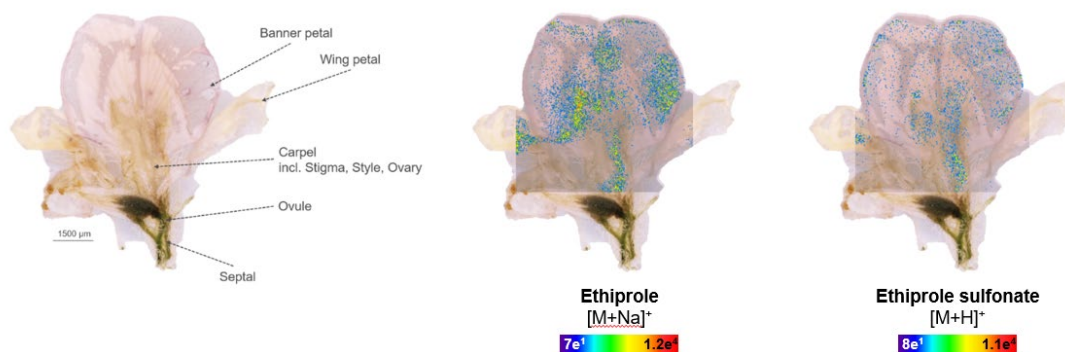


**Figure 53.** MALDI-imaging-HRMS of soybean flower after treatment with ethiprole (spatial resolution: 30  $\mu$ m, scan area: 6600x6600  $\mu$ m). Localization of ethiprole ( $[M+Na]^+$ ;  $m/z$  418.9718) and ethiprole sulfonate ( $[M+H]^+$ ;  $m/z$  400.9484).

In cross-section of upper main stem, directly under the flower ethiprole and ethiprole sulfone were detected mainly in the secondary phloem and parts of the pith. Secondary phloem and especially xylem are less developed at this development stage. In contrast, pith is large and

well developed. Sugars and nutrients are mainly transported via the secondary phloem from the formation site in the mesophyll of leaves to other plant parts.

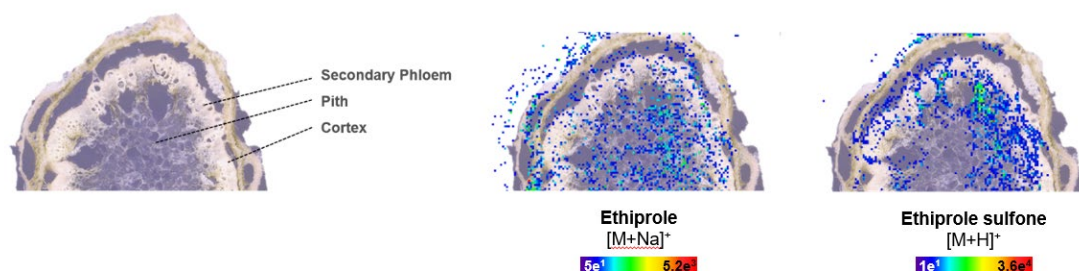


**Figure 54.** MALDI-imaging-HRMS of soybean stem after treatment with ethiprole (spatial resolution: 25  $\mu\text{m}$ , scan area: 3750x2000  $\mu\text{m}$ ). Localization of ethiprole ( $[\text{M}+\text{Na}]^+$ ;  $m/z$  418.9718) and ethiprole sulfone ( $[\text{M}+\text{H}]^+$ ;  $m/z$  412.9848).

Imaging of a transversal cross-section in the area of the wing petal showed similar spatial distribution of ethiprole, while it was detected mainly over the wing petal. Ethiprole monodechloro was also detected but with fewer signal intensities compared to the parent compound. Ethiprole sulfone was also found over the wing petal but slightly enriched in the ovary.

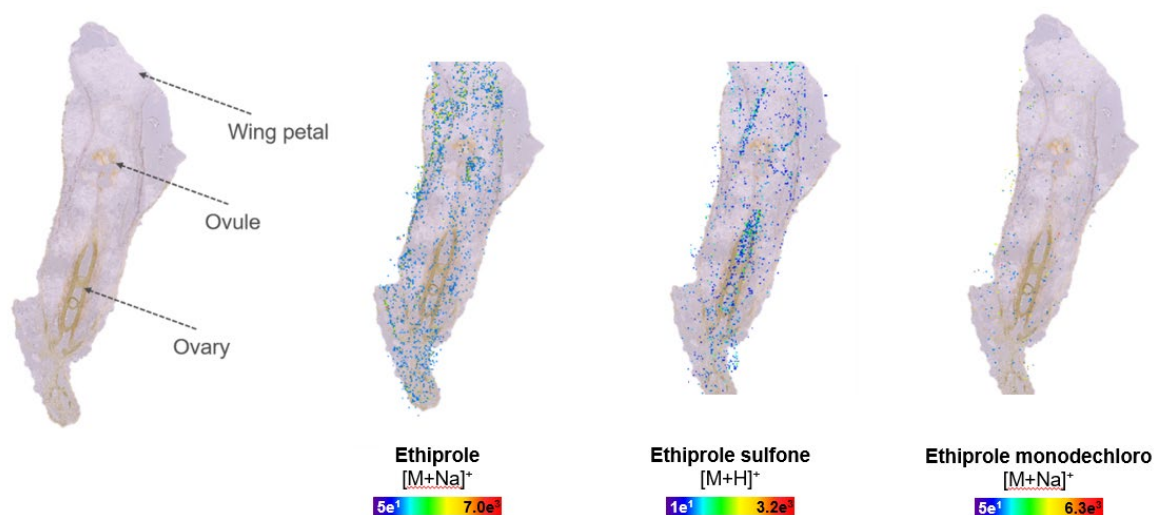


**Figure 55.** MALDI-imaging-HRMS of a transversal cross-section of soybean flower after treatment with ethiprole (spatial resolution: 25  $\mu\text{m}$ , scan area: 3625x8250  $\mu\text{m}$ ). Localization of ethiprole ( $[\text{M}+\text{Na}]^+$ ;  $m/z$  418.9718), ethiprole sulfone ( $[\text{M}+\text{H}]^+$ ;  $m/z$  412.9848) and ethiprole monodechloro ( $[\text{M}+\text{Na}]^+$ ;  $m/z$  385.01082).

Ethiprole was found to be distributed in a longitudinal cross-section of a whole soybean flower with an increased accumulation at the edges of banner petal and in the tissues of style and stigma.

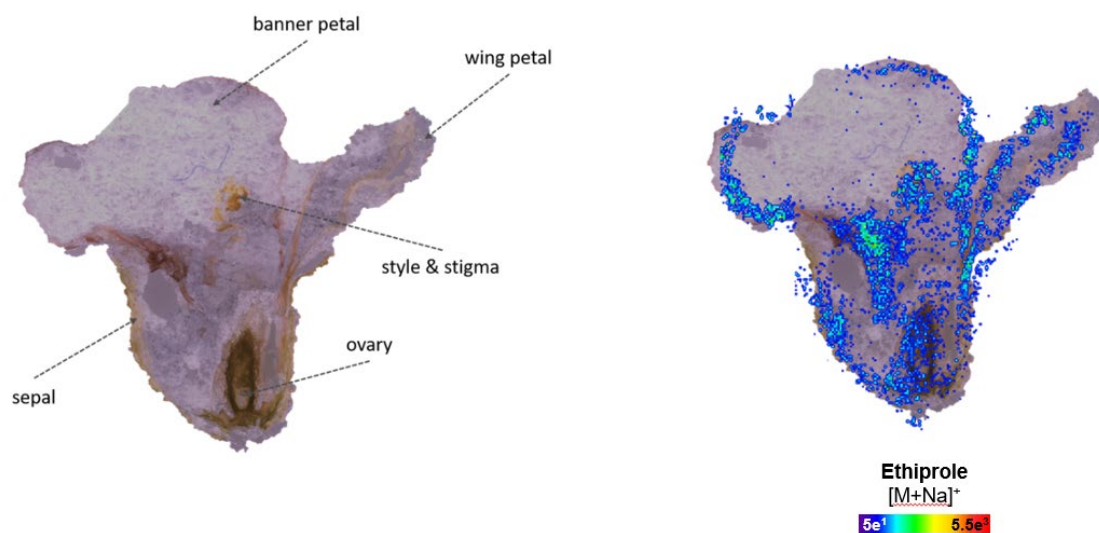


**Figure 56.** MALDI-imaging-HRMS of a transversal cross-section of soybean flower after treatment with ethiprole (spatial resolution: 25  $\mu\text{m}$ , scan area: 3625x8250  $\mu\text{m}$ ). Localization of ethiprole ( $[\text{M}+\text{Na}]^+$ ;  $m/z$  418.9718).

#### **4.6. Uptake and surface adsorption of propineb on adaxial leaf surface**

Detection and imaging of the fungicide propineb on the surface of tomato leaf have been achieved using MALDI-MSI. Whereas the parent compound remains on the plant surface (leaf, fruit), possible metabolites formed outside the plant can penetrate into it. Propineb provides complete coverage of treated leaves with good sticking property so that it is not easily washed off by rains, depending on its low water solubility (< 0.01 g/L) and low logP<sub>OW</sub> (-0.26). The degradation of propineb results in the formation of three major metabolites: propyleneurea (PU), propylenethiourea (PTU) and 5,6-dihydro-3H-imidazo-[2,1-C-1,2,4-dithiazolo-3-thione] (propineb-DIDT). The already established residue analysis method of propineb is based on the measurement of the carbon disulphide and propylendiamine (PDA) produced by acidic hydrolysis in the presence of stannous chloride. After derivatization to 1,2-bis(trifluoroacetamido)propane, GC-MS determines PDA with selective ion monitoring (Kazos *et al.*, 2007, Malik and Faubel, 1999). In this study MALDI-MSI was used to investigate degradation and metabolism of propineb *in-situ* on tomato leaves. Propineb was applied on tomato leaves as single microdroplets using as a water-dispersible granule formulation (WG70) with pure and spiked stable isotope-labeled propineb-DIDT to get further information about the degradation process(es) on the adaxial leaf surface of tomato plants. The formulated product contained 2000 ppm propineb and was spiked with 200 ppm [<sup>13</sup>C<sub>3</sub>, <sup>15</sup>N]propineb-DIDT. Finally, real field samples have been analyzed with mass spectrometry imaging to track the behavior of propineb in the field under naturally weather conditions (e.g., wind, rain).

##### **4.6.1. Uptake and surface adsorption of propineb on tomato leaves after droplet application**

The possible degradation of propineb due to the sample preparation process was investigated using MALDI MSI. Propineb was deposited onto the leaf of growing individual tomato leaves as a water dispersible granule formulation (WG70). The formulation was spiked with 200 ppm [<sup>13</sup>C<sub>3</sub>, <sup>15</sup>N]propineb-DIDT to get further information of the transformation processes leading to the metabolite PTU (see Figure 57). After initial application, the leaves were removed at different time points and prepared for direct MALDI mass spectrometry imaging analysis, without further sample preparation.

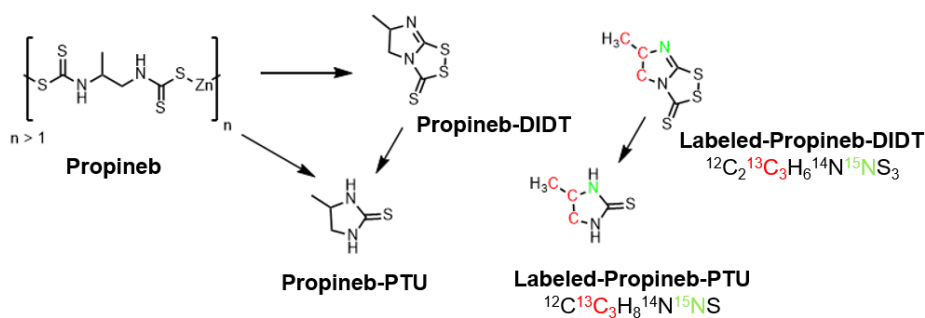


**Figure 57.** Proposed degradation pathway of propineb into propineb-DIDT and PTU with assigned incorporation of spiked stable isotope-labeled propineb-DIDT ( $[^{13}\text{C}_3, ^{15}\text{N}]$ propineb-DIDT) used for the MALDI-imaging experiment.

At the beginning of the experiment, propineb could be detected on the adaxial leaf surface without diffusion during the drying process (approx. 1 h) of the droplets (Figure 58). The cuticle of tomato leaves is composed of plates and protuberances of wax imbedded in various layer of cutin, a mixture of polymers of dicarboxylic and hydrocarboxylic acid esters. Within the sequential measurement, most of the cuticle might be gradually removed from the tissue by the laser. Most of the applied propineb is located on the leaf surface without penetration into the leaf. Spiked  $[^{13}\text{C}_3, ^{15}\text{N}]$ propineb-DIDT showed strong signal intensities for the quasi-molecular ion ( $m/z$  194.9837), while unlabeled propineb-DIDT was not detected. PTU was simultaneously visualized as the quasi-molecular ion ( $m/z$  117.0481) in the area of the droplet placement and showed nearly the same distribution as the active ingredient. MALDI-MS measurements of the application solution showed that the metabolite PTU (hydrolyzed) is already part of the formulation. DMSO as solvent was able to avoid hydrolysis of propineb into PTU in the presence of water (Figure 59). Water as solvent showed the same signals as the measurement in DMSO.  $[^{13}\text{C}_3, ^{15}\text{N}]$ PTU was neither detected on the leaf surface nor in the application solution at the beginning of the experiment.

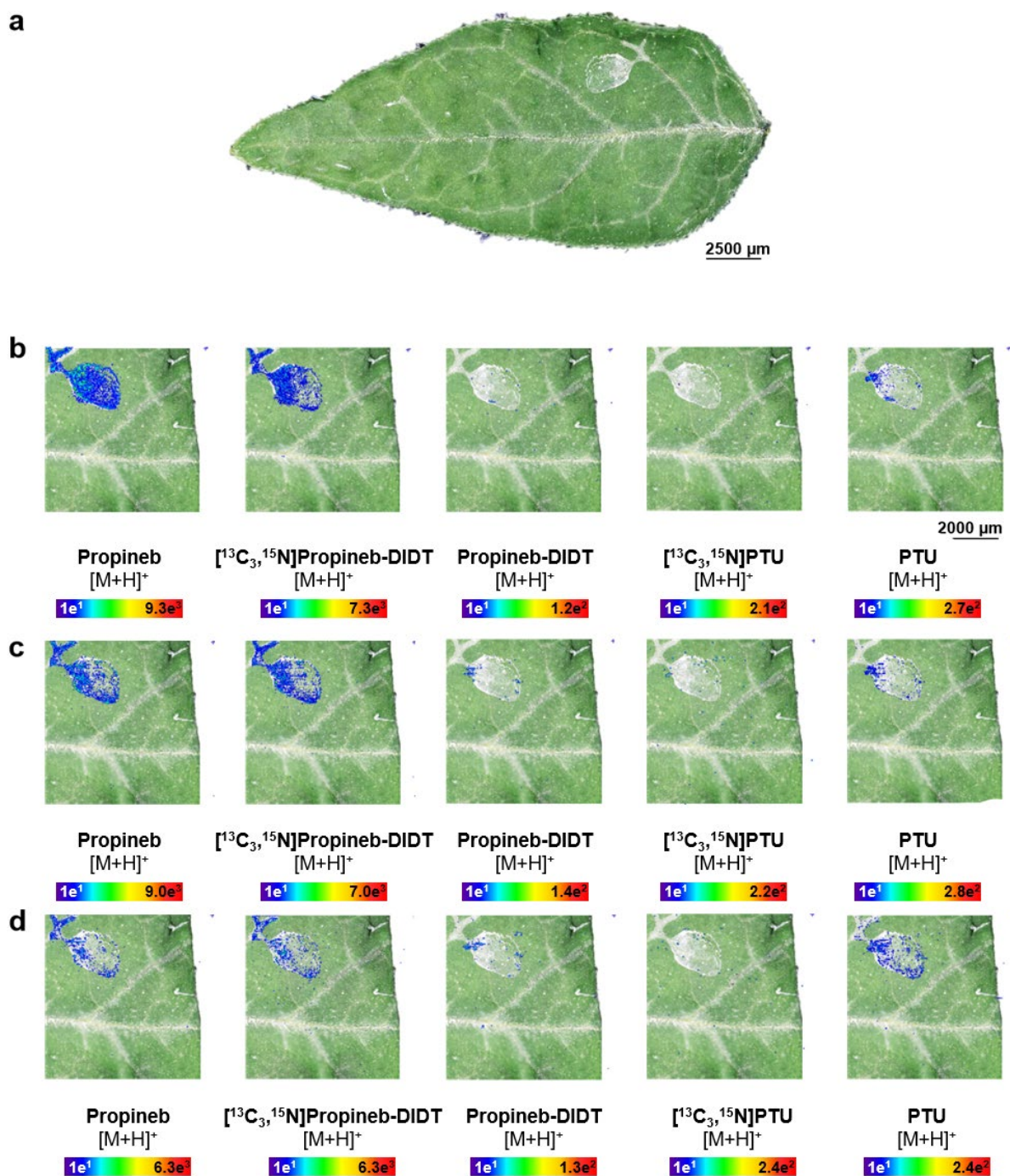


**Figure 58.** MALDI-imaging-HRMS of tomato leaf 1 h after treatment with propineb (spatial resolution: 25  $\mu\text{m}$ , scan area: 5000x5000  $\mu\text{m}$ ). **b-d** Localization of propineb ( $[3\text{M}-2\text{Zn}]^{2+}$ ;  $m/z$  368.9000), [<sup>13</sup>C<sub>3</sub>,<sup>15</sup>N]propineb-DIDT ( $[\text{M}+\text{H}]^+$ ;  $m/z$  194.9837), propineb-DIDT ( $[\text{M}+\text{H}]^+$ ;  $m/z$  190.9766), [<sup>13</sup>C<sub>3</sub>,<sup>15</sup>N] PTU ( $[\text{M}+\text{H}]^+$ ;  $m/z$  121.0552) and PTU ( $[\text{M}+\text{H}]^+$ ;  $m/z$  117.0481).

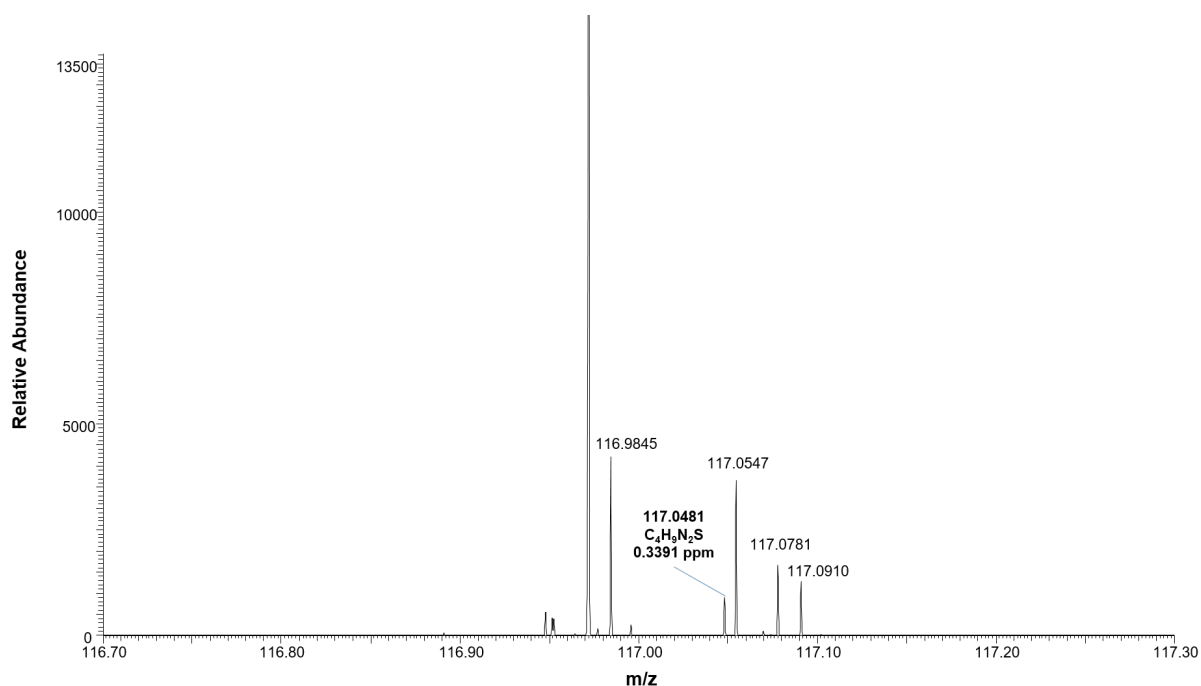


**Figure 59.** Expanded region of MALDI mass spectrum acquired of the WG70 application solution (200 ppm propineb) after dried-dropled method on a gold plate without MALDI matrix at beginning of the experiment. Metabolite PTU ( $C_4H_9N_2S$ ) was already detected in the application formulation.

3 Days after application, the parent compound showed a homogenous distribution on the leaf surface inside the area of the droplet placement (Figure 60). Propineb was still found on the leaf surface and no significant transcuticular penetration through the leaf cuticle was observed. Furthermore, unlabeled propineb-DIDT was detected inside the area of the droplet placement, which underlined the ongoing transformation of propineb on the leaf surface. PTU was still detected while no [ $^{13}C_3$ ,  $^{15}N$ ]-PTU formed by [ $^{13}C_3$ ,  $^{15}N$ ]propineb-DIDT was observed in the imaging measurements. MALDI measurements of the application solution showed that hydrolysis was already ongoing, while [ $^{13}C_3$ ,  $^{15}N$ ]-PTU was detected using the dried-droplet method of the aqueous application solution. Because of that, [ $^{13}C_3$ ,  $^{15}N$ ]-PTU during the imaging experiment might be below the detection limit (< LOD).



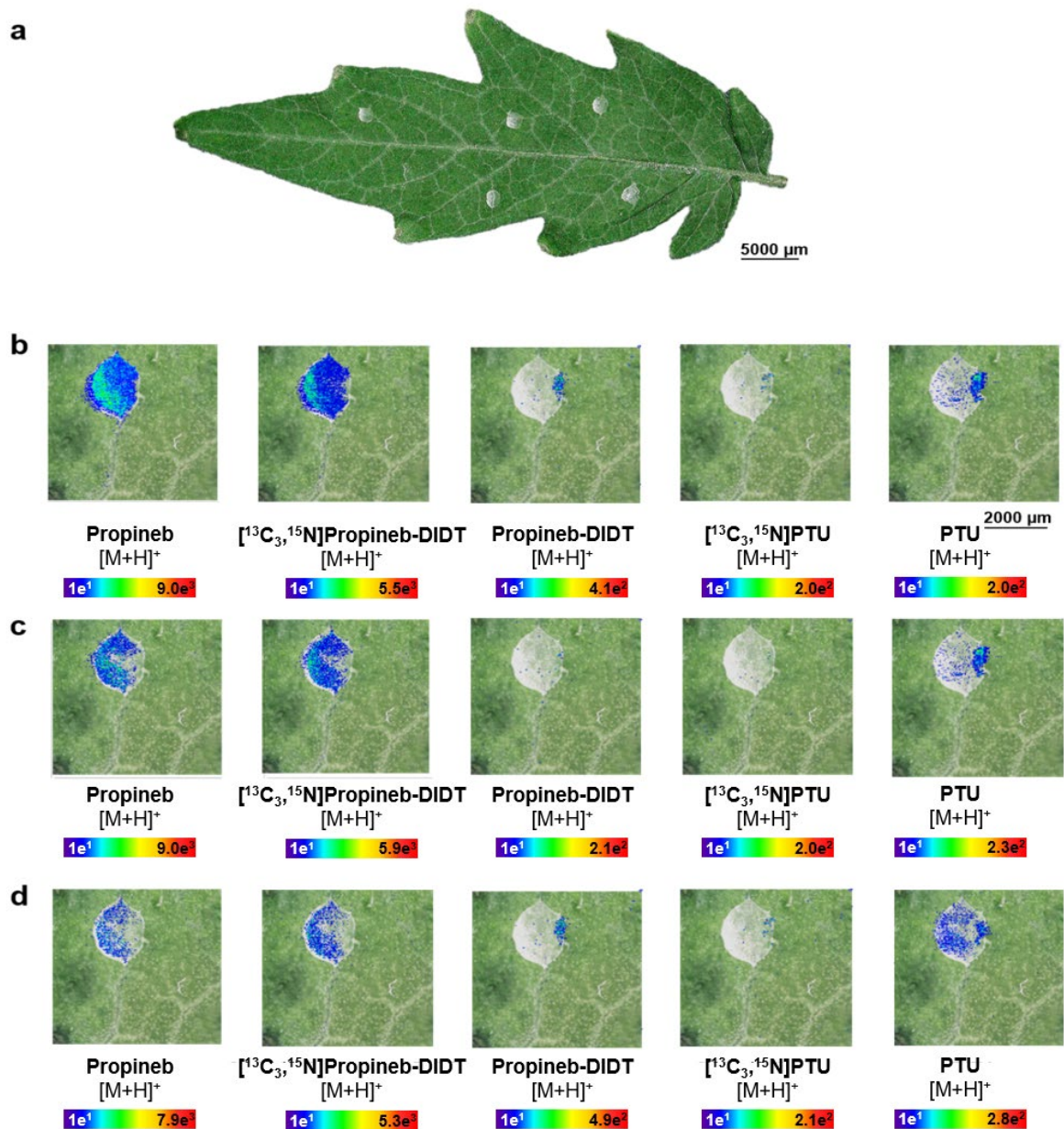


**Figure 60.** MALDI-imaging-HRMS of tomato leaf 3 days after treatment with propineb (spatial resolution: 25  $\mu\text{m}$ , scan area: 5000x5000  $\mu\text{m}$ ). **b-d** Localization of propineb ( $[3\text{M}-2\text{Zn}]^{2+}$ ;  $m/z$  368.9000), [<sup>13</sup>C<sub>3</sub>,<sup>15</sup>N]propineb-DIDT ( $[\text{M}+\text{H}]^+$ ;  $m/z$  194.9837), propineb-DIDT ( $[\text{M}+\text{H}]^+$ ;  $m/z$  190.9766), [<sup>13</sup>C<sub>3</sub>,<sup>15</sup>N] PTU ( $[\text{M}+\text{H}]^+$ ;  $m/z$  121.0552) and PTU ( $[\text{M}+\text{H}]^+$ ;  $m/z$  117.0481).

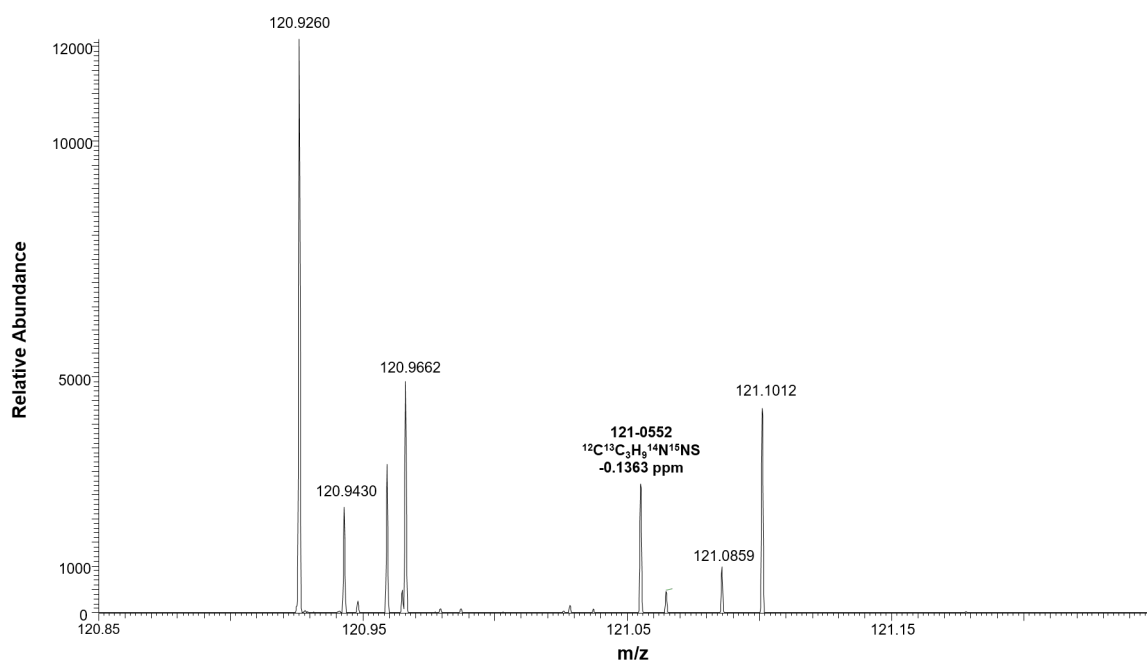


**Figure 61.** Expanded region of MALDI mass spectrum acquired of the WG70 application solution (200 ppm propineb) after dried-dropled method on a gold plate without MALDI matrix at the end of the experiment. [ $^{13}\text{C}_3,^{15}\text{N}$ ]PTU was detected in the application solution.

7 Days after application propineb, [ $^{13}\text{C}_3, ^{15}\text{N}$ ]-Propineb-DIDT and PTU were detected in the spot location zone. Unlabeled propineb-DIDT showed higher signal intensities, because of the ongoing hydrolysis of propineb on the leaf surface. Detection of [ $^{13}\text{C}_3, ^{15}\text{N}$ ]-PTU showed low signal intensities during the imaging experiment, while it was also found in the application solution. 14 days after application on the leaf surface a homogenous distribution of propineb, [ $^{13}\text{C}_3, ^{15}\text{N}$ ]-propineb-DIDT, unlabeled propineb-DIDT and PTU was observed. In addition, [ $^{13}\text{C}_3, ^{15}\text{N}$ ]-PTU could also be detected in similar signal intensities inside the area of the droplet placement and the results highlight, that both possible degradation routes of PTU (directly via propineb or further degradation via propineb-DIDT) take place after droplet application directly on tomato leaves.

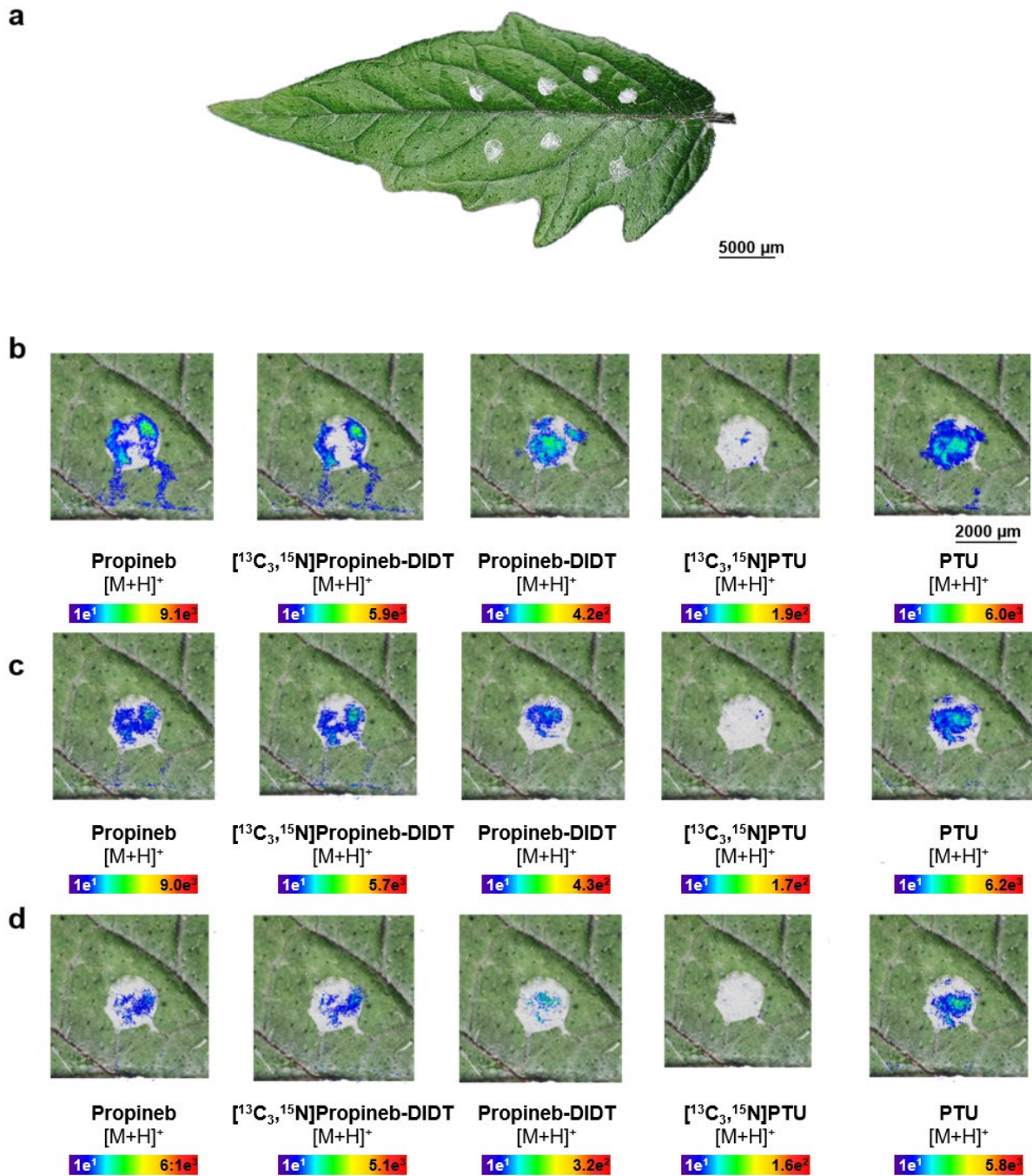


**Figure 62.** MALDI-imaging-HRMS of tomato leaf 7 days after treatment with propineb (spatial resolution: 25  $\mu\text{m}$ , scan area: 5000x5000  $\mu\text{m}$ ). **b-d** Localization of propineb ( $[\text{3M-2Zn}]^{2+}$ ;  $m/z$  368.9000),  $^{13}\text{C}_3,^{15}\text{N}$ propineb-DIDT ( $[\text{M}+\text{H}]^+$ ;  $m/z$  194.9837), propineb-DIDT ( $[\text{M}+\text{H}]^+$ ;  $m/z$  190.976,  $^{13}\text{C}_3,^{15}\text{N}$  PTU ( $[\text{M}+\text{H}]^+$ ;  $m/z$  121.0552) and PTU ( $[\text{M}+\text{H}]^+$ ;  $m/z$  117.0481).

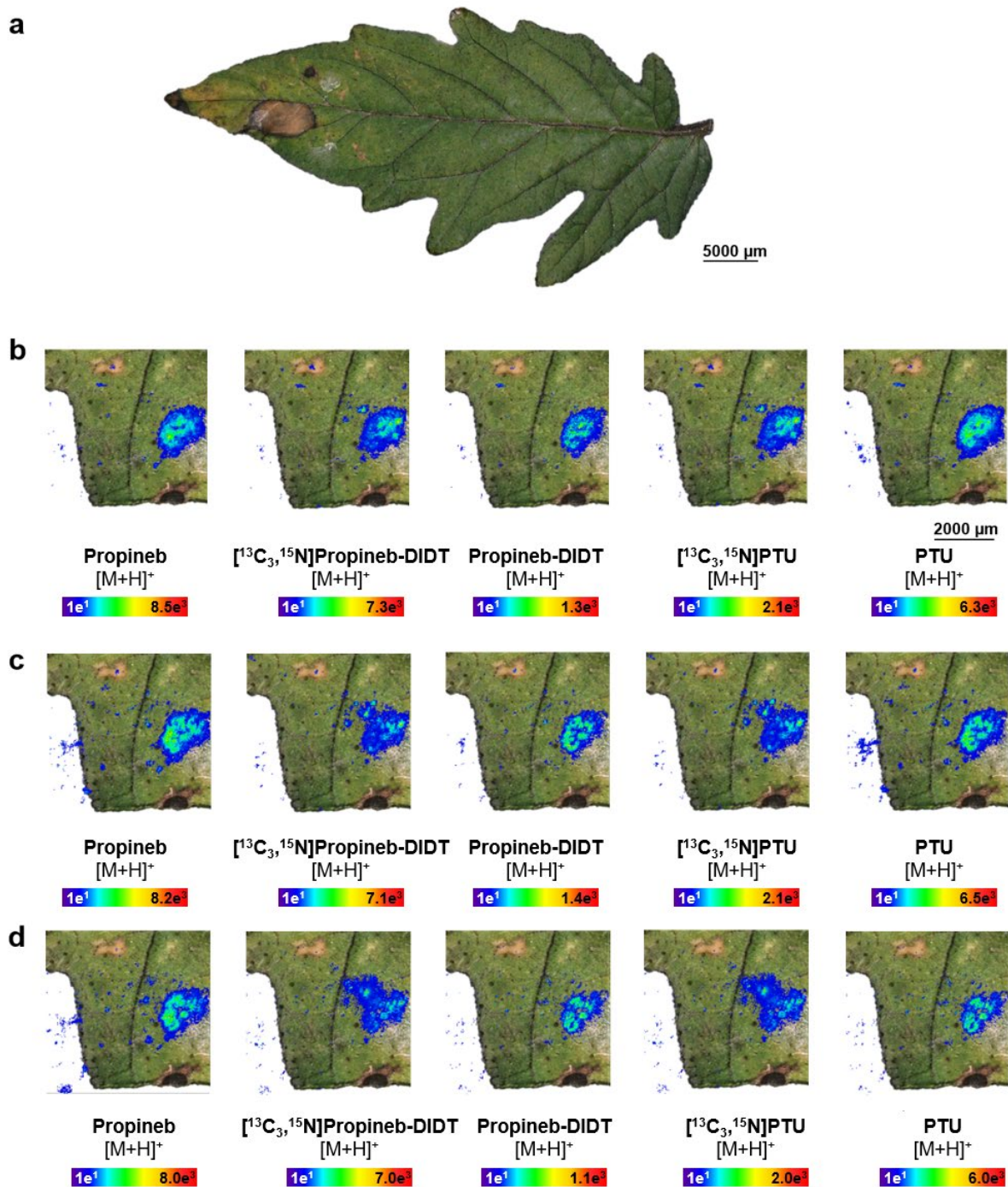


**Figure 63.** MALDI-imaging-HRMS of tomato leaf 14 days after treatment with propineb (spatial resolution: 25  $\mu\text{m}$ , scan area: 5000x5000  $\mu\text{m}$ ). **b-d** Localization of propineb ( $[3\text{M}-2\text{Zn}]^{2+}$ ;  $m/z$  368.9000), [<sup>13</sup>C<sub>3</sub>,<sup>15</sup>N] propineb-DIDT ( $[\text{M}+\text{H}]^+$ ;  $m/z$  194.9837), propineb-DIDT ( $[\text{M}+\text{H}]^+$ ;  $m/z$  190.9766), [<sup>13</sup>C<sub>3</sub>,<sup>15</sup>N] PTU ( $[\text{M}+\text{H}]^+$ ;  $m/z$  121.0552) and PTU ( $[\text{M}+\text{H}]^+$ ;  $m/z$  117.0481).

#### 4.6.2. Uptake and surface adsorption of propineb on tomato leaves in real field samples

Propineb was applied as a water dispersible granule formulation (WP70) at application rates of approx. 1.5 kg a.i./ha. Actual field tomato leaf samples were taken 0, 3, 7, 14, 28, 35 days after application, frozen in a deep-freezer (< -20 °C) and stored at -20 °C until analysis. At the beginning of the field trials, propineb was detected with a wide distribution all over the entire adaxial leaf surface, while droplet residues were still visible in the microscopic picture and underlined by the ion image of the active ingredient (Figure 64). The metabolites propineb-DIDT and PTU were detected in parallel, while propineb-DIDT showed higher signal intensities than PTU. This confirmed the hypothesis, that propineb-DIDT is already part of the water containing formulation, which was observed in the experiment with stable isotope-labeled propineb-DIDT. Within the experiment the signal intensities for propineb decrease with time and after 14 days only low signal intensities for the parent could be observed on the adaxial tomato leaf surface. The signal intensities for propineb-DIDT increased at the beginning of the experiment and already 3 days after application highest signal intensities were detected for the target analyte as the quasi-molecular ion in positive ion mode propineb-DIDT ( $[M+H]^+$ ;  $m/z$  190.9766). In the following samples, the signal intensities decrease similar to propineb. In contrast, the signal intensities for the degradation metabolite PTU increased over time within the ongoing experiment. The MALDI mass spectrometry imaging data underline the degradation process(es) of propineb after foliar application as a water-containing formulation on the leaf surface.

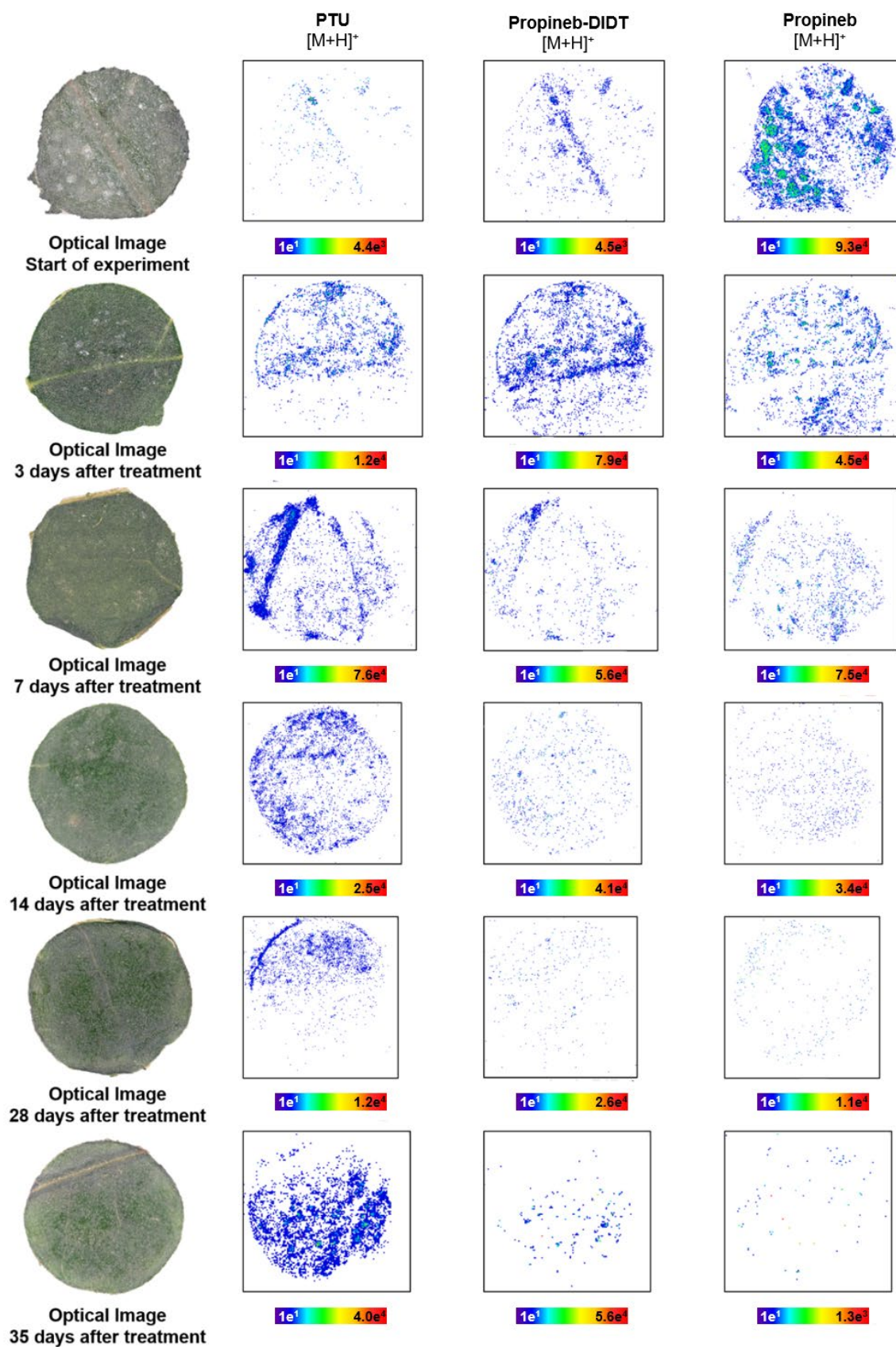


**Figure 64.** MALDI-imaging-HRMS of tomato leaf after treatment with propineb (spatial resolution: 40  $\mu\text{m}$ , scan area: 9000x8000  $\mu\text{m}$ ). Localization of propineb ( $[3\text{M}-2\text{Zn}]^{2+}$ ;  $m/z$  368.9000), propineb-DIDT ( $[\text{M}+\text{H}]^+$ ;  $m/z$  190.9766) and PTU ( $[\text{M}+\text{H}]^+$ ;  $m/z$  117.0481).

## 5 Conclusion and Outlook

This dissertation aimed to utilize the technique of matrix-assisted-laser-desorption/ionization mass spectrometry imaging to get further information about the uptake, transport, distribution, and behavior of a wide range of compounds of different agrochemical classes into several crop plants.

Additional analytical and radiochemical techniques like HPLC-MS and Autoradiography were done in parallel. Different pesticides from different classes like fungicides or herbicides and several application techniques like seed treatment or foliar application showed the potential of mass spectrometry imaging to determine the successful control of pesticides.

MALDI mass spectrometry imaging has a great potential for applications to studies involving the distribution and metabolism of agrochemicals in plants and the environment. Spatial information about the uptake and systemicity of agrochemicals within a crop plant is a significant element of the successful use of such products in agriculture.

Nevertheless, technological developments are still needed for further integration of MSI to detect agrochemicals in plants. One major limitation is the sensitivity of MSI to detect small molecules ( $m/z < 500$ ) such as agrochemicals. The sensitivity is based on intrinsic ionization yields of the target analyte and/or ion suppression effects. Another factor that affected the sensitivity of the technique is adduct formation (e.g.,  $[M+H]^+$ ,  $[M+K]^+$ ,  $[M+Na]^+$ ) reducing the intensity of individual ions.

Using Fourier-transform ion cyclotron resonance (FTICR) mass spectrometer such as the solarix MRMS from Bruker Daltonics GmbH (Bremen, Germany) can improve sensitivity and dynamic range. Another concept for high ionization efficiencies is the use of laser-induced postionization (MALDI-2) (Soltwitch *et al.*, 2015, Soltwitch *et al.*, 2020).

Another limitation is the time-consuming acquisition times, depending on the laser shot frequency. The used MALDI ion sources (AP-SMALDI10; AP-SMALDI5AF, both (TransMIT GmbH, Giessen, Germany) were coupled to an orbitrap mass spectrometer and imaging experiments were performed at a laser frequency and pulse rate of 60 Hz and 500 ms for the AP-SMALDI10 interface, while the parameters were set to 100 Hz and 500 ms for the AP-SMALDI5AF interface. The injection time was fixed to 300-500 ms to record mass spectra with the highest mass resolution (Q Exactive: 140,000 @  $m/z$  200; Q Exactive HF-X: 240,000 @  $m/z$  200), leading to a scan rate of approximately 1 Hz for the AP-SMALDI10 and 1.2 Hz for the SMALDI5AF, meaning that the scan speed was 1 pixel/s or 1.6 pixel/s. The scan speed of the SMALDI5AF Q-Exactive HF-X interface can be increased to 10 pixel/s in the 2D-line mode,

but therefore the mass resolution needs to be decreased significantly (17,500 @  $m/z$  200). These low mass resolution leads to overlapping signals, which is very problematic for mass spectrometry imaging, because chromatographic separation such as HPLC-MS to separate between two narrow mass spectral peaks based on their retention time is impossible. Therefore, the 2D-line mode is only practical for measurements with a minimal mass range, where interfering ions can be excluded and not for complex spectra, which are typically recorded in MSI approaches. MALDI ion sources, coupled to time-of-flight (ToF) mass spectrometer like the rapifleX Tissuetyper series from Bruker Daltonics (Bremen, Germany) use a laser frequency of 10 kHz, which can deliver fast acquisition times up to 40 pixel/s. The ToF mass spectrometer enables mass ranges up to 1,000,000  $m/z$ , which allows e.g., intact protein analysis, but the low mass resolution (50,000) is obstructive for the analysis of small molecules (< 500 Da) such as agrochemicals. On top of that, most common MALDI instruments are coupled to time-of-flight mass spectrometer using vacuum conditions within the ion source, while orbitrap coupled instruments use atmospheric-pressure (AP) within the ion source. Studies to compare vacuum MALDI with AP-MALDI showed, that the sensitivity of vacuum MALDI can be better for the detection of peptides and proteins, but the performance of vacuum MALDI is critically affected by source gas flows, potentials, and temperature (Schneider *et al.*, 2005, Keller *et al.*, 2018). Furthermore, some MALDI matrices such as 2-mercaptobenzothiazole (MBT) are not stable under vacuum conditions. MALDI mass spectrometry imaging can successfully generate qualitative and semiquantitative data; however, quantification is a subject that needs further development. The use of quantification software tools can be used for processing of raw data using baseline correction, subtraction, denoising and spectra smoothing followed by normalization to reduce the effects of artifacts, which are caused by inhomogeneous matrix crystals, various properties of tissue structures, including various pH and salt gradients, as well as variation in the chemical background of various tissue structures (Källback *et al.*, 2012).



## 6 References

Achilladelis, B., Schwarzkoff, A., Cines, M. A study of innovation in the pesticide industry: analysis of the innovation record of an industry sector in *Res Policy* **16**, 175-212 (1987).

Agüera, A., Contreras, M., Crespo, J., Fernández-Alba, A. R. Multiresidue method for the analysis of multiclass pesticides in agricultural products by gas chromatography-tandem mass spectrometry in *Analyst* **127**, 347-354 (2002).

Alder, L., Greulich, K., Kempe, G. and Vieth, B. Residue analysis of 500 high priority pesticides: Better by GC-MS or LC-MS/MS? In *Mass Spectrom Rev* **25**, 838-865 (2006).

Anderson, P. C., Hibberd, K. A. Evidence for the Interaction of an Imidazolinone Herbicide with Leucine, Valine, and Isoleucine Metabolism in *Weed Science* **33**, 479-483 (1985).

Annangudi, S. P., Myung, K., Adame, C. A., Gilbert, J. R. MALDI-MS Imaging Analysis of Fungicide Residue Distributions on Wheat Leaf Surfaces in *Environ Sci Technol* **49**, 5579-5583 (2015).

Anastassiades, M., Scherbaum, E., Taşdelen, B., Stajnbaher, D. Recent Developments in QuEChERS Methodology for Pesticide Multiresidue Analysis in *Pesticide Chemistry, Crop Protection*, Wiley-VCH, Weinheim, 439-458 (2007).

Baker, E.A., Hayes, A. L., Butler, R.C. Physicochemical properties of agrochemicals: their effects on foliar penetration in *Pestic Sci* **34**, 167-182 (1992).

Behringer, C., Bartsch, K., Schaller, A. Safeners recruit multiple signaling pathways for the orchestrated induction of the cellular xenobiotic detoxification machinery in *Arabidopsis* in *Plant Cell Environ* **34**, 1970-1985 (2011).

Benbrook, C. M. Trends in glyphosate herbicide use in the United States and globally in *Environ Sci Eur* **28**, 3 (2016).

Bhandari, D. R., Wang, Q., Friedt, W., Spengler, B., Gottwald, S., Römpf, A. High resolution mass spectrometry imaging of plant tissues: towards a plant metabolite atlas in *Analyst* **140**, 7696-7709 (2015).

Beffa, R., Menne, H., Köcher, H. Herbicide Resistance Action Committee (HRAC): Herbicide Classification, Resistance Evolution, Survey, and Resistance Mitigation Activities in *Modern Crop Protection Compounds*, 3rd ed., Wiley-VCH, Weinheim, 5-10 (2019).

Benninghoven, A. Surface analysis by Secondary Ion Mass Spectrometry (SIMS) in *Surf Sci* **299-300**, 246-260 (1994).

Berisha, A., Dold, S., Guenther, S., Desbenoit, N., Takats, Z., Spengler, B., Römpp, A. A comprehensive high-resolution mass spectrometry approach for characterization of metabolites by combination of ambient ionization, chromatography and imaging methods in *Rapid Commun Mass Spectrom* **28**, 1779-1791 (2014).

Billeci, T. M., Stults, J. T. Tryptic Mapping of Recombinant Proteins by Matrix-Assisted Laser Desorption/Ionization Mass Spectrometry in *Anal Chem* **65**, 1709-1716 (1993).

Bjarnholt, N., Li, B., D'Alviseb, J., Janfelt, C. Mass spectrometry imaging of plant metabolites – principles and possibilities in *Nat Prod Rep* **31**, 818-837 (2014).

Boughton, B. A., Thinagaran, D., Sarabia, D., Bacic, A., Roessner, U. Mass spectrometry imaging for plant biology: a review in *Phytochem rev* **15**, 445-488 (2016).

Bouschen, W., Schulz, O., Eikel, D., Spengler, B. Matrix vapor deposition/recrystallization and dedicated spray preparation for high-resolution scanning microprobe matrix-assisted laser desorption/ionization imaging mass spectrometry (SMALDI-MS) of tissue and single cells in *Rapid Commun Mass Spectrom* **24**, 355-364 (2010).

Brazier-Hicks, M., Howell, A., Cohn, J., Hawkes, T., Hall, G., Mcindoe, E., Edwards, R. Chemically induced herbicide tolerance in rice by the safener metcamifen is associated with a phased stress response in *J Exp Bot* **71**, 411-421 (2019).

Briggs, G. G., Bromilow, R. H., Evans, A. A. Relationships between lipophilicity and root uptake and translocation of non-ionised chemicals by barley in *Pestic Sci* **13**, 495-504 (1982).

Buchberger, A. R., DeLaney, K., Johnson, J., Li, L. Mass Spectrometry Imaging: A Review of Emerging Advancements and Future Insights in *Anal Chem* **90**, 240-265 (2018).

Buchholz, A., Trapp, S. How active ingredient localization in plant tissues determines the targeted pest spectrum of different chemistries in *Pest Manag Sci* **72**, 929-939 (2016).

Burden, R. S., Cooke, D.T., Carter, G. A. Inhibitors of sterol biosynthesis and growth in plants and fungi in *Phytochemistry* **28**, 1791-1804 (1989).

Chen, Y., Allegood, J., Liu, Y., Wang, E., Cachón-González, B., Cox, T.M., Merrill, A.H., Sullards, M. C. Imaging MALDI Mass Spectrometry Using an Oscillating Capillary Nebulizer Matrix Coating System and Its Application to Analysis of Lipids in Brain from a Mouse Model of Tay–Sachs/Sandhoff Disease in *Anal Chem* **80**, 2780–2788 (2008).

Chen, Y., Liu, Y., Allegood, J., Wang, E., Cachón-González, B., Cox, T. M., Merrill, A. H., Jr, Sullards, M. C. Imaging MALDI mass spectrometry of sphingolipids using an oscillating capillary nebulizer matrix application system. *Methods in molecular biology in Methods Mol Biol* **656**, 131–146 (2010).

Chughtai, K. Heeren, R. M. A. Mass spectrometric imaging for biomedical tissue analysis in *Chem Rev* **110**, 3237-3277 (2010).

Conrath, U., Beckers, G. J. M., Langenbach, C. J. G., Jaskiewicz, M. R. Priming for Enhanced Defense in *Annu Rev Phytopathol* **53**, 97-119 (2015).

Dashevskaya, S., Horn, R., Chudobova, I., Schillberg, S., Velez, S. M. R., Capell, T., Christou, P. Abscisic acid and the herbicide safener cyprosulfamide cooperatively enhance abiotic stress tolerance in rice in *Molecular Breeding* **32**, 463-484 (2013).

De O. Silvaa, R., De Menezes, M. G. G., De Castro, R. C., De A. Nobre, C., Milhome, M. A. L., Do Nascimentoa, R. F. Efficiency of ESI and APCI ionization sources in LC-MS/MS systems for analysis of 22 pesticide residues in food matrix in *Food Chem* **297**, 124934 (2019).

Dong, Y., Li, B., Malitsky, S., Rogachev, I., Aharoni, A., Kaftan, F., Svatoš, A., Franceschi, P. Sample Preparation for Mass Spectrometry Imaging of Plant Tissues: A Review in *Front Plant Sci* **7**, 1-16 (2016).

Du, Q.S., Shi, Y. X., Li, P. F., Zhao, Z. J., Zhu, W.P., Qian, X. H., Li, B. Novel plant activators with thieno [2,3-d]-1,2,3-thiadiazole-6- carboxylate scaffold: Synthesis and bioactivity in *Chinese Chemical letters* **24**, 967-969 (2013).

Ehring, H., Karas, M., Hillenkamp, F. Role of photoionization and photochemistry in ionization processes of organic molecules and relevance for matrix-assisted laser desorption ionization mass spectrometry in *Organic Mass Spectrometry* **27**, 472-480 (1992).

Ellis, S. R., Soltwisch, J., Heeren, R. M. Time-Resolved Imaging of the MALDI Linear-TOF Ion Cloud: Direct Visualization and Exploitation of Ion Optical Phenomena Using a Position- and Time-Sensitive Detector in *J Am Soc Mass Spectrom* **25**, 809-819 (2014).

Fernández, R., Garate, J., Martín-Saiz, L., Galetich, I., Fernández, J. A. Matrix Sublimation Device for MALDI Mass Spectrometry Imaging in *Anal Chem* **91**, 803–807 (2019).

Forster, W. A., Kimberley, M. O. The contribution of spray formulation component variables to foliar uptake of agrochemicals in *Pest Manag Sci* **71**, 1324-1334 (2015).

Frenich, A. G., Salvador, I. M., Vidal, J.L. M., Lopez-Lopez, T. Determination of multiclass pesticides in food commodities by pressurized liquid extraction using GC–MS/MS and LC–MS/MS in *Anal Bioanal Chem* **383**, 1106-1118 (2005)

Friesen, W. L., Schultz, B. J., Destino, J. F., Alivio, T. E., Steet, J. R., Banerjee, S., Wood, T. D. Two-dimensional graphene as a matrix for MALDI imaging mass spectrometry in *J Am Soc Mass Spectrom* **26**, 1963–1966 (2015).

Gentili, A., Marchese, S., Perret, D. MS techniques for analyzing phenols, their metabolites and transformation products of environmental interest in *Trends Anal Chem* **27**, 888– 903 (2008).

Gerbig, S., Brunn, H. E., Spengler, B., Schulz, S. Spatially resolved investigation of systemic and contact pesticides in plant material by desorption electrospray ionization mass spectrometry imaging (DESI-MSI) in *Anal Bioanal Chem* **407**, 7379–7389 (2015).

Gerwick, B. C., Sparks, T. C. Natural products for pest control: an analysis of their role, value and future in *Pest Manag Sci* **70**, 1169-1185 (2014).

Giampà, M., Lissel, M. B., Patschkowski, T., Fuchser, J., Hans, V. H., Gembruch, O., Bednarza, H., Niehaus, K. Maleic anhydride proton sponge as a novel MALDI matrix for the visualization of small molecules (<250 m/z) in brain tumors by routine MALDI ToF imaging mass spectrometry in *Chem Commun* **52**, 9801-9804 (2016).

Giannakopoulos, G., Dittgen, J., Schulte, W., Zoellner, P., Helmke, H., Lagojda, A., Edwards, R. Safening activity and metabolism of the safener cyprosulfamide in maize and wheat in *Pest Manag Sci* **76**, 3413-3422 (2020).

Glückmann, M., Pfenninger, A., Krüger, R., Thierolf, M., Karasaa, M., Horneffer, V, Hillenkamp, F., Strupat, K. Mechanisms in MALDI analysis: surface interaction or incorporation of analytes in *Int J Mass Spectrom* **210-211**, 121-132 (2001).

Godfray, H. C. J., Beddington, J. R., Crute, I. R., Haddad, L., Lawrence, D., Muir, J. F., Pretty, J., Robinson, S., Thomas, S. M., Toulmin, C. Food security: the challenge of feeding 9 billion people in *Science* **327**, 812-818 (2010).

Gozzo, F., Faoro, F. Systemic acquired resistance (50 years after discovery): moving from the lab to the field in *J Agr Food Chem* **61**, 12473-12491 (2013).

Green, J. M. The rise and future of glyphosate and glyphosate-resistant crops in *Pest Manag Sci* **74**, 1035-1039 (2018).

Gross, A. D., Coats, J. R., Duke, S. O., Seiber, J. N. Biopesticides: State of the Art and Future Opportunities in *J Agric Food Chem* **62**, 11613–11619 (2014).

Guenther, S., Koestler, M., Schulz, O., Spengler, B. Laser spot size and laser power dependence of ion formation in high resolution MALDI imaging in *International Journal of Mass Spectrometry* **294**, 7-15 (2010).

Gullino, M. L., Tinivella, F., Garibaldi, A., Kemmitt, G. M., Bacci, L., Sheppard, B. Manozeb: past, present and future in *Plant Dis* **29**,1076-1087 (2010).

Harijati, N., Azrianingsih, r., Prawaningtyas, E. A. the Study of Anatomy and Fiber Banana Leaf as a Potential Wrapping **4**, 1461-1465 (2013).

Haynes, C., Kirkwood R. C. Studies on the mode of action of diflufenican in selected crop and weed species: Basis of selectivity of pre- and early post-emergence applications in Pestic Sci **35**, 161-164 (1992).

Hermann, D., Stenzel, K. FRAC Mode-of-action Classification and Resistance Risk of Fungicides in Modern Crop Protection Compounds, 3rd ed., Wiley-VCH, Weinheim, 589-607 (2019).

Hogendoorn, E., Zoonen, P. Recent and future developments of liquid chromatography in pesticide trace analysis in J Chromatogr A **892**, 435-453 (200).

Horneffer, V., Dreisewerd, K., Lüdemann, H.C., Hillenkamp, F., Läge, M., Strupat, K. Is the incorporation of analytes into matrix crystals a prerequisite for matrix-assisted laser desorption/ionization mass spectrometry? A study of five positional isomers of dihydroxybenzoic acid in Int J Mass Spectrom **185-187**, 859–870 (1999).

Jackson, S. N., Mishra, S., Murray, K. K. On-line laser desorption/ionization mass spectrometry of matrix-coated aerosols in Rapid Commun Mass Spectrom **18**, 2041-2045 (2004).

Jeanmart, S., Edmunds, A. J. F., Lamberth, C., Pouliot, M. Synthetic approaches to the 2010-2014 new agrochemicals in Bioorg Med Chem **24**, 317-341 (2016).

Jeschke, P. Progress of modern agricultural chemistry and future prospects in Pest Manag Sci **72**, 433-455 (2016).

Jeschke, P., Witschel, M., Krämer, W., Schirmer, U. Modern Crop Protection Compounds. 3rd Edition, Wiley-VCH, Weinheim (2019).

Leopold, J., Popkova Y., Engel K. M., Schiller, J. Recent Developments of Useful MALDI Matrices for the Mass Spectrometric Characterization of Lipids in Biomolecules **8**, 173 (2018).

Kadam, S. U., Tiwari, B. K., O'Donnell, C. P. Application of Novel Extraction Technologies for Bioactives from Marine Algae in J Agric Food Chem **61**, 4667-4675 (2013).

Källback, P., Shariatgorji, M., Nilsson, A., Andrén, P. A. Novel mass spectrometry imaging software assisting labeled normalization and quantitation of drugs and neuropeptides directly in tissue sections in J Proteom **75**, 4941-4951 (2012).

Kaletaş, B. K., van der Wiel, I. M., Stauber, J., Dekker, L. J., Güzel, C., Kros, J.M., Luider, T. M., Heeren, R. M. A. Sample preparation issues for tissue imaging by imaging MS in Proteomics **9**, 2622-2633 (2009).

Karas, M., Bachmann, D., Hillenkamp, F. Matrix-assisted ultraviolet laser desorption of non-volatile compounds in *Int J Mass Spectrom Ion Process* **78**, 53-68 (1987).

Karas, M., Glückmann, M., Schäfer, J. Ionization in matrix-assisted laser desorption/ionization: singly charged molecular ions are the lucky survivors in *J Mass Spectrom* **35**, 1-12 (2000).

Karley, A. J., White, P. J. Moving cationic minerals to edible tissues: potassium, magnesium, calcium in *Curr Opin Plant Biol* **12**, 291-298 (2009).

Kaspar, S. Peukert, M., Svatos, A., Matros, A., Moch, H. P. MALDI-imaging mass spectrometry – An emerging technique in plant biology in *Proteomics* **11**, 1840-1850 (2011).

Kazos, E. A., Stalikas, C. D., Nanos, C. G., Konidari, C. N. Determination of dithiocarbamate fungicide propineb and its main metabolite propylenethiourea in airborne samples in *Chemosphere* **68**, 2104-2110 (2007).

Keller, C., Maeda, J., Jayaraman, D., Chakraborty, S., Sussmann, M. R., Harris, J. M., Ane, J., Li, L. Comparison of Vacuum MALDI and AP-MALDI Platforms for the Mass Spectrometry Imaging of Metabolites Involved in Salt Stress in *Medicago truncatula* in *Front Plant Sci* **9**, 1238 (2018).

Kirkwood, R. C. Recent developments in our understanding of the plant cuticle as a barrier to the foliar uptake of pesticides in *Pestic Sci* **55**, 69-77 (1999).

Klittich, C. J. R., Green, F. R., Ruiz, J.M., Weglarz, T., Blakeslee, B. A. Assessment of fungicide systemicity in wheat using LC-MS/MS in *Pest Manag Sci* **64**, 1267-1277 (2008).

Kompauer, M., Heiles, S., Spengler, B. Atmospheric pressure MALDI mass spectrometry imaging of tissues and cells at 1.4-mm lateral resolution in *Nature Methods* **14**, 90-96 (2017).

Kompauer, M., Heiles, S., Spengler, B. Autofocusing MALDI mass spectrometry imaging of tissue sections and 3D chemical topography of nonflat surfaces in *Nature Methods* **14**, 1156-1158 (2017).

Korte, A. R., Yandea-Nelson, M. D., Nikolau, B. J., Lee, Y. J. Subcellular-level resolution MALDI-MS imaging of maize leaf metabolites by MALDI-linear ion trap-Orbitrap mass spectrometer in *Anal Bioanal Chem* **407**, 2301-2309 (2015).

Kraehmer, H., Laber, B., Rosinger, C., Schulz, A. Herbicides as Weed Control Agents: State of the Art: I. Weed Control Research and Safener Technology: The Path to Modern Agriculture in *Plant Physio* **166**, 1119-1131 (2014).

Krause, J., Stoeckli, M., Schlunegger, U.P. Studies on the Selection of New Matrices for Ultraviolet Matrix-assisted Laser Desorption/Ionization Time-of-flight Mass Spectrometry in Rapid Commun Mass Spectrom **10**, 1927-1933 (1996).

Krieger, R. Hayes' Handbook of Pesticide Toxicology. 3rd Edition, Academic Press, Cambridge (2010).

Kruve, A., Kaupmees, K., Liigand, J., Oss, M., Leito, I. Sodium adduct formation efficiency in ESI source in J Mass Spectrom, **6**, 695–702 (2013).

Lamberth, C. Pyrazole chemistry in crop protection in Heterocycles **71**, 1467-1502 (2007).

Lamshöft, M, Gao, Z., Ressler, H., Schriever, C., Sur, R., Sweeney, P., Webb, S., Zillgens, B., Reitz, M. U. Evaluation of a novel test design to determine uptake of chemicals by plant roots in Sci Total Environ **613-614**, 10-19 (2018).

Laugesen, S., Roepstorff, P. Combination of Two Matrices Results in Improved Performance of MALDI MS for Peptide Mass Mapping and Protein Analysis in J Am Soc Mass Spectrom **14**, 992–1002 (2003).

Lee, H., León, J, Raskin, I. Biosynthesis and metabolism of salicylic acid in Proc Natl Acad Sci **92**, 4076-4079 (1995).

Lee, Y. J., Perdian, D. C., Song, Z., Yeung, E. S., Nikolau, B. Use of mass spectrometry for imaging metabolites in planta in The Plant Journal **70**, 81-95 (2012).

Lehotay, S. J. Supercritical fluid extraction of pesticides in foods in J Chromatogr A **785**, 289-312 (1997).

Leopold, J., Popkova, Y., Engel, K. M., Schiller, J. Recent Developments of Useful MALDI Matrices for the Mass Spectrometric Characterization of Lipids in Biomolecules **13**, 173 (2018).

Li, Q., Zhang, Y., Liu, Y., He, H., Han, M., Li, Y., Zeng, M., Wang, X. Recent advances in matrix-assisted laser desorption/ionisation mass spectrometry imaging (MALDI-MSI) for in situ analysis of endogenous molecules in plants in Phytocheml Anal **29**, 351-364 (2018).

Liebl, H. SIMS Instrumentation and Imaging Techniques in Scanning 3, 79-89 (1980).

Liu, N., Dong, F., Liu, X., Xu, J., Li, Y., Han, Y., Zhu, Y., Cheng, Y., Chen, Z., Tao, Y., Zheng, Y. Effect of household canning on the distribution and reduction of thiophanate-methyl and its metabolite carbendazim residues in tomato in Food Contr **43**, 115-120 (2014).

Lorsbach, B. A., Sparks, T. C., Cicchillo, R. M., Garizi, N. V., Hahn, D. R., Meyer, K. G. Natural products: a strategic lead generation approach in crop protection discovery in Pest Manag Sci **75**, 2301-2309 (2019).

Loso, M. R., Garizi, N., Hegde, V. B., Hunter, J., Sparks, T. C. Lead generation in crop protection research: a portfolio approach to agrochemical discovery in *Pest Manag Sci* **73** 678-685 (2017).

MacBean, C. *The Pesticide Manual: A World Compendium*, British Crop Protection Council, Hampshire, 2012.

Maienfisch, P., Edmunds, A. J. F. Thiazole and isothiazole ring-containing compounds in crop protection in *Adv Heterocycl Chem* **121**, 35-88 (2017).

Malik, A. K., Faubel, W. Methods of analysis of dithiocarbamate pesticides: A review in *Pesticide Science* **55**, 965-970 (1999).

Mullen, A.K., Clench, M.R., Crosland, S., Sharples, K.R. Determination of agrochemical compounds in soya plants by imaging matrix-assisted laser desorption/ionisation mass spectrometry in *Rapid Commun Mass Spectrom* **19**, 2507-2516 (2005).

Mullins, J. W. Imidacloprid. A new nitroguanidine insecticide in *Am Chem Soc Symp Series* **254**, 183-198 (1993).

Nauen, R., Slater, R., Sparks, T. C., Elbert, A., Mccaffrey, A. *RAC: Insecticide Resistance and Mode-of-action Classification of Insecticides in Modern Crop Protection Compounds*, 3rd ed., Wiley-VCH, Weinheim, 995-1013 (2019).

Nemes, P., Barton, A. A., Li, Y., Vertes, A. Ambient Molecular Imaging and Depth Profiling of Live Tissue by Infrared Laser Ablation Electrospray Ionization Mass Spectrometry in *Anal Chem* **80**, 4575-4582 (2008).

Nimesh, S., Mohottalage, S., Vincent, R., Kumarathasan, P. Current Status and Future Perspectives of Mass Spectrometry Imaging in *Int J Mol Sci* **14**, 11277-11301 (2013).

Norris, J. L., Caprioli, R. M. Analysis of Tissue Specimens by Matrix-Assisted Laser Desorption/Ionization Imaging Mass Spectrometry in Biological and Clinical in *Chem Rev* **113**, 2309–2342 (2013).

Ogawa, M., Kadowaki, A., Yamada, T., Kadooka, O. Applied development of a novel fungicide isotianil (Stout) in *Sumitomo Kagaku* **1**, 1–15 (2011).

O'Rourke, M.B., Djordjevic, S. P., Padula, M. P. The quest for improved reproducibility in MALDI mass spectrometry in *Mass Spectrom Rev* **37**, 217–228 (2018).

Pérez, S., Petrovic, M., Barceló, D. Analyzing transformation products of synthetic chemicals. *Handb. Environ. Chem. 2(Part P)*: 43– 81 (2009).



Vargas-Pérez, M., González, F. J. E., Frenich, A. G. Dissipation and residue determination of fluopyram and its metabolites in greenhouse crops in *J Sci Food Agric* **100**, 4826-4833 (2020).

Peukert, M., Matros, A., Lattanzio, G., Kaspar, S., Abadia, J., Mock, H. P. Spatially resolved analysis of small molecules by matrix-assisted laser desorption/ionization mass spectrometric imaging (MALDI-MSI) in *New Phytol* **193**, 806–815 (2012).

Pirkl, A., Soltwisch, J., Draude, F., Dreisewerd, K. Infrared Matrix-Assisted Laser Desorption/Ionization Orthogonal-Time-of-Flight Mass Spectrometry Employing a Cooling Stage and Water Ice As a Matrix in *Anal Chem* **84**, 5669-5676 (2012).

Qin, L., Zhang, Y., Liu, Y., He, H., Han, M. Li, Y., Zeng, M., Wang, X. Recent advances in matrix-assisted laser desorption/ionisation mass spectrometry imaging (MALDI-MSI) for in situ analysis of endogenous molecules in plants in *Phytochem Anal* **29**, 351-364 (2018).

Radjenovic, J., Petrovic, M., Barcelo, D. Complementary mass spectrometry and bioassays for evaluating pharmaceutical-transformation products in treatment of drinking water and wastewater in *Trends Anal Chem* **28**, 562– 580 (2009).

Richter, B. E., Jones, B. A., Ezzell, J. L., Porter, N. L., Avdalovic, N, Pohl, C. Accelerated Solvent Extraction: A Technique for Sample Preparation in *Anal Chem* **68**, 1033-1039 (1996).

Riechers, D. E., Kreu, K., Zhang, Q. Detoxification without Intoxication: Herbicide Safeners Activate Plant Defense Gene Expression in *Plant Physio* **153**, 3-13 (2010).

Robatscher, P., Eisenstecken, D., Innerebner, G., Roschatt, C., Raifer, B., Rohregger, H., Hafner, H., Oberhuber, M. 3-Chloro-5-trifluoromethylpyridine-2-carboxylic acid, a Metabolite of the Fungicide Fluopyram, Causes Growth Disorder in *Vitis vinifera* in *J Agric Food Chem* **67**, 7223-7231 (2019).

Robichaud, G., Garrard, K. P., Barry, J. A., Muddiman, D. C. MSiReader: an open-source interface to view and analyze high resolving power MS imaging files on Matlab platform in *J Am Soc Mass Spectrom* **24**, 718-721 (2013).

Robinson, S., Warburton, K., Seymour, M., Clench, M., Thomas-Oates, J. Localization of water-soluble carbohydrates in wheat stems using imaging matrix-assisted laser desorption ionization mass spectrometry in *New Phytologist* **173**, 438-444 (2007).

Rosinke, B., Strupat, K., Hillenkamp, F., Rosenbusch, J., Dencher, N., Krüger, U., Galla, H. Matrix-assisted laser desorption/ionization mass spectrometry (MALDI-MS) of membrane proteins and non-covalent complexes in *J Mass Spectrom* **30**, 1462-1498 (1995).

Rost, T. L., Reynolds, T. Reversal of Chlorsulfuron-Induced Inhibition of Mitotic Entry by Isoleucine and Valine in *Plant Physio* **77**, 481-482 (1985).

Shaner, D.L. The impact of glyphosate-tolerant crops on the use of other herbicides and on resistance management in *Pest Manag Sci* **56**, 320-326 (2000).

Schneider, B. B., Lock, C., Covey, T.R. AP and vacuum MALDI on a QqLIT instrument in *J Am Soc Mass Spectrom* **16**, 176–182 (2005).

Schwartz, S. A., Reyzer, M. L., Caprioli, R. M. Direct tissue analysis using matrix-assisted laser desorption/ionization mass spectrometry: practical aspects of sample preparation in *J Mass Spectrom* **37**, 699-708 (2003).

Shroff, R., Svatoš, A. Proton Sponge: A Novel and Versatile MALDI Matrix for the Analysis of Metabolites Using Mass Spectrometry in *Analytical Chemistry* **81**, 7954-7959 (2009).

Simon-Delso, N., Amaral-Rogers, V., Belzunces, L.P., Bonmatin, J. M., Chagnon, M., Downs, C., Furlan, L., Gibbons, D. W., Giorio, C., Girolami, V., Goulson, V., Kreuzweiser, D. P., Krupke, C. H., Liess, M., Long, E., McField, M., Mineau, P., Mitchell, E. A. D., Morissey, C. A., Noome, D. A., Pisa, L., Settele, J., Stark, J. D., Tapparo, A., Van Dyck, H., Van Praagh, J., Van der Sluijs, J. P., Whitehorn, P. R., Wiemers, M. Systemic insecticides (neonicotinoids and fipronil): trends, uses, mode of action and metabolites in *Environ Sci Pollut Res* **22**, 5–34 (2015).

Soltwisch, J., Göritz, G., Jungmann, J. H., Kiss, A., Smith, D. F., Ellis, S. R., Heeren, R. M. A. MALDI Mass Spectrometry Imaging in Microscope Mode with Infrared Lasers: Bypassing the Diffraction Limits in *Anal Chem* **86**, 321-325 (2014).

Soltwisch, J., Ketting, H., Vens-Cappell, S., Wiegelmann, M., Müthing, J., Dreisewerd, K. Mass spectrometry imaging with laser-induced postionization in *Science* **348**. 211-215 (2015).

Soltwisch, J., Heijs, B., Koch, A., Vens-Cappell, S., Höhndorf, J., Dreisewerd, K. MALDI-2 on a Trapped Ion Mobility Quadrupole Time-of-Flight Instrument for Rapid Mass Spectrometry Imaging and Ion Mobility Separation of Complex Lipid Profiles in *Anal Chem* **92**, 8697-8703 (2020).

Sparks, T. C., Insecticide discovery: an evaluation and analysis in *Pestic Biochem Physiol* **107**, 8-17 (2013).

Sparks, T.C., Wessels, F. J., Lorsbach, B. A., Nugent, B. M., Watson, G. B. The new age of insecticide discovery-the crop protection industry and the impact of natural products in *Pestic Biochem Phys* **191**, 12-22 (2019).

Swale, D. R. Perspectives on new strategies for the identification and development of insecticide targets in *Pestic Biochem Phys* **161**, 23-32 (2019).

Swor, C. D., Zakharov, L. N., Tyler, D. R. A Colorimetric Proton Sponge in *J Org Chem* **75**, 6977–6979 (2010).

Sugiura, Y., Shimma, S., Setou, M. Thin sectioning improves the peak intensity and signal-to-noise ratio in direct tissue mass spectrometry in *J Mass Spectrom Soc Jpn* **54**, 45–48 (2006).

Szájli, E., Fehér, T., Medzihradszky, K. F. Investigating the quantitative nature of MALDI-TOF MS in *Mol Cell Proteomics* **7**, 2410–2418 (2008).

Taillebois, E., Cartereau, A., Jones, A. K., Thany, S. H. Neonicotinoid insecticides mode of action on insect nicotinic acetylcholine receptors using binding studies in *Pestic Biochem Physiol* **151**, 59-66 (2018).

Thind, T. S., Hollomon, D. W. Thiocarbamate fungicides: reliable tools in resistance management and future outlook in *Pest Manag Sci* **74**, 1547-1551 (2018).

Tölgyesi, L., Kele, P., Torkos, K. Determination of propylenethiourea, the main metabolite of propineb, in tomato by HILIC-MS in *Chromatographia* **71**, 75-80 (2010).

Toquin, V., Sirven, C., Assmann, L., & Sawada, H. Host defense inducers. *Modern Crop Protection Compounds* **1**, 909-928 (2011).

Umetsu, N., Shirai, Y. Development of novel pesticides in the 21st century in *J Pestic Sci* **45**, 54-74 (2020).

Velickovic, D., Herdier, H., Philippe, G., Marion, D., Rogniaux, H., Bakan, B. Matrix-assisted laser desorption/ionization mass spectrometry imaging: a powerful tool for probing the molecular topology of plant cutin polymer in *The Plant Journal* **80**, 926–935 (2014).

Veloukas, T., Karaoglanidis, G. S. Biological activity of the succinate dehydrogenase inhibitor fluopyram against *Botrytis cinerea* and fungal baseline sensitivity in *Pest Manag Sci* **68**, 858-864 (2012).

Weißflog, J., Svatoš, A. 1,8-Di(piperidinyl)-naphthalene – rationally designed MAILD/MALDI matrix for metabolomics and imaging mass spectrometry in *RSC Adv* **6**, 75073-75081 (2016).

Yoshioka, N., Asano, M., Kuse, A., Mitsuhashi, T., Nagasaki, Y., Ueno, Y. Rapid determination of glyphosate, glufosinate, bialaphos, and their major metabolites in serum by liquid chromatography-tandem mass spectrometry using hydrophilic interaction chromatography in *J Chromatogr A* **1218**, 3675-3680 (2011).

Xu, L., Zhu, H., Ozkan, H. E., Bagley, W. E., Krause, C. R. Droplet evaporation and spread on waxy and hairy leaves associated with type and concentration of adjuvants in *Pest Manag Sci* **67**, 842-851 (2011).

Xu, L., Zhu, H.m Ozkan, H. E., Thistle, H. W. Evaporation rate and development of wetted area of water droplets with and without surfactant at different locations on waxy leaf surfaces in *Biosystems Engineering* **106**, 58-67 (2010).

Zhang, Y., Lorsbach, B. A., Castetter, S., Lambert, W. T., Kister, J., Wang, N. X., Klittich, C. J. R., Roth, J., Sparks, T. C., Loso, M. R. Physicochemical property guideline for modern agrochemicals in *Pest Manag Sci* **74**, 1979-1991 (2018).

Zhou, D., Guo, S., Zhang, M., Liu, Y., Chen, T., Li, Z. Mass spectrometry imaging of small molecules in biological tissues using graphene oxide as a matrix. *Anal Chim Acta* **962**, 52-59 (2017).

## Appendix

### Abbreviations

$\alpha$ -HCCA	$\alpha$ -Cyano-4-hydroxycinnamic acid
AChE	acetylcholinesterase
AGC	Automatic gain control
a.i.	Active ingredient
ALS	Acetolactate synthase
AP	Atmospheric pressure
BBCH	Biologische Bundesanstalt, Bundessortenamt und Chemische Industrie
BCS	Bayer Crop Science
CMC	Carboxymethyl cellulose
CI	Chemical ionization
CID	Collision-induced-decay
CRM	Charge residue model
CSA	Cyprosulfamide
DESI	Desorption electrospray ionization
DHB	2,5-Dihydroxybenzoic acid
DMAN	<i>N,N,N',N'</i> -Tetramethyl-1,8-naphthalenediamine
EPSPS	5-enolpyruvylshikimate-3-phosphate
ESI	Electrospray ionization
FRAC	Fungicide Resistance Action Committee
FT-ICR	Fourier transform ion cyclotron resonance
FWHM	Full Width at Half Maximum
GABA	Gamma-aminobutyric acid
glc	Glucose
gluc	Glucuronic acid
glyc	Glycoside
HCD	Higher-energy collisional dissociation
HESI	Heated- Electrospray ionization
HILIC	Hydrophilic interaction liquid chromatography
HPLC	High-performance liquid chromatography
HR	High resolved
HRAC	Herbicide Resistance Action Committee
HR-MS	High-resolution mass spectrometry
ICCD	Intensified charge-coupled device

IEM	Ion evaporation model
IR	Infrared
IRAC	Insecticide Resistance Action Committee
IT	Injection time
LC	Liquid-chromatography
LDI	Laser-Desorption/Ionization
LLE	Liquid-liquid extraction
LSC	Liquid scintillation counting
MALDI	Matrix-assisted Laser-Desorption/Ionization
MeOH	Methanol
MS	Mass spectrometry
MSI	Mass spectrometry Imaging
MS/MS	Tandem mass spectrometry
<i>m/z</i>	Mass-to-charge ratio
<i>n</i> AChR	Nicotinic acetylcholine receptor
NMR	Nuclear magnetic resonance
OCT	Optimum cutting compound
PDS	Phytoene desaturase
<i>pK<sub>b</sub></i>	Base dissociation constant
<i>pK<sub>s</sub></i>	Acid dissociation constant
<i>P<sub>ow</sub></i>	Partition coefficient
PPI	Photo-ionization
ppm	Parts per million
PPP	Plant protection product
PUF	Plant Uptake Factor
Q	Quadrupole
QuEChERS	quick, easy, cheap, effective, rugged, and safe
R <sup>2</sup>	Coefficient of determination
RD	Radio detection
SAR	Systemic acquired resistance
SC	Suspension concentrate
SDH	Succinate dehydrogenase
SE	Solvent extraction
SIMS	Secondary ion mass spectrometry
SLE	Solid-liquid extraction
SPE	Solid-phase extraction
TCM	Thiencarbazone-methyl

$t_R$	Retention time
TIC	Total ion current
TOF	Time-of-flight mass spectrometer
UV	Ultraviolet
3-NBA	3-Nitrobenzyl alcohol
@CID	At the collision energy of





Supplementary Figures



Figure 65. Experimental setup for root uptake of isotianil in wheat (*Triticum*) using a hydroponic system.



**Figure 66.** Tomato plants (*Solanum lycopersicum*) after acclimatization in the hydroponic test system.



**Figure 67.** Experimental setup for root uptake of  $^{14}\text{C}$ -labeled DCIT-acid in tomato (*Solanum lycopersicum*) using a hydroponic system.



**Figure 68.** Single droplet application of isotianil on tomato (*Solanum lycopersicum*).



**Figure 69.** Leaf application of isotianil and DCIT-acid on tomato (*Solanum lycopersicum*).



**Figure 70.** Tomato plant (*Solanum lycopersicum*) treated with DCIT-acid at day of application.



**Figure 71.** Leaf application of isotianil and DCIT-acid on banana (*Musa*).

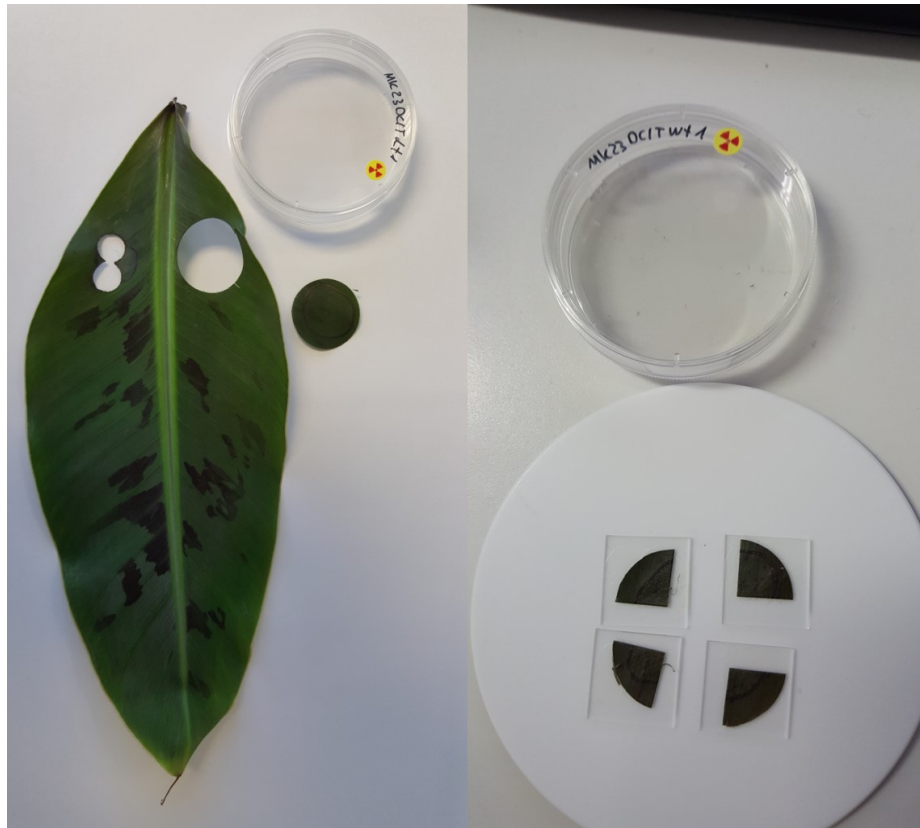


**Figure 72.** Sample preparation for MALDI MSI experiments of banana leaf (*Musa*) treated with  $^{14}\text{C}$ -labeled DCIT-acid.



**Figure 73.** Grape vine (*Vitis vinifera*) plants for quantification of fluopyram at t6 (259 days after application, fruits begin to swell).



**Figure 74.** Single grape vine (*Vitis vinifera*) plant for quantification of fluopyram at t2 (49 days after application, 50% leaves fallen).



**Figure 75.** Dry grape vine (*Vitis vinifera*) plant tissues for quantification of fluopyram before extraction.



**Figure 76.** Maize (*Zea mays*) treated with cyprosulfamide and Thiencarbazon-methyl on different leaves.



**Figure 77.** Single maize leaf (*Zea mays*) treated with cyprosulfamide.





Figure 78. Single droplet application of propineb on tomato (*Solanum lycopersicum*).

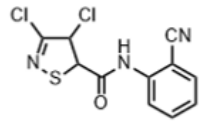


**Figure 79.** Optical image of tomato leaf (*Solanum lycopersicum*) with single droplet application of Propineb. Propineb as a WG70 formulation produces a homogenous layer on the tissue (left). Propineb mixed with HCCA produces a mesh of crystals on the tissue (right).

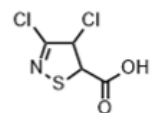


## Supplementary Tables

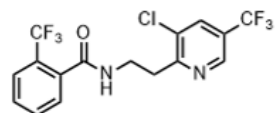
**Table 17.** Physicochemical properties of isotianil.

	Common name	Isotianil
	IUPAC name	3,4-dichloro-2`-cyano-1,2-thiazole-5-carboxanilide
	Molecular formula	C <sub>11</sub> H <sub>5</sub> Cl <sub>2</sub> N <sub>3</sub> OS
	Molecular mass	298.15 g/mol
	LogP <sub>ow</sub>	2.96 (25 °C)
	Solubility in water	0.5 mg/L (25 °C)
	FRAC Code	P3

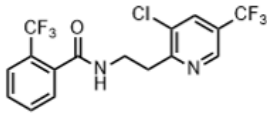
**Table 18.** Physicochemical properties of DCIT-acid.

	Common name	DCIT-acid
	IUPAC name	3,4-dichloro-1,2-thiazole-5-carboxylic acid
	Molecular formula	C <sub>4</sub> HCl <sub>2</sub> NO <sub>2</sub> S
	Molar mass	198.01 g/mol
	LogP <sub>ow</sub>	2.15 (25 °C)
Solubility in water	5 g/L (20 °C)	

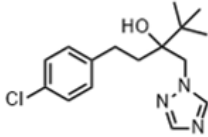
**Table 19.** Physicochemical properties of fluopyram.

	Common name	Fluopyram
	IUPAC name	N-[2-[3-chloro-5-(trifluoromethyl)-2-pyridinyl]ethyl]-2-(trifluoromethyl)benzamide
	Molecular formula	C <sub>16</sub> H <sub>11</sub> ClF <sub>6</sub> N <sub>2</sub> O
	Molar mass	397.72 g/mol
	LogP <sub>ow</sub>	-0.75 (25 °C)
	Solubility in water	16 mg/L (20 °C)
	FRAC Code	7

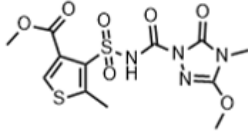
**Table 20.** Physiochemical properties of PCA.

	Common name	PCA
	IUPAC name	3-chloro-5-(trifluoromethyl)pyridine-2-carboxylic acid
	Molecular formula	C <sub>7</sub> H <sub>3</sub> ClF <sub>3</sub> N <sub>2</sub> O
	Molar mass	225.55 g/mol
	LogP <sub>ow</sub>	-0.75 (25 °C)
	Solubility in water	16 mg/L (20 °C)

**Table 21.** Physiochemical properties of tebuconazole.

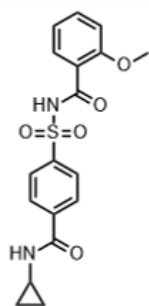
	Common name	Tebuconazole
	IUPAC name	1-(4-chlorophenyl)-4,4-dimethyl-3-(1,2,4-triazol-1-ylmethyl)pentan-3-ol
	Molecular formula	C <sub>16</sub> H <sub>22</sub> ClN <sub>3</sub> O
	Molar mass	307.82 g/mol
	LogP <sub>ow</sub>	3.70 (25 °C)
	Solubility in water	36.0 mg/L (20 °C)
FRAC Code	3	

**Table 22.** Physiochemical properties of thiencarbazon-methyl.

	Common name	Thiencarbazon-methyl
	IUPAC name	Methyl 4-[(3-methoxy-4-methyl-5-oxo-1,2,4-triazole-1-carbonyl)sulfamoyl]-5-methylthiophene-3-carboxylate
	Molecular formula	C <sub>12</sub> H <sub>14</sub> N <sub>4</sub> O <sub>7</sub> S <sub>2</sub>
	Molar mass	390.39 g/mol
	LogP <sub>ow</sub>	-1.98 (24 °C)
	Solubility in water	436 mg/L (20 °C)
HRAC Group	B	

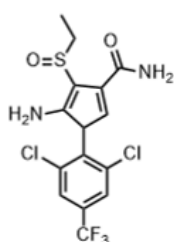
**Table 23.** Physiochemical properties of cyprosulfamide.

Common name	Cyprosulfamide
-------------	----------------



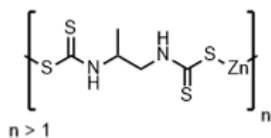
IUPAC name	<i>N</i> -[4-(cyclopropylcarbamoyl)phenylsulfonyl]- <i>o</i> -anisamide
Molecular formula	C <sub>18</sub> H <sub>18</sub> N <sub>2</sub> O <sub>5</sub> S
Molar mass	374.41 g/mol
LogP <sub>ow</sub>	-0.8 (25 °C)
Solubility in water	6.2 mg/L (20 °C)

**Table 24.** Physiochemical properties of ethiprole.



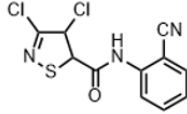
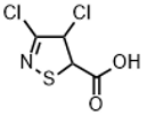
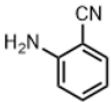
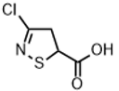
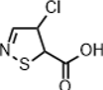
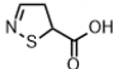
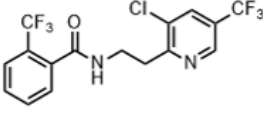
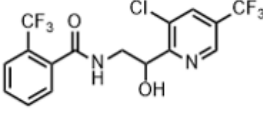
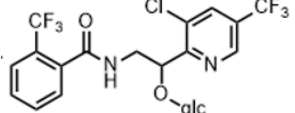
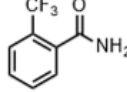
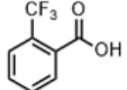
Common name	Ethiprole
IUPAC name	5-amino-1-[2,6-dichloro-4-(trifluoromethyl)phenyl]-4-ethylsulfanylpyrazole-3-carbonitrile
Molecular formula	C <sub>13</sub> H <sub>9</sub> Cl <sub>2</sub> F <sub>3</sub> N <sub>4</sub> OS
Molar mass	397.20 g/mol
LogP <sub>ow</sub>	1.99 (25 °C)
Solubility in water	<0.01 g/L (20 °C)
IRAC Group	2B

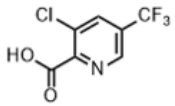
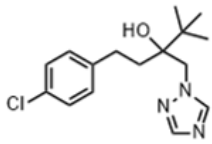
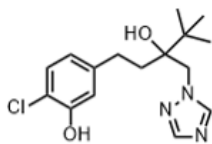
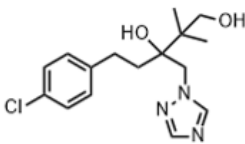
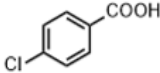
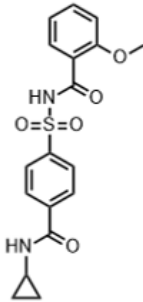
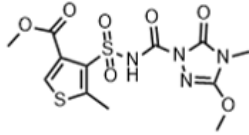
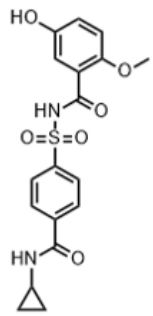
**Table 25.** Physiochemical properties of propineb.

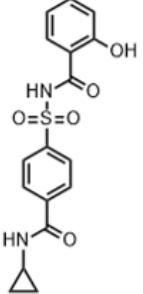
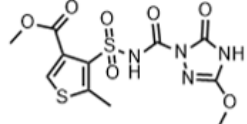
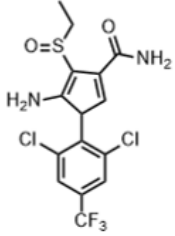
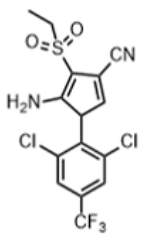
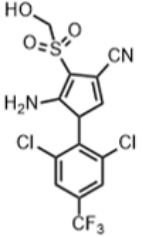
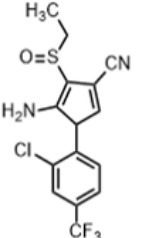


Common name	Propineb
IUPAC name	Polymeric zinc 1,2-propylenebis(dithiocarbamate)
Molecular formula	(C <sub>5</sub> H <sub>8</sub> N <sub>2</sub> Zn) <sub>n</sub>
Molar mass	289.8 g/mol (monomer)
LogP <sub>ow</sub>	-0.26 (25 °C)
Solubility in water	< 0.01 g/L (20 °C)
FRAC Code	M03

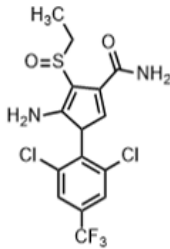
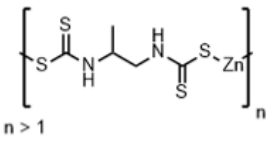
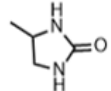
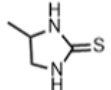
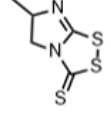
**Table 26.** List of agrochemicals and metabolites.

Compound	Sum formula	[M+H] <sup>+</sup>	Structure
Isotianil	C <sub>11</sub> H <sub>5</sub> Cl <sub>2</sub> N <sub>2</sub> OS	297.96031	
DCIT-acid	C <sub>4</sub> HCl <sub>2</sub> NO <sub>2</sub> S	197.91778	
Anthranilonitrile	C <sub>7</sub> H <sub>6</sub> N <sub>2</sub>	119.06037	
3-chloro-1,2-thiazole-5-carboxylic acid	C <sub>4</sub> H <sub>2</sub> ClNO <sub>2</sub> S	163.95675	
4-chloro-1,2-thiazole-5-carboxylic acid	C <sub>4</sub> H <sub>2</sub> ClNO <sub>2</sub> S	163.95675	
1,2-thiazole-5-carboxylic acid	C <sub>4</sub> H <sub>3</sub> NO <sub>2</sub> S	129.99573	
Fluopyram	C <sub>16</sub> H <sub>11</sub> ClF <sub>6</sub> N <sub>2</sub> O	397.05369	
Fluopyram-7-hydroxy	C <sub>16</sub> H <sub>11</sub> ClF <sub>6</sub> N <sub>2</sub> O <sub>2</sub>	413.04860	
Fluopyram-7-hydroxy-glc	C <sub>22</sub> H <sub>21</sub> ClF <sub>6</sub> N <sub>2</sub> O <sub>7</sub>	575.10142	
Fluopyram-benzamide	C <sub>8</sub> H <sub>6</sub> F <sub>3</sub> NO	190.04743	
Fluopyram-benzoic acid	C <sub>8</sub> H <sub>5</sub> F <sub>3</sub> O <sub>2</sub>	191.03144	

PCA	$C_7H_3ClF_3NO_2$	225.98772	
Tebuconazole	$C_{16}H_{22}ClN_3O$	308.15242	
o-Hydroxy-tebuconazole	$C_{16}H_{22}ClN_3O_2$	324.14733	
1-hydroxy-tebuconazole	$C_{16}H_{22}ClN_3O_2$	324.14733	
p-Chlorobenzoic acid	$C_7H_5ClO_2$	157.00508	
Cyprosulfamide	$C_{18}H_{18}N_2O_5S$	375.10092	
Thiencarbazone-methyl	$C_{12}H_{14}N_4O_7S_2$	391.03767	
Hydroxy-CSA	$C_{18}H_{18}N_2O_6S$	391.09583	

Demethylated-CSA	$C_{17}H_{16}N_2O_5S$	361.08527	
N-Demethylated TCM	$C_{11}H_{12}N_4O_7S_2$	377.02202	
Ethiprole	$C_{13}H_9Cl_2F_3N_4OS$	396.98990	
Ethiprole sulfone	$C_{13}H_9Cl_2F_3N_4O_2S$	412.98481	
Ethiprole sulfonate	$C_{14}H_9Cl_2F_3N_2O_3S$	412.97358	
Ethiprole monodechloro	$C_{15}H_{12}ClF_3N_2OS$	361.03837	



Ethiprole carboxamide	$C_{15}H_{13}Cl_2F_3N_2O_2S$	413.00996	
Propineb	$(C_5H_8N_2S_4Zn)_n$	288.89345 (monomer)	
Propineb-PU	$C_4H_8N_2O$	101.07094	
Propineb-PTU	$C_4H_8N_2S$	117.04810	
Propineb-DIDT	$C_5H_6N_2S_3$	190.97659	

**Table 27.** Dry weight of grape vine (*Vitis vinifera*) plant tissues for quantification of fluopyram.

No.	Sample ID	Sample description	Harvest point	m <sub>d.w.</sub> [g]
1	MK19POt1so	MK19 basfoliar active t1 soil	t1	16.22
2	MK19POt1r	MK19 basfoliar active t1 root	t1	25.06
3	MK19POt1c	MK19 basfoliar active t1 cork	t1	15.95
4	MK19POt1b	MK19 basfoliar active t1 bark	t1	6.12
5	MK19POt1vb	MK19 basfoliar active t1 vascular bundle	t1	69.77
6	MK19POt1s	MK19 basfoliar active t1 stem	t1	9.83
7	MK19POt1p	MK19 basfoliar active t1 petiole	t1	2.47
8	MK19POt1l	MK19 basfoliar active t1 leaf	t1	25.73
9	MK19POt1lw	MK19 basfoliar active t1 leaf wash	t1	4.25
10	MK19Pt1so	MK19 t1 soil	t1	20.10
11	MK19Pt1r	MK19 t1 root	t1	29.66
12	MK19Pt1c	MK19 t1 cork	t1	34.05
13	MK19Pt1b	MK19 t1 bark	t1	6.95
14	MK19Pt1vb	MK19 t1 vascular bundle	t1	92.27
15	MK19Pt1s	MK19 t1 stem	t1	19.52
16	MK19Pt1p	MK19 t1 petiole	t1	6.27
17	MK19Pt1l	MK19 t1 leaf	t1	37.12
	MK19Pt1lw	MK19 t1 leaf wash	t1	3.96
19	MK19POt2so	MK19 basfoliar active t2 soil	t2	27.72
20	MK19POt2r	MK19 basfoliar active t2 root	t2	21.14
21	MK19POt2c	MK19 basfoliar active 2 cork	t2	14.23
22	MK19POt2b	MK19 basfoliar active t2 bark	t2	3.04
23	MK19POt2vb	MK19 basfoliar active t2 vascular bundle	t2	46.49
24	MK19POt2s	MK19 basfoliar active t2 stem	t2	4.21
25	MK19POt2p	MK19 basfoliar active t2 petiole	t2	1.37
26	MK19POt2l	MK19 basfoliar active t2 leaf	t2	3.03
27	MK19POt2lw	MK19 basfoliar active t2 leaf wash	t2	2.02
28	MK19POt2lg	MK19 basfoliar active t2 leaf abscission	t2	9.41
29	MK19POt2lgw	MK19 basfoliar active t2 leaf abscission wash	t2	2.42
30	MK19Pt2so	MK19 t2 soil	t2	22.26
31	MK19Pt2r	MK19 t2 root	t2	24.26
32	MK19Pt2c	MK19 t2 cork	t2	25.89

<b>33</b>	MK19Pt2b	MK19 t2 bark	t2	8.76
<b>34</b>	MK19Pt2vb	MK19 t2 vascular bundle	t2	83.70
<b>35</b>	MK19Pt2s	MK19 t2 stem	t2	9.09
<b>36</b>	MK19Pt2p	MK19 t2 petiole	t2	2.17
<b>37</b>	MK19Pt2l	MK19 t2 leaf	t2	2.39
<b>38</b>	MK19Pt2lw	MK19 t2 leaf wash	t2	1.83
<b>39</b>	MK19POt2lg	MK19 basfoliar active t2 leaf abscission	t2	17.14
<b>40</b>	MK19POt2lgw	MK19 basfoliar active t2 leaf abscission wash	t2	2.03
<b>41</b>	MK19POt3so	MK19 basfoliar active t3 soil	t3	21.11
<b>42</b>	MK19POt3r	MK19 basfoliar active t3 root	t3	20.29
<b>43</b>	MK19POt3c	MK19 basfoliar active t3 cork	t3	7.10
<b>44</b>	MK19POt3b	MK19 basfoliar active t3 bark	t3	6.61
<b>45</b>	MK19POt3vb	MK19 basfoliar active t3 vascular bundle	t3	49.30
	MK19POt3s	MK19 basfoliar active t3 stem	t3	9.43
<b>47</b>	MK19Pt3so	MK19 t3 soil	t3	54.07
<b>48</b>	MK19Pt3r	MK19 t3 root	t3	20.05
<b>49</b>	MK19Pt3c	MK19 t3 cork	t3	7.61
<b>50</b>	MK19Pt3b	MK19 t3 bark	t3	6.30
<b>51</b>	MK19Pt3vb	MK19 t3 vascular bundle	t3	48.50
<b>52</b>	MK19Pt3s	MK19 t3 stem	t3	8.75
<b>53</b>	MK19POt4so	MK19 basfoliar active t4 soil	t4	45.86
<b>54</b>	MK19POt4r	MK19 basfoliar active t4 root	t4	29.40
<b>55</b>	MK19POt4c	MK19 basfoliar active t4 cork	t4	46.01
<b>56</b>	MK19POt4b	MK19 basfoliar active t4 bark	t4	6.05
<b>57</b>	MK19POt4vb	MK19 basfoliar active t4 vascular bundle	t4	69.01
<b>58</b>	MK19POt4s	MK19 basfoliar active t4 stem	t4	18.40
<b>59</b>	MK19POt4b	MK19 basfoliar active t4 bud	t4	0.54
<b>60</b>	MK19Pt4so	MK19 t4 soil	t4	59.17
<b>61</b>	MK19Pt4r	MK19 t4 root	t4	25.24
<b>62</b>	MK19Pt4c	MK19 t4 cork	t4	65.22
<b>63</b>	MK19Pt4b	MK19 t4 bark	t4	8.58
<b>64</b>	MK19Pt4vb	MK19 t4 vascular bundle	t4	97.82
<b>65</b>	MK19Pt4s	MK19 t4 stem	t4	20.43
<b>66</b>	MK19Pt4b	MK19 t4 bud	t4	0.56
<b>67</b>	MK19POt5so	MK19 basfoliar active t5 soil	t5	84.39
<b>68</b>	MK19POt5r	MK19 basfoliar active t5 root	t5	5.47

<b>69</b>	MK19POt5c	MK19 basfoliar active t5 cork	t5	29.27
<b>70</b>	MK19POt5b	MK19 basfoliar active t5 bark	t5	3.85
<b>71</b>	MK19POt5vb	MK19 basfoliar active t5 vascular bundle	t5	43.91
<b>72</b>	MK19POt5s	MK19 basfoliar active t5 stem	t5	5.46
<b>73</b>	MK19POt5p	MK19 basfoliar active t5 petiole	t5	2.05
<b>74</b>	MK19POt5l	MK19 basfoliar active t5 leaf	t5	5.71
<b>75</b>	MK19Pt5so	MK19 t5 soil	t5	146.52
<b>76</b>	MK19Pt5r	MK19 t5 root	t5	27.74
<b>77</b>	MK19Pt5c	MK19 t5 cork	t5	79.31
<b>78</b>	MK19Pt5b	MK19 t5 bark	t5	10.44
<b>79</b>	MK19Pt5vb	MK19 t5 vascular bundle	t5	59.49
<b>80</b>	MK19Pt5s	MK19 t5 stem	t5	34.59
<b>81</b>	MK19Pt5p	MK19 t5 petiole	t5	8.52
<b>82</b>	MK19Pt5l	MK19 t5 leaf	t5	20.75
<b>83</b>	MK19POt6so	MK19 basfoliar active t6 soil	t6	79.71
<b>84</b>	MK19POt6r	MK19 basfoliar active t6 root	t6	60.85
<b>85</b>	MK19POt6c	MK19 basfoliar active t6 cork	t6	35.21
<b>86</b>	MK19POt6b	MK19 basfoliar active t6 bark	t6	4.63
<b>87</b>	MK19POt6vb	MK19 basfoliar active t6 vascular bundle	t6	52.82
<b>88</b>	MK19POt6s	MK19 basfoliar active t6 stem	t6	77.98
<b>89</b>	MK19POt6p	MK19 basfoliar active t6 petiole	t6	31.97
<b>90</b>	MK19POt6l	MK19 basfoliar active t6 leaf	t6	113.59
<b>91</b>	MK19Pt6so	MK19 t6 soil	t6	85.14
<b>92</b>	MK19Pt6r	MK19 t6 root	t6	78.62
<b>93</b>	MK19Pt6c	MK19 t6 cork	t6	60.29
<b>94</b>	MK19Pt6b	MK19 t6 bark	t6	7.93
<b>95</b>	MK19Pt6vb	MK19 t6 vascular bundle	t6	90.43
<b>96</b>	MK19Pt6s	MK19 t6 stem	t6	148.65
<b>97</b>	MK19Pt6p	MK19 t6 petiole	t6	44.24
<b>98</b>	MK19Pt6l	MK19 t6 leaf	t6	190.6
<b>99</b>	MK19POt7so	MK19 basfoliar active t7 soil	t7	147.1
<b>100</b>	MK19POt7r	MK19 basfoliar active t7 root	t7	69.47
<b>101</b>	MK19POt7c	MK19 basfoliar active t7 cork	t7	40.17
<b>102</b>	MK19POt7b	MK19 basfoliar active t7 bark	t7	5.63
<b>103</b>	MK19POt7vb	MK19 basfoliar active t7 vascular bundle	t7	53.14
<b>104</b>	MK19POt7s	MK19 basfoliar active t7 stem	t7	214.46
<b>105</b>	MK19POt7p	MK19 basfoliar active t7 petiole	t7	40.19

<b>106</b>	MK19POt7l	MK19 basfoliar active t7 leaf	t7	267.52
<b>107</b>	MK19Pt7so	MK19 t7 soil	t7	124.5
<b>108</b>	MK19Pt7r	MK19 t7 root	t7	94.38
<b>109</b>	MK19Pt7c	MK19 t7 cork	t7	52.78
<b>110</b>	MK19Pt7b	MK19 t7 bark	t7	7.63
<b>111</b>	MK19Pt7vb	MK19 t7 vascular bundle	t7	59.87
<b>112</b>	MK19Pt7s	MK19 t7 stem	t7	306.21
<b>113</b>	MK19Pt7p	MK19 t7 petiole	t7	53.37
<b>114</b>	MK19Pt7l	MK19 t7 leaf	t7	359.36
<b>115</b>	MK19POt8so	MK19 basfoliar active t8 soil	t8	145.6
<b>116</b>	MK19POt8r	MK19 basfoliar active t8 root	t8	56.34
<b>117</b>	MK19POt8c	MK19 basfoliar active t8 cork	t8	49.89
<b>118</b>	MK19POt8b	MK19 basfoliar active t8 bark	t8	6.89
<b>119</b>	MK19POt8vb	MK19 basfoliar active t8 vascular bundle	t8	57.89
<b>120</b>	MK19POt8s	MK19 basfoliar active t8 stem	t8	256.87
<b>121</b>	MK19POt8p	MK19 basfoliar active t8 petiole	t8	139.60
<b>122</b>	MK19POt8l	MK19 basfoliar active t8 leaf	t8	280.43
<b>123</b>	MK19Pt8so	MK19 t8 soil	t8	132.8
<b>124</b>	MK19Pt8r	MK19 t8 root	t8	91.41
<b>125</b>	MK19Pt8c	MK19 t8 cork	t8	51.23
<b>126</b>	MK19Pt8b	MK19 t8 bark	t8	8.10
<b>127</b>	MK19Pt8vb	MK19 t8 vascular bundle	t8	61.89
<b>128</b>	MK19Pt8s	MK19 t8 stem	t8	506.26
<b>129</b>	MK19Pt8p	MK19 t8 petiole	t8	150.71
<b>130</b>	MK19Pt8l	MK19 t8 leaf	t8	322.28

t1: 1 day after application, end of wood maturation; t2: 49 days after application, 50% leaves fallen; t3: 95 days after application, end of leaf fall; t4: 164 days after application, budswell; t5: 199 days after application, 3<sup>rd</sup> leaves unfolded; t6: 259 days after application, fruits begin to swell; t7: 291 days after application, berries pea-size; t8: 308 days after application, berries gravest-ripe.

## Mass Spectra

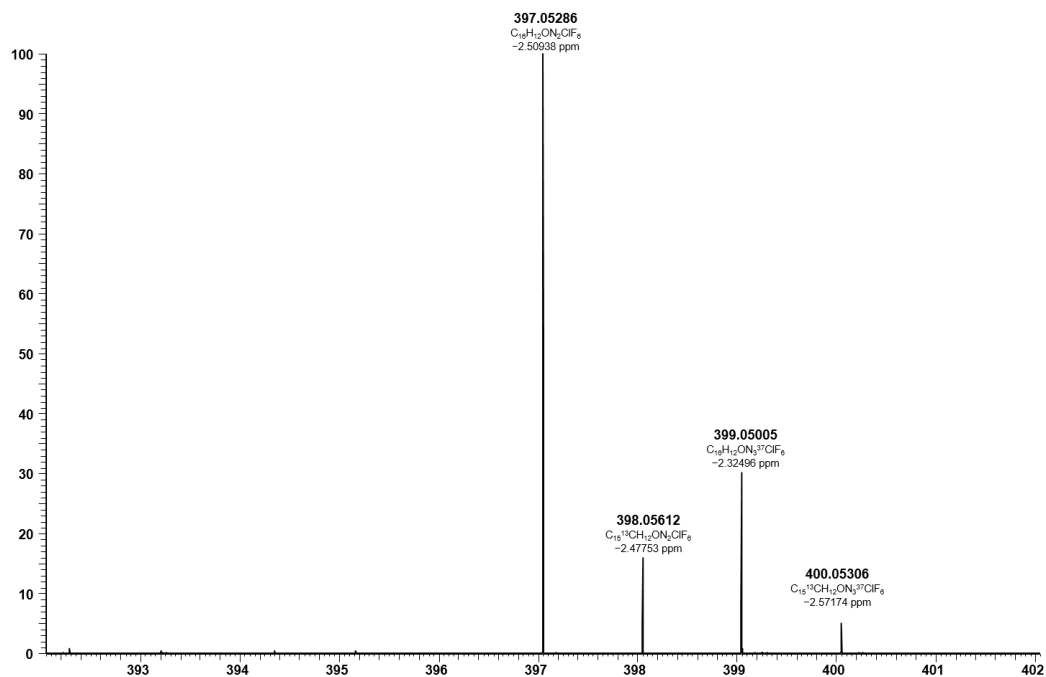


**Figure 80.** HR-ESI-MS mass spectrum in positive ion mode for mass range  $m/z$  392.06-402.06 of fluopyram ( $C_{16}H_{11}ON_2ClF_6$ ).

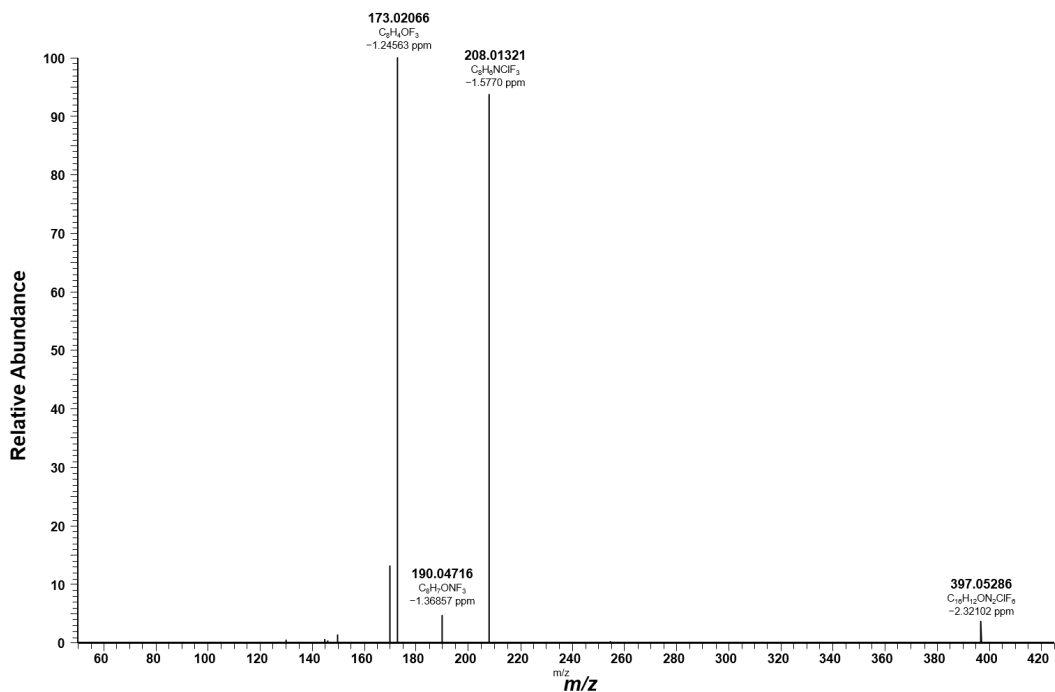


**Figure 81.** HR-ESI-MS/MS mass spectrum in positive ion mode of fluopyram (398.06@36 HCD).

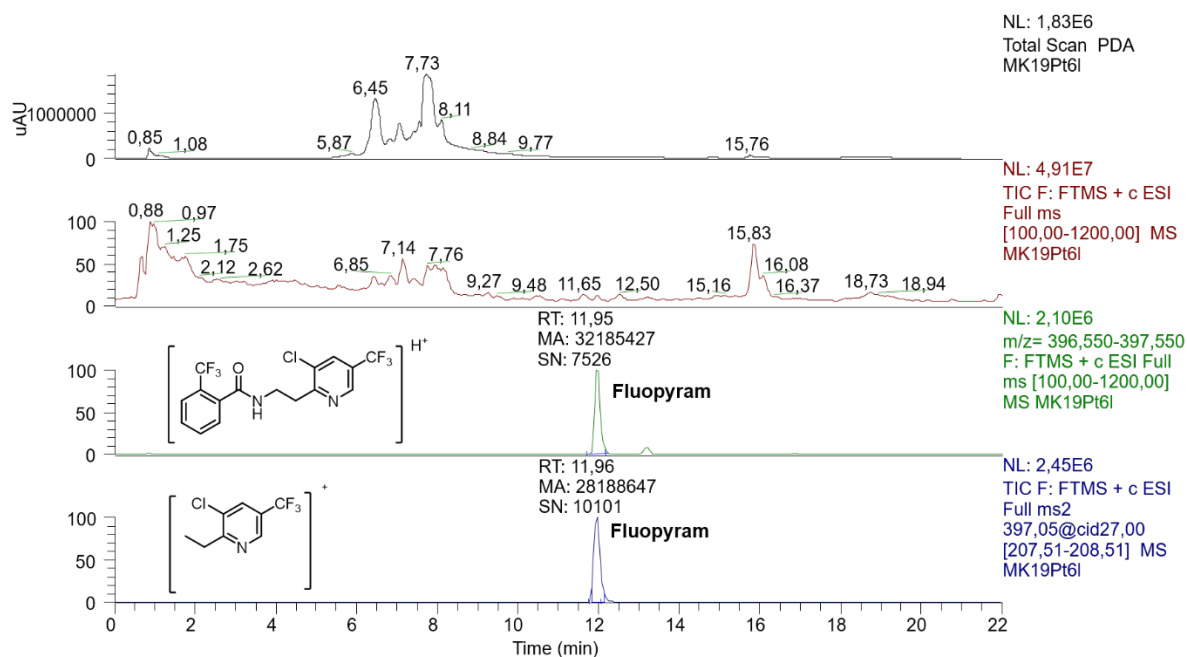


**Figure 82.** Example of ion chromatograms for quantification of fluopyram measured in SRM mode.

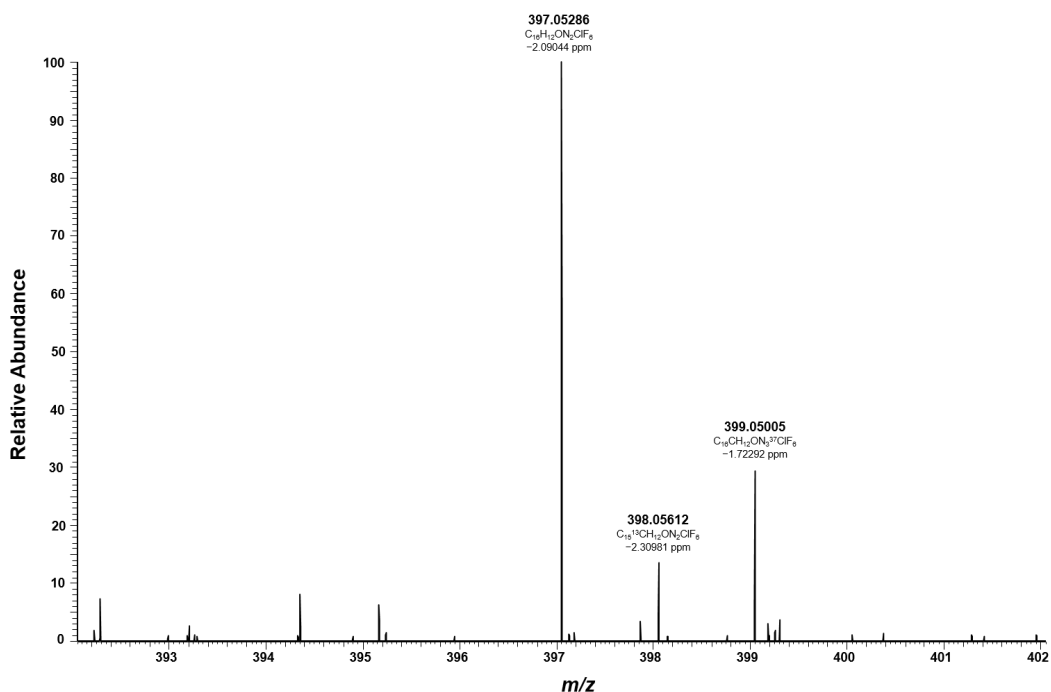


**Figure 83.** Single pixel (20  $\mu$ m) high resolution mass spectrum obtained from MALDI mass spectrometry experiments in 2,6-DHB. Mass spectrum in positive ion mode for mass range  $m/z$  392.06-402.06. Fluopyram was identified based on high mass accuracy ( $\leq 5$  ppm), labelled with measured mass and charge carrier.

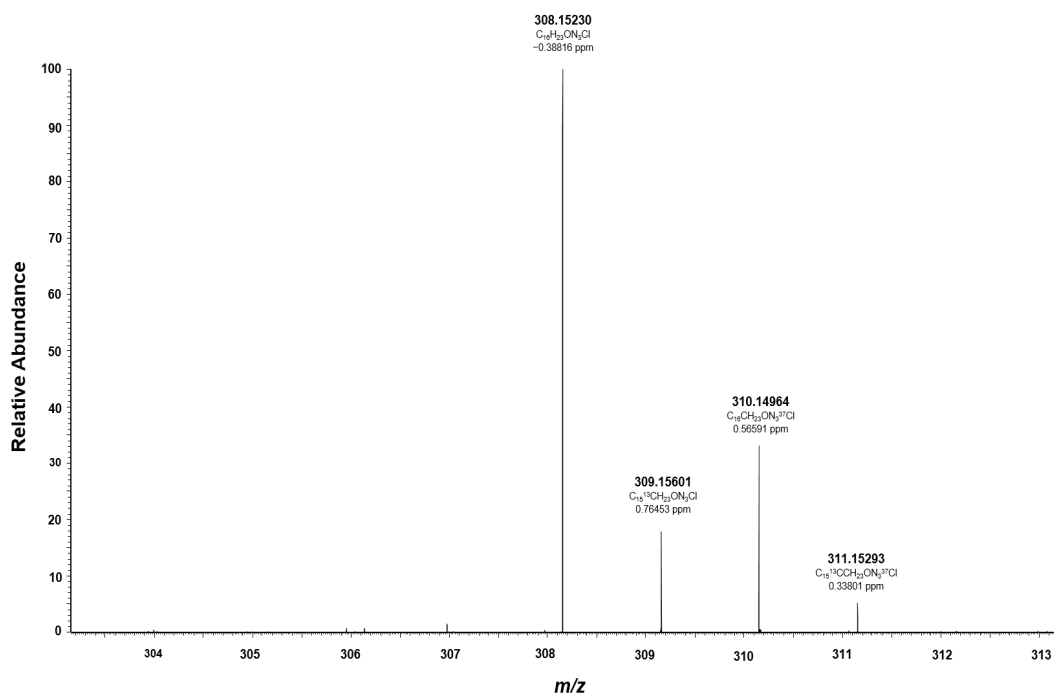


**Figure 84.** Single pixel (20  $\mu\text{m}$ ) high resolution mass spectrum obtained from MALDI mass spectrometry experiments in HCCA. Mass spectrum in positive ion mode for mass range  $m/z$  303.16-313.16. Tebuconazole (C<sub>16</sub>H<sub>22</sub>ON<sub>3</sub>Cl) was identified based on high mass accuracy ( $\leq 5$  ppm), labelled with measured mass and charge carrier.

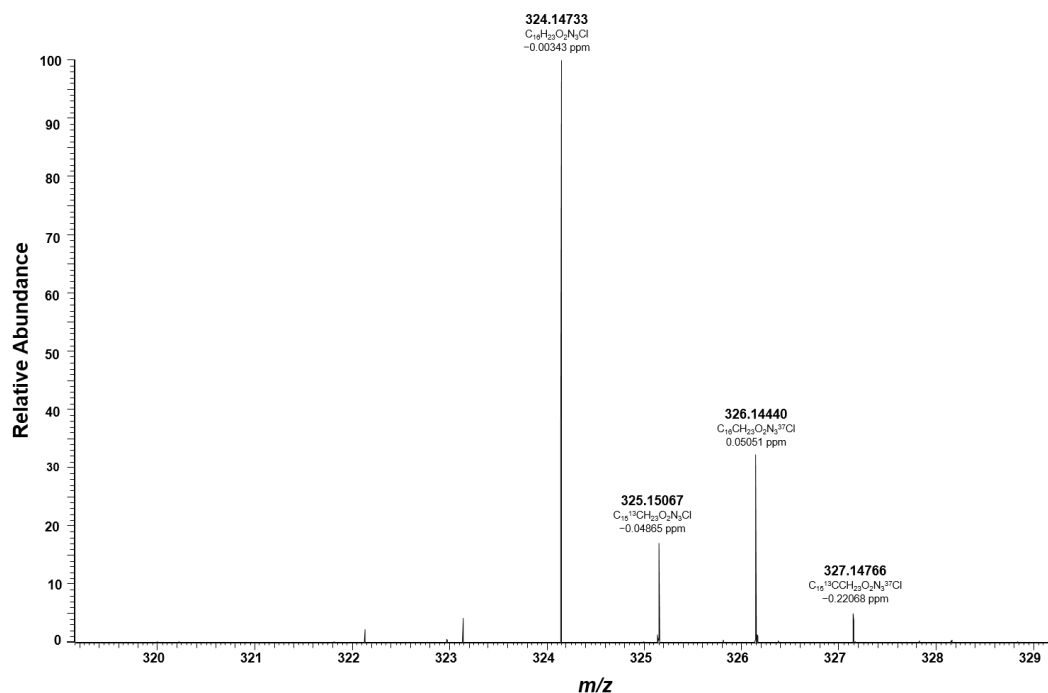


**Figure 85.** Single pixel (20  $\mu\text{m}$ ) high resolution mass spectrum obtained from MALDI mass spectrometry experiments in HCCA. Mass spectrum in positive ion mode for mass range  $m/z$  319.14-329.14. Hydroxy-Tebuconazole (C<sub>16</sub>H<sub>22</sub>O<sub>2</sub>N<sub>3</sub>Cl) was identified based on high mass accuracy ( $\leq 5$  ppm), labelled with measured mass and charge carrier.



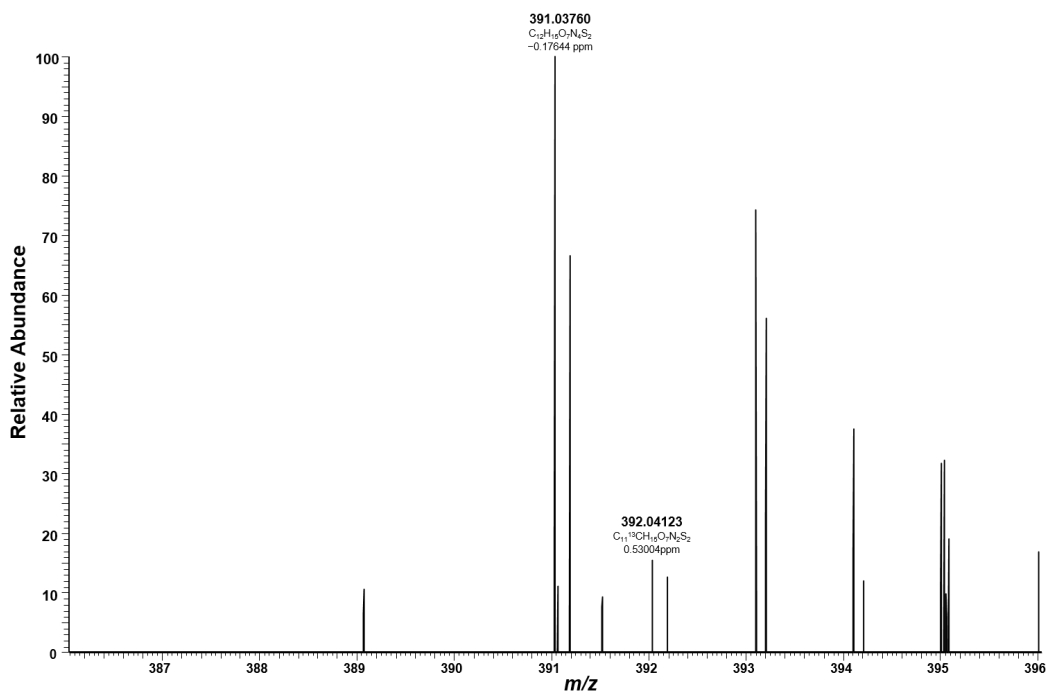


**Figure 86.** Single pixel ( $20\ \mu\text{m}$ ) high resolution mass spectrum obtained from MALDI mass spectrometry experiments in universal matrix (HCCA:DHB, 1:1, v/v). Mass spectrum in positive ion mode for mass range  $m/z$  386.04-396.04. TCM ( $C_{12}H_{14}O_8N_4S_2$ ) was identified based on high mass accuracy ( $\leq 5$  ppm), labelled with measured mass and charge carrier.

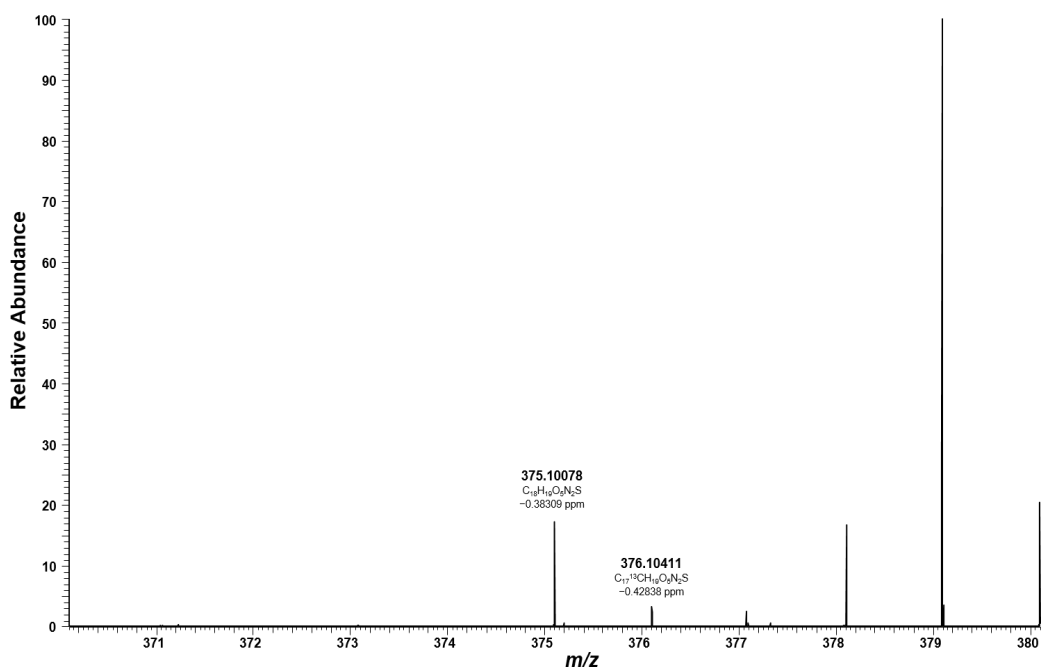


**Figure 87.** Single pixel ( $20\ \mu\text{m}$ ) high resolution mass spectrum obtained from MALDI mass spectrometry experiments in universal matrix (HCCA:DHB, 1:1, v/v). Mass spectrum in positive ion mode for mass range  $m/z$  380.10-380.10. CSA ( $C_{18}H_{18}O_6N_2S$ ) was identified based on high mass accuracy ( $\leq 5$  ppm), labelled with measured mass and charge carrier.

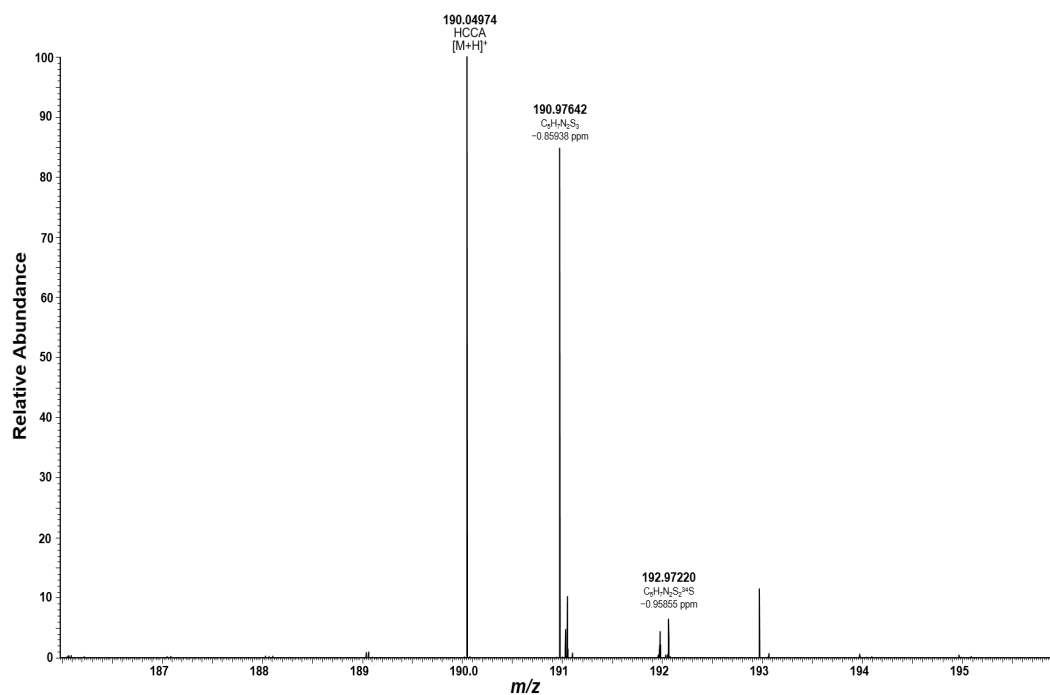


**Figure 88.** Single pixel (20  $\mu\text{m}$ ) high resolution mass spectrum obtained from MALDI mass spectrometry experiments in HCCA. Mass spectrum in positive ion mode for mass range  $m/z$  186.98-196.98. Propineb-DIDT ( $\text{C}_6\text{H}_6\text{N}_2\text{S}_3$ ) was identified based on high mass accuracy ( $\leq 6$  ppm), labelled with measured mass and charge carrier.

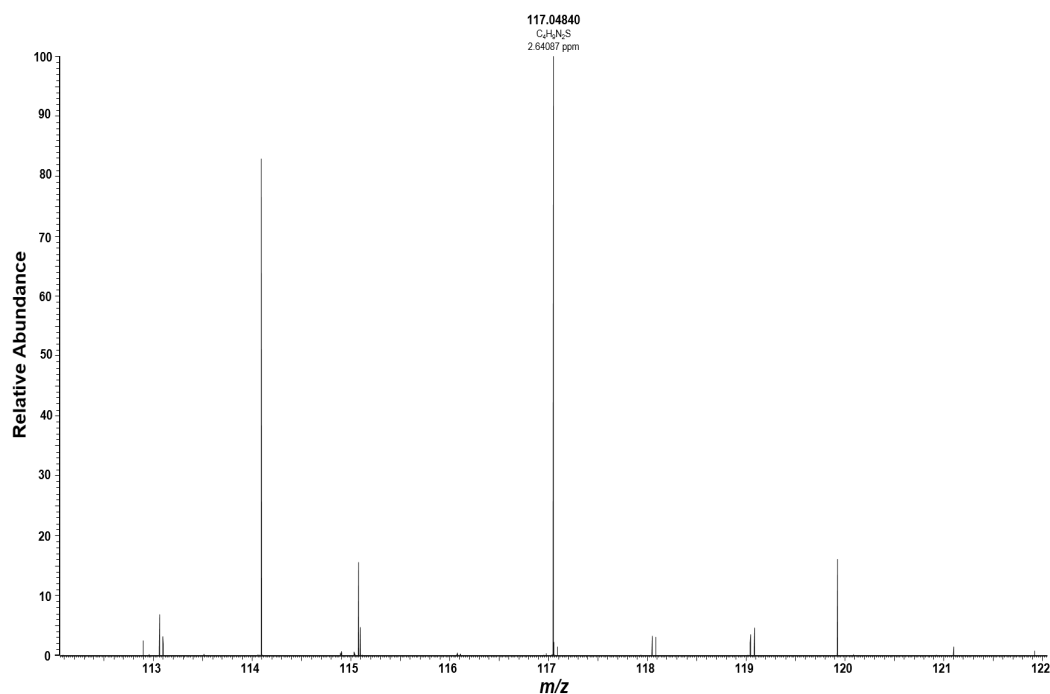


**Figure 89.** Single pixel (20  $\mu\text{m}$ ) high resolution mass spectrum obtained from MALDI mass spectrometry experiments in HCCA. Mass spectrum in positive ion mode for mass range  $m/z$  112.06-122.06. Propineb-PTU ( $\text{C}_4\text{H}_8\text{N}_2\text{S}$ ) was identified based on high mass accuracy ( $\leq 5$  ppm), labelled with measured mass and charge carrier.

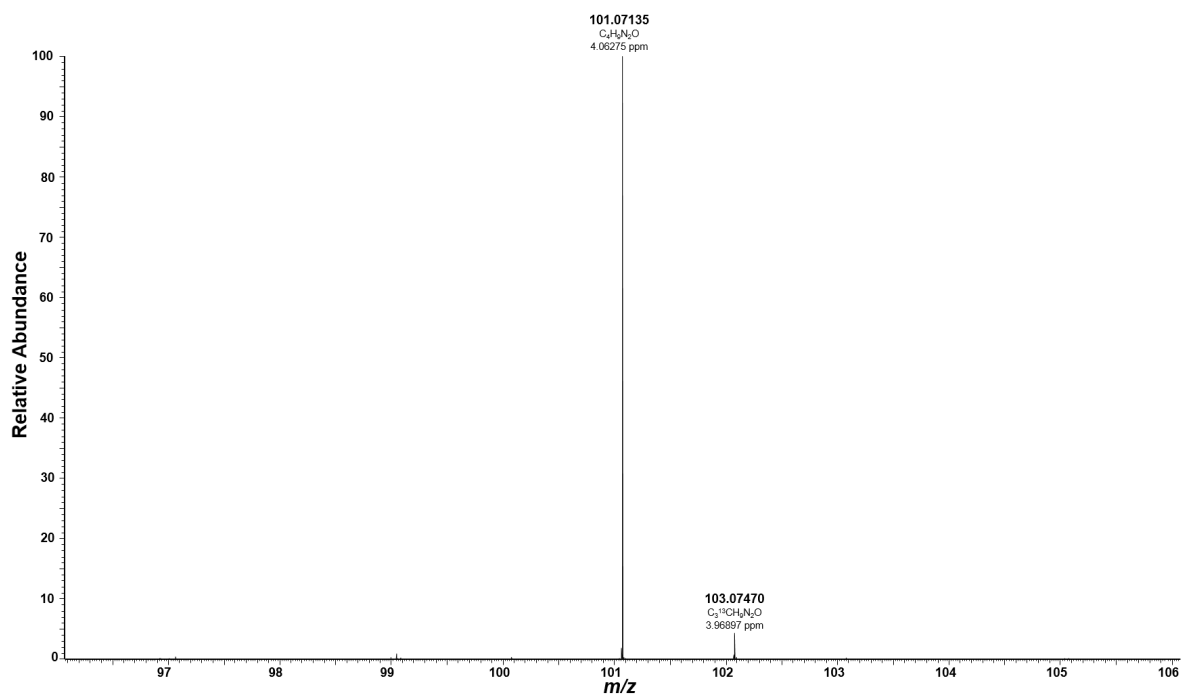


**Figure 90.** Single pixel (20  $\mu\text{m}$ ) high resolution mass spectrum obtained from MALDI mass spectrometry experiments in HCCA. Mass spectrum in positive ion mode for mass range  $m/z$  96.08-1036.08. Propineb-PU (C<sub>4</sub>H<sub>8</sub>N<sub>2</sub>O) was identified based on high mass accuracy ( $\leq 5$  ppm), labelled with measured mass and charge carrier.



## List of figures

<b>Figure 1.</b> Chemical structures of selected fungicides. ....	6
<b>Figure 2.</b> Major metabolic pathway of isotianil in rice (Ogawa et al., 2011). ....	7
<b>Figure 3.</b> Proposed metabolic pathway of fluopyram in several crop plants. Metabolites in brackets are postulated intermediates. G = grapes, P = potatoes, B = beans, RP = red pepper RC = rotational crops (Vargas-Pérez et al., 2020). ....	9
<b>Figure 4.</b> Proposed metabolic pathway of tebuconazole in selected crop plants. P = peanut, W = wheat (Jeschke et al., 2019). ....	10
<b>Figure 5.</b> Chemical structures of selected herbicides. ....	11
<b>Figure 6.</b> Chemical structures of selected insecticides. ....	13
<b>Figure 7.</b> Proposed metabolic pathway of ethiprole in plants (Lamberth et al., 2007). ....	14
<b>Figure 8.</b> Chemical structure of commonly used MALDI matrices. $\alpha$ -Cyano-4-hydroxycinnamic acid (HCCA), 2,5-Dihydroxybenzoic acid (DHB), 1,8-bis(dimethyl-amino)naphthalene (DMAN), 2-Mercaptobenzothiazole (MBT), 4-maleicanhydridopron sponge (MAPS) (Boughton et al., 2016). ....	21
<b>Figure 9.</b> Single droplet application of 3.0 $\mu$ L propineb-solution on the adaxial leaf surface of tomato ( <i>Solanum lycopersicum</i> ). ....	33
<b>Figure 10</b> MALDI-imaging-HRMS of isotianil in hydroponic grown wheat ( <i>Triticum</i> ) roots 10 days after treatment with isotianil (200 $\mu$ g/L, spatial resolution: 30 $\mu$ m, scan area: 2370x1710 $\mu$ m). Localization of Isotianil ( $[M+H]^+$ ; m/z 297.9603, $[M+K]^+$ ; m/z 335.9162) and primary plant metabolite asparagine ( $[M+K]^+$ ; m/z 171.0167). ....	42
<b>Figure 11.</b> MALDI-imaging-HRMS of DCIT-acid in hydroponic grown wheat ( <i>Triticum</i> ) roots 10 days after treatment with DCIT-acid (100 $\mu$ g/L, spatial resolution: 25 $\mu$ m). Localization of DCIT-acid ( $[M-H]^-$ ; m/z 195.9032). ....	43
<b>Figure 12.</b> Calculation of the plant uptake factor (Lamshöft et al., 2018). ....	45
<b>Figure 13.</b> Translocation of [ $^{14}$ C] DCIT-acid in tomato flower. Highest radioactivity is in red. ....	46
<b>Figure 14.</b> Spatial distribution of DCIT-acid ( $[M-H]^-$ ; m/z 195.9032) in tomato fruit of hydroponic grown tomato incubated with 0.2 ppm DCIT-acid after 34 days (spatial resolution: 25 $\mu$ m, scan area: 6766x6766 $\mu$ m). ....	47
<b>Figure 15.</b> Autoradiography and MALDI-imaging-HRMS of tomato leaf 2 days after treatment with Isotianil (spatial resolution: 75 $\mu$ m, scan area: 156x395 $\mu$ m). Translocation of [isothiazole-3- $^{14}$ C, carboxamide- $^{14}$ C]-Isotianil. Localization of Isotianil ( $[M+H]^+$ ; m/z 297.9603), anthranilonitrile ( $[M+H]^+$ ; m/z 119.0603) and plant hormone Indole-3-acetic acid ( $[M+H]^+$ ; m/z 176.07061). ....	49
<b>Figure 16.</b> Autoradiography and MALDI-imaging-HRMS of banana leaf 3 days after treatment (60% RH) with Isotianil (spatial resolution: 25 $\mu$ m, scan area: 5500x5500 $\mu$ m). <b>a:</b>	

Optical image of droplet application area. **b**: Translocation of [isothiazole-3-<sup>14</sup>C, carboxamide-<sup>14</sup>C]-Isotianil by autoradiography. **c-e**: Localization of Isotianil ([M+H]<sup>+</sup>; m/z 297.9603, [M+K]<sup>+</sup>; m/z 335.9162) and anthranilonitrile ([M+H]<sup>+</sup>; m/z 119.0603, [M+K]<sup>+</sup>; m/z 157.0163).....52

**Figure 17.** Autoradiography and MALDI-imaging-HRMS of banana leaf 7 days after treatment (60% RH) with Isotianil (spatial resolution: 25 μm, scan area: 5500x5500 μm). **a**: Optical image of droplet application area. **b**: Translocation of [isothiazole-3-<sup>14</sup>C, carboxamide-<sup>14</sup>C]-Isotianil by autoradiography. **c-e**: Localization of Isotianil ([M+H]<sup>+</sup>; m/z 297.9603, [M+K]<sup>+</sup>; m/z 335.9162) and anthranilonitrile ([M+H]<sup>+</sup>; m/z 119.0603, [M+K]<sup>+</sup>; m/z 157.0163).....53

**Figure 18.** Autoradiography and MALDI-imaging-HRMS of banana leaf 14 days after treatment (60% RH) with Isotianil (spatial resolution: 25 μm, scan area: 5500x5500 μm). **a**: Optical image of droplet application area. **b**: Translocation of [isothiazole-3-<sup>14</sup>C, carboxamide-<sup>14</sup>C]-Isotianil by autoradiography. **c-e**: Localization of Isotianil ([M+H]<sup>+</sup>; m/z 297.9603, [M+K]<sup>+</sup>; m/z 335.9162) and anthranilonitrile ([M+H]<sup>+</sup>; m/z 119.0603, [M+K]<sup>+</sup>; m/z 157.0163).....54

**Figure 19.** Autoradiography and MALDI-imaging-HRMS of banana leaf 3 days after treatment (100% RH) with Isotianil (spatial resolution: 25 μm, scan area: 5500x5500 μm). **a**: Optical image of droplet application area. **b**: Translocation of [isothiazole-3-<sup>14</sup>C, carboxamide-<sup>14</sup>C]-Isotianil by autoradiography. **c-e**: Localization of Isotianil ([M+H]<sup>+</sup>; m/z 297.9603, [M+K]<sup>+</sup>; m/z 335.9162) and anthranilonitrile ([M+H]<sup>+</sup>; m/z 119.0603, [M+K]<sup>+</sup>; m/z 157.0163).....55

**Figure 20.** Autoradiography and MALDI-imaging-HRMS of banana leaf 7 days after treatment (100% RH) with Isotianil (spatial resolution: 25 μm, scan area: 5500x5500 μm). **a**: Optical image of droplet application area. **b**: Translocation of [isothiazole-3-<sup>14</sup>C, carboxamide-<sup>14</sup>C]-Isotianil by autoradiography. **c-e**: Localization of Isotianil ([M+H]<sup>+</sup>; m/z 297.9603, [M+K]<sup>+</sup>; m/z 335.9162) and anthranilonitrile ([M+H]<sup>+</sup>; m/z 119.0603, [M+K]<sup>+</sup>; m/z 157.0163).....56

**Figure 21.** Autoradiography and MALDI-imaging-HRMS of banana leaf 14 days after treatment (100% RH) with Isotianil (spatial resolution: 25 μm, scan area: 5500x5500 μm). **a**: Optical image of droplet application area. **b**: Translocation of [isothiazole-3-<sup>14</sup>C, carboxamide-<sup>14</sup>C]-Isotianil by autoradiography. **c-e**: Localization of Isotianil ([M+H]<sup>+</sup>; m/z 297.9603, [M+K]<sup>+</sup>; m/z 335.9162) and anthranilonitrile ([M+H]<sup>+</sup>; m/z 119.0603, [M+K]<sup>+</sup>; m/z 157.0163).....57

**Figure 22.** MALDI-imaging-HRMS throughout the leaf section of banana leaf (spatial resolution: 20 μm, scan area: 5500x5500 μm); the red frame indicates the scanned area of the imaging experiment. **a**: Safranin-stained cross section. **b**: Localization of Isotianil

([M+H] <sup>+</sup> ; m/z 297.9603) 3 days after treatment (60% RH). <b>c</b> : Localization of Isotianil ([M+H] <sup>+</sup> ; m/z 297.9603) 7 days after treatment (60% RH).....	59
<b>Figure 23.</b> Autoradiography and MALDI-imaging-HRMS of banana leaf 3 days after treatment (60% RH) with DCIT-acid (spatial resolution: 25 μm, scan area: 5500x5500 μm). <b>a</b> : Optical image of droplet application area. <b>b</b> : Translocation of [isothiazole-3- <sup>14</sup> C, carboxylic acid- <sup>14</sup> C]-3,4- dichloro-1,2-thiazole-5-carboxylic acid. <b>c-e</b> : Localization of DCIT-acid ([M-H] <sup>-</sup> ; m/z 195.9032). .....	61
<b>Figure 24.</b> Autoradiography and MALDI-imaging-HRMS of banana leaf 7 days after treatment (60% RH) with DCIT-acid (spatial resolution: 25 μm, scan area: 5500x5500 μm). <b>a</b> : Optical image of droplet application area. <b>b</b> : Translocation of [isothiazole-3- <sup>14</sup> C, carboxylic acid- <sup>14</sup> C]-3,4- dichloro-1,2-thiazole-5-carboxylic acid. <b>c-e</b> : Localization of DCIT-acid ([M-H] <sup>-</sup> ; m/z 195.9032). .....	62
<b>Figure 25.</b> Autoradiography and MALDI-imaging-HRMS of banana leaf 14 days after treatment (60% RH) with DCIT-acid (spatial resolution: 25 μm, scan area: 5500x5500 μm). <b>a</b> : Optical image of droplet application area. <b>b</b> : Translocation of [isothiazole-3- <sup>14</sup> C, carboxylic acid- <sup>14</sup> C]-3,4-dichloro-1,2-thiazole-5-carboxylic acid. <b>c-e</b> : Localization of DCIT-acid ([M-H] <sup>-</sup> ; m/z 195.9032). .....	63
<b>Figure 26.</b> Autoradiography and MALDI-imaging-HRMS of banana leaf 3 days after treatment (100% RH) with DCIT-acid (spatial resolution: 25 μm, scan area: 5500x5500 μm). <b>a</b> : Optical image of droplet application area. <b>b</b> : Translocation of [isothiazole-3- <sup>14</sup> C, carboxylic acid- <sup>14</sup> C]-3,4-dichloro-1,2-thiazole-5-carboxylic acid. <b>c-e</b> : Localization of DCIT-acid ([M-H] <sup>-</sup> ; m/z 195.9032). .....	64
<b>Figure 27.</b> Autoradiography and MALDI-imaging-HRMS of banana leaf 7 days after treatment (100% RH) with DCIT-acid (spatial resolution: 25 μm, scan area: 5500x5500 μm). <b>a</b> : Optical image of droplet application area. <b>b</b> : Translocation of [isothiazole-3- <sup>14</sup> C, carboxylic acid- <sup>14</sup> C]-3,4- dichloro-1,2-thiazole-5-carboxylic acid. <b>c-e</b> : Localization of DCIT-acid ([M-H] <sup>-</sup> ; m/z 195.9032). .....	65
<b>Figure 28.</b> Autoradiography and MALDI-imaging-HRMS of banana leaf 14 days after treatment (100% RH) with DCIT-acid (spatial resolution: 25 μm, scan area: 5500x5500 μm). <b>a</b> : Optical image of droplet application area. <b>b</b> : Translocation of [isothiazole-3- <sup>14</sup> C, carboxylic acid- <sup>14</sup> C]-3,4-dichloro-1,2-thiazole-5-carboxylic acid. <b>c-e</b> : Localization of DCIT-acid ([M-H] <sup>-</sup> ; m/z 195.9032). .....	66
<b>Figure 29.</b> Distribution of [pyridyl-2,6- <sup>14</sup> C, carboxylic acid- <sup>13</sup> C]PCA in root system and leaf system of grape vine plants after 4 and 10 days of root uptake. ....	68
<b>Figure 30.</b> Total of damaged leaves 20 days after treatment with PCA. A: 500 μg/L. B: 5000 μg/L.....	70
<b>Figure 31.</b> Investigated growth stages of grape vine ( <i>Vitis vinifera</i> ) treated with fluopyram. .	71

**Figure 32.** MALDI-imaging-HRMS of grape vine (Sauvignon blanc) stem cross sections at BBCH95, 50% leaves fallen (spatial resolution: 25  $\mu\text{m}$ , scan area: 3300x3300  $\mu\text{m}$ ). Localization of fluopyram ( $[\text{M}+\text{K}]^+$ ; m/z 435.0096). Localization of primary plant metabolites: Glutamine ( $[\text{M}+\text{K}]^+$ ; m/z 185.0323), Sucrose ( $[\text{M}+\text{K}]^+$ ; m/z 381.0794), Raffinose ( $[\text{M}+\text{K}]^+$ ; m/z 543.1322), Stachyose ( $[\text{M}+\text{K}]^+$ ; m/z 705.1850). .....76

**Figure 33.** MALDI-imaging-HRMS of different grape vine (Sauvignon blanc) stem cross sections at BBCH97, end of leaf fall (spatial resolution: 25  $\mu\text{m}$ , scan area: 2800x2800  $\mu\text{m}$ ). Localization of fluopyram ( $[\text{M}+\text{K}]^+$ ; m/z 435.0096). Localization of primary plant metabolites: Glutamine ( $[\text{M}+\text{K}]^+$ ; m/z 185.0323), Sucrose ( $[\text{M}+\text{K}]^+$ ; m/z 381.0794), Raffinose ( $[\text{M}+\text{K}]^+$ ; m/z 543.1322), Stachyose ( $[\text{M}+\text{K}]^+$ ; m/z 705.1850). .....77

**Figure 34.** MALDI-imaging-HRMS of different grape vine (Sauvignon blanc) stem cross sections at BBCH13, 3<sup>rd</sup> leaves unfolded (spatial resolution: 25  $\mu\text{m}$ , scan area: 3000x3000  $\mu\text{m}$ ). Localization of fluopyram ( $[\text{M}+\text{K}]^+$ ; m/z 435.0096). Localization of primary plant metabolites: Glutamine ( $[\text{M}+\text{K}]^+$ ; m/z 185.0323), Sucrose ( $[\text{M}+\text{K}]^+$ ; m/z 381.0794), Raffinose ( $[\text{M}+\text{K}]^+$ ; m/z 543.1322), Stachyose ( $[\text{M}+\text{K}]^+$ ; m/z 705.1850). .....78

**Figure 35.** MALDI-imaging-HRMS of different grape vine (Sauvignon blanc) trunk cross sections at BBCH13, 3<sup>rd</sup> leaves unfolded (spatial resolution: 25  $\mu\text{m}$ , scan area: 2000x2000 $\mu\text{m}$ ). Localization of fluopyram ( $[\text{M}+\text{K}]^+$ ; m/z 435.0096). Localization of primary plant metabolites: Glutamine ( $[\text{M}+\text{K}]^+$ ; m/z 185.0323), Sucrose ( $[\text{M}+\text{K}]^+$ ; m/z 381.0794), Raffinose ( $[\text{M}+\text{K}]^+$ ; m/z 543.1322), Stachyose ( $[\text{M}+\text{K}]^+$ ; m/z 705.1850). .....79

**Figure 36.** MALDI-imaging-HRMS of different grape vine (Sauvignon blanc) stem trunk cross sections at BBCH76, berries pea-size (spatial resolution: 25  $\mu\text{m}$ , scan area: 4500x4000 $\mu\text{m}$ ). Localization of fluopyram ( $[\text{M}+\text{K}]^+$ ; m/z 435.0096). Localization of primary plant metabolites: Glutamine ( $[\text{M}+\text{K}]^+$ ; m/z 185.0323), Sucrose ( $[\text{M}+\text{K}]^+$ ; m/z 381.0794), Raffinose ( $[\text{M}+\text{K}]^+$ ; m/z 543.1322), Stachyose ( $[\text{M}+\text{K}]^+$ ; m/z 705.1850). .....80

**Figure 37.** MALDI-imaging-HRMS of different grape vine (Sauvignon blanc) stem cross sections at BBCH76, berries pea-size (spatial resolution: 25  $\mu\text{m}$ , scan area: 4000x4000 $\mu\text{m}$ ). Localization of fluopyram ( $[\text{M}+\text{K}]^+$ ; m/z 435.0096). Localization of primary plant metabolites: Glutamine ( $[\text{M}+\text{K}]^+$ ; m/z 185.0323), Sucrose ( $[\text{M}+\text{K}]^+$ ; m/z 381.0794), Raffinose ( $[\text{M}+\text{K}]^+$ ; m/z 543.1322), Stachyose ( $[\text{M}+\text{K}]^+$ ; m/z 705.1850). .....81

**Figure 38.** MALDI-imaging-HRMS of non-germinated (upper part) and 48 h germinated wheat (lower part) (*Triticum aestivum* 'Triso') seeds after seed-treatment with tebuconazole. Localization of tebuconazole ( $[\text{M}+\text{Na}]^+$ ; m/z 330.1344), seed coating colorants (Pigment Red 112  $[\text{M}+\text{H}]^+$ ; m/z 484.0381) and selected endogenous plant metabolites (Glutamine  $[\text{M}+\text{K}]^+$  m/z 185.0323; Fructose  $[\text{M}+\text{K}]^+$  m/z 219.0266; Sucrose  $[\text{M}+\text{Na}]^+$  m/z 365.1054).....84

**Figure 39.** MALDI-imaging-HRMS of tebuconazole in wheat (*Triticum aestivum* 'Triso') after seed treatment with ArenaC® (1 g/dt) at the two-leaf stage after 14 days. Localization of



tebuconazole ([M+Na] <sup>+</sup> ; m/z 330.1344, [M+K] <sup>+</sup> ; m/z 346.1083) and hydroxy-tebuconazole ([M+K] <sup>+</sup> ; m/z 362.1032).....	85
<b>Figure 40.</b> MALDI-imaging-HRMS of tebuconazole in wheat ( <i>Triticum aestivum</i> 'Triso') at the three-leaf stage after 24 days after seed treatment with ArenaC® (1 g/dt). Localization of tebuconazole ([M+K] <sup>+</sup> ; m/z 346.1083), hydroxy-tebuconazole ([M+K] <sup>+</sup> ; m/z 362.1032) and p-Chlorobenzoic acid ([M+Na] <sup>+</sup> ; m/z 178.9870). .....	86
<b>Figure 41.</b> MALDI-imaging-HRMS of non-germinated wheat ( <i>Triticum aestivum</i> 'Orcas') seeds after seed-treatment with BCS-CX51842 (10 g/dt). Localization of BCS-CX51842 ([M+H] <sup>+</sup> ; m/z 342.1413) and selected endogenous plant metabolite (Glutamine [M+K] <sup>+</sup> ; m/z 185.0323). .....	87
<b>Figure 42.</b> MALDI-imaging-HRMS of tebuconazole in wheat ( <i>Triticum aestivum</i> 'Orcas') at the two-leaf stage after 14 days after seed treatment with BCS-CX-51842 (10 g/dt). Localization of BCS-CX51842 ([M+H] <sup>+</sup> ; m/z 342.1413; [M+K] <sup>+</sup> , m/z 380.0971), hydroxy-BCS-CX51842 ([M+K] <sup>+</sup> ; m/z 396.0920) and selected endogenous plant metabolites (Glutamine [M+K] <sup>+</sup> ; m/z 185.0323; Asparagine [M+H] <sup>+</sup> ; m/z 133.0608). .....	88
<b>Figure 43.</b> MALDI-imaging-HRMS of tebuconazole in wheat ( <i>Triticum aestivum</i> 'Orcas') at the three-leaf stage after 24 days after seed treatment with BCS-CX-51842 (10 g/dt). Localization of BCS-CX51842 ([M+H] <sup>+</sup> ; m/z 342.1413, [M+K] <sup>+</sup> ; m/z 380.0971; [M+Na] <sup>+</sup> ; m/z 364.1232), hydroxy-BCS-CX51842 ([M+K] <sup>+</sup> ; m/z 396.0920), dihydroxy-BCS-CX51842 ([M+K] <sup>+</sup> ; m/z 412.0870, [M+Na] <sup>+</sup> ; m/z 396.1130), glc-BCS-CX51842 ([M+K] <sup>+</sup> ; m/z 542.1500, [M+Na] <sup>+</sup> ; m/z 364.526.1760) and selected endogenous plant metabolites Asparagine ([M+H] <sup>+</sup> ; m/z 133.0608), Glutamine ([M+K] <sup>+</sup> ; m/z 185.0323). .....	89
<b>Figure 44.</b> MALDI-imaging-HRMS of BCS-CX51842 in soybean ( <i>Glycine max.</i> ) at the two trifoliolate leaf stage after 26 days after application after seed treatment (10 g/dt). Localization of BCS-CX51842 ([M+K] <sup>+</sup> , m/z 380.0971), Hydroxy-BCS-CX51842 ([M+Na] <sup>+</sup> ; m/z 380.1181), dihydroxy-BCS-CX51842 ([M+K] <sup>+</sup> ; m/z 412.0870) and selected endogenous plant metabolite (Asparagine ([M+Na] <sup>+</sup> ; m/z 155.0427). .....	90
<b>Figure 45.</b> Chemical structures of thien carbazole-methyl and cyprosulfamide metabolites detected by MALDI MSI in maize leaves. ....	92
<b>Figure 46.</b> MALDI-imaging-HRMS of maize leaves 24 hours after micro droplet application of cyprosulfamide and thien carbazole-methyl on different leaves (spatial resolution: 50 µm, scan area: 9300x21250 µm; 6250x15350). Localization of thien carbazole-methyl ([M+H] <sup>+</sup> ; m/z 391.0377, [M+K] <sup>+</sup> ; m/z 428.9936), N-Demethylated-TCM ([M+Na] <sup>+</sup> ; m/z 399.0040), cyprosulfamide ([M+H] <sup>+</sup> ; m/z 375.1009, [M+K] <sup>+</sup> ; m/z 413.0568), Hydroxylated-CSA ([M+K] <sup>+</sup> ; m/z 429.0517) and Demethylated-CSA ([M+K] <sup>+</sup> ; m/z 399.0412). .....	93
<b>Figure 47.</b> MALDI-imaging-HRMS of maize leaves 4 days after micro droplet application of cyprosulfamide and thien carbazole-methyl on different leaves (spatial resolution: 50 µm,	

scan area: 9300x21250  $\mu\text{m}$ ; 6250x15350). Localization of thiencarbazone-methyl ( $[\text{M}+\text{H}]^+$ ;  $m/z$  391.0377,  $[\text{M}+\text{K}]^+$ ;  $m/z$  428.9936), N-Demethylated-TCM ( $[\text{M}+\text{Na}]^+$ ;  $m/z$  399.0040), cyprosulfamide ( $[\text{M}+\text{H}]^+$ ;  $m/z$  375.1009,  $[\text{M}+\text{K}]^+$ ;  $m/z$  413.0568), Hydroxylated-CSA ( $[\text{M}+\text{K}]^+$ ;  $m/z$  429.0517) and Demethylated-CSA ( $[\text{M}+\text{K}]^+$ ;  $m/z$  399.0412). .....94

**Figure 48.** MALDI mass spectrometry imaging of maize leaves 3 hours after micro droplet application of cyprosulfamide and thiencarbazone-methyl (spatial resolution: 50  $\mu\text{m}$ ). Localization of thiencarbazone-methyl ( $[\text{M}+\text{K}]^+$ ;  $m/z$  428.9936), N-Demethylated TCM ( $[\text{M}+\text{K}]^+$ ;  $m/z$  414.9780), cyprosulfamide ( $[\text{M}+\text{K}]^+$ ;  $m/z$  413.05680) and valine ( $[\text{M}+\text{K}]^+$ ;  $m/z$  156.04214) on adaxial leaf surface. ....96

**Figure 49.** MALDI mass spectrometry imaging of maize leaves 24hours after micro droplet application of cyprosulfamide and thiencarbazone-methyl (spatial resolution: 50  $\mu\text{m}$ ). Localization of thiencarbazone-methyl ( $[\text{M}+\text{K}]^+$ ;  $m/z$  428.99355), N-Demethylated TCM ( $[\text{M}+\text{K}]^+$ ;  $m/z$  414.9780), cyprosulfamide ( $[\text{M}+\text{K}]^+$ ;  $m/z$  413.05680) and valine ( $[\text{M}+\text{K}]^+$ ;  $m/z$  156.04214) on adaxial leaf surface. ....97

**Figure 50.** MALDI mass spectrometry imaging of maize leaves 4 days and 7 days after micro droplet application of cyprosulfamide and thiencarbazone-methyl (spatial resolution: 50  $\mu\text{m}$ ). Localization of thiencarbazone-methyl ( $[\text{M}+\text{K}]^+$ ;  $m/z$  428.99355), N-Demethylated TCM ( $[\text{M}+\text{K}]^+$ ;  $m/z$  414.9780), cyprosulfamide ( $[\text{M}+\text{K}]^+$ ;  $m/z$  413.05680) and valine ( $[\text{M}+\text{K}]^+$ ;  $m/z$  156.04214) on adaxial leaf surface. ....99

**Figure 51.** MALDI mass spectrometry imaging of maize leaves 24 after micro droplet application of cyprosulfamide and thiencarbazone-methyl (spatial resolution: 50  $\mu\text{m}$ ). Localization of valine ( $[\text{M}+\text{K}]^+$ ;  $m/z$  156.04214) on adaxial leaf surface. ....100

**Figure 52.** Chemical structures of ethiprole and its metabolites detected by MALDI MSI in soybean flowers. ....102

**Figure 53.** MALDI-imaging-HRMS of soybean flower after treatment with ethiprole (spatial resolution: 30  $\mu\text{m}$ , scan area: 6600x6600  $\mu\text{m}$ ). Localization of ethiprole ( $[\text{M}+\text{Na}]^+$ ;  $m/z$  418.9718) and ethiprole sulfonate ( $[\text{M}+\text{H}]^+$ ;  $m/z$  400.9484). ....102

**Figure 54.** MALDI-imaging-HRMS of soybean stem after treatment with ethiprole (spatial resolution: 25  $\mu\text{m}$ , scan area: 3750x2000  $\mu\text{m}$ ). Localization of ethiprole ( $[\text{M}+\text{Na}]^+$ ;  $m/z$  418.9718) and ethiprole sulfone ( $[\text{M}+\text{H}]^+$ ;  $m/z$  412.9848). ....103

**Figure 55.** MALDI-imaging-HRMS of a transversal cross-section of soybean flower after treatment with ethiprole (spatial resolution: 25  $\mu\text{m}$ , scan area: 3625x8250  $\mu\text{m}$ ). Localization of ethiprole ( $[\text{M}+\text{Na}]^+$ ;  $m/z$  418.9718), ethiprole sulfone ( $[\text{M}+\text{H}]^+$ ;  $m/z$  412.9848) and ethiprole monodechloro ( $[\text{M}+\text{Na}]^+$ ;  $m/z$  385.01082). ....103

**Figure 56.** MALDI-imaging-HRMS of a transversal cross-section of soybean flower after treatment with ethiprole (spatial resolution: 25  $\mu\text{m}$ , scan area: 3625x8250  $\mu\text{m}$ ). Localization of ethiprole ( $[\text{M}+\text{Na}]^+$ ;  $m/z$  418.9718). ....104

<b>Figure 57.</b> Proposed degradation pathway of propineb into propineb-DIDT and PTU with assigned incorporation of spiked stable isotope-labeled propineb-DIDT ( $^{13}\text{C}_3, ^{15}\text{N}$ propineb-DIDT) used for the MALDI-imaging experiment. ....	106
<b>Figure 58.</b> MALDI-imaging-HRMS of tomato leaf 1 h after treatment with propineb (spatial resolution: 25 $\mu\text{m}$ , scan area: 5000x5000 $\mu\text{m}$ ). <b>b-d</b> Localization of propineb ( $[\text{3M}-2\text{Zn}]^{2+}$ ; m/z 368.9000), $^{13}\text{C}_3, ^{15}\text{N}$ propineb-DIDT ( $[\text{M}+\text{H}]^+$ ; m/z 194.9837), propineb-DIDT ( $[\text{M}+\text{H}]^+$ ; m/z 190.9766), $^{13}\text{C}_3, ^{15}\text{N}$ PTU ( $[\text{M}+\text{H}]^+$ ; m/z 121.0552) and PTU ( $[\text{M}+\text{H}]^+$ ; m/z 117.0481). ....	107
<b>Figure 59.</b> Expanded region of MALDI mass spectrum acquired of the WG70 application solution (200 ppm propineb) after dried-dropled method on a gold plate without MALDI matrix at beginning of the experiment. Metabolite PTU ( $\text{C}_4\text{H}_9\text{N}_2\text{S}$ ) was already detected in the application formulation. ....	108
<b>Figure 60.</b> MALDI-imaging-HRMS of tomato leaf 3 days after treatment with propineb (spatial resolution: 25 $\mu\text{m}$ , scan area: 5000x5000 $\mu\text{m}$ ). <b>b-d</b> Localization of propineb ( $[\text{3M}-2\text{Zn}]^{2+}$ ; m/z 368.9000), $^{13}\text{C}_3, ^{15}\text{N}$ propineb-DIDT ( $[\text{M}+\text{H}]^+$ ; m/z 194.9837), propineb-DIDT ( $[\text{M}+\text{H}]^+$ ; m/z 190.9766), $^{13}\text{C}_3, ^{15}\text{N}$ PTU ( $[\text{M}+\text{H}]^+$ ; m/z 121.0552) and PTU ( $[\text{M}+\text{H}]^+$ ; m/z 117.0481). ....	109
<b>Figure 61.</b> Expanded region of MALDI mass spectrum acquired of the WG70 application solution (200 ppm propineb) after dried-dropled method on a gold plate without MALDI matrix at the end of the experiment. $^{13}\text{C}_3, ^{15}\text{N}$ PTU was detected in the application solution. ....	110
<b>Figure 62.</b> MALDI-imaging-HRMS of tomato leaf 7 days after treatment with propineb (spatial resolution: 25 $\mu\text{m}$ , scan area: 5000x5000 $\mu\text{m}$ ). <b>b-d</b> Localization of propineb ( $[\text{3M}-2\text{Zn}]^{2+}$ ; m/z 368.9000), $^{13}\text{C}_3, ^{15}\text{N}$ propineb-DIDT ( $[\text{M}+\text{H}]^+$ ; m/z 194.9837), propineb-DIDT ( $[\text{M}+\text{H}]^+$ ; m/z 190.9766), $^{13}\text{C}_3, ^{15}\text{N}$ PTU ( $[\text{M}+\text{H}]^+$ ; m/z 121.0552) and PTU ( $[\text{M}+\text{H}]^+$ ; m/z 117.0481). ....	111
<b>Figure 63.</b> MALDI-imaging-HRMS of tomato leaf 14 days after treatment with propineb (spatial resolution: 25 $\mu\text{m}$ , scan area: 5000x5000 $\mu\text{m}$ ). <b>b-d</b> Localization of propineb ( $[\text{3M}-2\text{Zn}]^{2+}$ ; m/z 368.9000), $^{13}\text{C}_3, ^{15}\text{N}$ propineb-DIDT ( $[\text{M}+\text{H}]^+$ ; m/z 194.9837), propineb-DIDT ( $[\text{M}+\text{H}]^+$ ; m/z 190.9766), $^{13}\text{C}_3, ^{15}\text{N}$ PTU ( $[\text{M}+\text{H}]^+$ ; m/z 121.0552) and PTU ( $[\text{M}+\text{H}]^+$ ; m/z 117.0481). ....	112
<b>Figure 64.</b> MALDI-imaging-HRMS of tomato leaf after treatment with propineb (spatial resolution: 40 $\mu\text{m}$ , scan area: 9000x8000 $\mu\text{m}$ ). Localization of propineb ( $[\text{3M}-2\text{Zn}]^{2+}$ ; m/z 368.9000), propineb-DIDT ( $[\text{M}+\text{H}]^+$ ; m/z 190.9766) and PTU ( $[\text{M}+\text{H}]^+$ ; m/z 117.0481). ....	114
<b>Figure 65.</b> Experimental setup for root uptake of isotianil in wheat ( <i>Triticum</i> ) using a hydroponic system. ....	133
<b>Figure 66.</b> Tomato plants ( <i>Solanum lycopersicum</i> ) after acclimatization in the hydroponic test system. ....	134

<b>Figure 67.</b> Experimental setup for root uptake of <sup>14</sup> C-labeled DCIT-acid in tomato ( <i>Solanum lycopersicum</i> ) using a hydroponic system. ....	134
<b>Figure 68.</b> Single droplet application of isotianil on tomato ( <i>Solanum lycopersicum</i> ).....	135
<b>Figure 69.</b> Leaf application of isotianil and DCIT-acid on tomato ( <i>Solanum lycopersicum</i> ). ....	136
<b>Figure 70.</b> Tomato plant ( <i>Solanum lycopersicum</i> ) treated with DCIT-acid at day of application. ....	136
<b>Figure 71.</b> Leaf application of isotianil and DCIT-acid on banana ( <i>Musa</i> ).....	137
<b>Figure 72.</b> Sample preparation for MALDI MSI experiments of banana leaf ( <i>Musa</i> ) treated with <sup>14</sup> C-labeled DCIT-acid. ....	138
<b>Figure 73.</b> Grape vine ( <i>Vitis vinifera</i> ) plants for quantification of fluopyram at t6 (259 days after application, fruits begin to swell).....	138
<b>Figure 74.</b> Single grape vine ( <i>Vitis vinifera</i> ) plant for quantification of fluopyram at t2 (49 days after application, 50% leaves fallen).....	139
<b>Figure 75.</b> Dry grape vine ( <i>Vitis vinifera</i> ) plant tissues for quantification of fluopyram before extraction.....	139
<b>Figure 76.</b> Maize ( <i>Zea mays</i> ) treated with cyprosulfamide and Thiencarbazon-methyl on different leaves.....	140
<b>Figure 77.</b> Single maize leaf ( <i>Zea mays</i> ) treated with cyprosulfamide.....	140
<b>Figure 78.</b> Single droplet application of propineb on tomato ( <i>Solanum lycopersicum</i> ).....	141
<b>Figure 79.</b> Optical image of tomato leaf ( <i>Solanum lycopersicum</i> ) with single droplet application of Propineb. Propineb as a WG70 formulation produces a homogenous layer on the tissue (left). Propineb mixed with HCCA produces a mesh of crystals on the tissue (right). ....	141
<b>Figure 80.</b> HR-ESI-MS mass spectrum in positive ion mode for mass range m/z 392.06-402.06 of fluopyram (C <sub>16</sub> H <sub>11</sub> ON <sub>2</sub> ClF <sub>6</sub> ). ....	154
<b>Figure 81.</b> HR-ESI-MS/MS mass spectrum in positive ion mode of fluopyram (398.06@36 HCD). ....	154
<b>Figure 82.</b> Example of ion chromatograms for quantification of fluopyram measured in SRM mode. ....	155
<b>Figure 83.</b> Single pixel (20 μm) high resolution mass spectrum obtained from MALDI mass spectrometry experiments in 2,6-DHB. Mass spectrum in positive ion mode for mass range m/z 392.06-402.06. Fluopyram was identified based on high mass accuracy (≤ 5 ppm), labelled with measured mass and charge carrier. ....	155
<b>Figure 84.</b> Single pixel (20 μm) high resolution mass spectrum obtained from MALDI mass spectrometry experiments in HCCA. Mass spectrum in positive ion mode for mass range m/z 303.16-313.16. Tebuconazole (C <sub>16</sub> H <sub>22</sub> ON <sub>3</sub> Cl) was identified based on high mass accuracy (≤ 5 ppm), labelled with measured mass and charge carrier. ....	156

**Figure 85.** Single pixel (20  $\mu\text{m}$ ) high resolution mass spectrum obtained from MALDI mass spectrometry experiments in HCCA. Mass spectrum in positive ion mode for mass range  $m/z$  319.14-329.14. Hydroxy-Tebuconazole ( $\text{C}_{16}\text{H}_{22}\text{O}_2\text{N}_3\text{Cl}$ ) was identified based on high mass accuracy ( $\leq 5$  ppm), labelled with measured mass and charge carrier.....156

**Figure 86.** Single pixel (20  $\mu\text{m}$ ) high resolution mass spectrum obtained from MALDI mass spectrometry experiments in universal matrix (HCCA:DHB, 1:1,v/v). Mass spectrum in positive ion mode for mass range  $m/z$  386.04-396.04. TCM ( $\text{C}_{12}\text{H}_{14}\text{O}_8\text{N}_4\text{S}_2$ ) was identified based on high mass accuracy ( $\leq 5$  ppm), labelled with measured mass and charge carrier. ....157

**Figure 87.** Single pixel (20  $\mu\text{m}$ ) high resolution mass spectrum obtained from MALDI mass spectrometry experiments in universal matrix (HCCA:DHB, 1:1, v/v). Mass spectrum in positive ion mode for mass range  $m/z$  380.10-380.10. CSA ( $\text{C}_{18}\text{H}_{18}\text{O}_6\text{N}_2\text{S}$ ) was identified based on high mass accuracy ( $\leq 5$  ppm), labelled with measured mass and charge carrier. ....157

**Figure 88.** Single pixel (20  $\mu\text{m}$ ) high resolution mass spectrum obtained from MALDI mass spectrometry experiments in HCCA. Mass spectrum in positive ion mode for mass range  $m/z$  186.98-196.98. Propineb-DIDT ( $\text{C}_6\text{H}_6\text{N}_2\text{S}_3$ ) was identified based on high mass accuracy ( $\leq 6$  ppm), labelled with measured mass and charge carrier.....158

**Figure 89.** Single pixel (20  $\mu\text{m}$ ) high resolution mass spectrum obtained from MALDI mass spectrometry experiments in HCCA. Mass spectrum in positive ion mode for mass range  $m/z$  112.06-122.06. Propineb-PTU ( $\text{C}_4\text{H}_8\text{N}_2\text{S}$ ) was identified based on high mass accuracy ( $\leq 5$  ppm), labelled with measured mass and charge carrier.....158

**Figure 90.** Single pixel (20  $\mu\text{m}$ ) high resolution mass spectrum obtained from MALDI mass spectrometry experiments in HCCA. Mass spectrum in positive ion mode for mass range  $m/z$  96.08-1036.08. Propineb-PU ( $\text{C}_4\text{H}_8\text{N}_2\text{O}$ ) was identified based on high mass accuracy ( $\leq 5$  ppm), labelled with measured mass and charge carrier.....159



## List of tables

<b>Table 1.</b> Mode of actions and FRAC code of selected fungicides (Hermann and Stenzel, 2019).....	6
<b>Table 2.</b> Mode of actions and HRAC code of selected herbicides (Befa et al., 2019). ....	11
<b>Table 3.</b> Mode of actions and IRAC code of selected insecticides (Nauen et al., 2019).....	13
<b>Table 4.</b> Overview of ionization methods for mass spectrometry imaging (Benninghoven, 1994, Nemes et al., 2008, Gerbig et al., 2015, Boughton et al., 2016).....	18
<b>Table 5.</b> Overview of mass spectrometers used for mass spectrometry imaging (Boughton et al., 2016, Buchberger et al., 2018).....	19
<b>Table 6.</b> Chromatographic Parameters LTQ-Orbitrap.....	34
<b>Table 7.</b> Chromatographic Parameters LTQ-Orbitrap XL. ....	34
<b>Table 8.</b> Chromatographic Parameters Fusion.....	35
<b>Table 9.</b> MALDI matrix selection based on the signal intensity for isotianil and DCI-acid using the dried-droplet method. ....	40
<b>Table 10.</b> Uptake results of isotianil and DCIT-acid in hydroponic grown tomato.....	44
<b>Table 11.</b> Distribution of [ <sup>14</sup> C]-DCIT-acid in tomato plants. ....	44
<b>Table 12.</b> Distribution of [ <sup>14</sup> C] DCIT-acid in tomato flower after root uptake of DCIT-acid (250 µg/L) for 34 days. ....	45
<b>Table 13.</b> Uptake of <sup>14</sup> C-PCA in hydroponic grown grapevine. ....	68
<b>Table 14.</b> Uptake of PCA in hydroponic grown grape vine ( <i>Vitis vinifera</i> ). ....	69
<b>Table 15.</b> Quantification of PCA in grape vine ( <i>Vitis vinifera</i> ).....	70
<b>Table 16.</b> Fluopyram residues [mg/kg] in selected tissues of grape vine ( <i>Vitis vinifera</i> ) after foliar application (750 g a.i./ha) during the whole winter period.....	73
<b>Table 17.</b> Physiochemical properties of isotianil. ....	143
<b>Table 18.</b> Physiochemical properties of DCIT-acid.....	143
<b>Table 19.</b> Physiochemical properties of fluopyram. ....	143
<b>Table 20.</b> Physiochemical properties of PCA. ....	144
<b>Table 21.</b> Physiochemical properties of tebuconazole.....	144
<b>Table 22.</b> Physiochemical properties of thiencarbazon-methyl.....	144
<b>Table 23.</b> Physiochemical properties of cyprosulfamide.....	144
<b>Table 24.</b> Physiochemical properties of ethiprole.....	145
<b>Table 25.</b> Physiochemical properties of propineb.....	145
<b>Table 26.</b> List of agrochemicals and metabolites.....	146
<b>Table 27.</b> Dry weight of grape vine ( <i>Vitis vinifera</i> ) plant tissues for quantification of fluopyram. ....	150

